Efficient Computation of Thermoacoustic Modes

vorgelegt von
Georg Atta Mensah, M.Sc.

Von der Fakultät V – Verkehrs- und Maschinensysteme
der Technischen Universität Berlin
zur Erlangung des akademischen Grades

Doktor der Ingenieurwissenschaften
– Dr.-Ing. –

genehmigte Dissertation

Promotionsausschuss:

Vorsitzende:	Prof. Dr.-Ing. Neda Djordjevic	TU Berlin
Gutachter:	Prof. Dr.-Ing. Jonas P. Moeck	NTNU Trondheim
Gutachter:	Prof. Matthew Juniper, Ph.D.	University of Cambridge
Gutachter:	Prof. Franck Nicoud, Ph.D.	Université de Montpellier
Gutachter:	Prof. Dr.-Ing. Christian Oliver Paschereit	TU Berlin

Tag der wissenschaftlichen Aussprache: 28. November 2018

Berlin 2019

Danksagung

Diese Dissertation habe ich im Rahmen meiner wissenschaftlichen Tätigkeit an der Technischen Universität Berlin von 2013 bis 2018 angefertigt. An dieser Stelle möchte ich meinen Dank Personen entgegenbringen, ohne deren Mithilfe die Anfertigung dieser Promotionsschrift niemals zustande gekommen wäre.

Mein Dank gilt zunächst meinem Doktorvater Herrn Prof. Jonas Moeck für die Betreuung dieser Arbeit und für die wissenschaftliche und methodische Unterstützung während der gesamten Bearbeitungsphase meiner Dissertation. Die zahlreichen Gespräche im Verlauf meiner Promotion und die hilfreichen Anmerkungen zu den betrachteten Problemstellungen werden mir immer als bereichernder und konstruktiver Austausch in Erinnerung bleiben. Diese Förderung hat auch früh Früchte getragen, so dass bereits unsere erste gemeinsame Veröffentlichung mit einem Best Paper Award ausgezeichnet wurde und ich somit gleich in der Arbeit bestärkt wurde.

Herrn Prof. Oliver Paschereit möchte ich für sein kurzfristiges Einspringen als mein Gutachter danken.

Ferner möchte ich meinen beiden anderen Gutachtern Prof. Matthew Juniper und Prof. Franck Nicoud ein herzliches Thank you und Merci sagen. Ihre vorangegangene Forschung hat diese Arbeit entschieden beeinflusst und ich hoffe, dass die dargelegten Erkenntnisse auch in umgekehrter Weise hilfreich sein werden.

Frau Prof. Neda Djordjevic danke ich für die Übernahme des Vorsitzes des Promotionsausschusses.

Erwähnt sei hier auch mein ehemaliger Kollege Joshua Gray, mit dem ich mir drei Jahre ein kleines Büro teilen durfte, bis es zu einer Damentoilette umgestaltet wurde. Die gemeinsame Arbeitszeit hat mir stets viel Spaß bereitet. Ihm danke ich für das kurzfristige Korrekturlesen und den fun with languages.

Des Weiteren danke ich für die Korrektur von Teilen dieser Arbeit und die vielen tollen Gespräche: Meinen Kollegen Myles Bohon, Sophie Knechtel und Alessandro Orchini. Einen besonderen Dank möchte ich an dieser Stelle noch an Philip Buschmann richten, der viele Kapitel korrigiert und der mir bei jeder Frage prompt geantwortet hat. Vor ein paar Jahren fing er an, mich als studentischer Mitarbeiter bei den ersten Implementierungen unseres Python-Codes zu unterstützen. Es freut mich daher sehr, dass er jetzt der Doktorand für den Code sein wird.

Ein weiteres Dankeschön gilt Luca Magri und Camilo Silva sowie erneut Alessandro Orchini, mit denen ich zusammen auf viele Probleme eine Lösung gefunden habe. Die ergebnisreichen Diskussionen haben mir immer Freude bereitet und die vielen wertvollen Anregungen haben mich in meiner Forschungsarbeit in beträchtlichem Maße vorangebracht.

Danke auch an meine anderen Kollegen und Mitarbeiter des Instituts, die mich sofort in ihre Gruppe aufgenommen haben. Die freundschaftliche Atmosphäre an unserem Institut hat mich immer gerne zur Arbeit gehen lassen. Auch die Arbeit an unserem Drei-Mann-Fachgebiet bleibt mir dank der kameradschaftlichen Zusammenarbeit mit Olaf Bölke in guter Erinnerung. Er griff mir glücklicherweise unter die Arme, wenn ich dann doch einmal ein Experiment mit Studenten machen musste und rettete somit nicht nur mich sondern auch das gesamte HF-Gebäude.

Dank gilt natürlich auch meinen Eltern und Geschwistern Ludwig und Martin. Sie haben stets ein offenes Ohr und mich immer auf meinem Weg bestärkt.

Nicht zuletzt danke ich aber Sarah für ihre Geduld, wenn ich die Wochenenden mit dem Anfertigen von Manuskripten verbrachte, ihre Unterstützung bei der Übersetzung französischsprachiger Literatur und umfangreiches Korrekturlesen.

Georg Atta Mensah
Berlin, Oktober 2018

Zusammenfassung

Moderne Gasturbinen sind eine Schlüsseltechnologie für eine zuverlässige und nachhaltige Energieversorgung. Damit die strengen Emissionsgesetzgebungen eingehalten werden können, werden magere Vormischflammen eingesetzt. Das macht die Maschinen anfällig für selbstangeregte Pulsationen des Druckes sog. thermoakustische Instabilitäten. Diese Schwingungen werden von der Wechselwirkung instationärer Wärmefreisetzung mit den akustischen Resonanzmoden der Brennkammer verursacht. Gasturbinen, die thermoakustische Instabilitäten aufweisen, verursachen mehr Lärm, einen höheren Schadstoffausstoß und haben eine geringere Effizienz.
Schlimmstenfalls führen die verursachten Schwingungen zu einem Totalausfall der Maschine. Die Verfügbarkeit effizienter numerischer Methoden zur Modellierung thermoakustischer Instabilitäten ist daher essentiell für die Gasturbinen-Entwicklung. In einer frühen Entwurfsphase kommen typischerweise lineare Methoden wie akustische Netzwerkmodelle oder Helmholtz-Löser zum Einsatz. Diese resultieren in Eigenwertproblemen, welche nicht-linear in ihrem Eigenwert sind.

Diese Arbeit trägt dazu bei, Lösungsalgorithmen für diese Probleme zu verbessern. Blochwellen-Theorie wird verwendet, um die diskrete Rotationssymmetrie annularer Brennkammern zur Reduktion des Rechengebietes zu nutzen. Anstatt des gesamten Annulus wird nur ein Brennkammer-Segment zur Berechnung benötigt. Dies verringert die Größe der Diskretisierungsmatrizen und dementsprechend den Berechnungsaufwand.

Bestehende adjungierten-basierte Störungsmethoden werden erweitert, um Approximationen beliebiger Ordnung für die Lösung nicht-linearer Eigenwertprobleme zu finden. Dies reduziert den Rechenaufwand umfangreicher Parameterstudien. Die Theorie hat zahlreiche Anwendungen. U.a. wird die Anwendung der Theorie zur schnellen Grenzzyklus-Berechnung und zur Unsicherheitsanalyse ohne den Einsatz von Monte-Carlo-Simulationen diskutiert. Die Störungstheorie ermöglicht die Formulierung verbesserter iterativer Lösungsverfahren für das thermoakustische Eigenwertproblem. Es wird gezeigt, dass eine Kombination dieser Verfahren mit integrationsbasierten Eigenwertlösern in der Lage ist, alle Eigenfrequenzen in einem vorgegebenen Bereich der komplexen Zahlenebene mit hoher Genauigkeit zu finden.

Die Arbeit betont die Implementierung der vorgestellten Methoden in einem FEM-basierten Helmholtz-Löser. Ein Rijke-Rohr und ein annularer Modellbrenner werden zur Veranschaulichung der Theorie genutzt. Sie lässt sich jedoch auch auf industrielle Brennkammern anwenden.

Zusätzlich zu diesen Verbesserungen der Lösungstheorie des thermoakustischen Eigenwertproblems werden Parameterkombinationen, die zu einer unendlich großen Sensitivität der Eigenfrequenz in Bezug auf Veränderungen in diesen Parametern führen, diskutiert. Die Rolle dieser sog. exceptional points für das Verständnis intrinsischer thermoakustischer Moden sowie die Folgen der unendlichen Sensitivität für die vorgestellten Lösungsverfahren werden ausgeführt.

Abstract

Modern gas turbines are a key technology for reliable and sustainable power generation. In order to meet strict emission regularizations they utilize lean premixed combustion. This renders the engines susceptible to self-excited pressure oscillations known as thermoacoustic instabilities. These oscillations arise from an interaction of the unsteady heat release of the flame and the acoustic resonant modes of the combustor. Gas turbines exhibiting thermoacoustic instabilities have higher noise and pollutant emissions and suffer from decreased efficiency. In the worst case, structural vibrations caused by the thermoacoustic oscillations can even lead to a complete failure of the machine. The availability of efficient numerical methods for the modeling of thermoacoustic instabilities is, thus, crucial for gas turbine design. At an early design stage modal approaches such as acoustic network models or Helmholtz solvers are commonly deployed to assess thermoacoustic instabilities. They result in eigenvalue problems that are nonlinear with respect to the eigenvalue.

This thesis aims at improving solution algorithms for these problems. Bloch-wave theory is used to exploit the discrete rotational symmetry of annular combustion chambers. Most importantly, this allows for a reduction of the necessary computational domain from the full annulus to a single burner-flame segment only. Thus, the size of the discretization matrices and, ultimately, the computational effort to solve the problem will shrink accordingly.

Existing adjoint-based perturbation methods are extended to find arbitrary-order power series expansions to the solutions of nonlinear eigenvalue problems. This reduces the computational costs of extensive parameter studies. Various applications may benefit from the perturbation theory. For example, how to use this theory for fast limit-cycle computations and Monte-Carlo-free uncertainty quantification of the model results is discussed. Moreover, the perturbation theory allows for the formulation of enhanced iterative solution schemes to solve thermoacoustic eigenvalue problems. Combination of these schemes with integration-based eigenvalue solvers is shown to find all eigenfrequencies in a predefined subset of the complex plane at high accuracy.

The thesis emphasizes how to implement the presented methods into a FEM-based Helmholtz solver. A non-dimensionalized Rijke tube and a laboratory annular model combustor serve as the main test cases for the demonstration of the theory. However, the findings are also applicable to models of industrial combustion chambers.

In addition to these improvements to the solution of thermoacoustic eigenvalue problems, parameter combinations that yield eigenfrequencies featuring an infinite sensitivity with respect to changes in the parameters are discussed. It is shown that these so-called exceptional points play a role in the understanding of intrinsic thermoacoustic modes and the implications of infinite sensitivity to the presented solution algorithms are discussed.

Contents

List of Figures

List of Tables

List of Algorithms

Nomenclature

Acronyms

BC	boundary condition
DoF	degree of freedom
EP	exceptional point
EVP	eigenvalue problem
FDF	flame describing function
FEM	finite element method
FTF	flame transfer function
LES	large eddy simulation
MC	Monte Carlo
PDF	probability density function
RF	risk factor
TF	transfer function
UQ	uncertainty quantification

Greek Symbols

α	attenuation coefficient	1/s
Γ	boundary contour	-
γ	ratio of specific heats	-
δ	Dirac's delta	-
ε	perturbation parameter	-
$\boldsymbol{\mu}$	multi-index	-
ρ	density	kg/m^3

σ	standard deviation	-
τ	time delay	s
φ	angular coordinate	-
Φ	shape function	-
$\psi_{\tilde{b}}$	periodic part of Bloch wave with wavenumber b	-
Ω	domain	-
ω	complex frequency / eigenvalue	Hz

Roman Symbols

B	degree of discrete rotational symmetry	-
$\mathbf{B}$	boundary mass matrix	-
b	Bloch wavenumber	-
c	speed of sound	m/s
$\mathbf{C}$	damping matrix	-
$d(\vec{x})$	distribution	-
e	mass-specific internal energy	J/kg
$\mathbf{F}$	flame matrix without FTF	-
$\mathbb{F}$	set of FEM ansatz functions	
$\mathbf{K}$	stiffness matrix	-
$\mathcal{L}$	linear operator family	-
$\mathbf{L}$	discretized linear operator family	-
$\mathbf{M}$	mass matrix	-
n	interaction index	-
$\vec{n}$	outward pointing unit normal	-
p	pressure	Pa
p_0	static pressure	Pa
$\mathbf{Q}$	flame matrix	-
$\mathcal{Q}$	heat release operator	-
q	heat release rate	W
$R_{\text{sp.}}$	specific gas constant	J/(kg·K)

$\mathcal{R}_{\pm}$	reflection operator	-
r	right hand term	-
r	radial coordinate	m
$\mathcal{R}_B$	discrete rotational operator of degree B	-
T	temperature	K
t	time	s
V	volume	m^3
v	mass-specific volume	m^3/kg
$\vec{u}$	fluid velocity	m/s
$\mathbf{W}$	Fourier matrix	-
$\mathbf{X}$	some matrix	-
x	Cartesian coordinate	m
$\mathbf{Y}$	some matrix	-
y	Cartesian coordinate	m
z	Cartesian coordinate	m
Z	impedance	-

Superscripts

$(\cdot)^{\dagger}$	adjoint
$(\cdot)^{\Psi}$	pseudo-inverse / pseudo-solution
$(\cdot)^{\{n\}}$	nth iterate
$(\cdot)'$	fluctuating quantity
$(\cdot)^{\mathrm{H}}$	Hermitian transposed
$\overline{(\cdot)}$	complex conjugate
$\widehat{(\cdot)}$	Fourier transform

Subscripts

$(\cdot)_{\mathrm{EP}}$	value at an exceptional point
$(\cdot)_{\tilde{b}}$	Bloch wave of Bloch wavenumber b

Other Symbols

$[L/M]$	Padé approximant with numerator order L and denominator order M
$\langle\cdot\vert\cdot\rangle$	scalar product

Introduction

Motivation

This thesis concerns efficient computation methods for thermoacoustic instabilities. Their relevance in engineering arises from their occurrence in technical devices such as gas turbines and rocket engines. Especially, modern gas turbines are prone to this phenomenon. Ultimately, this is due to environmental reasons. Figure 1 shows the contribution of various economical sectors to the total emission of nitrogen oxides (NO_X) in the European Union in 2016. 17% of the emission are related to the energy production and distribution sector. NO_X is a pollutant gas that causes acid rain, contributes to the formation of ozone in the atmosphere, and is harmful to health. Ever stricter environmental regulations aim at reducing the emissions of NO_X. This triggered a shift in gas-turbine design from diffusion flames to lean premixed combustion. Due to a lower flame temperature, gas turbines operating in lean-premixed mode emit much less NO_X. However, these turbines have a higher susceptibility to thermoacoustic instabilities [2, 3], Thermoacousticly driven oscillations in gas turbines may cause flash-back, blow-off, high thermal loads of the components, and strong vibrations inducing structural damage. In the worst case, they can lead to the complete failure of the engine [4].

In the Paris agreement, the international community has declared to limit the increase of the average global temperature to 2K as compared to preindustrial levels. Although renewable energy technologies such as wind turbines or solar plants will, thus, become more and more important, gas turbines will still play an essential role in the energy sector. Because of the operational flexibility of the engines, they are ideally suited to compensate for the fluctuations of the energy production from renewable sources. This makes them a key component of reliable power grids. Moreover, if the fuel produced from renewable materials, gas turbines become a carbon-neutral energy technology.

For environmental as well as economical reasons there is, thus, a need to develop reliable gas turbines. This thesis improves existing tools for the numerical assessment of thermoacoustic stability.

History and basic concepts

Although the research interest of the gas-turbine community is a development of the last decades, the fundamentals of this phenomenon are known for more than 100 years.

Presumably, Higgins gave the first scientific report of the phenomenon in 1777 [5]. He observed that a flame inside a tube is capable of producing sound and named this a *singing flame*. In 1858,

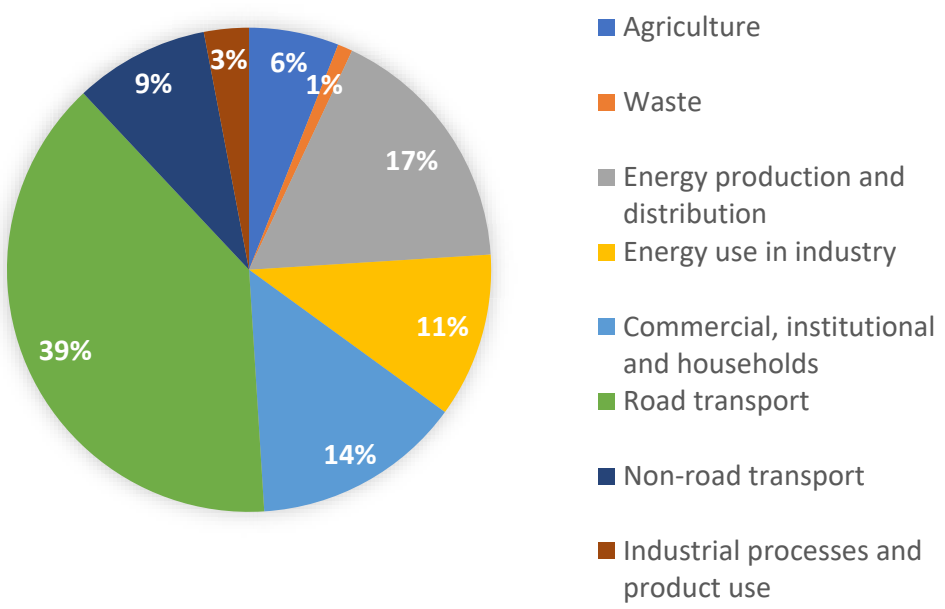

Figure 1: Share of various economical sectors on the total NO_X-emissions in the EU in 2016. Adapted from [1].

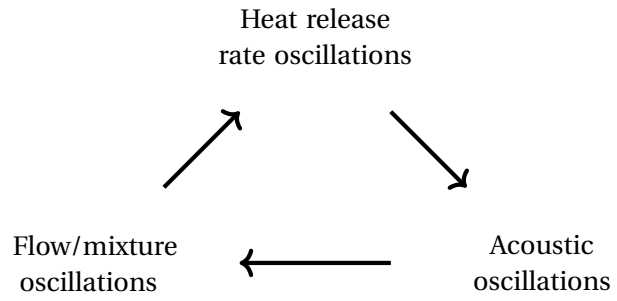

Figure 2: Thermoacoustic feedback loop. Illustration adapted from [8].

LeConte described the pulsation of a flame when excited with audible music [6]. This pulsation was synchronous with the beat of the music. In 1859, Rijke observed a similar phenomenon in a vertical tube in which he placed a heated metal gauze [7]. If the gauze was placed in the lower half of the tube, the configuration generated noise.

These experiments demonstrate possible interactions of acoustic waves and unsteady sources of heat. Indeed, the experiments of Higgins and Rijke are examples for thermoacoustic instabilities. They contain the same essential physics that also drive thermoacoustic instabilities in modern gas turbines and other devices. Figure 2 illustrates the feedback loop causing the phenomenon. Oscillations in the heat release rate can trigger acoustic fluctuations, which in turn influence the flow and mixture conditions. These can lead to a fluctuation in the heat release again. Under certain conditions the feedback loop becomes unstable and generates a thermoacoustic instability.

It was Lord Rayleigh who first stated a necessary criterion for this to happen: thermoacoustic instabilities may occur if the fluctuation in the heat release q' and the pressure p' are sufficiently

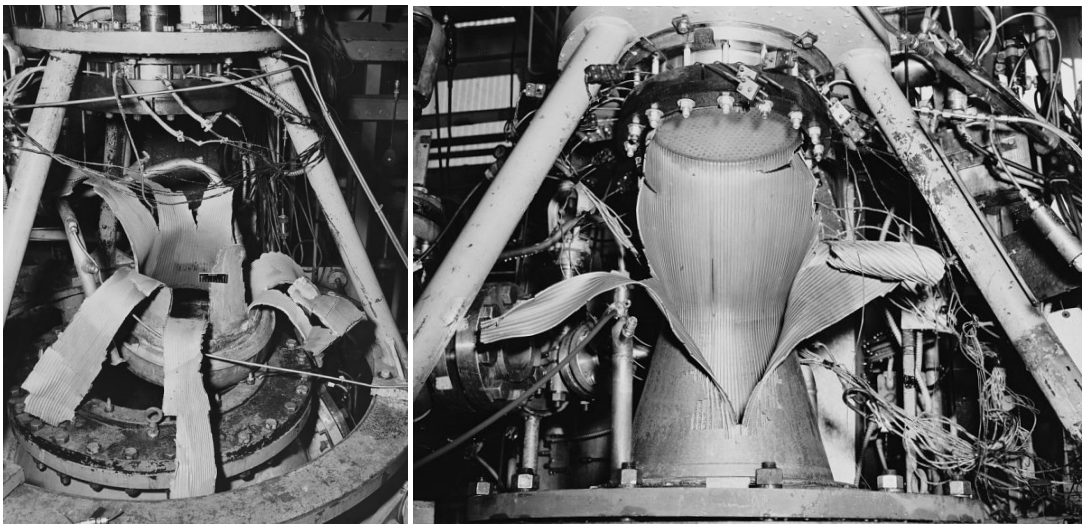

Figure 3: Broken liquid rocket engines. The damage is caused by thermoacoustic instabilities encountered during engine tests conducted by NASA 1958 (left) and 1960 (right). (Imagery is taken from the Library of Congress, Reproduction Numbers HAER OH-124-A-35 and HAER OH-124-A-46) .

in-phase [9]. More precisely, it is necessary that the acoustic energy produced by the interaction of the unsteady heat release and the pressure oscillations is greater than the losses in the considered system. The Rayleigh criterion is, hence, written as

$$\int_V \int_0^T q' p' \, \mathrm{d}t \, \mathrm{d}\vec{x} > \text{acoustic energy dissipation.} \tag{1}$$

Here, T is the period of oscillation and V the control volume.

While these first discussions of thermoacoustic phenomena were purely academic in nature, the interest has dramatically increased in the course of the cold-war's space programs. This was because rocket engines are highly susceptible to combustion instabilities [10]. Figure 3 shows the damage to liquid rocket engines caused by combustion instabilities. However, the capacity of computer hardware was rather poor at the time. Using complex mathematical models for thermoacoustic stability assessment was, thus, not feasible. Hence, the design of rocket engines was strongly based on full-scale tests. For instance, the F-1 engines of the Saturn V underwent more than 3200 full-scale tests between October 1962 and September 1966, approximately 2000 of which were concerned with combustion instabilities [11].

As mentioned before, emission regulations have also made thermoacoustic instabilities a relevant topic in gas turbine design.

Numerical modeling of thermoacoustic instabilities

A key challenge in modeling thermoacoustic instabilities is the broad number of physical mechanisms that can close the thermoacoustic feedback loop. Possible mechanisms include fluctuations in the equivalence ratio [12], vortex-induced fluctuations of the flame surface [13], entropy waves [14], and strain rate effects leading to hydrodynamically unstable flames [15]. A general discussion

of the energy transfer of small disturbances in fluid flow and , therefore, of possible mechanisms closing the thermoacoustic feedback loop can be found in [16]. However, to date the process is not yet fully understood and research effort continues to fully explain the phenomenon with experimental and numerical studies [17].

Numerical modeling methods must resolve the relevant physics to an adequate degree. Due to the high computational costs, direct numerical simulation that resolves the complete physics is only used to study fundamental academic flame configurations (e.g., [18] or [19]).

Large eddy simulations (LES) are better suited to obtain detailed information on thermoacoustic instabilities [20]. LES shows reasonable agreement to results obtained from experiments and can be used to derive input quantities for other stability analysis tools [21, 22]. Only recently, the available computer technology allowed for LES of complete annular combustion chambers [23, 24]. However, these simulations require massively parallel computer architectures. Consequently, extensive parameter studies are extremely expensive. Moreover, because only the combustion chamber and not the entire gas turbine can be currently simulated, complicated incorporation of boundary conditions at the combustor inlet and outlet is needed. Therefore, LES is no option for early stage gas turbine design [17].

An alternative with very low computational costs is low order network modeling [25, 26, 27]. Network models simplify the problem by grouping entities like ducts, injectors, and chambers and defining mostly linear physically or empirically justified relations between the inputs and outputs of these parts. The acoustics in these models are incorporated in terms of a flame transfer function which relates the heat release rate fluctuations to perturbations in the upstream velocity [28] or transfer matrices [29]. A dispersion relation is then derived, whose solution yields mode frequencies and growth rates as well as the associated mode shapes. The computational effort of these methods is low and the resulting frequencies and growth rates may provide a good estimate for those of the actual system. It is, however, difficult to take into account detailed effects such as a spatially distributed flame response, especially when these features are not acoustically compact.

Models based on linearized balance equations that were transformed to frequency domain provide a good compromise between the computational effort and the accuracy of the results. They fully resolve the combustor geometry and, thus, yield a three-dimensional description of the mode shape. As for the network models, the flame response may be incorporated in terms of flame transfer functions and transfer matrices. In the simplest case, inviscid linearized Euler equations for a quiescent medium are considered. In frequency domain, this yields a Helmholtz equation with non-self-adjoint term accounting for the flame response [30]. As shown in [31], it is possible to model entropy-wave induced instabilities with a Helmholtz solver. Moreover, damping effects due to hydrodynamic-acoustic interactions can be included by means of internal boundary conditions [32]. However, the usage of the complete linearized Euler equations and even linearized Navier–Stokes equations becomes increasingly popular in the thermoacoustic community [33, 34, 35].

Flame response modeling

Because of the complex physics, it is common to use black box models to describe the response of the flame to acoustic fluctuations. In the linear limit transfer functions are used for this purpose. They link the axial acoustic velocity fluctuations u' upstream of the flame to the fluctuations of the

heat release q' in the flame

$$q'(t) = \frac{q_0}{u_0} \mathrm{FTF}(t) * u'(t). \tag{2}$$

While the flame transfer functions depend on many parameters like the engine geometry, the operating conditions, and the deployed fuel, they typically show a low-pass and phase-shifting behavior. The phase shift can be attributed to convective time scales of the underlying feedback mechanisms. A simple model that picks up this idea is the n–τ-model [28]:

$$q'(t) = \frac{q_0}{u_0} n u'(t-\tau). \tag{3}$$

Numerical modeling techniques currently used to deduce the flame transfer function of a given configuration include G-equation models [36], direct numerical simulations [19], and large eddy simulations [22].

In contrast to rocket applications, the acoustic amplitudes in gas turbines are comparatively low. Therefore, a acoustic description of the problem in terms of linear gas dynamics is still a good modeling assumption. However, even at low acoustic amplitudes the flame response might show a significant nonlinear behavior [17]. Because flame transfer functions are linear, they cannot capture such effects. Flame describing functions have been suggested to fill this gap [37, 38]. They additionally depend on the amplitude level of the velocity fluctuation. This allows to model phenomena like limit cycles.

Challenges in solving linearized equations

Although the combination of flame transfer functions and linearized balance equations yields adequate tools that meet the requirements of gas-turbine design, there is still potential to improve these methods. A key challenge is that the models constitute eigenvalue problems that depend nonlinearly on their eigenvalues. This is due to the time-lag of the flame transfer function and may also be caused by frequency-depended impedance boundary conditions [30]. The dependence of the solution on model parameters is only implicitly known and the models need to be solved for each new parameter set. The same problem arises in other fields. For instance, in quantum mechanics Schrödinger's equation also constitutes an eigenvalue problem. However, perturbation theory and other methods are well established tools to ease the solution of Schrödinger's equation [39]. These tools can be applied to other fields involving eigenvalue problems. For example, spectral perturbation methods are deployed for the analysis of hydrodynamic stability [40]. Nevertheless, Schrödinger's equation is a linear eigenvalue problem and the problems encountered in hydrodynamic stability analysis are, typically, linear or quadratic with respect to their eigenvalue. Application of these methods for thermoacoustic problems, thus, requires a proper adaptation of the theory. Only recently, the thermoacoustic community started to apply these methods, beginning with [41]. This thesis discusses how to further reduce the computational costs when using numerical models for thermoacoustic stability assessment.

Scope of the thesis

The reductions in computational costs result from

(i) exploitation of the symmetry of annular combustion chambers in a Bloch-wave framework,

(ii) extensive usage of perturbation theory, and

(iii) utilization of advanced solution algorithms for nonlinear eigenvalue problems.

Examples considering the thermoacoustic Helmholtz equation will demonstrate the findings. Yet, the presented theory is not limited to this equation an can be readily used with models based on the linearized Euler and linearized Navier–Stokes equations which resolve more aspects of the relevant physics.

The thesis is divided into four parts:

Part I summarizes the fundamental theory to an extent that is necessary to understand the questions and ideas discussed in this work. Chapter 1 presents a detailed derivation of the thermoacoustic Helmholtz equation. The three model configurations that are used throughout the thesis are introduced in Chap. 2. They constitute a Rijke tube, a Kronig–Penney model, and the MICCA annular combustor. An overview of the finite element method with a particular emphasis of its benefits when solving the thermoacoustic adjoint Helmholtz equation is given in Chap. 3. Chapter 4 is the first of four chapters discussing the theory of nonlinear eigenvalue problems as they arise from the discretization of the thermoacoustic Helmholtz equation. It introduces key notions and theorems and summarizes the solution algorithms presented in [30], which is currently the standard algorithm in the thermoacoustic community.

Part II focuses on the discrete rotational symmetry of annular combustion chambers. It explains Bloch's theorem in Chap. 5 which allows for reducing the computational domain of perfectly symmetric combustion chambers to a single cell. Large order perturbation theory for nonlinear eigenvalue problems is derived in Chap. 6 to handle cases where the symmetry of the combustion chamber is broken. How, to compute limit cycles of thermoacoustic modes in annular combustors using both Bloch-wave theory and perturbation methods is shown in Chap. 7.

Indeed, perturbation theory is a versatile tool. Consequently, Part III discusses applications of the perturbation theory that go beyond annular combustion chambers. In Chap. 8 rapidly converging solution algorithms for nonlinear eigenvalue problems are tailored from this theory. Chapter 9 discusses how to use it for fast Monte-Carlo-free uncertainty quantification.

Part IV is literally exceptional. It contains only a single chapter discussing so called *exceptional points* in spectra of thermoacoustic systems. These points are deeply linked to the asymptotic perturbation theory presented before as they define the radius of convergence of the stipulated power series. Moreover, they are the centers of regions in the parameter space featuring extremely high sensitivities and play a role in the modeling of intrinsic thermoacoustic modes.

Note that all presented methods are implemented in the Helmholtz solver PyHoltz that was developed at TU Berlin in the course of this thesis. The Python code is publicly available for download [1].

[1] `https://bitbucket.org/pyholtzdevelopers/public`

Part I

Fundamentals

Chapter 1

The thermoacoustic Helmholtz equation

This chapter shortly discusses the derivation of the thermoacoustic Helmholtz equation which serves as a main model equation for thermoacoustic instabilities in this thesis. A comprehensive introduction to acoustics can be found in [42] and a short derivation of the necessary equations in the context of thermoacoustics instabilities is given in [30]. A detailed discussion of the heat release term and combustion instabilities in general is presented in [43, chapters 4 and 9].

The thermoacoustic Helmholtz equation is derived from the mass balance, the momentum balance, and the entropy balance of an ideal gas for which nonviscid flow is assumed:

$$\frac{\partial \rho}{\partial t} + \nabla \cdot \left(\rho \vec{u}\right) = 0, \tag{1.1}$$

$$\frac{\partial \rho \vec{u}}{\partial t} + \nabla \cdot \left(\rho \vec{u} \vec{u}\right) = -\nabla p, \tag{1.2}$$

$$\frac{\partial s}{\partial t} + \vec{u} \cdot \nabla s = \frac{q}{\rho T}. \tag{1.3}$$

Here, t denotes the time, ρ the density, $\vec{u}$ the velocity, p the pressure, s the volumetric entropy, T the temperature and q the volumetric heat release rate. Assuming a fluid at rest and only small perturbations, splitting all quantities into a temporarily constant mean field $(\cdot)_0$ and a fluctuating part $(\cdot)'$

$$p = p_0 + p' \tag{1.4}$$

$$\vec{u} = \vec{u}' \tag{1.5}$$

$$s = s_0 + s' \tag{1.6}$$

$$T = T_0 + T' \tag{1.7}$$

$$q = q_0 + q' \tag{1.8}$$

leads to the following linearized balances:

$$\frac{\partial \rho'}{\partial t} + \nabla \cdot \left(\rho_0 u'\right) = 0, \tag{1.9}$$

$$\rho_0 \frac{\partial \vec{u}'}{\partial t} = -\nabla p', \tag{1.10}$$

$$\frac{\partial s'}{\partial t} = \frac{q'}{\rho_0 T_0}. \tag{1.11}$$

In order to combine these three balances, a connection between the pressure, the density, and the entropy is needed:

$$\frac{\mathrm{D}\, p}{\mathrm{D}\, t} = \left.\frac{\partial p}{\partial \rho}\right|_{s=\text{const.}} \frac{\mathrm{D}\,\rho}{\mathrm{D}\, t} + \left.\frac{\partial p}{\partial s}\right|_{\rho=\text{const.}} \frac{\mathrm{D}\, s}{\mathrm{D}\, t}. \tag{1.12}$$

The partial derivatives in this relation can be obtained from the law of a calorically perfect ideal gas undergoing an adiabatic compression $\frac{p}{\rho^\gamma} = \text{const.}$ and Gibbs' law for an isochoric process $\frac{\partial e}{\partial s}|_{\rho=\text{const.}} = T$. Here, $\gamma := \frac{c_p}{c_v}$ denotes the ratio of specific heats, with c_p and c_v being the heat capacity at constant pressure and constant volume, respectively. e denotes the internal energy.

Starting with the adiabatic compression, the following reasoning for $\left.\frac{\partial p}{\partial \rho}\right|_{s=\text{const.}}$ is found:

$$p = p_0 \rho_0^{-\gamma} \rho^\gamma \qquad |\frac{\partial}{\partial \rho} \tag{1.13}$$

$$\frac{\partial p}{\partial \rho} = p_0 \rho_0^{-\gamma} \gamma \rho^{\gamma-1} \qquad |\text{evaluate at } \rho = \rho_0 \tag{1.14}$$

$$\left.\frac{\partial p}{\partial \rho}\right|_0 = p_0 \rho_0^{-1} \gamma = \gamma R_{\text{sp.}} T_0. \tag{1.15}$$

Here, $R_{\text{sp.}}$ denotes the specific gas constant.

In order to find $\left.\frac{\partial p}{\partial s}\right|_{\rho=\text{const.}}$, Gibbs equation is utilized. Because in this partial derivative ρ is kept constant, the process can be seen as isochoric. Hence, the following reasoning holds:

$$\mathrm{d}e = T\mathrm{d}s - p\mathrm{d}v \qquad |\mathrm{d}v = \mathrm{d}\left(\frac{1}{\rho}\right) = 0 \tag{1.16}$$

$$c_v \mathrm{d}T = T\mathrm{d}s \qquad |\text{ideal gas: } T = pv/R_{\text{sp.}} \tag{1.17}$$

$$c_v \frac{v}{R_{\text{sp.}}} \mathrm{d}p = \frac{pv}{R_{\text{sp.}}} \mathrm{d}s \tag{1.18}$$

$$\left.\frac{\partial p}{\partial s}\right|_0 = \frac{p_0}{c_v}. \tag{1.19}$$

Thus, for a fluid at rest the following linearized pressure-density-entropy relation is obtained:

$$\frac{\partial p'}{\partial t} = \underbrace{\gamma R_{\text{sp.}} T_0}_{:=c_0^2} \frac{\partial \rho'}{\partial t} + \frac{p_0}{c_v} \frac{\partial s'}{\partial t}. \tag{1.20}$$

Here, the substitution $c_0 = \sqrt{\gamma R_{\text{sp.}} T_0}$ denotes the mean field of the speed of sound. That this value is truly the velocity at which acoustic waves travel, can be directly concluded from the final result of this section.

Introducing the linearized mass balance (1.9) and entropy balance (1.11) into the above rela-

tion yields

$$\frac{\partial p'}{\partial t} + c_0^2 \rho_0 \nabla \cdot u' = \frac{p_0}{c_v} \frac{q'}{\rho_0 T_0}, \tag{1.21}$$

which can be rearranged to

$$\nabla \cdot \vec{u}' = -\frac{1}{\rho_0 c_0^2} \frac{\partial p'}{\partial t} + \frac{p_0}{c_v \rho_0^2 c_0^2 T_0} q'. \tag{1.22}$$

Taking the divergence of the linearized momentum balance (1.10) results in

$$\frac{\partial}{\partial t} \nabla \cdot \vec{u}' + \nabla \cdot \left(\frac{1}{\rho_0} \nabla p' \right) = 0. \tag{1.23}$$

Inserting (1.22) into this equation gives

$$-\frac{\partial}{\partial t} \frac{1}{\rho_0 c_0^2} \frac{\partial p'}{\partial t} + \frac{p_0}{c_v \rho_0^2 c_0^2 T_0} \frac{\partial}{\partial t} q' + \nabla \cdot \left(\frac{1}{\rho_0} \nabla p' \right) = 0 \tag{1.24}$$

$$\Leftrightarrow \frac{\partial^2 p'}{\partial t^2} - \frac{p_0}{c_v \rho_0 T_0} \frac{\partial}{\partial t} q' - \rho_0 c_o^2 \nabla \cdot \left(\frac{1}{\rho_0} \nabla p' \right) = 0. \tag{1.25}$$

Because $\rho_0 c_0^2 = \rho_0 \gamma R T_0 = \gamma p_0$ - or equivalently $\frac{1}{\rho_0} = \frac{c_0^2}{p_0 \gamma}$ - the above equation amounts to

$$\frac{\partial^2 p'}{\partial t^2} - \frac{p_0}{c_v \rho_0 T_0} \frac{\partial}{\partial t} q' - \gamma p_0 \nabla \cdot \left(\frac{c_0^2}{p_0 \gamma} \nabla p' \right) = 0. \tag{1.26}$$

For a fluid at rest there cannot be any pressure gradient. Therefore, the static pressure field is also constant in space: $p_0(\vec{x}) = \text{const.}$. This allows to rearrange equation (1.26) to

$$\frac{\partial^2 p'}{\partial t^2} - \frac{p_0}{c_v \rho_0 T_0} \frac{\partial}{\partial t} q' - \nabla \cdot \left(c_0^2 \nabla p' \right) = 0. \tag{1.27}$$

Leveraging the ideal gas law again, it can be shown that

$$\frac{p_0}{c_v \rho_0 T_0} = \frac{R}{c_v} = \frac{c_p - c_v}{c_v} = \frac{c_p - c_v}{c_v} \frac{\frac{1}{c_v}}{\frac{1}{c_v}} = \gamma - 1. \tag{1.28}$$

Hence, the following inhomogeneous wave equation is finally obtained:

$$\nabla \cdot \left(c_0^2 \nabla p' \right) - \frac{\partial^2 p'}{\partial t^2} = -(\gamma - 1) \frac{\partial q'}{\partial t}. \tag{1.29}$$

This equation characterizes acoustic pressure fluctuations as waves traveling at speed c_0, hence, the name speed of sound. Unsteady heat release is identified as a source for acoustic perturbations.

Converting the thermoacoustic wave equation into the frequency domain by means of the Fourier transform $(\cdot)'(t) \mapsto \widehat{(\cdot)} \exp(\mathrm{i}\omega t)$, an inhomogeneous Helmholtz equation is obtained:

$$\nabla \cdot (c_0^2 \nabla \widehat{p}) + \omega^2 \widehat{p} = -\mathrm{i}\omega(\gamma - 1) \widehat{q}. \tag{1.30}$$

Here, $\hat{p}$ denotes the pressure fluctuation amplitude, and $\hat{q}$ the Fourier transform of the volumetric unsteady heat release rate, ω the complex frequency of oscillation. Note that by the given conventions the ngetaive imgainary part of ω indicates the growth rate of the mode.

Boundary conditions

Of course, this equation has to be solved with appropriate boundary conditions. These are commonly modeled in terms of impedances Z or reflection coefficients R. The wall impedance is defined as the ratio of the pressure fluctuation amplitude $\hat{p}$ and the normal component of the velocity fluctuation amplitude $\hat{\vec{u}}$ at a wall or more precisely a domain boundary

$$Z_{\text{wall}} := \frac{\hat{p}}{\hat{\vec{u}} \cdot \vec{n}}. \tag{1.31}$$

For convenience the impedance might be non-dimensionalized using the local speed of sound and the local density at the wall:

$$Z = \frac{Z_{\text{wall}}}{\rho_0 c_0}. \tag{1.32}$$

The non-dimensionalized impedance is referred to as normalized impedance.

Together with the Fourier transform of the linearized momentum balance

$$\hat{\vec{u}} = \frac{\mathrm{i}}{\rho_0 \omega} \nabla \hat{p}, \tag{1.33}$$

this definition allows to specify all boundary conditions in terms of a Robin condition:

$$\hat{p} - Z_{\text{wall}} \hat{\vec{u}} \cdot \vec{n} = 0 \tag{1.34}$$

$$\hat{p} - \frac{\mathrm{i} Z_{\text{wall}}}{\omega \rho_0} \nabla \hat{p} \cdot \vec{n} = 0 \tag{1.35}$$

$$\hat{p} - \frac{\mathrm{i} c_0 Z}{\omega} \nabla \hat{p} \cdot \vec{n} = 0. \tag{1.36}$$

In these equations $\vec{n}$ denotes a outwards-pointing unit vector. All three conditions are equivalent. In this thesis the formulation with the normalized impedance will be utilized, because as compared to the thermoacoustic Helmholtz equation the only new modelling quantity is Z.

Alternatively, boundary conditions can be specified in terms of the reflection coefficient. It is defined as the ratio of the amplitudes of an incoming and the corresponding reflected wave at a boundary. The conversion of the impedance to the reflection coefficient is given by the formula

$$R = \frac{Z - 1}{Z + 1}. \tag{1.37}$$

The different scientific communities use various names for the boundary associated with vanishing pressure fluctuation or a vanishing normal component of the velocity fluctuation or a freely propagating acoustic wave. Table 1.1 summarizes the various notions for these boundary conditions. In general, the impedance is a frequency dependent function

Table 1.1: Special impedances with corresponding reflection coefficients, physical interpretations and their common names.

impedance	**reflexion coeff.**	**physics**	**name**
$Z = 0$	$R = -1$	$\widehat{p} = 0$	sound soft, pressure node
$Z = 1$	$R = 0$	$\widehat{p} = \rho_0 c_0 \widehat{\vec{u}} \cdot \vec{n}$	non-reflecting, free field, anechoic
$Z = \infty$	$R = 1$	$\widehat{\vec{u}} \cdot \vec{n} = 0$	sound hard, pressure antinode, rigid wall

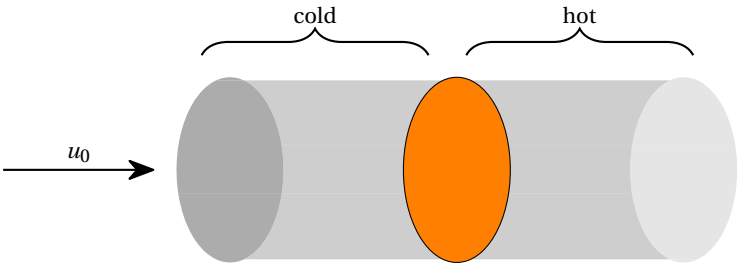

Figure 1.1: Illustration of the heat release relation. Fuel and oxidizer flow with constant mean value into a tube. The mean global heat release is then proportioal to the cross-sectional area (orange) and the mean velocity u_0.

$$Z = Z(\omega) \tag{1.38}$$

which is best obtained from experiments. However, mathematical modeling requires special care as the impedance should be analytic in ω [44].

Flame transfer function

Relating the fluctuations in heat release to the velocity fluctuation at a reference point by means of a flame transfer function closes the problem. This is because via the linearized momentum balance (1.10) the velocity fluctuation is in turn related to the pressure fluctuation amplitude at the same position.

$$\widehat{q} = \frac{q_0}{u_0} \mathrm{FTF}(\omega) \widehat{\vec{u}}_{\mathrm{ref}} \cdot \vec{n}_{\mathrm{ref}} = \frac{\mathrm{i} q_0}{u_0 \rho_{0,\mathrm{u}} \omega} \mathrm{FTF}(\omega) \left. \nabla \widehat{p} \right|_{\vec{x}_{\mathrm{ref}}} \cdot \vec{n}_{\mathrm{ref}} \tag{1.39}$$

where $\left. \nabla \widehat{p} \right|_{\vec{x}_{\mathrm{ref}}}$ denotes the gradient of the Fourier transform of pressure fluctuation at the reference position. This reference position is located somewhere in the unburnt gas region which is why the mean density there is denoted by $\rho_{0,\mathrm{u}}$. The thermoacoustic Helmholtz equation takes the form:

$$\nabla \cdot (c_0^2 \nabla \widehat{p}) + \omega^2 \widehat{p} = \frac{q_0}{u_0} \frac{\gamma - 1}{\rho_{0,\mathrm{u}}} \mathrm{FTF}(\omega) \left. \nabla \widehat{p} \right|_{\vec{x}_{\mathrm{ref}}} \cdot \vec{n}_{\mathrm{ref}}. \tag{1.40}$$

For simple tubular configurations the ratio $\frac{q_0}{u_0}$ can be deduced from the change in the speed of sound, assuming that there are no heat losses, a constant flow profile, and a homogeneous distribution of q_0 in the flame domain – i.e., $q_0 = Q_0 / V$ where Q_0 is the global heat release rate and V is the volume of the flame domain. The setup is illustrated in Fig. 1.1. Let A denote the

cross-section of the tube, then heat release in the tube is

$$Q_0 = \rho_{0,\mathrm{u}} c_p u_0 A \left(T_{0,\mathrm{b}} - T_{0,\mathrm{u}}\right). \tag{1.41}$$

Division by u_0 and multiplication with $\frac{\gamma-1}{\rho_{\mathrm{u}}}$ yields

$$\begin{aligned}
\frac{q_0}{u_0}\frac{\gamma-1}{\rho_{0,\mathrm{u}}} &= \frac{1}{V} c_p A (T_{0,\mathrm{b}} - T_{0,\mathrm{u}})(\gamma-1) = \frac{1}{V}\frac{c_p}{\gamma R} A\gamma \left(c_{0,\mathrm{b}}^2 - c_{0,\mathrm{u}}^2\right)(\gamma-1) && (1.42)\\
&= \frac{1}{V}\frac{c_p}{\gamma(c_p - c_v)} A\gamma \left(c_{0,\mathrm{b}}^2 - c_{0,\mathrm{u}}^2\right)(\gamma-1) = \frac{1}{V}\frac{1}{\gamma-1} A\gamma \left(c_{0,\mathrm{b}}^2 - c_{0,\mathrm{u}}^2\right)(\gamma-1) && (1.43)\\
&= \frac{A}{V}\gamma \left(c_{0,\mathrm{b}}^2 - c_{0,\mathrm{u}}^2\right). && (1.44)
\end{aligned}$$

However, the thermoacoustic Helmholtz equation is an eigenvalue problem with the eigenvalue ω and the corresponding mode shape $\widehat{p}$. Due to the flame transfer function, it is nonlinear in its eigenvalue. For convenience, the problem can be concisely written as

$$\mathcal{L}(\omega)\widehat{p} = 0 \tag{1.45}$$

where

$$\mathcal{L}(\omega)\widehat{p} := \nabla\cdot(c^2\nabla\widehat{p}) + \omega^2\widehat{p} - \frac{q_0}{u_0}\frac{\gamma-1}{\rho_{0,\mathrm{u}}}\,\mathrm{FTF}(\omega)\,\nabla\widehat{p}\big|_{\vec{x}_{\mathrm{ref}}}\cdot\vec{n}_{\mathrm{ref}}. \tag{1.46}$$

Obtaining a solution to the nonlinear eigenvalue problem is a computationally costly task. This is especially a problem if a large number of parameter sets is to be evaluated. The following chapters will discuss how to compute solutions and how to reduce the numerical costs to obtain them.

Limits of the thermoacoustic Helmholtz equation

Various assumptions have been made in order to derive this thermoacoustic wave equation. Most notably:

- diffusive effects like viscosity were neglected,
- volumetric forces like gravity and magnetism were neglected,
- the gas was assumed to behave like an ideal gas,
- the specific gas constant was assumed to be constant in time, i.e., no change in the molecular weight of the gas was assumed,
- the ratio of specific heats was assumed to be constant,
- the mean velocity was neglected,
- and the acoustic perturbations were assumed to be small.

At the time of writing of this thesis most industrial gas turbines operate with gas compositions which are essentially methane-air mixtures, for which the global-reaction equation

$$\mathrm{CH_4} + 2\left(\mathrm{O_2} + \frac{79}{21}\mathrm{N_2}\right) \longrightarrow \mathrm{CO_2} + 2\mathrm{H_2O} + \frac{158}{21}\mathrm{N_2} \tag{1.47}$$

indicates an isomolaric reaction. This is especially true, when considering that lean premixed combustion reduces the formation of nitrogen oxides. In general, lean premixed combustion utilizing air as an oxidizer can be seen as isomolaric, because large amounts of nitrogen do not participate in the combustion process. Thus, an isomolaric reaction process is a well justified assumption. However, for environmental reasons hydrogen combustion

$$2\mathrm{H_2} + \mathrm{O_2} \longrightarrow \mathrm{H_2O} \tag{1.48}$$

becomes more and more important. Thermoacoustic models for hydrogen-enriched combustion processes should, therefore, account for a change in the number of moles.

Neglecting the mean flow is definitely a strong assumption for gas turbines. Incorporation of the mean flow is possible using linearized Euler equations and linearized Navier–Stokes equations. Both give rise to eigenvalue problems that are nonlinear with respect to their eigenvalue [34]. The concepts derived in this thesis will, therefore, eqally ease the computation of thermoacoustic modes when using these models.

Chapter 2

Models

2.1 The Rijke tube

The simplest thermoacoustic devices are Rijke tubes. These are tubes which are equipped with a heat release source. They are named after Rijke who first discovered and described their ability to show thermoacoustic instabilities in [7]. This discovery is probably the earliest scientific investigation of thermoacoustic instabilities. To date Rijke tubes (and tubular configurations in general) are used as academic thermoacoustic models. This regards to both experimental (e.g., [45, 46, 47]) and numerical (e.g., [48, 30, 41, 49, 50]) studies. More references can be found in the review article of Raun et al. [51].

From a numerical viewpoint the Rjke tube can be considered as basically one-dimensional with a compact heat source. The thermoacoustic Helmholtz equation, hence, reads

$$\frac{\mathrm{d}}{\mathrm{d}x}\left(c^2\frac{\mathrm{d}}{\mathrm{d}x}\widehat{p}\right)+\omega^2\widehat{p}=Q\delta(x-x_{\mathrm{flm}})\left.\frac{\mathrm{d}}{\mathrm{d}x}\widehat{p}\right|_{x=x_{\mathrm{ref}}}. \tag{2.1}$$

Here, x_{flm} is the position of the heat source, i.e., the flame. Due to its assumed compactness, it is modeled as δ-function. x_{ref} is a reference position upstream of the flame where the velocity fluctuation governing the flame response is taken.

At the inlet and the outlet, impedance boundary conditions are to be prescribed:

$$\widehat{p}-\frac{\mathrm{i}cZ}{\omega}\frac{\mathrm{d}}{\mathrm{d}x}\widehat{p}=0. \tag{2.2}$$

The topology of the Rijke-tube model is depicted in Fig.2.1. Throughout this thesis when using the Rijke-tube model, the equations are considered to be non-dimensional as the thermoacoustic Helmholtz equation can be non-dimensionalized using a characteristic length scale $\tilde{L}$ and speed of sound $\tilde{c}$. This does not change the mathematical appearance of the equation. However, the heat release will be expressed by $Q=n\exp(-\mathrm{i}\omega\tau)$.

Non-dimensionalized or not, the simple model equations of the Rijke tube have the advantage

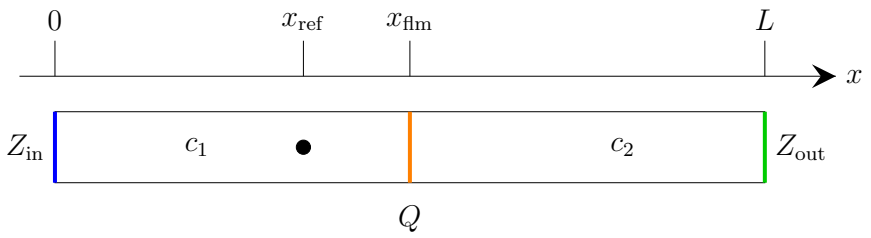

Figure 2.1: Illustration of the Rijke-tube set-up. A source term Q is set at the flame (orange) which is related to velocity fluctuations in the reference point (black dot). Different soundspeeds c_1 and c_2 are set upstream and downstream to the flame. Impedance Z_{in} and Z_{out} determine the boundary conditions at the inlet (blue) and the outlet (green) of the tube.

that they can be solved almost analytically [52] using the ansatz

$$\hat{p}(x) = \begin{cases} A\cos\left(\frac{\omega}{c_1}x\right) + B\sin\left(\frac{\omega}{c_1}x\right) & \text{for } x \in [0, x_{\mathrm{flm}}] \\ C\cos\left(\frac{\omega}{c_2}x\right) + D\sin\left(\frac{\omega}{c_2}x\right) & \text{for } x \in]x_{\mathrm{flm}}, L] \end{cases} \tag{2.3}$$

Here, A,B,C, and D are constants which are to be computed, in order to determine the mode shape corresponding to the eigenfrequency ω.

Evaluating the boundary conditions at the inlet yields

$$A\underbrace{\cos\left(\frac{\omega}{c_1}0\right)}_{=1} + B\underbrace{\sin\left(\frac{\omega}{c_1}0\right)}_{=0} + A\mathrm{i}Z_{\mathrm{in}}\underbrace{\sin\left(\frac{\omega}{c_1}0\right)}_{=0} - B\mathrm{i}Z_{\mathrm{in}}\underbrace{\cos\left(\frac{\omega}{c_1}x\right)}_{=1} = 0. \tag{2.4}$$

Analogously,

$$C\cos\left(\frac{\omega}{c_2}L\right) + D\sin\left(\frac{\omega}{c_2}L\right) + C\mathrm{i}Z_{\mathrm{in}}\sin\left(\frac{\omega}{c_2}L\right) - D\mathrm{i}Z_{\mathrm{in}}\cos\left(\frac{\omega}{c_2}L\right) = 0 \tag{2.5}$$

is found at the outlet.

Further equations result from the jump condition obtained when integrating across the flame:

$$\left[c^2\frac{\mathrm{d}}{\mathrm{d}x}\hat{p}\right]_{x_{\mathrm{flm}}^-}^{x_{\mathrm{flm}}^+} + \omega^2\int_{x_{\mathrm{flm}}^-}^{x_{\mathrm{flm}}^+}\hat{p}\,\mathrm{d}x = Q\left.\frac{\mathrm{d}}{\mathrm{d}x}\hat{p}\right|_{x=x_{\mathrm{ref}}}. \tag{2.6}$$

The second term is trivially zero because the antiderivative of $\hat{p}$ will be continuous

$$\int_{x_{\mathrm{flm}}^-}^{x_{\mathrm{flm}}^+}\hat{p}\,\mathrm{d}x = 0. \tag{2.7}$$

Hence, follows

$$\left[c^2\frac{\mathrm{d}}{\mathrm{d}x}\hat{p}\right]_{x_{\mathrm{flm}}^-}^{x_{\mathrm{flm}}^+} = Q\left.\frac{\mathrm{d}}{\mathrm{d}x}\hat{p}\right|_{x=x_{\mathrm{ref}}}. \tag{2.8}$$

Note that this relation is yielding a jump in the gradient of the pressure fluctuation amplitude even if there is no active flame fluctuation, i.e., $Q = 0$, but only a jump in the mean speed of sound.

The Fourier transform of the one-dimensional linearized momentum balance is $\mathrm{i}\omega\rho_0\widehat{u} = -\frac{\mathrm{d}}{\mathrm{d}x}\widehat{p}_0$. Furthermore, the jump in c is due to a jump in the mean temperature. Therefore, the jump in $c^2\,\frac{1}{\rho_0}$ – and consequently the above jump condition – can be interpreted as a jump condition for the velocity fluctuation. In particular, the velocity fluctuation will be continuous if there is no active flame.

Because the jump condition only affects the gradient of the pressure fluctuation, the pressure fluctuation itself must be continuous across the flame:

$$\left[\widehat{p}\right]_{x_{\mathrm{flm}}^-}^{x_{\mathrm{flm}}^+} = 0. \tag{2.9}$$

That the solution is continuous in $\widehat{p}$ is often derived by physical reasoning: Integration of the momentum balance (1.10) across the flame and assuming no accumulation of momentum proves the continuity. However, a mathematical rationale is necessary, to exclude the existence of discontinuous solutions. This aspect is important for the derivation of finite element schemes solving the thermoacoustic problem, as will be further discussed in Sec. 3.5.

Introducing the ansatz into Eq.(2.9) yields

$$C\cos\left(\frac{\omega}{c_2}x_{\mathrm{flm}}\right) + D\sin\left(\frac{\omega}{c_2}x_{\mathrm{flm}}\right) - A\cos\left(\frac{\omega}{c_1}x_{\mathrm{flm}}\right) - B\sin\left(\frac{\omega}{c_1}x_{\mathrm{flm}}\right) = 0 \tag{2.10}$$

and from Eq. (2.8)

$$\begin{aligned} &- C\omega c_2\sin\left(\frac{\omega}{c_2}x_{\mathrm{flm}}\right) + D\omega c_2\cos\left(\frac{\omega}{c_2}x_{\mathrm{flm}}\right) + A\omega c_1\sin\left(\frac{\omega}{c_1}x_{\mathrm{flm}}\right) - B\omega c_1\cos\left(\frac{\omega}{c_1}x_{\mathrm{flm}}\right) \\ &= Q\left[-A\frac{\omega}{c_1}\sin\left(\frac{\omega}{c_1}x_{\mathrm{ref}}\right) + B\frac{\omega}{c_1}\cos\left(\frac{\omega}{c_1}x_{\mathrm{ref}}\right)\right]. \end{aligned} \tag{2.11}$$

The equations (2.4),(2.5),(2.10), and (2.11) form an eigenvalue problem nonlinear in ω:

$$\mathbf{L}(\omega)\underbrace{\begin{bmatrix} A \\ B \\ C \\ D \end{bmatrix}}_{:=\boldsymbol{p}} = \begin{bmatrix} 0 \\ 0 \\ 0 \\ 0 \end{bmatrix} \tag{2.12}$$

where

$$\begin{aligned} [\mathbf{L}]_{1,1} &= 1, \qquad [\mathbf{L}]_{1,2} = -\mathrm{i}Z_{\mathrm{in}} \qquad [\mathbf{L}]_{1,3} = 0, \qquad [\mathbf{L}]_{1,4} = 0, \qquad [\mathbf{L}]_{2,1} = 0, \qquad [\mathbf{L}]_{2,2} = 0 \\ [\mathbf{L}]_{2,3} &= \cos\left(\frac{\omega}{c_2}L\right) + \mathrm{i}Z_{\mathrm{out}}\sin\left(\frac{\omega}{c_2}L\right), \qquad [\mathbf{L}]_{2,4} = \sin\left(\frac{\omega}{c_2}L\right) - \mathrm{i}Z_{\mathrm{out}}\cos\left(\frac{\omega}{c_2}L\right), \\ [\mathbf{L}]_{3,1} &= -\cos\left(\frac{\omega}{c_1}x_{\mathrm{flm}}\right), \qquad [\mathbf{L}]_{3,2} = -\sin\left(\frac{\omega}{c_1}x_{\mathrm{flm}}\right), \qquad [\mathbf{L}]_{3,3} = \cos\left(\frac{\omega}{c_2}x_{\mathrm{flm}}\right), \qquad [\mathbf{L}]_{3,4} = \sin\left(\frac{\omega}{c_2}x_{\mathrm{flm}}\right) \\ [\mathbf{L}]_{4,1} &= c_1\sin\left(\frac{\omega}{c_1}x_{\mathrm{flm}}\right) + \frac{Q}{c_1}\sin\left(\frac{\omega}{c_1}x_{\mathrm{ref}}\right), \qquad [\mathbf{L}]_{4,2} = c_1\cos\left(\frac{\omega}{c_1}x_{\mathrm{flm}}\right) + \frac{Q}{c_1}\cos\left(\frac{\omega}{c_1}x_{\mathrm{ref}}\right) \\ [\mathbf{L}]_{4,3} &= -c_2\sin\left(\frac{\omega}{c_2}x_{\mathrm{flm}}\right), \qquad [\mathbf{L}]_{4,4} = c_2\cos\left(\frac{\omega}{c_2}x_{\mathrm{flm}}\right). \end{aligned}$$

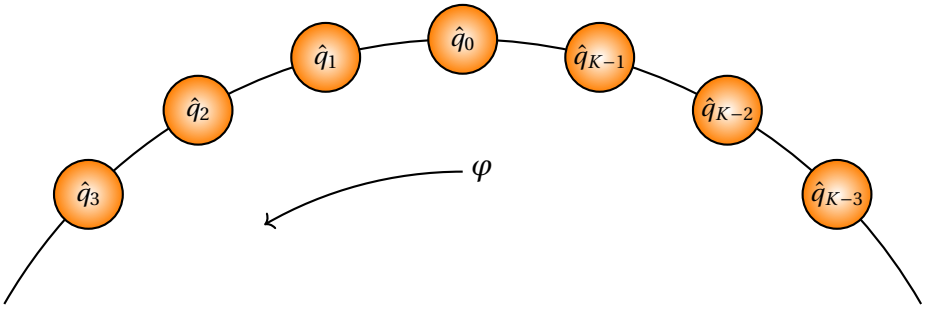

Figure 2.2: Schematic illustration of the topology of the Kronig-Penney model. K source terms are equidistantly arranged on a one-dimensional ring.

The eigenvalues of which can be found by computing the characteristic function from the determinant explicitly and using a numerical root-finding algorithm to find its roots. The corresponding mode shapes are then easily found by computing A, B, C, and D from the kernel.

The approach used to solve the Rijke-tube model can actually be generalized. This gives rise to the so-called lumped network models. These models describe thermoacoustic systems in terms of one-dimensional elements on which plane wave propagation is assumed. Ansatz functions which describe left and right traveling waves are stipulated for each individual element. Linking them together through appropriate continuity and jump conditions describing the connection between two adjacent elements is then resulting in a nonlinear eigenvalue problem. See, e.g., [25, 26, 53] for more details on this method. Apart from its application to the Rijke-tube model, in this thesis such a network approach is also used to solve the Kronig-Penney model presented in the next section.

2.2 The Kronig-Penney model

Modern gas turbines feature annular or can-annular combustion chambers, rendering them periodic in the azimuthal direction. A one-dimensional model featuring such a periodicity is the Kronig-Penney model. It has been originally devised to study the quantum-mechanical behavior of electrons in crystal lattices [54]. The conception of the model was triggered by the theorem of Bloch on how to easily compute solutions of the Schrödinger equation. Bloch's theorem and its application to combustion chambers is the topic of Chap. 5. A modified version of the Kronig-Penney model will, therefore, serve as an exemplifying mathematical model where the high complexity of a realistic combustor model prohibits its extensive study. The Kronig-Penney model has first been adapted in [55] as a surrogate for a realistic thermoacoustic model to illustrate the potential of Bloch's theorem. The model describes a one-dimensional ring featuring K equidistant flames $\hat{q}_k$ with point support. The topology of the model is illustrated in Fig. 2.2.

The model equations read:

$$\frac{\mathrm{d}^2}{\mathrm{d}\varphi^2}\hat{p} + \omega^2\hat{p} = -\mathrm{i}\omega \sum_{k=0}^{K} \hat{q}_k \delta\left(\varphi - k\frac{2\pi}{K}\right) \tag{2.13}$$

$$\hat{p}(2\pi) = \hat{p}(0). \tag{2.14}$$

Note that the Kronig-Penney model does not feature a distributed speed of sound. The eigenvalue

ω takes the interpretation of a wave number. The symbol ω is kept for consistency with the perturbation theory presented in the later chapters. Also note that because the model only accounts for the azimuthal dimension φ, it is impossible to link the flame responses $\widehat{q}_k$ to the axial gradient of $\widehat{p}$ at some reference point. For simplicity the flame response $\widehat{q}_k$ is, thus, related to $\widehat{p}(k\frac{2\pi}{K})$ directly, i.e.,

$$\widehat{q}_k = Q_k \widehat{p}\left(k\frac{2\pi}{K}\right). \tag{2.15}$$

Analogous to the Rijke-tube model of the previous section, analytic solutions to the model can be computed by a network approach. In contrast to the Rijke-tube model, the ansatz function is defined using a local coordinate $\varphi_k := \varphi - k\frac{2\pi}{K}$ at each sector between two flames $\widehat{q}_k$ and $\widehat{q}_{k+1}$, i.e.:

$$\widehat{p}(\varphi) = \widehat{p}_k(\varphi_k) := A_{2k}\cos\left(\omega\varphi_k\right) + A_{2k+1}\sin\left(\omega\varphi_k\right) \qquad \text{if} \qquad \varphi \in]k\frac{2\pi}{K}, (k+1)\frac{2\pi}{K}]. \tag{2.16}$$

The conditions across the flames are (i) continuity in the pressure fluctuation:

$$\widehat{p}_{k+1}(0) - \widehat{p}_k\left(\frac{2\pi}{K}\right) = 0 \tag{2.17}$$

$$\Rightarrow A_{2(k+1)} - A_{2k}\cos\left(\omega\frac{2\pi}{K}\right) - A_{2k+1}\sin\left(\omega\frac{2\pi}{K}\right) = 0 \tag{2.18}$$

and (ii) a jump in the derivative:

$$\frac{\mathrm{d}}{\mathrm{d}\varphi}\widehat{p}_{k+1}(0) - \frac{\mathrm{d}}{\mathrm{d}\varphi}\widehat{p}_k\left(\frac{2\pi}{K}\right) = -\mathrm{i}\omega Q_k \widehat{p}_{k+1}(0) \tag{2.19}$$

$$\Rightarrow \omega A_{2(k+1)+1} + \omega A_{2k}\sin\left(\omega\frac{2\pi}{K}\right) - \omega A_{2k+1}\cos\left(\omega\frac{2\pi}{K}\right) + \mathrm{i}\omega A_{2(k+1)}Q_k = 0. \tag{2.20}$$

Taking condition (2.18) and division of (2.20) by ω gives rise to the following eigenvalue problem:

$$\underbrace{\begin{bmatrix} -S & 1 & & & & & & & -C \\ -C & \mathrm{i}Q_0 & 1 & & & & & & S \\ & -C & -S & 1 & & & & & \\ & S & -C & \mathrm{i}Q_1 & 1 & & & & \\ & & & & \ddots & & & & \\ & & & & & -C & -S & 1 & \\ & & & & & S & -C & \mathrm{i}Q_{K-2} & 1 \\ & & & & & & & -C & -S & 1 \\ 1 & & & & & & & S & -C & \mathrm{i}Q_{K-1} \end{bmatrix}}_{:=\mathbf{L}(\omega)} \underbrace{\begin{bmatrix} A_1 \\ A_2 \\ A_3 \\ A_4 \\ \vdots \\ A_{2K-3} \\ A_{2K-2} \\ A_{2K-1} \\ A_{2K} \end{bmatrix}}_{:=\boldsymbol{p}} = \begin{bmatrix} 0 \\ 0 \\ 0 \\ 0 \\ \vdots \\ 0 \\ 0 \\ 0 \\ 0 \end{bmatrix} \tag{2.21}$$

Here, the abbreviations $S = \sin(\omega\frac{2\pi}{K})$ and $C = \cos(\omega\frac{2\pi}{K})$ are used.

Note that when choosing identical flame dynamics Q_k, the operator is a block-circulant matrix, i.e., cyclicly permuting the kth column by two entries is identical to the $k+2$nd column. Periodic-

matrix structures are a general feature of discretization matrices arising from periodic problems. Their eigenmodes are Fourier-like modes [56]. This can also be seen as a consequence of Bloch's theorem and will greatly simplify the computation of eigenvalues and eigenvectors. These aspects are further discussed in Chap. 5.

In this thesis n–τ-models will be deployed when considering the Kronig-Penney model: $Q_k := n_k \exp(-\mathrm{i}\omega\tau_k)$.

2.3 MICCA

The annular combustor geometry discussed in this section has been developed in the course of the "méthodes pour les instabilités de combustion couplées par l'acoustique" program at laboratoire EM2C in France and is, therefore, commonly referred to as MICCA. A main motivation for its development was the lack of experimental data to study the physics of combustion instabilities in annular combustors. Since its introduction in [57] the MICCA combustor has served as a laboratory scale platform and was investigated in various experimental and numerical studies [58, 59, 60, 61, 62, 63, 64, 65]. Due to the broad availability of data, it provides an optimal benchmark case for demonstrating novel computation methods. The model set-up in this work is similar to the one used by Laera et al. [62] to create a Helmholtz model of the MICCA combustor.

Like industrial annular and can-annular combustors, the MICCA combustor features a discrete rotational symmetry. In the case of the MICCA combustor the chamber can be circumferentially subdivided into 16 equal sections. Analogously to the jargon used in solid-state physics one such section is referred to as *unit cell*. In this work, the unit cells are defined from the centers of the flames. The corresponding unit cell is the set of points which are no closer to any other flame center, i.e., the unit cells are the intersection of the MICCA chamber with the Voronoi cells generated from the flame centers. In accordance to the grid classification scheme introduced by Brillouin in [66] for the modeling of free electrons in metals, such domain is also called the first Brillouin zone. Figure 2.3 shows the dimensions of one unit cell as it is used in the current work. While using any other set of 16 equally-spaced points on the circumference to define a unit cell, the specific choice of putting them on the center axis of the injectors has the advantage that the unit cells are additionally mirror-symmetric. A unit cell can, therefore, be split into two halves which will be referred to as half cells. For the MICCA chamber the half cells cannot be further reduced by exploiting a symmetry. In the jargon of crystals they correspond to irreducible Brillouin zone, see, e.g., [67].

Note that resolving the perforation of the matrix injectors would require elaborate meshing. The injector is, thus, modeled as two tubes with different diameters such that the blocking ratio is identical to the one of the matrix injectors. However, unlike the geometry in [62], the model does not include holes in the plenum as they are needed to fit pressure transducers connected to the combustion chamber. Nevertheless, these can be considered as acoustically compact and, therefore, neglected.

The symmetries of annular combustion chambers has useful consequences for the computation of their thermoacoustic modes. Most importantly it allows to compute the thermoacoustic modes from a single unit cell by Bloch-wave theory as will be discussed in Chap. 5. Special care is, therefore, necessary when creating a mesh for a numerical model of an annular combustor. For instance, the numerical mesh used in this thesis for the MICCA combustor is created in a three-step process. First the mesh of a half cell is generated. This mesh is then reflected to obtain

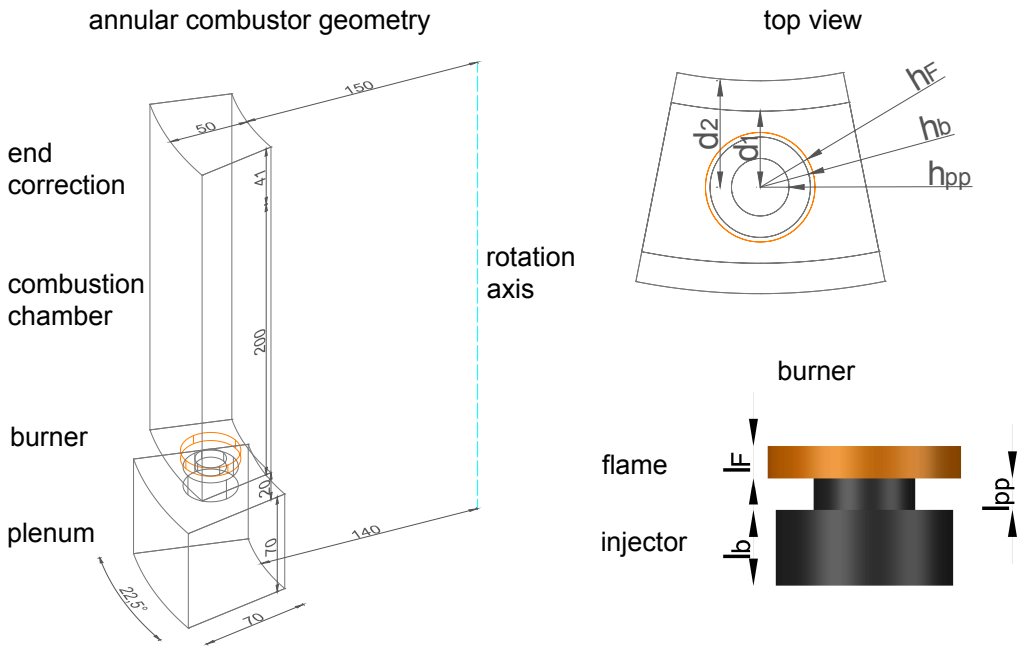

Figure 2.3: Dimensions of one burner flame segment of the MICCA combustor. The full combustor features 16 of these segments. Note that the azimuthal sides of the segments are no physical walls. The stated length are given in mm. $l_b = 14$mm, $l_{pp} = 6$mm, $l_F = 6$mm, $h_F = 18$mm, $h_b = 16.5$mm, $h_{pp} = 9.45$mm, $d_1 = 25$mm, $d_2 = 35$mm .

a unit cell. Finally, by creating rotated copies of the unit cell mesh, the full-combustor mesh is obtained. Figure 2.4 illustrates this process. The procedure guarantees that the numerical mesh features the same symmetry properties as the model to be discretized. The shown mesh is indeed the numerical mesh that will be used throughout the thesis for computations of the MICCA combustor. It is a tetrahedral mesh created with the open source mesh generation tool Gmsh version 2.15.0 . Table 2.1 lists the number of points, edges, and tetrahedra forming the half cell, the unit cell, and the full chamber. As will be explained in Chap. 3, the number of points and edges will determine the size of the discretized operator in a finite element analysis which utilizes quadratic ansatz functions. The mesh resolution is relatively high in the flame regions and the injectors. This is to accurately resolve the flame domains and the regions containing the reference points, which are located at the injector inlets. For the first axial and the first two azimuthal modes – which are the modes discussed in this thesis – it was confirmed that the mesh is sufficiently fine to yield

Table 2.1: Properties of the mesh used to discretize the MICCA model

	half	unit	full
points	115	179	2608
edges	543	958	14848
tetrahedra	329	658	10528

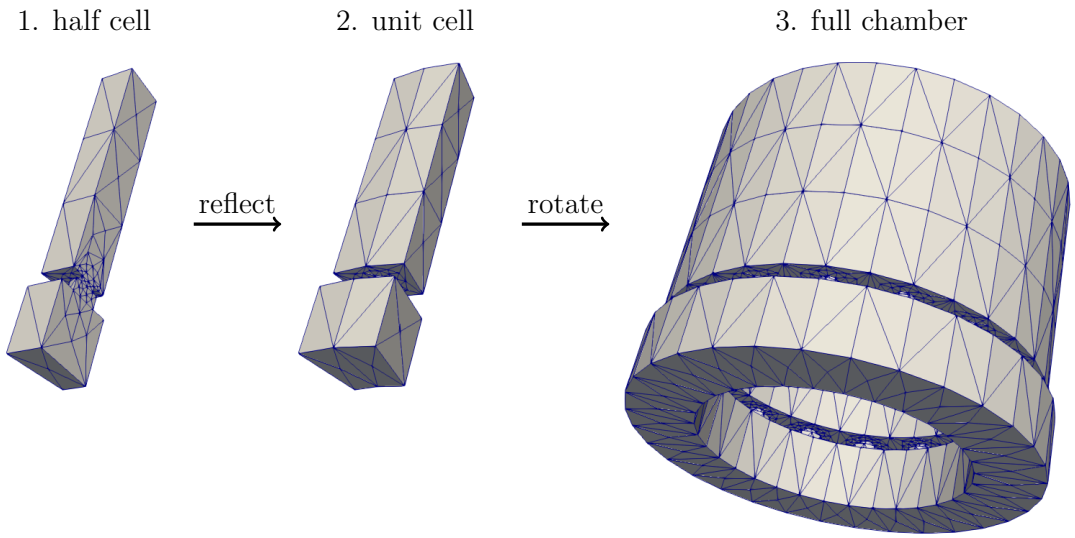

Figure 2.4: Illustration of a symmetry-preserving mesh generation procedure. First a mesh is created for a half cell. Then the mesh is reflected to create unit cell. Finally, by creating rotated copies of the unit cell the full combustor geometry is obtained. The depicted mesh is the mesh used throughout the thesis for the MICCA model.

mesh-independent results.

In order to model the open end, the length of the combustion chamber was extended by 41 mm and sound-soft boundary condition is set at the top end. This is in accordance to measurements that have shown a pressure node 41 mm above the combustor. All other boundaries are assumed to be sound hard. The thermodynamic properties of the gas are assumed to be identical with air. The local speed of sound is computed from the local temperature distribution. In the combustion chamber this distribution is obtained from interpolating measured data. The raw data for this interpolation was provided courtesy of Davide Laera. In the computational domain that was added to model the open end, the temperature is set constant. In the plenum and the injectors the temperature is assumed to be $T = 300\text{K}$. The temperature distribution is illustrated in Fig. 2.5. For each burner the mean heat release rate to velocity ratio is set to $Q_0/u_0 = 2080\text{W}/0.66\frac{\text{m}}{\text{s}} = 3151.51\frac{\text{kgm}}{\text{s}^2}$. These settings are the same as operating point B in [62]. The flame transfer function will also correspond to data given for this operating point. Yet, it will be a function not only of the frequency but also of the growth rate of a mode. This is done to obtain a function that is analytic in ω. How to process the measurement data in order to obtain this function will be discussed in Sec. 3.5.

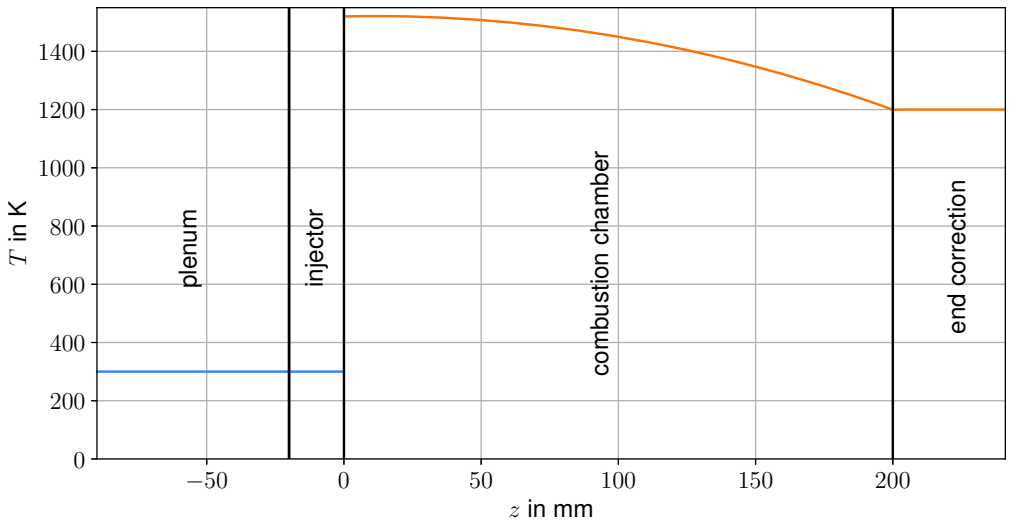

Figure 2.5: Temperature distribution set in the MICCA combustor model. The distribution is a function of the axial coordinate only. The coordinate system is centered at the bottom of the combustion chamber. Thus, negative values of z refer to positions below the combustion chamber, i.e., in the plenum and the injectors. The data is courtesy of Davide Laera and the same as used in [62] .

Chapter 3

Adjoints and finite element discretization

The perturbation theory introduced later will require an adjoint solution of the thermoacoustic Helmholtz equation. How to derive and interpret the adjoint thermoacoustic Helmholtz equation is discussed in this chapter. Adjoint equations are closely connected to finite element discretizations, as both arise from a weak form of the equation of interest [40]. Hence, details of the finite element method will also be discussed in this chapter as far as they concern the ideas of this thesis. For example, an important aspect frequently discussed in the literature is how the numerical solution obtained for the adjoint equation is affected by discretization [68, 40]. Often, different discretization matrices are obtained when either first adjoining a differential equation and then discretizing it or starting with a discretized system which is then adjoined. While the former is known as *continuous* adjoint, the latter is commonly referred to as *discrete* adjoint. For the Bubnov-Galerkin method discussed here, this distinction is irrelevant as both the continuous and the discrete adjoint approach will result in the same discretization matrices for this particular discretization method.

3.1 Weak form of the thermoacoustic Helmholtz equation

Both the adjoint and the finite element discretization of the thermoacoustic Helmholtz equation are obtained from its weak form. Given an inner product $\langle\cdot|\cdot\rangle$ and a linear equation

$$\mathcal{L}\,\widehat{p} = 0, \tag{3.1}$$

the weak form is obtained by taking the inner product of the equation with some test function $\widehat{\psi}$:

$$\left\langle \widehat{\psi} \middle| \mathcal{L}\,\widehat{p} \right\rangle = 0. \tag{3.2}$$

Here, $\mathcal{L}$ is a linear differential operator. In the applications discussed in this thesis it will be a family of operators $\mathcal{L}(z;\varepsilon)$ and the eigenvalues of this family will be of major interest. However, details of the parametrization of $\mathcal{L}$ in z and ε are not relevant for this chapter and, thus, not explicitly included in the notation.

The weak form (3.2) might be interpreted as a necessary condition for $\widehat{p}$ being a solution to (3.1). It must hold in an integral sense. Hence, all solutions of (3.1) will obviously satisfy (3.2). However, given a pair $\widehat{p}$ and $\widehat{\psi}$ that solves equation (3.2), the converse is not automatically true.

For this reason, the equation is named a *weak* formulation, as it imposes weaker conditions on $\widehat{p}$ than the original equation (3.1), which is often referred to as *strong* formulation. It is also the reason for calling $\widehat{\psi}$ a test function because the weak form is a test for $\widehat{p}$ being a solution of (3.1).

Depending on the scientific field and the given context, different names are used for the test function $\widehat{\psi}$. It might be referred to as adjoint solution[1]. This is because there exists a corresponding linear equation

$$\mathcal{L}^\dagger \psi = 0 \tag{3.3}$$

which if tested with the direct variable $\widehat{p}$, results in a weak form equivalent to (3.2):

$$\left\langle \mathcal{L}^\dagger \widehat{\psi} \middle| \widehat{p} \right\rangle = \left\langle \widehat{\psi} \middle| \mathcal{L}\widehat{p} \right\rangle \tag{3.4}$$

and this is the definition of the adjoint operator (compare (3.11)). It might also be called a weighting function, because the weak form (3.2) might be seen as weighted measure for the residual of (3.1) [69].

In this thesis the equation of interest is the thermoacoustic Helmholtz equation:

$$\nabla \cdot \left(c_0^2 \nabla \widehat{p}\right) + \omega^2 \widehat{p} - \frac{q_0}{u_0} \frac{\gamma - 1}{\rho_{0,\mathrm{u}}} \mathrm{FTF}(\omega)\, \nabla \widehat{p}\big|_{\vec{x}_{\mathrm{ref}}} \cdot \vec{n}_{\mathrm{ref}} = 0 \text{ in } \Omega \tag{3.5a}$$

$$\widehat{p} - \frac{\mathrm{i} c_0 Z}{\omega} \nabla \widehat{p} \cdot \vec{n} = 0 \text{ on } \partial\Omega \tag{3.5b}$$

and the inner product is given by multiplication and integration over the considered domain Ω:

$$\langle a | b \rangle = \int_\Omega \overline{a} b \, \mathrm{d}V. \tag{3.6}$$

Here, $\overline{a}$ denotes the complex conjugate of a.

The equation linearly combines different terms which can be individually cast into weak form due to the linearity of the inner product. For the Laplacian term, $\int_\Omega \overline{\widehat{\psi}} \nabla \cdot \left(c_0^2 \nabla \widehat{p}\right) \mathrm{d}V$ is found as a weak form. It is convenient to further simplify it by integration by parts

$$\int_\Omega \overline{\widehat{\psi}} \nabla \cdot \left(c_0^2 \nabla \widehat{p}\right) \mathrm{d}V = -\int_\Omega \nabla \overline{\widehat{\psi}} \cdot \left(c_0^2 \nabla \widehat{p}\right) \mathrm{d}V + \oint_{\partial\Omega} \overline{\widehat{\psi}} c_0^2 \nabla \widehat{p} \cdot \vec{n} \, \mathrm{d}S \tag{3.7}$$

$$= -\int_\Omega \nabla \overline{\widehat{\psi}} \cdot \left(c_0^2 \nabla \widehat{p}\right) \mathrm{d}V + \oint_{\partial\Omega} \frac{\omega c_0^2}{\mathrm{i} c_0 Z} \widehat{p} \overline{\widehat{\psi}} \, \mathrm{d}S \tag{3.8}$$

$$= -\int_\Omega c_0^2 \overline{\nabla \widehat{\psi}} \cdot \nabla \widehat{p} \, \mathrm{d}V - \oint_{\partial\Omega} \omega \frac{\mathrm{i} c_0}{Z} \overline{\widehat{\psi}} \widehat{p} \, \mathrm{d}S. \tag{3.9}$$

The benefit from these manipulations is that the result explicitly reveals the contribution of the boundary values to the weak form. Moreover, it balances the differentiability assumptions imposed on $\widehat{p}$ and $\widehat{\psi}$: neglecting the conjugation, both contribute identically to the expression with no higher than first order derivatives appearing. Note how in comparison to the strong form – which features second derivatives of $\widehat{p}$ – this is indeed a weaker condition. Also note that using an impedance is the most general way of modeling the boundary conditions. The formulations for sound-soft and sound-hard boundaries are obtained by taking the limits $Z \to 0$ and $Z \to \infty$,

[1] Indeed, later chapters will refer to the weighting function as $\widehat{p}^\dagger$.

respectively.

Together with the other two terms this gives rise to the following version of the weak formulation of the thermoacoustic Helmholtz equation:

$$\int_\Omega \omega^2 \overline{\widehat{\psi}}\,\widehat{p} - c_0^2 \overline{\nabla\widehat{\psi}} \cdot \nabla\widehat{p} - \overline{\widehat{\psi}} \frac{q_0}{u_0} \frac{\gamma-1}{\rho_{0,\mathrm{u}}} \mathrm{FTF}(\omega)\, \nabla\widehat{p}\big|_{\vec{x}_{\mathrm{ref}}} \cdot \vec{n}_{\mathrm{ref}}\, \mathrm{d}V - \oint_{\partial\Omega} \omega \frac{\mathrm{i}c_0}{Z} \overline{\widehat{\psi}}\,\widehat{p}\, \mathrm{d}S = 0. \tag{3.10}$$

3.2 Adjoint thermoacoustic Helmholtz equation

Definition

Given a differential operator $\mathcal{L}$ and an inner product $\langle\cdot|\cdot\rangle$ the adjoint operator $\mathcal{L}^\dagger$ is defined as

$$\langle a|\mathcal{L}b\rangle = \left\langle \mathcal{L}^\dagger a \middle| b \right\rangle + \text{const.} \tag{3.11}$$

The constant appearing in this equation is arising from an integration by parts. It will be linear in both the direct and the adjoint variable and is called bilinear concomitant [70] or boundary conjunct [71]. It is convenient to choose the boundary conditions for the adjoint equation such that the constant vanishes and $\langle a|\mathcal{L}b\rangle = \left\langle \mathcal{L}^\dagger a \middle| b \right\rangle$, e.g., [68]. Only rarely the meaning of the constant is discussed in the literature. For instance, [70] compares the choice of driving the bilinear concomitant towards zero with the concept of virtual work. This gives a stronger motivation than mere convenience. [71] discusses the role of the boundary concomitant [2] when perturbing the boundary conditions of eigenvalue problems. The findings of that particular publication are especially useful when perturbing the considered domain shape and consequently displacing the boundary.

The adjoint thermoacoustic Helmholtz equation is obtained by further manipulating the weak form such that $\widehat{p}$ appears isolated from all linear operators and a strong formulation in $\widehat{\psi}$ is obtained. The definitions of the adjoint operator immediately implies that the concept of adjoint operators is linear. Therefore, as for the weak form, the adjoint of the Helmholtz equation can be found by a term-by-term or more precisely by an operator-by-operator discussion, as will be done in the following.

Wave operator

The first term in Eq. (3.10) $\int_\Omega \omega^2 \overline{\widehat{\psi}}\,\widehat{p}\,\mathrm{d}V$ already features the desired form. However, it will turn out that it is more practical to denote it as $\int_\Omega \overline{\omega^2}\,\overline{\widehat{\psi}}\,\widehat{p}\,\mathrm{d}V$.

Another integration by parts may remove the differentiation operator from $\widehat{p}$ in the second term $-\int_\Omega c_0^2 \overline{\nabla\widehat{\psi}} \nabla\widehat{p}\,\mathrm{d}V$:

$$-\int_\Omega c_0^2 \overline{\nabla\widehat{\psi}} \cdot \nabla\widehat{p}\,\mathrm{d}V = \int_\Omega \overline{\nabla \cdot c_0^2 \nabla\widehat{\psi}}\,\widehat{p}\,\mathrm{d}V - \oint_{\partial\Omega} c_0^2 \overline{\nabla\psi}\,\widehat{p} \cdot \vec{n}\,\mathrm{d}S. \tag{3.12}$$

Without loss of generality, the boundary values of $\widehat{\psi}$ can be expressed in terms of impedance

[2] It is called *conjunct* there.

boundary conditions: $\widehat{\psi} - \frac{ic_0 Z^\dagger}{\overline{\omega}} \nabla\widehat{\psi} \cdot \vec{n} = 0$. This allows for rephrasing the boundary integral as

$$-\oint_{\partial\Omega} c_0^2 \overline{\nabla\widehat{\psi}}\,\widehat{p} \cdot \vec{n}\,\mathrm{d}S = +\oint_{\partial\Omega} \overline{\overline{\omega}\frac{\mathrm{i}c_0}{Z^\dagger}\widehat{\psi}\,\widehat{p}}\,\mathrm{d}S. \tag{3.13}$$

Flame operator

The third term models the unsteady heat release fluctuation in a flame. Standard models linearly link this fluctuation to a fluctuation of the velocity in a reference region using a flame transfer function. As shown in Chap. 1, the heat release operator then amounts to

$$-\frac{q_0}{u_0}\frac{\gamma-1}{\rho_{0,\mathrm{u}}}\,\mathrm{FTF}(\omega)\,\nabla\widehat{p}\big|_{\vec{x}_{\mathrm{ref}}} \cdot \vec{n}_{\mathrm{ref}} =: Q(\vec{x},\omega)\,\nabla\widehat{p}\big|_{\vec{x}_{\mathrm{ref}}} \cdot \vec{n}_{\mathrm{ref}}. \tag{3.14}$$

Note that the dependency of Q on omega will be dropped in the following for brevity. $\nabla\widehat{p}\big|_{\vec{x}_{\mathrm{ref}}}$ is the pressure fluctuation gradient at a reference point. Yet, for the derivation of the adjoint equation it is more convenient to consider it being an average pressure fluctuation gradient in a reference region Ref. The average is calculated as $\int_{\mathrm{Ref}} \nabla\widehat{p}\, d(\vec{x}-\vec{x}_{\mathrm{ref}})\,\mathrm{d}\vec{x}$. Here, $d(\vec{x})$ is a weighting function with support Ref. It vanishes on the boundary of the reference domain, i.e., $d(\vec{x}) = 0$ if $\vec{x} \in \partial\mathrm{Ref}$. This approach has been used, e.g., in [72] to implement the adjoint equation in CERFACS' AVSP code following a continuous adjoint approach that used a Gaussian distribution for the weighting function. However, if the reference domain will be a single point $\vec{x}_{\mathrm{ref}}$, the weighting function reduces to a delta distribution $\delta(\vec{x})$.

These considerations allow for the following manipulations ultimately removing all operators from $\widehat{p}$:

$$\int_\Omega \overline{\widehat{\psi}} Q(\vec{x})\,\nabla\widehat{p}\big|_{\vec{x}_{\mathrm{ref}}} \cdot \vec{n}_{\mathrm{ref}}\,\mathrm{d}V(\vec{x}) \tag{3.15}$$

$$= \int_{\mathrm{supp}(Q(\vec{x})):=\mathrm{Flame}} \overline{\widehat{\psi}} Q(\vec{x})\,\nabla\widehat{p}\big|_{\vec{x}_{\mathrm{ref}}} \cdot \vec{n}_{\mathrm{ref}}\,\mathrm{d}V(\vec{x}) \tag{3.16}$$

$$= \int_{\mathrm{Flame}} \overline{\widehat{\psi}(\vec{x})} Q(\vec{x}) \int_\Omega \nabla_{\vec{y}}\widehat{p}(\vec{y}) d(\vec{y}-\vec{x}_{\mathrm{ref}})\,\mathrm{d}V(\vec{y}) \cdot \vec{n}_{\mathrm{ref}}\,\mathrm{d}V(\vec{x}) \tag{3.17}$$

$$= \int_{\mathrm{Flame}} \overline{\widehat{\psi}(\vec{x})} Q(\vec{x}) \int_{\mathrm{supp}(d(\vec{y})):=\mathrm{Ref}} \nabla_{\vec{y}}\widehat{p}(\vec{y}) d(\vec{y}-\vec{x}_{\mathrm{ref}})\,\mathrm{d}V(\vec{y}) \cdot \vec{n}_{\mathrm{ref}}\,\mathrm{d}V(\vec{x}) \tag{3.18}$$

$$= \int_{\mathrm{Flame}} \overline{\widehat{\psi}(\vec{x})} Q(\vec{x}) \vec{n}_{\mathrm{ref}}\,\mathrm{d}V(\vec{x}) \cdot \int_{\mathrm{Ref}} \nabla_{\vec{y}}\widehat{p}(\vec{y}) d(\vec{y}-\vec{x}_{\mathrm{ref}})\,\mathrm{d}V(\vec{y}) \tag{3.19}$$

$$= \int_{\mathrm{Flame}} \overline{\widehat{\psi}(\vec{x})} Q(\vec{x}) \vec{n}_{\mathrm{ref}}\,\mathrm{d}V(\vec{x}) \cdot \left(-\int_{\mathrm{Ref}} \widehat{p}(\vec{y}) \nabla_{\vec{y}} d(\vec{y}-\vec{x}_{\mathrm{ref}})\,\mathrm{d}V(\vec{y}) + \int_{\partial\mathrm{Ref}} \widehat{p}(\vec{y}) \underbrace{d(\vec{y}-\vec{x}_{\mathrm{ref}})}_{=0 \text{ on } \partial\mathrm{Ref}} \mathrm{d}A(\vec{y}) \right) \tag{3.20}$$

$$= -\int_{\mathrm{Flame}} \overline{\widehat{\psi}(\vec{x})} Q(\vec{x}) \vec{n}_{\mathrm{ref}}\,\mathrm{d}V(\vec{x}) \cdot \int_{\mathrm{Ref}} \widehat{p}(\vec{y}) \nabla_{\vec{y}} d(\vec{y}-\vec{x}_{\mathrm{ref}})\,\mathrm{d}V(\vec{y}) \tag{3.21}$$

$$= \int_{\mathrm{Ref}} -\int_{\mathrm{Flame}} \overline{\widehat{\psi}(\vec{x})} Q(\vec{x})\,\mathrm{d}V(\vec{x})\ \vec{n}_{\mathrm{ref}} \cdot \nabla_{\vec{y}} d(\vec{y}-\vec{x}_{\mathrm{ref}}) \widehat{p}(\vec{y})\,\mathrm{d}V(\vec{y}) \qquad |\text{swap } \vec{x} \text{ and } \vec{y} \tag{3.22}$$

$$= \int_{\mathrm{Ref}} -\int_{\mathrm{Flame}} \overline{\widehat{\psi}(\vec{y})} Q(\vec{y})\,\mathrm{d}V(\vec{y})\ \vec{n}_{\mathrm{ref}} \cdot \nabla_{\vec{x}} d(\vec{x}-\vec{x}_{\mathrm{ref}}) \widehat{p}(\vec{x})\,\mathrm{d}V(\vec{x}) \tag{3.23}$$

$$= \overline{\int_\Omega -\int_{\mathrm{Flame}} \widehat{\psi}(\vec{y}) \overline{Q(\vec{y})}\,\mathrm{d}V(\vec{y})\ \vec{n}_{\mathrm{ref}} \cdot \nabla_{\vec{x}} d(\vec{x}-\vec{x}_{\mathrm{ref}}) \widehat{p}(\vec{x})\,\mathrm{d}V(\vec{x})}. \tag{3.24}$$

Thus, the adjoint flame operator reads (for a point supported reference region) :

$$\left(-\frac{q_0}{u_0}\frac{\gamma-1}{\rho_{0,\mathrm{u}}}\,\mathrm{FTF}(\omega)\,\nabla(\cdot)|_{\vec{x}_{\mathrm{ref}}}\cdot\vec{n}_{\mathrm{ref}}\right)^{\dagger} = -\int_{\mathrm{Flame}}(\cdot)\overline{Q(\vec{y},\omega)}\,\mathrm{d}V(\vec{y})\nabla\delta(\vec{x}-\vec{x}_{\mathrm{ref}}) \tag{3.25}$$

$$= \int_{\mathrm{Flame}}(\cdot)\overline{\frac{q_0}{u_0}\frac{\gamma-1}{\rho_{0,\mathrm{u}}}\,\mathrm{FTF}(\vec{y},\omega)}\,\mathrm{d}V(\vec{y})\nabla\delta(\vec{x}-\vec{x}_{\mathrm{ref}}). \tag{3.26}$$

This result may seem strange at first. Nevertheless, it nicely exhibits the nature of the adjoint equation to turn matters "upside down". The direct flame operator utilizes the d-weighted average gradient of a given reference region as excitation in the flame region scaled by the FTF. The adjoint does the complete opposite. It takes the average of the flame region weighted by the FTF to create an excitation in the reference region scaled by the gradient of the weighting function d. This reversal of cause and effect is much akin to the time reversal induced by adjoints in the time domain (see, e.g., [68]) and the very reason why the adjoint equation can be used as a sensitivity analysis tool. Note that as each occurrence of the eigenfrequency in the adjoint equation is accompanied by complex conjugation, time reversal also appears in the adjoint equation. This swaps the meaning of growth and decay while keeping the frequency of oscillation unchanged.

The strong form of the adjoint equation

Putting the results together the weak form amounts to

$$\int_\Omega \overline{\left[\overline{\omega}^2\widehat{\psi}+\nabla\cdot c_0^2\nabla\widehat{\psi}+\int_{\mathrm{Flame}}\widehat{\psi}\overline{\frac{q_0}{u_0}\frac{\gamma-1}{\rho_{0,\mathrm{u}}}\,\mathrm{FTF}(\vec{y},\omega)}\,\mathrm{d}V(\vec{y})\nabla\delta(\vec{x}-\vec{x}_{\mathrm{ref}})\right]\widehat{p}}\,\mathrm{d}V$$

$$+\oint_{\partial\Omega}\overline{\overline{\omega}\frac{\mathrm{i}c_0}{Z^\dagger}\widehat{\psi}}\,\widehat{p}-\omega\frac{\mathrm{i}c_0}{Z}\overline{\widehat{\psi}}\,\widehat{p}\,\mathrm{d}S=0. \tag{3.27}$$

Choosing $Z^\dagger=-\overline{Z}$ the boundary integral vanishes. Therefore, if $\widehat{\psi}$ satisfies

$$\overline{\omega}^2\widehat{\psi}+\nabla\cdot\left(c_0^2\nabla\widehat{\psi}\right)+\int_{\mathrm{Flame}}\widehat{\psi}\overline{\frac{q_0}{u_0}\frac{\gamma-1}{\rho_{0,\mathrm{u}}}\,\mathrm{FTF}(\vec{y},\omega)}\,\mathrm{d}V(\vec{y})\nabla\delta(\vec{x}-\vec{x}_{\mathrm{ref}})=0\ \text{in}\ \Omega \tag{3.28a}$$

$$\widehat{\psi}+\frac{\mathrm{i}c_0\overline{Z}}{\overline{\omega}}\nabla\widehat{\psi}\cdot\vec{n}=0\ \text{on}\ \partial\Omega \tag{3.28b}$$

the weak form holds for arbitrary $\widehat{p}$. Consequently, (3.28) is a strong form formulated in $\widehat{\psi}$ and is, thus, the adjoint equation of the thermoacoustic Helmholtz equation (3.5). Moreover, from (3.27) the concomitant of the thermoacoustic Helmholtz equation can be identified as the boundary integral $\oint_{\partial\Omega}\overline{\overline{\omega}\frac{\mathrm{i}c_0}{Z^\dagger}\widehat{\psi}}\,\widehat{p}-\omega\frac{\mathrm{i}c_0}{Z}\overline{\widehat{\psi}}\,\widehat{p}\,\mathrm{d}S$. As expected, it is sesquilinear in the complex-valued setting discussed here.

Comparing the direct and the adjoint equation (3.5) and (3.28) shows that apart from the flame operator both equations obey the same structure. Hence, if neglecting the heat release, the problem becomes self-adjoint. This is a well known property of the Helmholtz equations. Self-adjointness implies useful properties, such as pairwise orthogonal eigenvectors and real eigenvalues. However, as discussed in [30] the thermoacoustic modes are generally not pairwise orthogonal and, hence, the problem cannot be self-adjoint. This is in line with the explicit derivation of the adjoint equation presented here, which shows that the heat-release term is breaking the self-

adjointness. Note that the self-adjoint structure is also lost if the real-part of the boundary impedance is non-zero because then $\overline{Z} \neq -Z$ and the two problems do not coincide.

Yet, these considerations are rather mathematical because the appearance of the adjoint equation can be changed by changing

(i) the inner product used to define the weak form and, hence, the adjoint equation or

(ii) the boundary conditions chosen for the adjoint variable $\widehat{\psi}$.

For instance, any linear second order differential equation can be made self-adjoint by choosing an appropriate inner product. This becomes evident when casting the problem into Sturm-Liouville form, see the supplemental appendix of [40] and references therein. Moreover, the definition of the adjoint differential equation only requires $\langle \widehat{\psi} | \mathcal{L}\widehat{p} \rangle - \langle \mathcal{L}^\dagger \widehat{\psi} | \widehat{p} \rangle = \text{const}$. The constant term is given by the concomitant that arose from integration by parts. It is not necessary to choose the boundary conditions of the adjoint problem such that the boundary concomitant vanishes. However, a standard inner product and a vanishing boundary conjunct are the most convenient choices. This is because then the adjoint solution $\widehat{\psi}$ can be directly interpreted as a local measure for sensitivity. An interpretation that would not be straightforward if contributions from the boundary conjunct or a weighting factor included in the inner product would also need to be accounted for. This viewpoint will be further explained in Chap. 6.

3.3 Finite element discretization

The finite element method is a discretization technique widely used in science and engineering to obtain solutions for partial differential equations. Its popularity can be attributed to its flexibility when dealing with complicated domain shapes, its potential for easy implementation – especially in a parallel computation framework – and the availability of high-quality software packages. The mathematical fundamentals of this method can be found in many textbooks, e.g., [73, 74, 75]. The special application to flow problems is the topic of the book of Donea and Huerta [69]. The first utilization of a finite element approach to solve the thermoacoustic Helmholtz equation was given in [30]. Since then many studies have used this approach in thermoacoustics, e.g., [76, 77, 78, 62]. A detailed derivation of the method using linear shape functions in order to discretize the thermoacoustic Helmholtz equation can be found in [79]. This section discusses the fundamentals of the method as far as they concern the objectives of the thesis.

The key idea behind finite element discretization is the interpretation of the weak form as a test for $\widehat{p}$ being a solution of the considered problem. Because it is necessary that the weak form is satisfied, using a Galerkin discretization of the weak form will result in a system of equations that approximates the solution of the infinite-dimensional problem. In general any ansatz functions that satisfy the regularity requirements of the problem (defined on the considered domain, weak differentiability, compliance with the boundary conditions etc.) can be chosen for $\widehat{p}$ and $\widehat{\psi}$ in order to discretize the problem. However, finite element methods constitute the special case where the supports of the ansatz functions are just a few open cells Ω_i from a tessellation of the considered domain Ω. Such a tessellation is defined through the following properties:

$$\overline{\Omega} = \bigcup_{i=1}^{N_{\text{Tet}}} \overline{\Omega_i} \tag{3.29}$$

$$\Omega_i \cap \Omega_j = \begin{cases} \neq \emptyset & \text{if } i = j \\ = \emptyset & \text{if } i \neq j \end{cases} \tag{3.30}$$

Here N_{Tet} denotes the total number of cells and $\overline{\Omega_i}$ the closure of Ω_i. It is common to refer to the tesselation as computational grid or mesh. In this work its cells Ω_i will be simplices. The discussion here focuses on the most general case of considering the three-dimensional space, i.e., the simplices will be tetrahedra. The two- and one-dimensional discretizations are readily obtained as special cases.

A tetrahedron can be uniquely defined from four points X_A, X_B, X_C, and X_D not all lying in a common plane. The notation $\text{tet}(X_A, X_B, X_C, X_D)$ will be used to define a tetrahedron with vertices X_A, X_B, X_C, and X_D. The tessellation implies the following integration rules:

$$\int_\Omega f \,\mathrm{d}V = \sum_i \int_{\Omega_i} f \,\mathrm{d}V \tag{3.31}$$

$$\oint_{\partial\Omega} f \,\mathrm{d}S = \sum_i \oint_{\partial\Omega_i} f \,\mathrm{d}S \qquad | \text{ if } f \text{ is continuous in } \Omega \tag{3.32}$$

The same ansatz functions ϕ_i will be used for $\widehat{p}$ and $\widehat{\psi}$ when discretizing the weak form:

$$\widehat{p} = \sum_i p_i \phi_i, \qquad \widehat{\psi} = \sum_j \psi_j \phi_j. \tag{3.33}$$

This is known as Bubnov-Galerkin finite element method.

Again it is convenient to discuss the different terms of the weak form individually. Plugging the ansätze into the first term of the weak form (3.10) yields $\int_\Omega \omega^2 \overline{\widehat{\psi}} \widehat{p} \,\mathrm{d}V$. A quick calculation shows:

$$\int_\Omega \overline{\widehat{\psi}} \widehat{p} \,\mathrm{d}V = \sum_i \sum_j \overline{\psi_j} p_i \underbrace{\int_\Omega \overline{\phi_j} \phi_i \,\mathrm{d}V}_{:=[\mathbf{M}]_{ij}} = \boldsymbol{\psi}^{\mathrm{H}} \mathbf{M} \boldsymbol{p} \tag{3.34}$$

where in the last step the problem has been reformulated using matrix-vector notation. The entries of the vectors are defined as $[\boldsymbol{\psi}]_j := \psi_j$ and $[\boldsymbol{p}]_i := p_i$. Following the standard vernacular in the field, the matrix $\mathbf{M}$ will be called *mass matrix*. Note that because the mass matrix represents the inner product of $\widehat{\psi}$ and $\widehat{p}$, it is positive definite. The discretization of an inner product, therefore, will be the sesquilinear-form induced by $\mathbf{M}$. Nonetheless, the results yield $\boldsymbol{\psi}^{\mathrm{H}} \omega^2 \mathbf{M} \boldsymbol{p}$ for the discretization of the first term in the weak form.

For the second term the following expression is found

$$\int_\Omega c_0^2 \overline{\nabla \widehat{\psi}} \cdot \nabla \widehat{p} \,\mathrm{d}V = \sum_i \sum_j \overline{\psi_j} p_i \underbrace{\int_\Omega c_0^2 \overline{\nabla \phi_j} \cdot \nabla \phi_i \,\mathrm{d}V}_{:=[\mathbf{K}]_{ij}} = \boldsymbol{\psi}^{\mathrm{H}} \mathbf{K} \boldsymbol{p}. \tag{3.35}$$

The matrix $\mathbf{K}$ originating from the discretization of the Laplacian is commonly referred to as *stiff-*

ness matrix. Substitution of the ansätze into the boundary integral results in

$$\oint_{\partial\Omega} c_0 \overline{\widehat{\psi}} \widehat{p} \, \mathrm{d}S = \sum_i \sum_j \overline{\psi_j} p_i \underbrace{\oint_{\partial\Omega} \frac{\mathrm{i}c_0}{Z} \overline{\phi_j} \phi_i \, \mathrm{d}S}_{:=[\mathbf{B}]_{ij}} = \boldsymbol{\psi}^{\mathrm{H}} \mathbf{B} \boldsymbol{p}. \tag{3.36}$$

The matrix $\mathbf{B}$ will be referred to as *boundary mass matrix*. Note that the impedance Z may depend on the spatial coordinate $\vec{x}$ and the eigenfrequency ω. The boundary mass matrix may, thus, be also frequency dependent and it might be convenient to perform the surface integration on locations with different impedances separately. Also note that for sound-soft boundary conditions – i.e., $Z = 0$ – the boundary conditions to the direct and the adjoint equation read $\widehat{p} = 0$ and $\widehat{\psi} = 0$, respectively. Therefore, the ansatz functions ϕ_i associated to nodes on sound-soft boundaries are commonly removed from the set of considered ansatz functions to implement this boundary condition. This approach is known as implementing sound-soft boundary conditions as an *essential* boundary condition as it reduces the dimension of the considered function space. However, in this thesis all boundary conditions will be modeled as impedance boundary conditions via the boundary mass matrix $\mathbf{B}$ and very small values of Z. This ensures that the size of the discretization matrices will not change while perturbing a sound-soft boundary – a property that is necessary for the perturbation theory presented in Chap. 6.

The discretization of the heat release operator is special, as it acts non-locally on $\widehat{p}$. Hence, it involves the use of test and trial functions with different support. While only those trial functions supported at the reference position will enter the discretization, only test functions from the domain of heat release are accounted for:

$$\int_\Omega \overline{\widehat{\psi}} \, \nabla \widehat{p}\big|_{\vec{x}_{\mathrm{ref}}} \cdot \vec{n}_{\mathrm{ref}} \, \mathrm{d}V = \sum_i \sum_j \overline{\psi_j} p_i \underbrace{\int_{\Omega_{\mathrm{Flame}}} \overline{\phi}_j \, \mathrm{d}V \, \nabla \phi_i\big|_{\vec{x}_{\mathrm{ref}}} \cdot \vec{n}_{\mathrm{ref}}}_{:=[\boldsymbol{F}]_{ij}} = \boldsymbol{\psi}^{\mathrm{H}} \boldsymbol{F} \boldsymbol{p}. \tag{3.37}$$

The discretization matrix $\mathbf{F}$, which will be called the *flame matrix* in the following, is, therefore, extremely sparse with very low rank. In contrast to all other discretization matrices, it would not feature a diagonal structure on a structured grid, but would have a few entries along some of its columns. If there is only one flame, it can be phrased as an outer product:

$$\sum_i \sum_j \overline{\psi_j} p_i \underbrace{\int_{\Omega_{\mathrm{Flame}}} \overline{\phi}_j \, \mathrm{d}V \, \nabla \phi_i\big|_{\vec{x}_{\mathrm{ref}}} \cdot \vec{n}_{\mathrm{ref}}}_{:=[\boldsymbol{F}]_{ij}} = \left(\sum_j \overline{\psi_j} \underbrace{\int_{\Omega_{\mathrm{Flame}}} \overline{\phi}_j \, \mathrm{d}V}_{[\boldsymbol{q}]_j} \right) \left(\sum_i p_i \underbrace{\nabla \phi_i\big|_{\vec{x}_{\mathrm{ref}}} \cdot \vec{n}_{\mathrm{ref}}}_{:=[\boldsymbol{g}]_i} \right) = \boldsymbol{\psi}^{\mathrm{H}} \boldsymbol{q} \boldsymbol{g}^{\mathrm{T}} \boldsymbol{p} \tag{3.38}$$

or short

$$\boldsymbol{F} = \boldsymbol{q} \boldsymbol{g}^{\mathrm{T}}. \tag{3.39}$$

Note that the vector $\boldsymbol{q}$ is the load vector commonly appearing in finite element discretizations of non-homogeneous problems. If there are multiple flames, like in annular combustors, the flame matrix is a sum of such outer products and the rank of the flame matrix would in general coincide with the number of flames if the flame dynamics depend on single reference points. Also note

that discretization of the flame operator as an outer product is not an exclusive feature of the finite element method. The finite volume method utilized in CERFACS' AVSP code also facilitates such a factorization [79]. Indeed, the flame operator itself is based on an outer product in an infinite-dimensional space. Therefore, it can be expected that the feature is inherited by the discretization matrix.

The special structure of the flame matrix has two advantages when dealing with the FEM discretization of the thermoacoustic Helmholtz equation:

(i) The assembly of the flame matrix can be easily implemented by generating $\boldsymbol{q}$ and $\boldsymbol{g}$ and taking the outer product.

(ii) When solving a system $(\mathbf{A} + \mathrm{FTF}(\omega)\mathbf{F})\boldsymbol{x} = \boldsymbol{y}$, first the influence of the flame matrix can be neglected and well-established solvers for the operator $\mathbf{A}$ can be utilized. In a second step the result can be correctly updated exploiting the low-rank nature of $\mathbf{F}$ using the Sherman-Morrison-Woodbury formula [3]. Such computations will occur in solvers for nonlinear eigenvalue problems and in algorithms computing perturbative approximations.

Summarizing all results, the discretization of the weak form reads

$$\boldsymbol{\psi}^{\mathrm{H}}(\mathbf{K} + \omega\mathbf{C} + \omega^2\mathbf{M} + \mathrm{FTF}(\omega)\mathbf{F})\boldsymbol{p} = 0. \tag{3.40}$$

Here, $\mathbf{C}$ is a matrix obtained from factorizing ω from all discretized operators featuring a factor ω. It is commonly referred to as *damping matrix*. The factorized matrices are boundary mass matrices or terms $\mathrm{i}\alpha\mathbf{M}$ originating from extra terms $\mathrm{i}\omega\alpha\widehat{p}$ added to the Helmholtz equation in order to model viscous damping effects, e.g., [62]. The factor α denotes the induced damping rate.

A trivial solution of the discretized weak form would be to compute $(\mathbf{K}+\omega\mathbf{C}+\omega^2\mathbf{M}+\mathrm{FTF}(\omega)\mathbf{F})\boldsymbol{p}$ for some ω and then choose a $\boldsymbol{\psi}$ orthogonal to it. However, the weak form should hold for all possible $\boldsymbol{\psi}$. Hence, pairs of ω and $\boldsymbol{p}$ are sought such that

$$\underbrace{(\mathbf{K} + \omega\mathbf{C} + \omega^2\mathbf{M} + \mathrm{FTF}(\omega)\mathbf{F})}_{:=\mathbf{L}(\omega)}\boldsymbol{p} = 0, \tag{3.41}$$

which is a finite-dimensional eigenvalue problem nonlinear in its eigenvalue ω. Alternatively, when $\boldsymbol{p}$ is considered the test vector, the eigenvalue problem

$$\underbrace{(\mathbf{K}^{\mathrm{H}} + \overline{\omega}\mathbf{C}^{\mathrm{H}} + \overline{\omega}^2\mathbf{M}^{\mathrm{H}} + \overline{\mathrm{FTF}(\omega)}\mathbf{F}^{\mathrm{H}})}_{=\mathbf{L}^{\mathrm{H}}(\omega)}\boldsymbol{\psi} = \mathbf{0} \tag{3.42}$$

is obtained, which is the adjoint eigenvalue problem to (3.41).

The equations (3.41) and (3.42) are the FEM discretizations of the direct and the adjoint thermoacoustic Helmholtz equation, respectively. Again it shall be emphasized, that because using a Bubnov-Galerkin approach this discretization of the adjoint equation is obtained regardless of whether a continuous or a discrete approach is followed. This is due to the connection of the weak form. Figure 3.1 schematically summarizes how the various versions of the thermoacoustic Helmholtz equation are related. The weak form is at the center of these relations and consequently

[3] $\left(\mathbf{A} + \mathbf{U}\boldsymbol{\Sigma}\mathbf{V}^{\mathrm{H}}\right)^{-1} = \mathbf{A}^{-1} - \mathbf{A}^{-1}\mathbf{U}\left(\boldsymbol{\Sigma}^{-1} + \mathbf{V}^{\mathrm{H}} + \mathbf{A}^{-1}\mathbf{U}\right)^{-1}\mathbf{V}\mathbf{A}^{-1}$

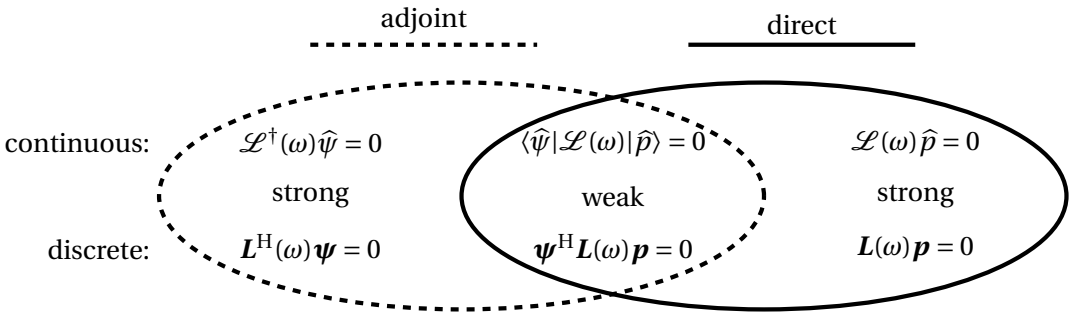

Figure 3.1: Hierarchy of equations. The strong and the weak form of the thermoacoustic Helmholtz equation feature identical weak forms. When using Bubnov-Galerkin FEM the same is true for their discretized versions. A distinction of continuous and discrete adjoint approaches is, thus, not necessary.

using Bubnov-Galerkin FEM discretization renders the typical distinction of continuous and discrete adjoint obsolete.

3.4 Notes on implementation

Implementation of the finite element method depends on the choice of ansatz functions. First and second order Lagrangian elements are used in this thesis. This means that linear and quadratic ansatz functions are utilized. In finite element analyses the ansatz functions are interpolants. More precisely, for a given set of points $\mathbb{X} = \{X_1, \ldots, X_N\}$ in the domain Ω there is a corresponding set of ansatz functions $\mathbb{F} = \{\phi_1, \ldots, \phi_N\}$ such that

$$\phi_i(\vec{X}_j) = \begin{cases} 1 & \text{if } i = j \\ 0 & \text{if } i \neq j \end{cases} \tag{3.43}$$

The points in $\mathbb{X}$ are called the *degrees of freedom* or *nodes* of the discretization. Because their number N is equal to the number of ansatz functions, this number will also be the size of the discretized problem. For first order elements the nodes will be placed at the vertices of the tetrahedra. For second order Lagrange elements there will be additional nodes at the centers of the edges of the tetrahedra.

An ansatz function will be designed such that its support encompasses only the tetrahedra that are connected to its defining node:

$$\phi_i(\vec{x}) = 0 \text{ on } \Omega_l \text{ if } X_i \notin \overline{\Omega_l}. \tag{3.44}$$

This locality of the ansatz functions greatly simplifies the computation of the entries of the mass matrix, the stiffness matrix, and the boundary mass matrix. This is because the integrands evaluated in (3.34)-(3.36) vanish when considering two shape functions that cannot be associated with a common tetrahedron. Consequently, these matrices are sparse.

It is convenient to formulate the ansatz functions on each element individually, using local coordinate systems. In the case of tetrahedra the coordinates are *barycentric coordinates*. Given a tetrahedron $\Omega_l = \mathrm{tet}(X_A, X_B, X_C, X_D)$ the barycentric coordinates $\xi_{A,l}, \xi_{B,l}, \xi_{C,l}, \xi_{D,l}$ define a point

$\vec{x} \in \mathbb{R}^3$ through

$$\vec{x} = \vec{X}_A \xi_{A,l} + \vec{X}_B \xi_{B,l} + \vec{X}_C \xi_{C,l} + \vec{X}_D \xi_{D,l}. \tag{3.45}$$

Though there are four barycentric coordinates, each of which associated to one of the four vertices, only three of them are independent. This is because the coordinates must additionally satisfy $\xi_{A,l} + \xi_{B,l} + \xi_{C,l} + \xi_{D,l} = 1$. Hence, if one barycentric coordinate is 1, then the other three coordinates must be 0 and the coordinates describe one of the four vertices. This means that if only three independent barycentric coordinates are considered, the three unit vectors $(1,0,0)$,$(0,1,0)$, and $(0,0,1)$ are mapped to three vertices, and the origin $(0,0,0)$ is mapped to the remaining vertex. These four points define the unit tetrahedron Ω_{unit}. Barycentric coordinates can, therefore, be interpreted as a coordinate transform from the unit tetrahedron Ω_{unit} to the considered tetrahedron Ω_l. The coordinate transform explicitly reads:

$$\vec{x} = \begin{pmatrix} x \\ y \\ z \end{pmatrix} = \underbrace{\begin{bmatrix} x_A - x_D & x_B - x_D & x_C - x_D \\ y_A - y_D & y_B - y_D & y_C - y_D \\ z_A - z_D & z_B - z_D & z_C - z_D \end{bmatrix}}_{:= \frac{\mathrm{d}\vec{x}}{\mathrm{d}\vec{\xi}_l}} \underbrace{\begin{pmatrix} \xi_{A,l} \\ \xi_{B,l} \\ \xi_{C,l} \end{pmatrix}}_{\vec{\xi}_l} + \begin{pmatrix} x_D \\ y_D \\ z_D \end{pmatrix} \tag{3.46}$$

or short:

$$\vec{x}(\vec{\xi}_l) = \frac{\mathrm{d}\vec{x}}{\mathrm{d}\vec{\xi}} \vec{\xi}_l + X_D. \tag{3.47}$$

The main advantage of the local barycentric coordinates for finite element discretization is that they allow to easily define the ansatz functions ϕ_i. For linear Lagrange elements, the degrees of freedom lie at the vertices of the tetrahedra. The shape functions of one element can then be defined as

$$\phi_i(\vec{x}) = \xi_{i,l}(\vec{x}) \text{ on } \overline{\Omega_l} \text{ if } \vec{x} \in \overline{\Omega_l}. \tag{3.48}$$

For quadratic elements, the centers of the 6 edges of a tetrahedron constitute additional degrees of freedom. Using barycentric coordinates the ansatz functions associated with the vertices are

$$\phi_i(\vec{x}) = (2\xi_{i,l}(\vec{x}) - 1)\xi_{i,l}(\vec{x}) \text{ on } \overline{\Omega_l} \text{ if } \vec{x} \in \overline{\Omega_l}, \tag{3.49}$$

while for the functions associated with the edges

$$\phi_i(\vec{x}) = 4\xi_{j,l}(\vec{x})\xi_{k,l}(\vec{x}) \text{ on } \overline{\Omega_l} \text{ if } \vec{x} \in \overline{\Omega_l} \tag{3.50}$$

is found.

Note that these definitions are consistent on the surface $\Gamma := \overline{\Omega_+} \cap \overline{\Omega_-}$ between two adjacent tetrahedra $\Omega_+ = \text{tet}(X_A, X_B, X_C, X_+)$ and $\Omega_- \text{tet}(X_A, X_B, X_C, X_-)$. This is because on the surface Γ the local barycentric coordinates ξ_- and ξ_+ vanish if evaluated from Ω_- and Ω_+, respectively. Evaluation from both sides – i.e., both tetrahedra – will, therefore, result in the same value on a point $\vec{x} \in \Gamma$. Figure 3.2 illustrates the relations between Cartesian coordinates and the barycentric coordinates.

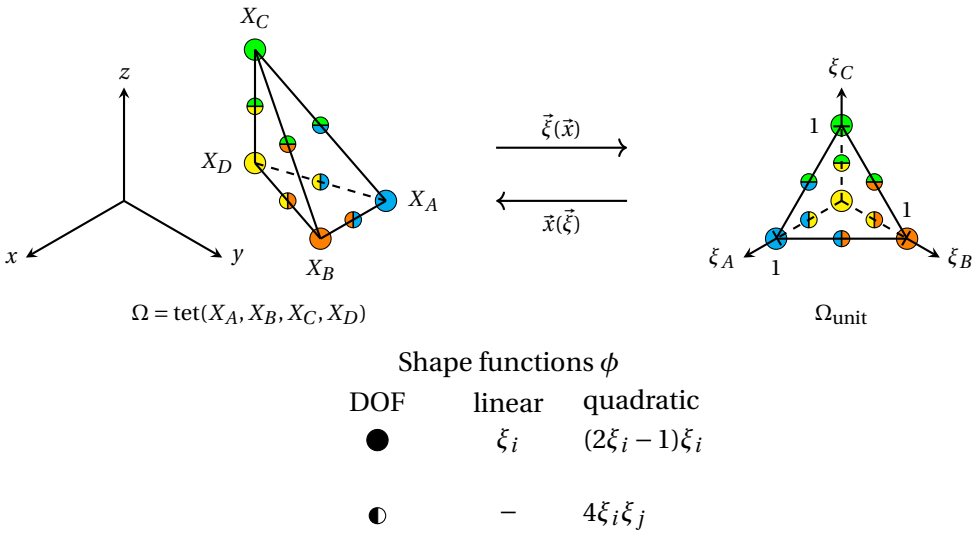

Figure 3.2: Illustration of barycentric coordinates as a coordinate transform from the unit tetrahedron. The circles illustrate the degrees of freedom. Note the different orientation of the actual tetrahedron and the unit tetrahedron in this example.

Integrating the shape functions in order to obtain the entries of the discretization matrices is an easy task: the coordinates are transformed using the coordinate transform to barycentric coordinates and integration is performed on the unit tetrahedron. Details can be found in standard text books on FEM like [73]. It is only the formation of the flame matrix that requires special care. As already outlined in the previous section the flame operator acts non-locally and the flame matrix can be better represented in terms of an outer product $\boldsymbol{q}\boldsymbol{g}^{\mathrm{T}}$. While the computation of the load vector $\boldsymbol{q}$ is a standard topic in finite element analysis, the assembly of the gradient vector is exclusive to thermoacoustics. Its computation requires the identification of the tetrahedron containing the reference point $\vec{x}_{\mathrm{ref}}$. This can be tested for using barycentric coordinates. The tetrahedron Ω_l contains the reference point if its representation in the local barycentric coordinate system features only coordinate values between 0 and 1. Because the derivative of the ansatz functions is not continuous from one tetrahedron to another, it is important to design the discretization mesh such that the reference point is contained in one tetrahedron and does not lie on the boundaries between two tetrahedra. Reference points that lie on the boundary between two adjacent tetrahedra are only admissible if the reference direction $\vec{n}_{\mathrm{ref}}$ is orthogonal to the surface normal $\boldsymbol{n}$ of the surface Γ between the two tetrahedra. In this case evaluation from either of the two sides will result in identical values. However, once the reference element Ω_{ref} is identified, the gradient vector $\boldsymbol{g}$ can be computed as

$$[\boldsymbol{g}]_k = \begin{cases} \left.\frac{\mathrm{d}\phi_k}{\mathrm{d}\vec{\xi}_{\mathrm{ref}}}\right|_{\vec{x}_{\mathrm{ref}}} \left(\frac{\mathrm{d}\vec{x}}{\mathrm{d}\vec{\xi}_{\mathrm{ref}}}\right)^{-1} \vec{n}_{\mathrm{ref}} & \text{if } X_k \in \Omega_{\mathrm{ref}} \\ 0 & \text{else .} \end{cases} \tag{3.51}$$

3.5 Incorporation of experimental data

The best discretization method is meaningless unless it is equipped with realistic modeling data. For the thermoacoustic Helmholtz equation the local distribution of the speed of sound and the flame transfer function are needed. Both can be retrieved from experiments. However, they will only be given as discrete data points. Further processing of the data is, therefore, needed to incorporate them into the model.

Speed of sound

For the speed of sound the incorporation is relatively easy. The data must be interpolated on the entire domain. The simplest interpolation method would be to choose constant speed of sound on each element, i.e., each considered tetrahedron Ω_l. This approach is utilized for FEM discretizations of the Rijke-tube model, which assumes only two different temperature levels. Although the coefficient functions would not be continuous anymore, no special jump conditions must be implemented in the finite element model as the correct jumps will naturally arise from the weak form.

This becomes evident when generalizing the jump condition (2.8) to three dimensions: let Γ denote the surface between two neighboring tetrahedra Ω_- and Ω_+. Furthermore the speed of sound on these tetrahedra are c_- and c_+, respectively. Then a discontinuity in the speed of sound, i.e., $c_-(\Gamma) \neq c_+(\Gamma)$ introduces the following jump condition to the Helmholtz equation

$$\int_{\Gamma_+} c_+^2 \nabla \hat{p} \vec{n}_+ \,\mathrm{d}S + \int_{\Gamma_-} c_-^2 \nabla \hat{p} \vec{n}_- \,\mathrm{d}S = 0 \tag{3.52}$$

where subscripts $-$ and $+$ indicate evaluation of the quantities from Ω_- and Ω_+, respectively. Now, considering a local weak form on each tetrahedron Ω_k of the tessellation of the domain Ω, the integration rules for a tessellation and the jump condition yields

$$\begin{aligned}
&\sum_k \left(\int_{\Omega_k} c_k^2 \overline{\nabla \widehat{\psi}} \nabla \hat{p} \,\mathrm{d}V + \oint_{\partial\Omega_k} \omega \frac{\mathrm{i}c}{Z} \overline{\widehat{\psi}} \hat{p} \,\mathrm{d}S \right) \overset{(3.31)}{=} \sum_k \int_{\Omega_k} c_k^2 \overline{\nabla \widehat{\psi}} \nabla \hat{p} \,\mathrm{d}V + \sum_k \oint_{\partial\Omega_k} \omega \frac{\mathrm{i}c}{Z} \overline{\widehat{\psi}} \hat{p} \,\mathrm{d}S \\
&= \int_\Omega c^2 \overline{\nabla \widehat{\psi}} \nabla \hat{p} \,\mathrm{d}V + \sum_k \oint_{\partial\Omega_k} \omega \frac{\mathrm{i}c}{Z} \overline{\widehat{\psi}} \hat{p} \,\mathrm{d}S \overset{(3.52)}{=} \int_\Omega c^2 \overline{\nabla \widehat{\psi}} \nabla \hat{p} \,\mathrm{d}V + \oint_{\partial\Omega} \omega \frac{\mathrm{i}c}{Z} \overline{\widehat{\psi}} \hat{p} \,\mathrm{d}S.
\end{aligned} \tag{3.53}$$

The last expression is exactly the global weak form (3.10). Therefore, evaluating the weak form on the entire domain while ignoring the surface integrals on boundaries between two tetrahedra naturally enforces the correct jump conditions.

This approach is not suitable for more complicated speeds of sound, as they appear in the MICCA model. This is because correctly resolving the distribution would require a fine mesh resolution, which would be otherwise unnecessary. The speed of sound is, therefore, not considered constant on a tetrahedron but linearly interpolated using exactly the linear ansatz functions presented before.

Flame transfer function

The flame transfer function is different from the speed of sound in that it is a function of the complex frequency ω. Moreover, in this thesis the flame transfer function is not a function of space. If it would be a function of space, e.g., like in [78], the space dependence could be treated similar to the speed of sound by interpolation. The perturbation theory developed in Chap. 6 will require the flame transfer function to be analytic in the complex frequency ω. However, if the function is modeled from measured data, it will be given as a discrete set of data points. These data points are typically measured for real ω. Hence, a method is needed that evaluates the data in the complex plane. The difficulties of obtaining flame transfer functions from experimental data have been addressed in [80]. The work compared three strategies of expanding the measured data into the complex plane: (i) extrusion, i.e., only accounting for the real part of the complex frequency, (ii) approximation by a second-order Taylor polynomial, and (iii) fitting to an analytic function using Laplace transforms. Although the first method is straightforward, the authors emphasized that the obtained flame transfer function is not analytic in ω, and, therefore, lack physical meaning. They conclude that, wherever possible, method (iii) should be applied because the Taylor polynomial obtained from method (ii) will be the Taylor polynomial to the analytic function generated with method (iii). These ideas were further improved in [81] where it was shown that the analytic functions model the flame dynamics better than a tuned n–τ-model.

Nonetheless, originally the data is given for discrete points only. Therefore, the continuation of the measured flame transfer function is not unique. Moreover, the measurement of the data is subject to errors. While these errors might be rather small on the real axis they may lead to significantly different values of the fit transfer function when evaluating complex-valued frequencies. Better approximation might be computed when the fit model is based on data taken at complex-frequencies. This, however, would require experiments in which the flame is excited with signals that increase or decay exponentially. It is not only that this would be a challenge in terms of finding appropriate measurement equipment but also the interpretation of such experiments would be difficult as the usage of flame transfer functions implies linearity of the flame response. An assumption that will be definitely violated when reaching large excitation amplitudes. Nevertheless, these questions do not concern the ideas of this thesis. Note, however, that extrapolation of analytic functions is an active field of mathematical research. See, e.g., the recent article on stable extrapolation of analytic functions [82] and references therein.

In this thesis the analytic function is generated by finding a linear state space model, that features a transfer function TF similar to the measured flame transfer function data.

The state space model reads,

$$\frac{\mathrm{d}}{\mathrm{d}t}\boldsymbol{s} = \mathbf{S}_1\boldsymbol{s} + \mathbf{S}_2 u_{\mathrm{ref}} \tag{3.54}$$

$$q = \mathbf{S}_3\mathbf{s} + \mathbf{S}_4 u_{\mathrm{ref}} \tag{3.55}$$

where the reference velocity u_{ref} and the fluctuation of the heat release rate constitute the input and output of the system, respectively. $\mathbf{s}$ is the state vector of the system. Typically $\mathbf{S}_1$ is called the *system matrix*, $\mathbf{S}_2$ the *input matrix*, $\mathbf{S}_3$ the *output matrix*, and $\mathbf{S}_4$ the *feedthrough matrix*.

Using a Fourier transform to the complex frequency space, the output q becomes an explicit

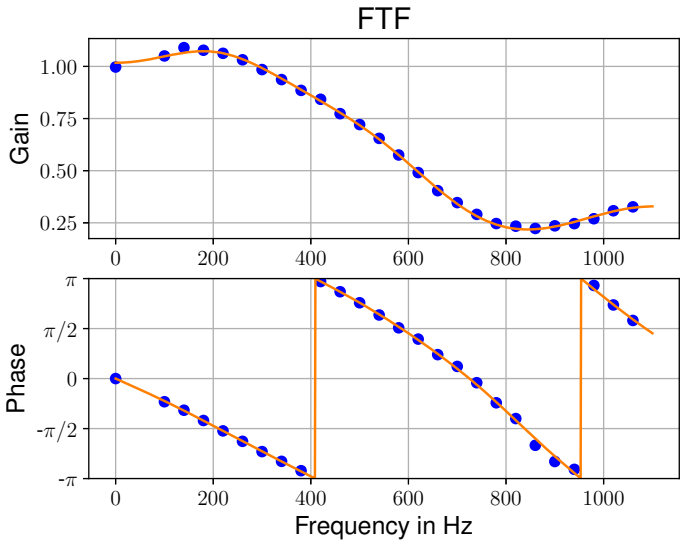

Figure 3.3: Comparison between the state space model approximation of the flame transfer function evaluated at purely real values of ω (orange line) and the data measured from experiments [62] (blue dots).

function of the input u_{ref} in terms of a transfer function TF

$$\widehat{q} = \text{TF}(\omega)\, u_{\text{ref}} := \underbrace{\left(\boldsymbol{S}_3 \left(\mathrm{i}\omega \boldsymbol{I} - \boldsymbol{S}_1\right)^{-1} \boldsymbol{S}_2 + \boldsymbol{S}_4\right)}_{\text{FTF}} \widehat{u}_{\text{ref}}. \tag{3.56}$$

This state space representation of the transfer function allows for a variety algebraic manipulations. Most importantly, exact derivatives of the transfer function can be computed as

$$\frac{\partial^k}{\partial \omega^k} \text{TF}(\omega) = (-\mathrm{i})^k k! \mathbf{S}_3 \left(\mathrm{i}\omega I - \mathbf{S}_1\right)^{-(k+1)} \mathbf{S}_2 \text{ for } k \geq 1. \tag{3.57}$$

This circumstance will be crucial for an accurate implementation of the perturbation theory derived later.

Finding a state space model such that $\text{TF}(\omega_k) = \text{FTF}(\omega_k)$ at the measured frequencies ω_k basically means finding matrices $\mathbf{S}_i$ such that the difference between the measured and predicted transfer function is as small as possible. This is achieved by deploying the *vector fitting* algorithm presented in [83, 84]. Besides the measured flame transfer function data, the assumed dimension of the state space model is an important input quantity to the algorithm. For this thesis this dimension has been chosen to be six, which is the lowest dimension to yield reasonable results. Figure 3.3 shows a comparison of the measured data and the six-dimensional state-space-model predictions. The FTF data is taken from [62].

Although exemplified here with flame transfer function data, transfer functions from state space models might be used to model any other frequency-dependent quantity. For example, a state space model could be designed to incorporate frequency-dependent impedances.

Chapter 4

Nonlinear eigenvalue problems I: basics

The last chapters have shown how discretizing the thermoacoustic Helmholtz equation results in an eigenvalue problem being nonlinear with respect to its eigenvalue. There is a comprehensive theory on such eigenvalue problems and an in-depth discussion is clearly beyond the scope of this thesis. However, four chapters deal with the theory as far as it is relevant for this work. This is the first of these chapters. It introduces the basic theory of nonlinear eigenvalue problems for the case of finite-dimensional operators. In particular, it presents the iterative algorithm introduced in [30] to solve the discretized thermoacoustic Helmholtz equation, which can currently be considered as the standard solver for this problem used in the thermoacoustic research community.

4.1 Basic definitions

Nomenclature

A finite-dimensional nonlinear eigenvalue problem can be defined by an N-dimensional operator family $\mathbf{L}(z)$. This is a mapping from a scalar to a matrix:

$$\mathbb{C} \to \mathbb{C}^{N\times N} \tag{4.1}$$

$$z \mapsto \mathbf{L} \tag{4.2}$$

All numbers ω for which $\mathbf{L}(z)$ is not invertible are called eigenvalues. By definition, each eigenvalue corresponds with a non-empty nullspace of $\mathbf{L}(\omega)$. The vectors $\boldsymbol{p} \in \text{null}(\mathbf{L}(\omega))$ and the nullspace itself are referred to as the to ω corresponding *eigenvectors* and *eigenspace* of $\mathbf{L}$.

The *spectrum* of $\mathbf{L}$ is the set of all its eigenvalues denoted by:

$$\text{spec}(\mathbf{L}) := \{\omega \in \mathbb{C} | \text{null}(\mathbf{L}(\omega) \neq \emptyset\}\,. \tag{4.3}$$

Finally, computing the spectrum of $\mathbf{L}$ or subsets of it and finding the corresponding eigenspaces, i.e., solving

$$\mathbf{L}(\omega)\boldsymbol{p} = \mathbf{0} \quad \text{with} \quad \boldsymbol{p} \neq \mathbf{0} \tag{4.4}$$

is referred to as a *nonlinear eigenvalue problem*.

Note that the nomenclature on such problems is not consistent in the literature. This thesis follows a traditional approach where the standard eigenvalue problems induced by $\mathbf{L} = (\mathbf{X} - \omega\mathbf{I})\boldsymbol{p} = \mathbf{0}$ and the generalized eigenvalue problems $\mathbf{L} = (\mathbf{X} - \omega\mathbf{Y})\boldsymbol{p} = \mathbf{0}$ are referred to as *linear*. Moreover, those of the form $\mathbf{L} = \sum_{k=0}^{K} \mathbf{A}_k \omega^k$ are called *polynomial*. In particular, for $K = 2$ the problems are named *quadratic*, while $K = 1$ reduces to the linear cases. As already stated, any $\mathbf{L} = \mathbf{L}(z)$ is referred to as nonlinear. However, some authors name these eigenvalue problems linear and reserve the term *nonlinear eigenvalue problems* exclusively for the case of nonlinear operators, i.e., operators acting nonlinearly on the eigenvector, see, e.g., [85]. Presumably, this is because the modern theory on the topic allows for treating the case of linear operators in a single mathematical framework, where the classic eigenvalue problems are just special cases. Except for the limit-cycle computations in Chap. 7, this thesis is not dealing with nonlinear operators and, therefore, uses the traditional naming conventions.

The adjoint eigenvalue problem

Given an inner product $\langle \cdot | \cdot \rangle$, to each operator family $\mathbf{L}$ an *adjoint* operator family $\mathbf{L}^\dagger$ can be defined by the relation:

$$\langle \boldsymbol{y} | \mathbf{L}\boldsymbol{x} \rangle = \left\langle \mathbf{L}^\dagger \boldsymbol{y} \middle| \boldsymbol{x} \right\rangle \forall \boldsymbol{x}, \boldsymbol{y}. \tag{4.5}$$

An operator family is called self-adjoint if $\mathbf{L}^\dagger = \mathbf{L}$. The probably simplest *self-adjoint* operator is the unit matrix $\mathbf{I}$.

The definition of the adjoint operator family implies that for the product of two operator families $\mathbf{A}$, $\mathbf{B}$

$$\langle \boldsymbol{y} | \mathbf{A}\mathbf{B}\boldsymbol{x} \rangle = \left\langle \mathbf{A}^\dagger \boldsymbol{y} \middle| \mathbf{B}\boldsymbol{x} \right\rangle = \left\langle \mathbf{B}^\dagger \mathbf{A}^\dagger \boldsymbol{y} \middle| \boldsymbol{x} \right\rangle \tag{4.6}$$

holds. Hence:

$$(\mathbf{A}\mathbf{B})^\dagger = \mathbf{B}^\dagger \mathbf{A}^\dagger. \tag{4.7}$$

By definition, for any $z \notin \operatorname{spec}(\mathbf{L})$ there is an inverse operator $\mathbf{L}^{-1}(z)$ such that $\mathbf{L}(z)\mathbf{L}^{-1}(z) = \mathbf{I}$. From (4.7) it can be concluded that $\left(\mathbf{L}(z)\mathbf{L}^{-1}(z)\right)^\dagger = \mathbf{I}^\dagger$ is the same equation as $\left(\mathbf{L}^{-1}(z)\right)^\dagger \mathbf{L}^\dagger(z) = \mathbf{I}$. This proves that

$$\left(\mathbf{L}^\dagger\right)^{-1} = \left(\mathbf{L}^{-1}\right)^\dagger \tag{4.8}$$

if $\mathbf{L}$ is invertible. In particular, this implies that $\mathbf{L}^\dagger$ cannot possess an inverse if $\mathbf{L}$ does not possess one. Hence,

$$\operatorname{spec}(\mathbf{L}^\dagger) = \operatorname{spec}(\mathbf{L}). \tag{4.9}$$

Note that the direct and the adjoint eigenspace corresponding to the same eigenvalue ω do not necessarily need to be equal.

Also note that in the theory of linear eigenvalue problems, eigenvalues are considered as belonging to the operator $\mathbf{X}$ instead of the operator family $\mathbf{X} - \omega\mathbf{I}$. Following this viewpoint, the eigenvalue problem is given by $\mathbf{X}\boldsymbol{p} = \omega\boldsymbol{p}$, and when adjoining the operator the eigenvalue is not pulled to the left side of the inner product. Therefore, some authors state that the spectrum of the adjoined is the complex conjugate of the direct spectrum (e.g., [40]). However, this is not consistent with the use of operator families as done in this thesis.

4.2 Solution structure

Unsurprisingly, the solution structure of nonlinear eigenvalue problems is more involved as compared to the case of linear eigenvalue problems. Yet, some concepts from linear eigenvalue problems directly generalize to the nonlinear case. For instance, an eigenvalue must satisfy

$$\operatorname{char}(\omega) := \det(\mathbf{L}(\omega)) = 0, \tag{4.10}$$

i.e., it is a root of the characteristic function of the considered operator family. Yet, in the nonlinear case the characteristic function is not necessarily polynomial in ω with degree N. For instance, in case of polynomial eigenvalue problems with degree K the characteristic function would be a polynomial of degree KN. For the case of the discretized Helmholtz equation, the function is not polynomial as it features exponential delay terms. These considerations show that, unlike for classic eigenvalue problems, in the case of nonlinear eigenvalue problems the total number of eigenvalues can be greater than the considered matrix dimensions. In particular, this allows for different eigenvalues to share linearly dependent eigenvectors. The characteristic function enables counting the algebraic multiplicity of an eigenvalue as the multiplicity of ω as a root of $\operatorname{char}(\omega)$. As for linear eigenvalue problems the geometric multiplicity is defined as the dimension of the corresponding eigenspace, i.e., the number of linearly independent eigenvectors corresponding to ω.

The standard classification for eigenvalues applies. They are called degenerate if the algebraic multiplicity is greater than 1. In general, three important cases are commonly distinguished:

- **simple** eigenvalues
  Eigenvalues whose algebraic multiplicity is 1. In these cases the geometric multiplicity must also be 1.
- **semi-simple, degenerate** eigenvalues
  Eigenvalues whose algebraic and geometric multiplicity is equal but greater 1. The term semi-simple also covers simple eigenvalues, however, these are non-degenerate.
- **defective** eigenvalues
  Eigenvalues whose algebraic multiplicity is greater than their geometric multiplicity.

Depending on the considered operator family the spectrum might feature special symmetries. For instance, the operator families discussed in this thesis are obtained by Fourier transformation of boundary value problems and subsequent discretization. Therefore, their spectrum is symmetric with respect to the imaginary axis, i.e., it features a $\breve{(\cdot)}$-symmetry[1]: if $\omega \in \operatorname{spec}(\mathbf{L})$, then $\breve{\omega} \in \operatorname{spec}(\mathbf{L})$.

[1] Note that $\breve{(\cdot)}$ denotes reflection at the imaginary axis not conjugation!

For simple eigenvalues the direct and the adjoint eigenvector can always be normalized such that:

$$\left\langle \boldsymbol{p}^{\dagger} \middle| \mathbf{L}'(\omega)\boldsymbol{p} \right\rangle = 1. \tag{4.11}$$

Here, $\mathbf{L}'$ is a shorthand for $\frac{\partial}{\partial z}\mathbf{L}$.

It can be shown that this normalization generalizes to all semi-simple eigenvalues, in the sense that it is always possible to biorthonormalize the bases for the direct and the adjoint eigenspace with respect to $\mathbf{L}'$:

$$\left\langle \boldsymbol{p}_i^{\dagger} \middle| \mathbf{L}'(\omega)\boldsymbol{p}_j \right\rangle = \begin{cases} 1 \text{ if } i = j \\ 0 \text{ otherwise} \end{cases} . \tag{4.12}$$

The biorthonormality relations can be even further generalized for the case of defective eigenvalues. This will involve generalized eigenvectors, see, e.g., Theorem 2.5 and further references in [86]. However, this is beyond the scope of this thesis.

Theoretically, eigenvalues could be computed by first finding the roots of the characteristic functions and subsequently computing the corresponding eigenspaces. Nonetheless, numerical issues prohibit this approach. For large dimensions N the determinant of an operator and, hence, the characteristic function of an operator family cannot be reliably computed. This is due to round-off errors. Round-off errors might also impede the correct computation of nullspaces. Therefore, numerical solvers not resting on the characteristic function must be considered.

Although the mathematical notions were introduced for finite-dimensional operator families $\mathbf{L}(z)$, most of the definitions readily apply to the case of infinite-dimensional operator families $\mathcal{L}(z)$. This is the case for the definition of spectra, adjoint operators, and geometric multiplicities. A notable difference is the definition of algebraic multiplicity as a characteristic function could not generally be defined for this class of operators. Algebraic multiplicity is then counted using more abstracts concepts than counting the multiplicity of roots, see [85].

However, the mathematical concepts introduced in this section directly relate to physical concepts and phenomena: in science and engineering the relation obtained from finding the roots of the characteristic function (4.10) is commonly called *dispersion* relation. Semi-simple degenerate modes are often induced by symmetry and might manifest as a pairs of clockwise and counterclockwise spinning modes in annular combustion chambers. This will be discussed in Part II. Finally, defective modes are strongly linked to intrinsic thermoacoustic modes as will be shown in Chap. 10.

The next section introduces the solution algorithm originally devised by Nicoud et al. in [30] for solving the thermoacoustic Helmholtz equation.

4.3 Nicoud's fixed-point algorithm

Introduction to nonlinear eigenvalue problem solvers

Although, there are efficient algorithms to solve the standard eigenvalue problem $(\mathbf{X} - \omega\mathbf{I})\boldsymbol{p} = \mathbf{0}$ and the generalized eigenvalue problem $(\mathbf{X} - \omega\mathbf{Y})\boldsymbol{p} = \mathbf{0}$, solving an eigenvalue problem which is

nonlinear in the eigenvalue ω is intrinsically harder. A plethora of algorithms has been suggested to solve such problems, see the reviews [87, 86] and references therein. All methods have in common that at some point the problem is reduced to an eigenvalue problem linear in the eigenvalue.

- Eigenvalue problems that are polynomial in ω with order K can be rephrased to a linear eigenvalue problem of dimension KN.
- The problem can also be linearized in ω by Taylor expansion. Iteration of this procedure may converge to an eigenvalue. This method can be generalized by truncating the expansion at higher order to obtain a polynomial eigenvalue problem.
- Contour integration methods reduce the eigenvalue problem to a linear eigenvalue problem possessing only the eigenvalues of $\mathbf{L}$ inside a given contour in the complex plane.

Hence, the corner stone of any eigenvalue problem solver is the availability of an algorithm solving the linear eigenvalue problem for $\mathbf{X}-\omega\mathbf{Y}$. Throughout this thesis it is assumed that there is a routine $\mathbf{\Omega}, \mathbf{P} \leftarrow \text{EIG}(\mathbf{X}, \mathbf{Y})$ capable of computing a diagonal matrix $\mathbf{\Omega}$ of the eigenvalues and a corresponding matrix of eigenvectors $\mathbf{P}$, such that $\mathbf{XP} - \mathbf{YP\Omega} = \mathbf{0}$. In the case of dense matrices this will be some global solver, e.g., a QR iteration that finds all eigenpairs. For sparse matrices Krylov subspace solvers are commonly deployed. For instance, both Matlab and SciPy provide wrappers to the implicitly restarted Arnoldi algorithm as it is implemented in the ARPACK library through their `eigs` commands. These iterative solvers are capable of computing a few eigenvalues in the vicinity of a complex number $z^{\{0\}}$ together with the corresponding eigenvectors. They are initialized with a starting vector $\boldsymbol{v}^{\{0\}}$ which is used to generate a Krylov subspace of the considered matrix family. In this work it is assumed that such a method is available as $\omega, p \leftarrow \text{EIGS}(\mathbf{X}, \mathbf{Y}, z^{\{0\}}, \boldsymbol{v}^{\{0\}})$ such that $\omega, \boldsymbol{p}$ is the eigenpair closest to $z^{\{0\}}$ found in the Krylov space generated from $\boldsymbol{v}^{\{0\}}$. Note that if Arnoldi's algorithm is utilized, it is beneficial if $\mathbf{Y}$ is a positive-definite matrix [88, 89].

Despite this well established knowledge of nonlinear eigenvalue problem solvers, the thermoacoustic community widely uses the algorithm proposed in [30]. This fixed-point method has proven to sucesssfully solve the thermoacoustic Helmholtz equation and is probably the most frequently deployed solution algorithm in the community (e.g., used in [90, 24, 49, 78, 62]). Yet, except for the short discussion in [91] there is no reference in the literature discussing the details and limitations of this method. Later chapters will fill this gap and propose other methods that are better suited to solve nonlinear eigenvalue problems as they arise from the thermoacoustic Helmholtz equation. The current chapter summarizes the state of the art in the thermoacoustic community.

The algorithm

In their seminal 2007 paper Nicoud et al. proposed a fixed-point iteration to solve the nonlinear eigenvalue problem arising from a discretization of the thermoacoustic Helmholtz equation. The algorithm is specifically designed to solve

$$\mathbf{L}(\omega)\boldsymbol{p} = \left(\mathbf{K} + \omega\mathbf{C} + \omega^2\mathbf{M} + \mathbf{Q}(\omega)\right)\boldsymbol{p} = 0. \tag{4.13}$$

The algorithm exploits that the problem is quadratic in ω except for the heat release term and possibly frequency-dependent impedance boundary conditions both included in $\mathbf{Q}(\omega)$. The key idea

Algorithm 4.1: Nicoud's algorithm

function ITERATE($\omega^{\{1\}}, \boldsymbol{p}^{\{1\}}, \mathrm{tol}_\omega, \mathrm{maxiter}, \mathbf{K}, \mathbf{C}, \mathbf{M}, \mathbf{Q}$)
  $\omega^{\{0\}} \leftarrow \infty$
  $n \leftarrow 1$
  $\tilde{\boldsymbol{p}}^{\{1\}} \leftarrow \begin{bmatrix} \boldsymbol{p}^{\{1\}} \\ \omega^{\{1\}}\boldsymbol{p}^{\{1\}} \end{bmatrix}$
  $\mathbf{Y} \leftarrow \begin{bmatrix} \mathbf{I} & \mathbf{0} \\ \mathbf{0} & \mathbf{M} \end{bmatrix}$
  while $|\omega_n - \omega^{\{n-1\}}| > \mathrm{tol}_\omega$ **and** $n < \mathrm{maxiter}$ **do**
    $\mathbf{X} \leftarrow \begin{bmatrix} \mathbf{0} & -\mathbf{I} \\ \mathbf{K} + \mathbf{Q}(\omega^{\{n\}}) & \mathbf{C} \end{bmatrix}$
    $\boldsymbol{\omega}^{\{n+1\}}, \tilde{\boldsymbol{p}}^{\{n+1\}} \leftarrow \mathrm{EIGS}(-\mathbf{X}, \mathbf{Y}, \omega^{\{n\}}, \tilde{\boldsymbol{p}}^{\{n\}})$
    $n \leftarrow n+1$
  end while
  $\boldsymbol{p}^{\{n\}} \leftarrow \tilde{\boldsymbol{p}}^{\{n\}}[1 : N+1]$ ▷ Because the EVP is expanded: $\tilde{\boldsymbol{p}} = \begin{bmatrix} \boldsymbol{p} \\ \omega\boldsymbol{p} \end{bmatrix}$
  return $\omega^{\{n\}}, \boldsymbol{p}^{\{n\}}, n$
end function

is, therefore, to iteratively improve an initial guess $\omega^{\{1\}}$ by rephrasing the problem as a linear eigenvalue problem of doubled size and then perform a Picard iteration in the nonlinear terms. The iteration terminates if the difference between the results of two successive iterations is less than a prescribed tolerance or is aborted if a predefined maximum number of iterations is reached. As an initial guess usually the acoustic eigenfrequencies of the system are considered, i.e., the eigenfrequencies if $\mathbf{Q} = \mathbf{0}$. The pseudocode for the subsequent iteration is given in Alg. 4.1. Note that an additional guess $\boldsymbol{p}^{\{1\}}$ for the eigenvector is also passed to the algorithm, in order to support the convergence of the Krylov-subspace method. Also note that if using Bubnov-Galerkin FEM discretizations, the matrix $\mathbf{M}$ is positive-definite[2] and, hence, so is $\mathbf{Y}$. Thus, the eigenvalue problem $\left(\mathbf{X}(\omega^{\{n\}}) - \omega^{\{n+1\}}\mathbf{Y}\right)\tilde{\boldsymbol{p}}^{\{n+1\}} = 0$ appearing at each iteration can be easily solved with the routines available in ARPACK.

Nicoud's procedure defines a mapping $\omega^{\{n+1\}} = f(\omega^{\{n\}})$ for which fixed-points ω are sought. This fixed-point map is implicitly defined by the eigenvalue problem given by the operator family

$$\mathbf{L}_{\mathrm{Nic}}(f;\omega) = \mathbf{X}(\omega) + f\mathbf{Y}. \tag{4.14}$$

It explicitly reads:

$$\mathbf{L}_{\mathrm{Nic}}(f;\omega)\tilde{\boldsymbol{p}} = \left(\begin{bmatrix} \mathbf{0} & -\mathbf{I} \\ \mathbf{K} + \mathbf{Q}(\omega) & \mathbf{C} \end{bmatrix} + f\begin{bmatrix} \mathbf{I} & \mathbf{0} \\ \mathbf{0} & \mathbf{M} \end{bmatrix}\right)\begin{bmatrix} \tilde{\boldsymbol{p}}_{\mathrm{I}} \\ \tilde{\boldsymbol{p}}_{\mathrm{II}} \end{bmatrix} = \mathbf{0}. \tag{4.15}$$

At a fixed-point $\omega = f(\omega)$ the first of the two matrix-equations in (4.15) states $\boldsymbol{p}_{\mathrm{II}} = \omega\tilde{\boldsymbol{p}}_{\mathrm{I}}$. Thus, the second equation then reduces to $\mathbf{L}(\omega)\boldsymbol{p}_{\mathrm{I}} = 0$, which proves that the fixed-points of f are eigenvalues of $\mathbf{L}$ and vice versa. Moreover, $\tilde{\boldsymbol{p}} = \begin{bmatrix} \boldsymbol{p} \\ \omega\boldsymbol{p} \end{bmatrix}$ relates the eigenvectors of the two problems.

[2] This is also true for the finite volume discretization used in CERFACS' AVSP code where $\mathbf{M}$ amounts to $\mathbf{I}$ [79, 92].

Several issues arise when using this algorithm in an attempt to find all relevant eigenfrequencies:

- (i) It is unclear whether all solutions can be found by fixed-point iterations at all, i.e., whether all fixed-points are attracting and
- (ii) even if they are attracting, how many iterations are necessary to find a fixed-point at reasonable accuracy.
- (iii) Moreover, there might be eigenfrequencies which do not originate from acoustic solutions [93]. If these so-called *intrinsic thermoacoustic modes* (ITA) appear, initializing the algorithm with just the acoustic frequencies cannot result in finding all modes in the relevant frequency range.

The items (i) and (ii) concern the convergence properties of the fixed-point iteration. A topic that is usually tackled by Banach's fixed-point theorem. It states that a fixed-point on a domain where the mapping f is a contraction can be found by fixed-point iteration. Nicoud et al. wrote:

> "*In any case, obtaining general results about the contracting properties of the operator f from physical arguments is out of reach of the current understanding of the thermoacoustic instabilities.*"

The perturbation theory presented in the second chapter on nonlinear eigenvalue problems will facilitate exactly this study of the contraction properties of f (Chap. 6). Therefore, the discussion of the contraction properties of Nicoud's algorithm is postponed to the third chapter on the topic (Chap. 8). Item (iii) concerns adequate initialization methods. The usage of integration-based algorithms for this purpose will also be discussed in Chap. 8.

A simplified variant of Nicoud's algorithm

Because solving a quadratic eigenvalue problem is computationally more expensive than solving a linear one, a slightly modified version of Nicoud's fixed-point iteration might be considered. This iteration simply performs a Picard iteration in the ω^2-term. The iteration scheme is given in Alg 4.2.

Note that the eigenvalue here is actually the square of ω. Standard techniques for the solution of generalized eigenvalue problems can, therefore, be readily applied. The square root of the resulting eigenvalue is then an approximation to the sought eigenfrequency. As in the original algorithm the generalized eigenvalue problem solved at every iteration uses a positive-definite matrix, which is simply M in the current case. Again fixed-points of the iteration are valid solution to the considered nonlinear eigenvalue problem.

Relaxation

A common technique to improve the convergence properties of fixed-point iteration is relaxation. This means that the update of the iterated value is additionally governed by a relaxation parameter

Algorithm 4.2: Direct Picard iteration

```
1: function ITERATE(ω^{1}, p^{1}, tol_ω, maxiter, K, C, M, Q)
2:     ω_0 ← ∞
3:     n ← 1
4:     while |ω^{n} − ω^{n−1}| > tol_ω and n < maxiter do
5:         X ← K + ω^{n} C + Q(ω^{n})
6:         ω^{n+1}, p^{n+1} ← EIGS(−X, M, ω^{n}, p^{n})
7:         ω^{n+1} ← √(ω^{n+1})
8:         n ← n + 1
9:     end while
10:    return ω^{n}, p^{n}, n
11: end function
```

$\xi \neq 0$ in the following way:

$$\omega^{\{n+1\}} = \underbrace{\xi f(\omega^{\{n\}}) + \omega^{\{n\}}(1-\xi)}_{\tilde{f}(\omega^{\{n\}};\xi)}. \tag{4.16}$$

This relaxation defines a new family of fixed-point mappings $\tilde{f}(\omega^{\{n\}};\xi)$ parametrized in ξ (note that $\tilde{f}(\omega^{\{n\}},1) = f(\omega^{\{n\}})$). Improving the convergence properties, thus, amounts to choosing ξ such that $\tilde{f}$ features better convergence properties than f.

Banach's fixed-point theorem requires that $|\tilde{f}'| < 1$ for the iteration to converge. Moreover, it can be shown that super-linear convergence is achieved if $\tilde{f}' = 0$. A quick calculation shows $\tilde{f}' = 1 + (f' - 1)\xi$ and, hence, choosing

$$\xi = \frac{1}{1 - f'(\omega)} \tag{4.17}$$

would be an optimal choice. Nevertheless, as the fixed-point ω is not known a priori, the equation is useless for actual computations. A remedy is to approximate the derivative from the results of two consecutive iterations

$$f'(\omega) \approx f'^{\{n\}} := \frac{f(\omega^{\{n\}}) - f(\omega^{\{n-1\}})}{\omega^{\{n\}} - \omega^{\{n-1\}}} \tag{4.18}$$

and then use the relaxation parameter

$$\xi^{\{n\}} = \frac{1}{1 - f'^{\{n\}}} \tag{4.19}$$

at the nth iteration. Note that division by zero is not an issue in (4.18), because if $\omega^{\{n\}} - \omega^{\{n-1\}} = 0$, a fixed-point has been found. This adaptive relaxation method is currently implemented in CERFACS' Helmholtz solver AVSP [94, Appendix C].

Instead of estimating the derivative from finite differences, it can also be evaluated at $\omega^{\{n\}}$ using perturbation theory, as it will be presented in Chap. 6. This approach should allow for faster and more precise computations of f'. However, if perturbation theory is leveraged to compute a derivative, it should be fed into a Newton method directly, guaranteeing super-linear convergence.

Adaptive relaxation strategies are, therefore, not further considered in this work but Newton-type iteration will be discussed in Chap. 8.

4.4 Application to a Rijke-tube model

This section applies the presented theory to the Rijke-tube model. Here, it serves basically as a validation case. The chosen parameters are $L = 1$, $x_{\mathrm{flm}} = x_{\mathrm{ref}} = 0.5$, $c_1 = 1$, $c_2 = 2$, $n = 1$, and $\tau = 2$.

The network discretization of the Rijke tube can be considered as an exact solution of the problem and, therefore, constitutes an ideal benchmark for validation purposes. To find eigenvalues, the dispersion relation of the network model has been solved using the numerical root-finding routine FSOLVE from the SciPy Library version 1.0.0 with default settings. Initializing the solver with starting values taken from an axis-parallel grid of 1001×201 points distributed equidistantly between $0 - 1\mathrm{i}$ and $10 - 1\mathrm{i}$ allowed for finding four thermoacoustic modes in the same region. Figure 4.1 shows the results of this brute-force search for eigenvalues. The depicted region of the complex plane is identical to the regions from which the initial guesses are sampled. The colors indicate to which eigenvalue the initial guess will converge. White indicates solutions which converged to eigenvalues outside of the shown domain. Black highlights the position of starting values for which the method does not converge while using no more than 500 calls to the dispersion relation.

Yet, when considering the passive flame case ($n = 0$) only two modes can be found. All computed eigenvalues are listed in Tab. 4.1 together with eigenvalues computed using a finite element discretization of the problem on a uniform mesh featuring 32 degrees of freedom and applying 15 iterations of the Nicoud and the Picard algorithm, respectively. The two fixed-point iterations are not capable of finding the active modes #R3 and #R4. One problem is that there are only two passive eigenvalues to start with. These are obviously not enough to find four modes. However, even when initializing the algorithm with the eigenvalues found from the network model, the modes #R3 and #R4 cannot be found. This raises the question whether these two modes do really exist and the fixed-point iterations are just not appropriate means to find them, or whether they arise from numerical issues of the network model. Indeed, the theory presented later in this thesis will show that the two modes do also exist for the FEM model. Note that the eigenvalue of the active mode #R1 is close to the eigenvalue of the passive mode #R1. The same is true for the active and the passive mode #R2. Apparently, the passive modes evolve to these two active modes which justifies labeling the modes with the same descriptor for both the active and the passive flame case. For the network model, which is considered an exact solution of the problem, the eigenfrequency of #R2 remains even unchanged. Observing closed-by pairs of active and passive modes is in-line with the motivation for using the passive eigenfrequencies to initialize Nicoud's algorithm. However, there seems to be no passive counterpart for the modes #R3 and #R4, which is a first hint that these two modes are intrinsic.

Figure 4.2 shows the mode shapes found with the network and the finite element model for both the active and the passive flame case. Solving the FEM model with either Nicoud's algorithm or the Picard iteration yield identical mode shapes (dotted and dashed lines, respectively). However, they show minor deviations from the mode shapes computed using the network model. These deviations can be attributed to a discretization error. Moreover, the results support the hypothesis that the passive modes #R1 and #R2 evolved into the active modes #R1 and #R2, because

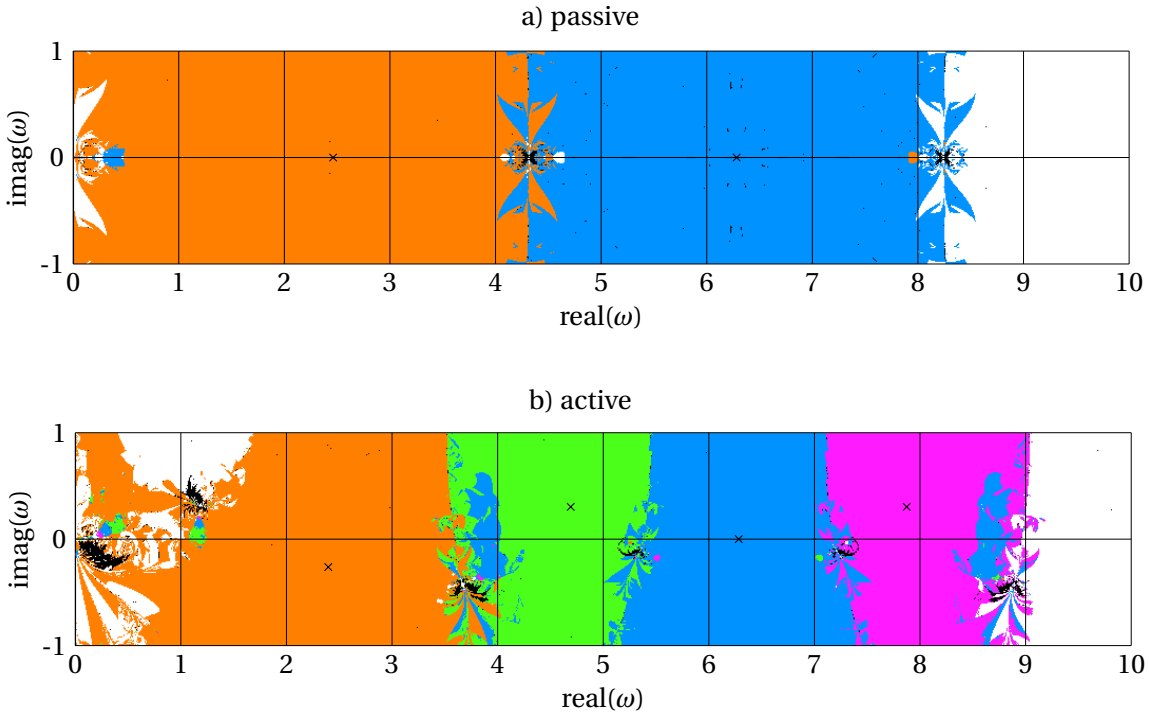

Figure 4.1: Convergence map for a) the passive and b) the active flame when solving the dispersion relation numerically using FSOLVE from SciPy. The complex plane has been sampled from a grid of 1001×201 starting values that are uniformly distributed in the shown region. The colors indicate to which eigenfrequency the initial guess converges: orange – #R1, cyan – #R2, green – #R3, purple – #R4, white – eigenvalues outside of the shown rectangle, black – no convergence. The black crosses highlight the position of the eigenvalues

the mode shapes are very similar.

Note that the phase of mode #R2 occasionally jumps by an amount of 2π when comparing the various cases (active and passive) and solution methods (fsolve, Nicoud, Picard). This is due to the periodicity of the phase angle. The phases and, thus, the mode shapes can, therefore, be considered to be almost identical. The similarity can be attributed to the pressure anti-node of mode #R2 at $x = 0.5$. This is exactly the reference point for the flame model. Hence, this mode cannot excite the flame and consequently the passive and active mode shapes are identical and feature identical eigenfrequencies with zero growth rate. This behavior is correctly resolved by the network model. On the contrary, the FEM model predicts $\mathrm{imag}(\omega) = -0.0261$ for the active case, which means this mode is slowly growing. Definitely this small deviation is due to to the spatial discretization of the problem: in the FEM model a single point cannot be exactly resolved, hence, the mode shape does not feature an exact pressure anti-node at the reference point. This in turn implies a small interaction with the flame.

However, it can be summarized that the modes #R1 and #R2 are computed sufficiently accurate by the finite element approach. How to find the modes #R3 and #R4 remains an open question. It will be answered in Chap. 8.

Table 4.1: Eigenvalues ω of the Rijke-tube model computed by a) solving the dispersion relation obtained from the network discretization using FSOLVE from SciPy, b) applying Nicoud's algorithm to a FEM discretization of the model, and c) applying the Picard iteration to the model.

#	n	Net–fsolve	FEM–Nicoud	FEM–Picard
			passive	
#R1	0	$2.4619 + 0.0000\mathrm{i}$	$2.4230 + 0.0000\mathrm{i}$	$2.4230 + 0.0000\mathrm{i}$
#R2	0	$6.2832 + 0.0000\mathrm{i}$	$6.2899 + 0.0000\mathrm{i}$	$6.2899 + 0.0000\mathrm{i}$
			active	
#R1	1	$2.3960 - 0.2623\mathrm{i}$	$2.3687 - 0.2657\mathrm{i}$	$2.3687 - 0.2657\mathrm{i}$
#R2	1	$6.2832 + 0.0000\mathrm{i}$	$6.4226 - 0.0261\mathrm{i}$	$6.4226 - 0.0261\mathrm{i}$
#R3	1	$4.6921 + 0.3036\mathrm{i}$	–	–
#R4	1	$7.8742 + 0.3036\mathrm{i}$	–	–

4.5 Application to the Kronig-Penney model

In this section the theory is applied to the Kronig-Penney model. The model is considered for $K = 12$ sources. All interaction indices are set to $n_k = n = 0.1$ and the delay times to $\tau_k = \tau = 0.34$. The model is, thus, identical to the model presented in [55]. Exact eigenvalues for the model are computed by solving the dispersion relation of the network discretization (2.21) with `fsolve` and compared to solutions obtained from an FEM discretization of the problem. The FEM discretization featured 84 equidistantly distributed nodes, i.e., 7 nodes per unit cell. This relatively low resolution is chosen on purpose in order to demonstrate effects of the mesh on the solution.

Here, the eigenvalues in an axis-parallel region between $-\mathrm{i}$ and $24 + \mathrm{i}$ are discussed. In the passive case ($n = 0$) the eigenvalues are algebraically known to be $\omega = 0, 1, \ldots, 24$. For $\omega = 0$ the associated eigenspace $\widehat{p}(\varphi) \in \mathrm{span}(\{1\})$ while for the other eigenvalues the geometric multiplicity is two and the eigenspaces read $\widehat{p}(\varphi) \in \mathrm{span}(\{\cos(\omega\varphi), \sin(\omega\varphi)\})$.

Figure 4.3 shows the eigenvalue found for the active case computed from the network model and from the FEM discretization utilizing the two fixed point strategies with a tolerance of $\mathrm{tol}_\omega = 0.01$. The fixed-point iterations converged within 3 iterations to this accuracy. For low $\mathrm{real}(\omega)$ the eigenvalues found from the network model using the fixed-point iterations correspond well with the solutions from the network model. Yet, there is an increasing deviation the higher $\mathrm{real}(\omega)$ is. This is because the higher $\mathrm{real}(\omega)$ is, the shorter are the wavelengths of the considered mode shapes and accurately resolving them then requires finer mesh resolutions. However, these mesh effects do not concern the current matter.

What matters is that again more eigenvalues are found from the network model in the active case as compared to the passive case. The main reason for this is a loss of symmetry. The passive flame features a rotational symmetry which is not discrete. This is the reason why all eigenspaces corresponding to a non-zero eigenvalue ω are degenerate: given an eigenfunction $\cos(\omega\varphi)$ it can be converted into $\sin(\omega\varphi)$ by an appropriate rotation. The two functions are linearly independent. However, they must be associated with the same eigenvalue as any rotation is not changing the model equations. On the contrary, in the active case the problem features a discrete rotational symmetry of degree 12. Therefore, if a solution is rotated by increments of $\frac{2\pi}{12}$, the result will still

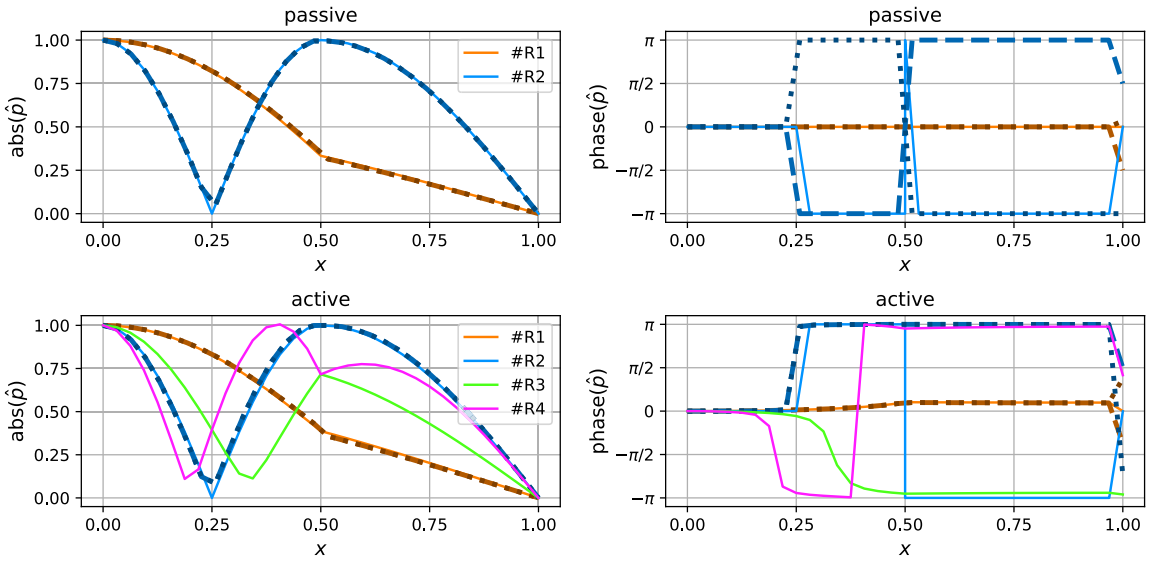

Figure 4.2: Comparison of mode shapes from the network model (solid) and the finite element discretization solved with the original (dots) and modified (dashed) version of Nicoud's algorithm. Both versions of the algorithm are unable to find the modes #R3 and #R4.

be a solution. Yet, only if $m \bmod 6 \neq 0$ the resulting mode shape will be linearly independent from the original mode shape and the mode will be still degenerate. For solutions whose azimuthal mode order m satisfies $m \bmod 6 = 0$, the result will be linearly dependent with respect to the original mode and it can, therefore, be expected to be non-degenerate. Consequently, the originally twofold degenerate modes split if $m \bmod 6 \neq 0$ in the active flame case. $\omega = 0$ is special as the mode is already simple in the passive case. However, because the sources are modeled proportional to $\omega n \exp(-\mathrm{i}\omega\tau)$ they vanish if $\omega = 0$. Consequently, the eigenpair $\omega = 0$ and $\hat{p} \in \mathrm{span}(\{1\})$ will remain unchanged.

As 5 modes split, there will be at least $24 + 5 = 29$ modes in the active case (additional intrinsic modes may occur). The fixed-point iteration initialized with 24 passive solutions, therefore, cannot find all these modes. As illustrated with this example, symmetry breaking which results in split modes is a particular challenge for fixed-point algorithms.

4.6 Application to MICCA

This section applies the theory to the MICCA model. The first axial (labeled #M0) and the first two azimuthal modes (#M1 and #M2) are considered. The passive eigenvalue problem is polynomial and can, therefore, be directly solved. For the active flame the two fixed-point algorithms are utilized with the tolerance set to $\mathrm{tol}_\omega = 0.01 \times 2\pi\mathrm{s}^{-1}$. Table 4.2 lists the results of this study. Note that for the active mode #M1 relaxation was necessary as it otherwise converged to the active mode #M2. Both algorithms needed the same number of iterations to converge within the specified tolerance. To further assess the quality of the algorithms the norm of the residual vector was

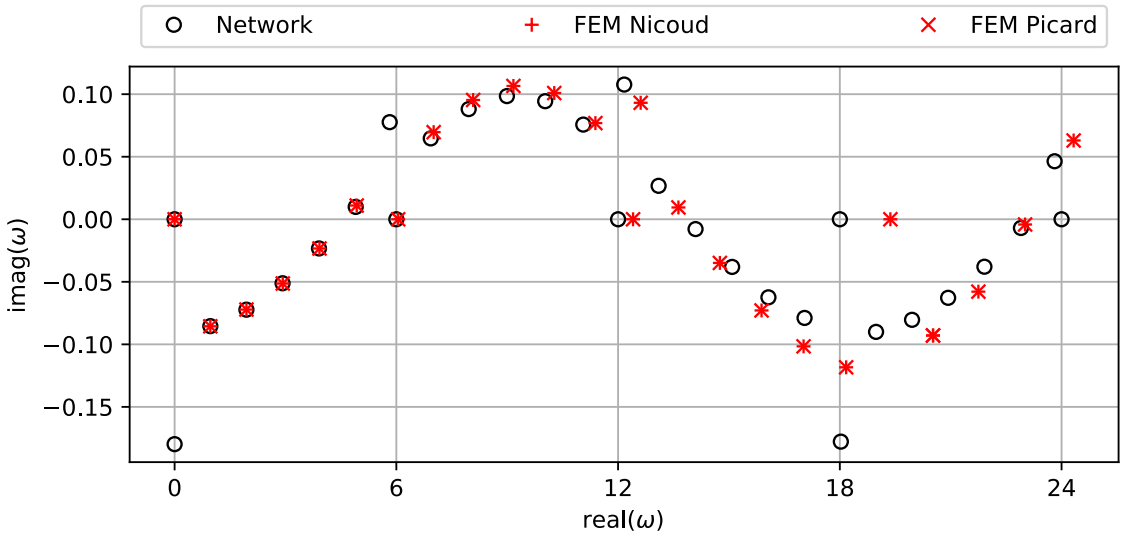

Figure 4.3: Comparison of eigenvalues of the Kronig-Penney model obtained from the network formulation and FEM computations. The FEM model featured 84 equidistantly distributed nodes. The network solutions can be considered as exact. Note how the FEM solutions increasingly deviate from the network predictions. This is attributed to the relatively low mesh resolution. The fixed-point algorithm also fails to find the $\omega = 0$ mode. Also note that for $\mathrm{imag}(\omega) = 6n$, where $n \in \mathbb{N}$,there are two distinct eigenvalues. This is a consequence of loss of symmetry.

computed as

$$\text{Res.} = \frac{\|\mathbf{L}(\omega)\boldsymbol{p}\|_2}{\|\boldsymbol{p}\|_2}. \tag{4.20}$$

According to these calculations, the Picard iteration yields better estimates than Nicoud's iteration. Nevertheless, when compared to the residual of the passive solution both iteration strategies have significantly higher residual norms. This is clearly because for the passive case the eigenvalue problem is quadratic and can, thus, be solved to machine precision by reformulation as a (larger) linear eigenvalue problem. On the other hand, the iterations used to solve the active case were terminated if the change in ω between to consecutive iterations steps was less than $0.01 \times 2\pi\mathrm{s}^{-1}$. This,

Table 4.2: Passive mode frequencies of the MICCA model and active mode frequencies found using the fixed-point iterations. The columns labeled Itr. state the number of iteration necessary to reach the stopping criterion tol=$0.01 \times 2\pi\mathrm{s}^{-1}$ with the respective algorithms. The columns entitled Res. report the norm of the residual of the found solutions computed as $\|\mathbf{L}(\omega)\boldsymbol{p}\|_2/\|\boldsymbol{p}\|_2$.

	passive		active					
					Nicoud		Picard	
mode	$\omega\frac{\mathrm{s}}{2\pi}$	Res.	$\omega\frac{\mathrm{s}}{2\pi}$	ξ	Itr.	Res.	Itr.	Res.
#M0	332.0	6.88E−12	154.5 + 67.9i	1.00	24	137	24	3.10E−3
#M1	471.8	6.35E−12	511.4 − 79.4i	0.75	16	95.7	16	2.04E−3
#M2	731.4	5.65E−12	713.1 − 2.3i	1.00	6	24.5	6	1.39E−3

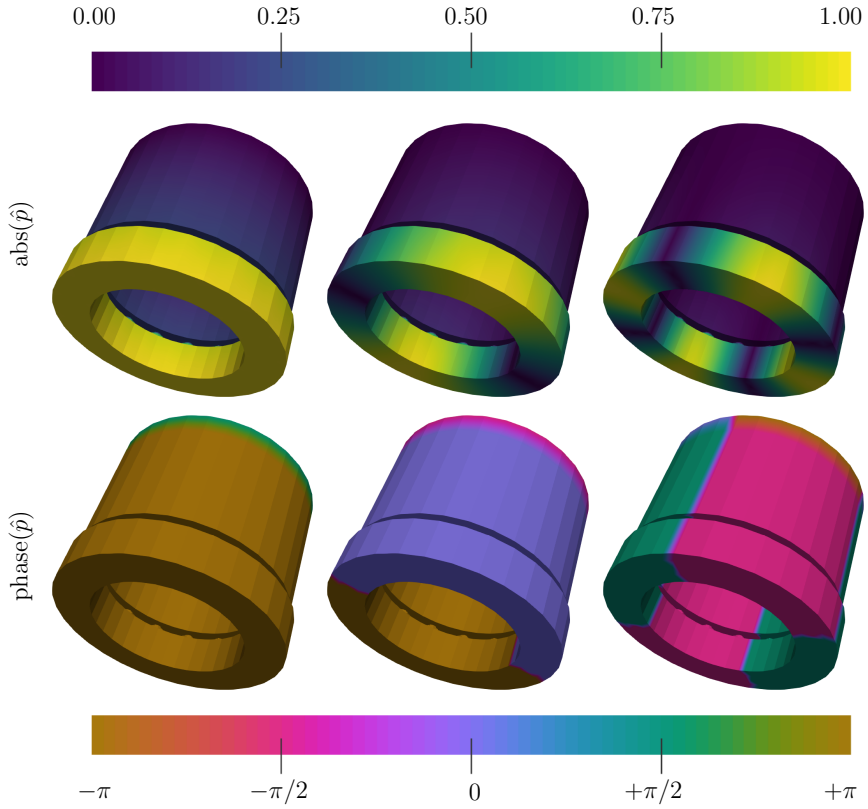

Figure 4.4: Passive modes computed for the MICCA model. From left to right the figure shows the modes #M0, #M1, and #M2. The top row depicts the magnitude, the bottom row the phase of the modes. Note that the phase jump at the outlet is attributed to the undefined phase at a sound-soft boundary ($\hat{p} = 0$).

of course, does not guarantee finding machine-precise solutions to the problem. That the norm of the residual is higher for Nicoud's iteration than for the Picard iteration, might be attributed to the fact that after reformulating the problem as a linear eigenvalue problem the eigenvector explicitly depends on ω (See (4.15) and comments below). Hence, the error in ω contributes twice to the residual: it not only appears in $\mathbf{L}(\omega)$ but also in $\boldsymbol{p}$ taken from $\tilde{\boldsymbol{p}} = \begin{bmatrix} \boldsymbol{p}_\mathrm{I} \\ \omega \boldsymbol{p}_\mathrm{II} \end{bmatrix} = \begin{bmatrix} \boldsymbol{p} \\ \omega \boldsymbol{p} \end{bmatrix}$. Note that the error in ω will effect $\boldsymbol{p}$ regardless of whether $\boldsymbol{p}_\mathrm{I}$ or $\boldsymbol{p}_\mathrm{II}$ is used to deduce $\boldsymbol{p}$. This is because $\boldsymbol{p}_\mathrm{I}$ and $\boldsymbol{p}_\mathrm{II}$ are coupled.

Figure 4.4 shows the passive mode shapes. The mode shapes for the active case are shown in Fig. 4.5. The passive mode frequency of 471.8 Hz agrees with the value of 472 Hz stated in [62]. Because the active flame models differ in the flame dynamics model, direct comparison of the solutions is not possible. The unusually high magnitude of the imaginary part of the frequency of modes #M0 may be attributed to the continuation of the measured flame transfer function data into the complex plane using the fit to a state space model. More raw data or a better continuation method might improve the predictions. For the objectives of this thesis, however, this aspect is not relevant.

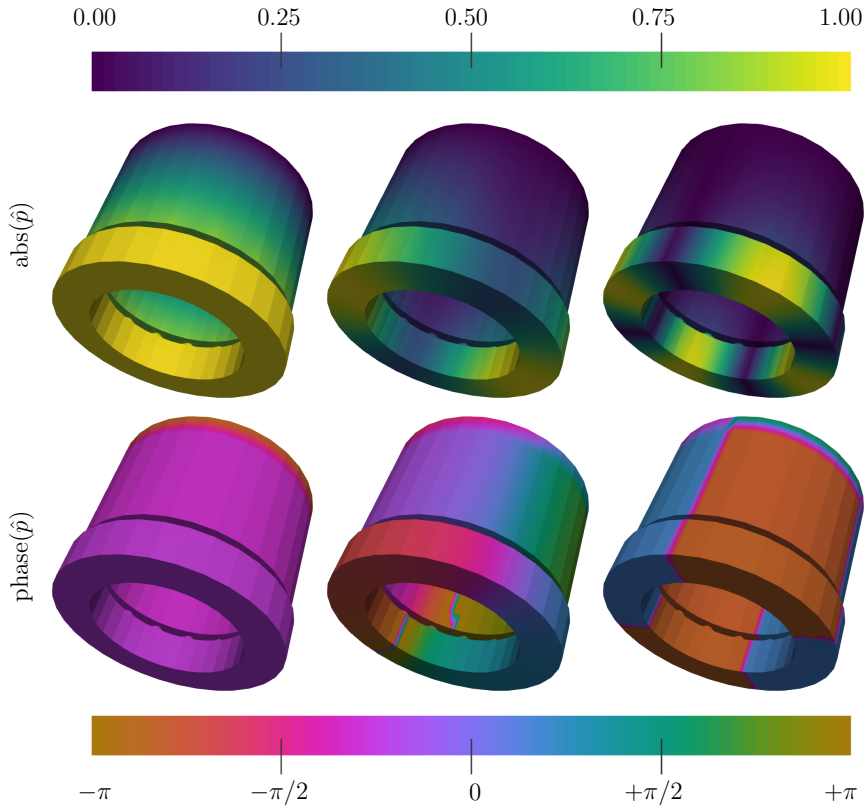

Figure 4.5: Active modes computed for the MICCA model. From left to right the figure shows the modes #M0, #M1, and #M2. The top row depicts the magnitude, the bottom row the phase of the modes. The imagery shown here is obtained from the Picard iteration. Results from the Nicoud iteration would look identical. As for the passive case the phase discontinuity at the outlet is attributed to the undefined phase at a sound-soft boundary. The azimuthal jump occurring in the phase of #M1 is an artifact from the plotting software which fails to accurately color a jump from $-\pi$ to $+\pi$.

Part II

Exploiting the Symmetry of Annular Combustion Chambers

Chapter 5

Bloch-wave theory

Annular combustion chambers feature periodic structure giving them a discrete rotational symmetry, i.e., they consist of B identical sectors. Stationary gas turbines typically feature about 24 of these sectors. This symmetry gives rise to the idea of considering only one such sector for the stability analysis of the full combustors. Bloch wave theory facilitates such a single-sector computation.

Bloch-wave theory has been first developed in the field of quantum mechanics by Felix Bloch [95] to model the behavior of electrons in periodic crystal lattices. The problem is modeled by solving the Schrödinger equation with periodic potentials. Mathematically this equation is equivalent to the thermoacoustic Helmholtz equation. The main mathematical difference between the two is that the potentials in Schrödinger equations are usually considered to be real-valued and independent of the eigenvalue (the energy) which renders the equation a self-adjoint linear eigenvalue problem. On the contrary, the flame operator – which is the thermoacoustic counterpart of the potential – is complex valued and depends nonlinearly on the eigenvalue. However, Bloch's concept of decomposing the solution into Bloch waves to enable unit-cell computations still applies.

Because the only condition needed to apply Bloch's theorem is discrete rotational symmetry, it can be readily used in scientific fields other than quantum mechanics as long as the considered problems feature an appropriate periodicity. It has been used to model a variety of wave phenomena in periodic domains, for instance, electromagnetic or acoustic-wave propagation in periodic waveguides [96, 97] and vibration analysis in structural mechanics [98, 99]. In analogy to its origin in modeling electron propagation in crystalline structures, the notions photonic and phononic crystal have been coined, see, e.g., [100] and references therein. From this viewpoint annular combustion chambers are *thermoacoustic* crystals and it is natural to deploy Bloch's theorem to them as well. The idea of utilizing Bloch-wave theory to ease stability assessment of thermoacoustic modes in annular combustors was first proposed by Moeck in his thesis [55]. He briefly demonstrated its applicability with a network discretization of the Kronig-Penney model. Indeed, reducing the effort for such computations by means of symmetry was already considered by Walz et al. and allowed to reduce the computational domain to one quarter of a full annulus [101]. The approach has been successfully applied to compute thermoacoustic modes in the Ansaldo AE94.3A combustion chamber [78]. However, Bloch-wave theory enables unit-cell computations which in the case of the AE94.3A and many other industrial chambers comprise a single burner-flame-pair. Nevertheless, the approach is capable of modeling effects induced by the mutual flame interaction

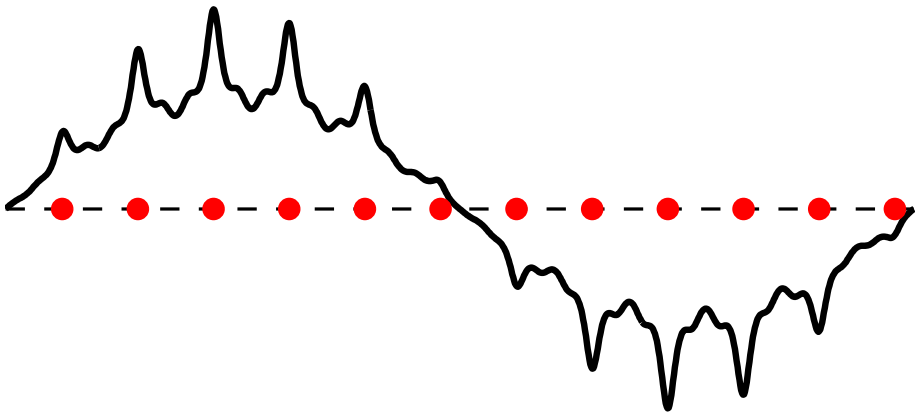

Figure 5.1: Example illustration of the imaginary part of a Bloch wave with Bloch wavenumber $b = 1$ and $B = 12$ cells. Note how the sine function is periodically modulated. Illustration taken from [104].

as reported by Dawson and Worth [102].

Parts of this chapter have been previously published with Jonas Moeck in [103] and [104]. The latter was written together with Giovanni Campa and contains application of the theory for thermoacoustic stability assessment of an industrial gas turbine.

5.1 Bloch's Theorem

Bloch's theorem can be stated as follows:

Bloch's Theorem

The eigenmodes $\widehat{p}$ of the eigenvalue problem $\mathcal{L}(\omega)\widehat{p}$ describing a problem that is invariant under rotations by an angle of $2\pi/B$ can be formulated using basis functions $\widehat{p}_{\widetilde{b}}$ of the form

$$\widehat{p}_{\widetilde{b}}(\varphi, r, z) = e^{\mathrm{i}b\varphi}\psi_b(\varphi, r, z) \tag{5.1}$$

where ψ_b is a $2\pi/B$-periodic function:

$$\psi_b(\varphi + 2\pi/B, r, z) = \psi_b(\varphi, r, z). \tag{5.2}$$

The functions $\widehat{p}_{\widetilde{b}}$ are called Bloch waves. Here B is a positive integer called the resolution. In this context it will correspond to the degree of cyclic symmetry of the combustion chamber. Moreover, the integer b is called the Bloch wavenumber.

Figure 5.1 shows the imaginary part of a one-dimensional example of a Bloch wave. The shown domain features B=12 cells and a Bloch wavenumber of b=1.

Although, any integer b can serve as a Bloch wavenumber, not all of them are independent.

This is because

$$\widehat{p_{\widetilde{b+B}}}(\varphi) = e^{\mathrm{i}(b+B)\varphi}\psi_{b+B}(\varphi) = e^{\mathrm{i}b\varphi}\underbrace{e^{\mathrm{i}B\varphi}\psi_{b+B}}_{\psi_b(\varphi)}(\varphi) = e^{\mathrm{i}b\varphi}\psi_b(\varphi) = \widehat{p}_{\widetilde{b}}(\varphi) \tag{5.3}$$

holds for a given resolution B. Hence, a Bloch wave of wavenumber b can be rephrased as one of Bloch wavenumber $b+B$ and vice versa. Two Bloch wavenumbers b and β are independent if $(b-\beta) \bmod B \neq 0$. Thus, it suffices to consider only Bloch wavenumbers b ranging from 0 to $B-1$.

The special structure of Bloch waves admits

$$\widehat{p}_{\widetilde{b}}(\varphi + 2\pi/B) = e^{\mathrm{i}b2\pi/B}e^{\mathrm{i}b\varphi}\psi_b(\varphi) = e^{\mathrm{i}b2\pi/B}\widehat{p}_{\widetilde{b}}(\varphi). \tag{5.4}$$

This property is called Bloch periodicity. It is the key ingredient enabling unit cell computations, because applying it multiple times allows to determine the values of the Bloch wave everywhere knowing only values on an interval $[a; a+2\pi/B[$. Moreover, it clarifies what boundary conditions to impose on the newly created boundaries when cutting a unit cell from the entire domain. As these boundaries are separated by an angle of $\Delta\varphi = 2\pi/B$, the solution on these two boundaries is linked through the Bloch periodicity. Without loss of generality the coordinate system can be chosen such that $\varphi = 0$ is located in the middle of the unit cell. The boundaries are then located at $\varphi = -\pi/B$ and $\varphi = +\pi/B$, respectively. The boundary condition to be imposed then reads:

$$\widehat{p}_{\widetilde{b}}\left(-\frac{\pi}{B}, r, z\right) = e^{\mathrm{i}b\frac{2\pi}{B}}\widehat{p}_{\widetilde{b}}\left(\frac{\pi}{B}, r, z\right). \tag{5.5}$$

Note that Bloch periodic boundary conditions enforce a phase shift and are, therefore, conceptually related to phase-lagged boundary conditions developed in [105] to efficiently compute transonic flows in periodic turbomachinery components in time-domain. See, e.g., [106] for a recent application of this approach in a large eddy simulation.

However, the Bloch periodicity depends on the Bloch wavenumber and imposing boundary conditions with different Bloch wavenumbers will yield different modes. Instead of solving the full problem $\mathcal{L}(\omega)\widehat{p} = 0$, B surrogate problems $\mathcal{L}_{\mathrm{Bloch}}(\omega; b)\widehat{p}_{\widetilde{b}} = 0$ where $b = 0, \ldots, B-1$, formulated on a unit cell, are to be solved. Unifying the spectra of the surrogate systems yields the spectrum of the original operator:

$$\mathrm{spec}(\mathcal{L}(z)) = \bigcup_{b=0}^{B-1} \mathrm{spec}(\mathcal{L}_{\mathrm{Bloch}}(z; b)). \tag{5.6}$$

The corresponding eigenvectors are obtained by extrapolating the eigenvectors from the surrogate systems using the Bloch periodicity.

The Bloch wavenumber is also related to the azimuthal mode order: the azimuthal mode order of a mode $\widehat{p}$ is defined as the smallest integer m for which the periodicity $\widehat{p}(\varphi + 2\pi/m)$ in the azimuthal coordinate φ holds. Because

$$\widehat{p}_{\widetilde{b}}(\varphi)(\varphi + 2\pi/|b|) = e^{\mathrm{i}b(\varphi+2\pi/|b|)}\psi_b(\varphi + 2\pi/|b|) = e^{\mathrm{i}b\varphi+\mathrm{i}\,\mathrm{sgn}(b)2\pi}\psi_b(\varphi) = \widehat{p}_{\widetilde{b}}(\varphi) \tag{5.7}$$

a mode of azimuthal order m can be represented by a Bloch wave featuring a Bloch wavenumber of modulus m. Due to (5.3) two Bloch wavenumbers b and β for which $b \bmod B = \beta \bmod B$ correspond to identical surrogate systems: $\mathcal{L}_{\mathrm{Bloch}}(z; b) = \mathcal{L}_{\mathrm{Bloch}}(z, \beta)$. Consequently, the surrogate

system $\mathcal{L}_{\text{Bloch}}(z;b)$ contains only modes whose azimuthal mode orders satisfy $\min(b \bmod B, B-(b \bmod B)) = \min(m \bmod B, B-(m \bmod B))$.

5.2 Proof of Bloch's theorem

Bloch's original proof rests on arguments from group theory. In modern books on quantum mechanics the standard proof for the applicability of Bloch's theorem focuses on linear eigenvalue problems (see, e.g., [107]) as the Schrödinger equation is usually linear in its eigenvalue. Fortunately, as already demonstrated by Bloch's proof, linearity in the eigenvalue is not a necessary condition for the applicability of Bloch's theorem. Here, another proof is presented avoiding the more involved group theory. The proof is based on basic ideas from linear algebra and Fourier transforms as they are also used for the case of linear eigenvalue problems. However, the presented proof is generalized to the nonlinear case. As a byproduct it proves many useful properties of Bloch waves.

The proof starts with showing that Bloch waves $f_{\tilde{b}}$ featuring independent Bloch wavenumbers are linearly independent. Repeatedly applying the Bloch periodicity (5.4), i.e., rotations by an angle of $2\pi/B$ yields

$$f_{\tilde{b}}(\varphi + k2\pi/B) = \left(e^{\mathrm{i}2\pi/B}\right)^{bk} f_{\tilde{b}}(\varphi). \tag{5.8}$$

Because of the 2π-periodicity of the Bloch wave, applying the Bloch periodicity B times yields $f_{\tilde{b}}(\varphi + B2\pi/B) = f_b(\varphi + 2\pi) = f_{\tilde{b}}(\varphi)$. Hence, for the following considerations only increments of $k \in \{0,1,\ldots,B-1\}$ are of interest. Furthermore, without loss of generality it is assumed that $f_b(\varphi_0) = 1$. Now writing 0 as linear combination of Bloch waves of different Bloch wavenumbers results in

$$0 = \sum_b \lambda_b f_{\tilde{b}}(\varphi) \qquad \text{|evaluate at some } \varphi = \varphi_0 \text{ and } \varphi = \varphi_0 + k2\pi/B \tag{5.9}$$

$$\Rightarrow 0 = \sum_b \lambda_b f_{\tilde{b}}(\varphi_0) = \sum_b \lambda_b f_{\tilde{b}}(\varphi_0 + k2\pi/B) \qquad \forall k \in \{0,1,\ldots,B-1\} \qquad \text{|Bloch periodicity} \tag{5.10}$$

$$\Rightarrow 0 = \sum_b \lambda_n \left(e^{\mathrm{i}2\pi/B}\right)^{bk} f_{\tilde{b}}(\varphi_0) \qquad \forall k \in \{0,1,\ldots,B-1\} \qquad \text{|by assumption } f_{\tilde{b}}(\varphi_0) = 1 \tag{5.11}$$

$$\Rightarrow 0 = \sum_b \lambda_n \left(e^{\mathrm{i}2\pi/B}\right)^{bk} \qquad \forall k \in \{0,1,\ldots,B-1\} \tag{5.12}$$

It is convenient to rephrase the last B equations using matrix-vector notation:

$$\mathbf{0} = \mathbf{W}\boldsymbol{\lambda} \tag{5.13}$$

where $\boldsymbol{\lambda}$ is the vector of coefficients $\lambda_n =: [\boldsymbol{\lambda}]_n$ and the matrix $\mathbf{W}$ has the entries[1] $[\mathbf{W}]_{b,k} = \left(e^{\mathrm{i}2\pi/B}\right)^{bk}$. This matrix is the same matrix that appears in B-point discrete Fourier transform and is, thus,

[1] For convenience, the indexing of the Fourier matrix entries is started with zero.

known as Fourier matrix. It is invertible ($[\mathbf{W}^{-1}]_{b,k} = 1/B\left(e^{-\mathrm{i}2\pi/B}\right)^{bk}$). Hence, $\boldsymbol{\lambda} = \mathbf{0}$, which means that there is no linear combination except for the trivial one which combines Bloch waves of independent Bloch wavenumbers to zero at φ_0. Consequently, Bloch waves with independent Bloch wavenumbers are linearly independent.

Moreover it can be concluded that any 2π-periodic function $f(\varphi)$ can be uniquely decomposed into B linearly independent Bloch waves, such that

$$f(\varphi) = \sum_{b=0}^{B-1} f_{\tilde{b}}(\varphi) \tag{5.14}$$

holds. Bloch periodicity enables rewriting the expansion (5.14) as

$$f(\varphi + k2\pi/B) = \sum_{b=0}^{B-1} \left(e^{\mathrm{i}2\pi/B}\right)^{bk} f_{\tilde{b}}(\varphi) \tag{5.15}$$

for each $k \in \{0, 1, \ldots, B-1\}$. Again the system matrix is found to be the Fourier matrix $\mathbf{W}$. Applying the inverse $\mathbf{W}^{-1}$ allows for computing the Bloch waves $f_{\tilde{b}}(\varphi)$ from the function $f(\varphi)$ according to the formula

$$f_{\tilde{b}}(\varphi) = \frac{1}{B} \sum_{k=0}^{B-1} \left(e^{-\mathrm{i}2\pi/B}\right)^{bk} f(\varphi + k2\pi/B). \tag{5.16}$$

Loosely speaking, this result allows to interpret decomposition of the solution into Bloch waves as performing a discrete Fourier transform over a sequence of unit cells.

Note that this concept is related to the expansion of an arbitrary function as a sum of an even and an odd function. There is a symmetry operator $\mathcal{R}$ which connects a set of points from the function domain. In the case of Bloch waves this is an incremental rotation operator $\mathcal{R} = \mathcal{R}_B$: $\varphi \mapsto \varphi + 2\pi/B$ and in the case of even and odd functions its a reflection operator $\mathcal{R} = \mathcal{R}_\pm : \varphi \mapsto -\varphi$. The values of these points are connected through a restriction law, which is $f(\mathcal{R}_B\varphi) = e^{\mathrm{i}b2\pi/B} f(\varphi)$ for the Bloch wave case and $f(\mathcal{R}_\pm\varphi) = \pm f(\varphi)$ in the case of even and odd functions. In both cases a unique expansion exists. For convenience the notation $\mathcal{R}f(\varphi) = f(\mathcal{R}\varphi)$ is introduced, i.e., applying the symmetry operator to a function denotes performing the symmetry action on its argument.

The restriction laws may be interpreted as eigenequations of their respective operators: while even and odd functions are the eigenfunctions of the reflection operator $\mathcal{R}_\pm$ corresponding to the eigenvalues 1 and -1, respectively, Bloch waves $f_{\tilde{b}}$ are the eigenfunctions of the incremental rotation operator $\mathcal{R}_B$ corresponding to the eigenvalues $e^{\mathrm{i}b2\pi/B}$:

$$\begin{aligned}
\mathcal{R}_n f_{\tilde{b}}(\varphi) &= f_b(\varphi + 2\pi/B) && (5.17)\\
&= e^{\mathrm{i}b(\varphi+2\pi/B)} \psi_b(\varphi + 2\pi/B) && (5.18)\\
&= e^{\mathrm{i}b2\pi/B} e^{ib\varphi} \psi_b(\varphi) && (5.19)\\
&= e^{\mathrm{i}b2\pi/B} f_{\tilde{b}}(\varphi). && (5.20)
\end{aligned}$$

This again proves the linear independence of Bloch waves with independent Bloch wavenumbers, as the eigenfunctions of an operator corresponding to different eigenvalues are linearly independent. It was the connection to symmetry operators and their eigenfunctions that Bloch used in his

group-theoretical proof of the theorem.

A differential operator family $\mathcal{L}(z)$ features a discrete rotational symmetry of degree B if it commutes with the $2\pi/B$ rotation operation $\mathcal{R}_B$, i.e.,

$$\mathcal{R}_B\mathcal{L}(z) = \mathcal{L}(z)\mathcal{R}_B. \tag{5.21}$$

Note that z denotes the parameter of $\mathcal{L}$ for which eigenvalues are sought and not a spatial coordinate.

Applying an operator from the family $\mathcal{L}(z)$ to a Bloch wave $f_{\tilde{b}}$ results in a Bloch wave of the same Bloch wavenumber. This directly follows from the definition of Bloch waves and the discrete rotational symmetry of $\mathcal{L}(z)$:

$$\mathcal{R}_B\mathcal{L}(z)f_{\tilde{b}}(\varphi) = \mathcal{L}(z)\mathcal{R}_B f_{\tilde{b}}(\varphi) = \mathcal{L}(z)f_{\tilde{b}}(\varphi + 2\pi/B) = \mathcal{L}(z)e^{\mathrm{i}b2\pi/B}f_{\tilde{b}}(\varphi) = e^{\mathrm{i}b2\pi/B}\mathcal{L}(z)f_{\tilde{b}}(\varphi). \tag{5.22}$$

The eigenvalues ω and corresponding eigenfunctions f of an operator are determined by the equation

$$\mathcal{L}(\omega)f = 0. \tag{5.23}$$

The hitherto presented theory showed that any function can be uniquely decomposed in a Bloch-wave series. Therefore, the above equation can be rephrased as:

$$\mathcal{L}(\omega)\sum_{b=0}^{B-1} f_{\tilde{b}} = 0 \tag{5.24}$$

$$\sum_{b=0}^{B-1} \mathcal{L}(\omega)f_{\tilde{b}} = 0. \tag{5.25}$$

Because $\mathcal{L}(\omega)f_{\tilde{b}}$ is again a Bloch wave of wavenumber b and because the different Bloch waves are linearly independent it follows

$$\mathcal{L}(\omega)f_{\tilde{b}} = 0. \tag{5.26}$$

Thus, the Bloch-wave components of an eigenfunction are eigenfunctions to the same eigenvalue themselves. This means that the eigenspaces of an operator featuring a discrete rotational symmetry are spanned by Bloch waves and concludes the proof.

5.3 Orthogonality of Bloch waves

Another useful feature of Bloch waves is the pairwise orthogonality of Bloch waves with independent Bloch wavenumbers: let $b, \beta \in \{0, 1, \ldots, B-1\}$ be Bloch wavenumbers and $f_{\tilde{b}} = e^{\mathrm{i}b\varphi}\psi_b(\varphi)$ and $f_{\tilde{\beta}} = e^{\mathrm{i}\beta\varphi}\psi_\beta(\varphi)$ the corresponding Bloch waves. Then

$$\left\langle f_{\tilde{\beta}} | f_{\tilde{b}} \right\rangle = \int_0^{2\pi} \overline{f_{\tilde{\beta}}(\varphi)} f_{\tilde{b}}(\varphi)\,\mathrm{d}\varphi \qquad \text{|Bloch periodicity} \tag{5.27}$$

$$= \sum_{k=0}^{B-1} e^{-\mathrm{i}\beta\frac{2\pi}{B}k} e^{\mathrm{i}b\frac{2\pi}{B}k} \underbrace{\int_0^{\frac{2\pi}{B}} \overline{f_{\tilde{\beta}}(\varphi)} f_{\tilde{b}}(\varphi)\,\mathrm{d}\varphi}_{\text{const:}=C} \tag{5.28}$$

$$= C \sum_{k=0}^{B-1} e^{\mathrm{i}(b-\beta)\frac{2\pi}{B}k} \tag{5.29}$$

$$= \begin{cases} CB & \text{if } b = \beta \\ 0 & \text{else} \end{cases} \tag{5.30}$$

The last equality originates from the fact that if $b = \beta$, then the exponential amounts to 1 and, thus, summation of the B terms yields B. If on the contrary $b \neq \beta$, $e^{\mathrm{i}(b-\beta)\frac{2\pi}{B}k}$ are vertices of a regular polygon in the complex plane centered around the origin. Hence, the summation amounts to zero. This result proves that discrete rotational symmetry induces orthogonality between certain modes. Note that not all modes are mutually orthogonal, because one Bloch wavenumber is shared by several modes. Thus, symmetry is of course not fixing non-normal behavior. However, the interplay of different modes emerging in transient growth is limited to modes featuring the same Bloch wavenumber. In other words, non-normal effects can be completely studied from the surrogate systems obtained when utilizing Bloch periodicity. An important non-normal feature in the context of thermoacoustic modes are defective eigenvalues. As shown in Chap. 10 they can be linked to intrinsic thermoacoustic modes.

5.4 Symmetry and degeneracy

Bloch-wave theory helps understanding symmetry-induced mode degeneracy. This knowledge can be used to further reduce the computational effort. Two types of symmetry generically induce degeneracy in systems with discrete rotational symmetry: reflection symmetry and time-reversal symmetry. More precisely, having at least one of these two additional symmetries is a sufficient condition for mode degeneracy in systems already featuring a discrete rotational symmetry. In quantum mechanics it is common to call the two types of symmetry $\mathcal{P}$-symmetry and $\mathcal{T}$-symmetry, respectively (see, e.g., [108]). This is because in quantum mechanics reflection-symmetry is commonly called *parity*-symmetry and the reflection operator $\mathcal{R}_\pm$ is denoted by $\mathcal{P}$. The time-reversal operator is defined as $\mathcal{T} : t \mapsto -t$. Because, $\widehat{(\cdot)} \exp(-\mathrm{i}\omega t) = \widehat{(\cdot)}\overline{\exp(\mathrm{i}\omega t)}$, this operation correspond to complex conjugation in frequency domain.

$\mathcal{P}$-symmetry

If the considered system $\mathcal{L}$ features a reflection symmetry, it commutes with the reflection operator $\mathcal{R}_\pm$:

$$\mathcal{R}_\pm \mathcal{L} = \mathcal{L} \mathcal{R}_\pm. \tag{5.31}$$

Thus, given an eigenpair ω and $\hat{p}$ the reflection of the mode shape $\mathcal{R}_\pm \hat{p}$ will also be an eigenfunction corresponding to the same eigenvalue. This is because then

$$\mathcal{L}(\omega)\mathcal{R}_\pm \hat{p} = \mathcal{R}_\pm \mathcal{L}(\omega)\hat{p} = \mathcal{R}_\pm 0 = 0 \tag{5.32}$$

holds. Now assuming that the system features a discrete rotational symmetry, in virtue of Bloch's theorem the eigenmode can be phrased as a Bloch wave $\widehat{p}_{\widetilde{b}}(\varphi)$. Without loss of generality the coordinate system can be chosen such that $\mathcal{R}_{\pm} f(\varphi) = f(-\varphi)$. The reflection of a Bloch wave of Bloch wavenumber b will, thus, be a Bloch wave of Bloch wavenumber $-b$

$$\mathcal{R}_{\pm} f_{\widetilde{b}}(\varphi) = f_{\widetilde{b}}(-\varphi) = e^{\mathrm{i}b[-\varphi]}\psi_b(-\varphi) = e^{\mathrm{i}[-b]\varphi}\psi_b(-\varphi) = e^{\mathrm{i}[-b]\varphi}\psi_{-b}(\varphi) = f_{\widetilde{-b}}(\varphi). \tag{5.33}$$

Note that by definition $\psi_b(\varphi)$ is $2\pi/B$ periodic, therefore, $\psi_b(-\varphi)$ must also feature this period. This justifies relabeling it $\psi_{-b}(\varphi)$ after identifying the multiplier $e^{\mathrm{i}[-b]\varphi}$ in order to show that the term is a Bloch wave of wavenumber $-b$.

Due to Eq. (5.32), $\widehat{p}_{\widetilde{b}}$ and $\widehat{p}_{\widetilde{-b}}$ correspond to the same eigenvalue. The eigenvalue will, thus, be semi-simple degenerate if the two Bloch waves are linearly independent. This will be the case if the Bloch wavenumbers b and $-b$ are independent, i.e., if

$$(b-(-b)) \bmod B = 2b \bmod B \neq 0. \tag{5.34}$$

In applications featuring not only a discrete rotational symmetry but also a reflection-symmetry, it is, thus, convenient to specify the range of independent Bloch wavenumbers from $-(B-1)/2$ to $(B-1)/2$ or $-B/2+1$ to $B/2$ depending on whether B is odd or even. Only solutions for non-negative Bloch wavenumbers are then explicitly computed while the Bloch waves of negative Bloch wavenumbers are found by reflection.

$\mathcal{T}$-symmetry

The eigenvalues can also be degenerate if the system features a time-reversal symmetry, i.e., the equations are invariant under a substitution $t \mapsto -t$ in the time domain. Given the time reversal property of the Fourier transform and assuming that all coefficients of the operator are real, this corresponds to complex conjugation in the frequency domain. Thus, in the frequency domain such an operator features time-reversal symmetry if

$$\overline{\mathcal{L}(z)} = \mathcal{L}(z). \tag{5.35}$$

Note that it is not necessary that the operator features this symmetry for all z but for its eigenvalues ω to induce degeneracy. A relevant class of such operators in this thesis are Helmholtz operators with no flame feedback and sound-soft or sound-hard boundary conditions. For physical reasons, their modes neither grow nor decay with time: acoustic energy cannot enter or leave the system at the domain boundary nor is generated or dissipated by some feedback mechanism. Their eigenvalues are, therefore, real[2]. Thus, $\overline{\omega} = \omega$ and time-reversal symmetry is given because the operator $\nabla \cdot c\nabla(\cdot) - \omega^2(\cdot) = 0$ is invariant with respect to complex conjugation.

The proof that the complex conjugate $\overline{\widehat{p}}$ of a solution $\widehat{p}$ will correspond to the same eigenvalue given the time-reversal symmetry is equivalent to Eq. (5.32):

$$\overline{\mathcal{L}(\omega)\widehat{p}} = \mathcal{L}(\omega)\overline{\widehat{p}} = 0. \tag{5.36}$$

As for the reflection symmetry, time-reversal symmetry – i.e., complex conjugation – trans-

[2] Could also be proven mathematically as these operators are self-adjoint.

forms a Bloch wave of Bloch wavenumber b into a Bloch wave of Bloch wavenumber $-b$:

$$\overline{f_{\widetilde{b}}} = \overline{e^{\mathrm{i}b\varphi}\psi_b(\varphi)} = \overline{e^{\mathrm{i}b\varphi}} \underbrace{\overline{\psi_b(\varphi)}}_{:=\psi_{-b}(\varphi)} = e^{-\mathrm{i}b\varphi}\psi_{-b}(\varphi) = f_{\widetilde{-b}}(\varphi). \tag{5.37}$$

Thus, degeneracy is completely equivalent to the reflection-symmetric case: it suffices to compute solutions for Bloch wavenumbers ranging from 0 to $B/2$ or $(B-1)/2$ and obtain the degenerate modes by complex conjugation for Bloch wavenumbers satisfying $2b \bmod B \neq 0$.

5.5 Numerical implementation

Bloch periodicity can be implemented in a finite element framework as an essential boundary condition [109]. Note that implementation of Bloch-wave theory is possible for any discretization method on the matrix level if a periodic discretization mesh is used. This is because then the discretization matrices can be arranged such that they possess a block-circulant structure. As a generalization of circulant matrices – which always possess Fourier modes as eigenvectors [56] – the eigenvectors and eigenvalues of block-circulant matrices can be computed from a set of matrices featuring the size of a single block. The proof is the finite-dimensional equivalent to Bloch's theorem and can be found in [110]. A recent discussion of this approach with applications to periodic fluid systems is given by Schmid et al. in [111]. This approach would work for matrix-free implementations of the Helmholtz solver like CERFACS' AVSP code. However, using the implementation as an essential boundary condition is consistent with the derivation of the finite element method from the weak formulation.

As any essential boundary condition, Bloch periodicity reduces the number of degrees of freedom. Instead of using independent ansatz functions ϕ_k on the entire domain, only ansatz functions on a single unit cell are specified, which are extended to the other cells by means of Bloch periodicity. It is common to refer to the single unit cell which is actually considered for the computations as the *reference* cell, while the other cells are called *image* cells. It is the reduction of degrees of freedom that yields the savings in the computational effort. The approach is a generalization of the special case of periodicity ($b = 0$) and relates to the discretization of the reference cell using Neumann boundary conditions in contrast to Bloch-periodic boundary conditions [109]. Figure 5.2 shows the ansatz function to implement Neumann, periodic, and Bloch-periodic boundary conditions on a reference cell. In comparison to the Neumann case, corresponding ansatz functions at the beginning (black) and the end (yellow) of the unit cell are merged into one ansatz function (black), compliant with the specified type of periodicity:

$$\widetilde{\phi}_k = \begin{cases} \phi_k + e^{\mathrm{i}b\Delta\varphi}\phi_{\mathrm{map}^{-1}(k)} & \text{if } \phi_k \in \mathrm{map}(\mathbb{F}_{\mathrm{img}}) \\ \phi_k & \text{else} \end{cases} \qquad \forall k \in \mathbb{F}_{\mathrm{cll}} \tag{5.38}$$

Here, ϕ_k is an ansatz function that is associated with a degree of freedom at the image boundary of the cell. The set of these functions is denoted by $\mathbb{F}_{\mathrm{img}}$. The function 'map' maps the index k to the index of the function it is joined with. The set of ansatz functions on the unit cell associated to a degree of freedom which is not associated with the image boundary is indicated by $\mathbb{F}_{\mathrm{cll}}$. Because ϕ_k is joined with $\phi_{\mathrm{map}(k)}$, the total number of degrees of freedom for the Bloch-periodic discretization is less than the number of degrees of freedom of the Neumann discretization of the

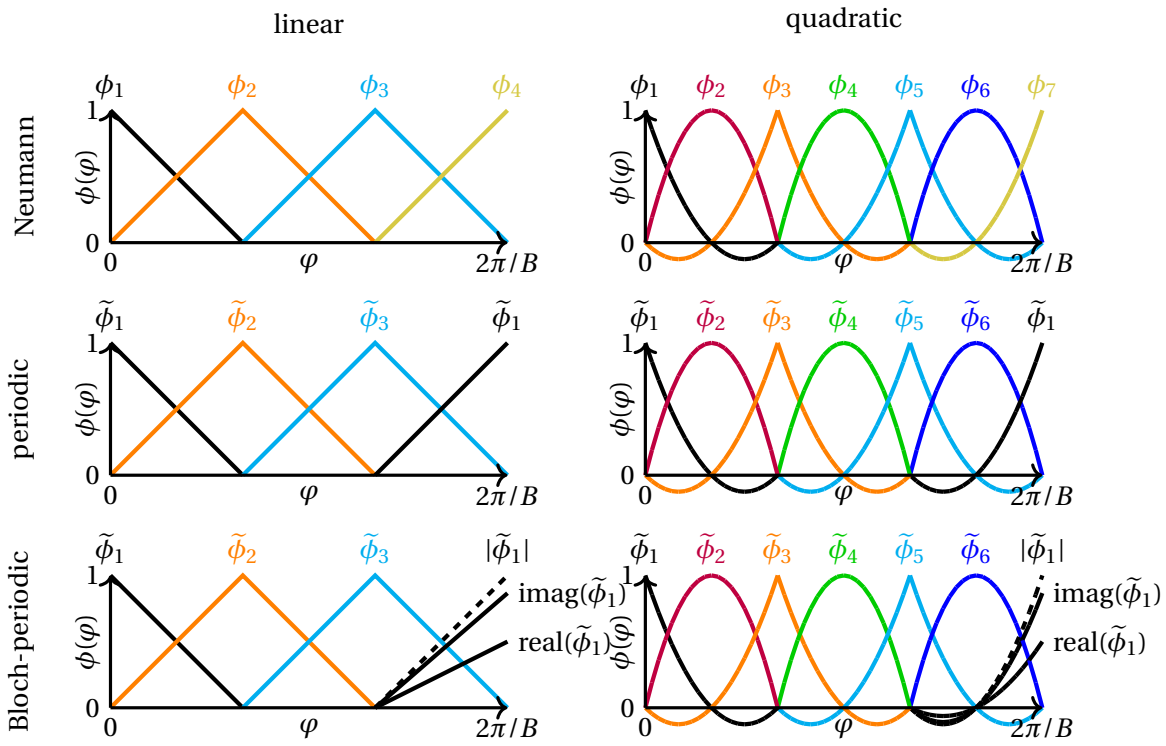

Figure 5.2: Illustration of ansatz functions for Neumann, periodic, and Bloch-periodic boundary conditions. Linear ansatz functions right, quadratic left. Illustration partly adapted from [109].

unit cell. However, assuming that the local integrals for the assembly of the discretization matrix $\mathbf{L}$ for the case of Neumann boundary conditions are already computed, the local integrals for the discretization matrix in case of the Bloch-periodic boundary condition can be directly deduced. On each element the integral value changes as follows

$$\langle \phi_k | \mathcal{L} \phi_l \rangle \mapsto \begin{cases} e^{\mathrm{i}b\Delta\varphi} \langle \phi_k | \mathcal{L} \phi_{\mathrm{map}(l)} \rangle & \text{if } \phi_k \notin \mathbb{F}_{\mathrm{img}} \text{ and } \phi_l \in \mathbb{F}_{\mathrm{img}} \\ e^{-\mathrm{i}b\Delta\varphi} \langle \phi_{\mathrm{map}(k)} | \mathcal{L} \phi_l \rangle & \text{if } \phi_k \in \mathbb{F}_{\mathrm{img}} \text{ and } \phi_l \notin \mathbb{F}_{\mathrm{img}} \\ \langle \phi_{\mathrm{map}(k)} | \mathcal{L} \phi_{\mathrm{map}(l)} \rangle & \text{if } \phi_k, \phi_l \in \mathbb{F}_{\mathrm{img}} \\ \langle \phi_k | \mathcal{L} \phi_l \rangle & \text{else} \end{cases} \tag{5.39}$$

This allows for implementing Bloch periodicity straightforwardly into an existing FEM code, by manipulating a matrix assembled for Neumann BCs. Algorithm 5.1 illustrates how to process a matrix $\mathbf{L}$ representing any operator discretized on a unit cell with Neumann boundary conditions to obtain its Bloch periodic counterpart, i.e., the algorithm facilitates the following mapping

$$\begin{aligned} &\mathbb{C}^{(N_{\mathrm{cll}}+N_{\mathrm{img}})\times(N_{\mathrm{cll}}+N_{\mathrm{img}})} \to \mathbb{C}^{N_{\mathrm{cll}}\times \mathrm{cll}} \\ &\mathbf{L} \mapsto e^{\mathrm{i}b\Delta\varphi}\mathbf{L}_{\mathrm{Bloch}}(\omega; b) = \mathbf{A}_+ + \mathbf{A} + e^{-\mathrm{i}b\Delta\varphi}\mathbf{A}_-. \end{aligned} \tag{5.40}$$

For the presented approach to work, it is necessary to create a mesh which features a matching set of points on the reference and the image boundary of the unit cell. In addition to the discrete rotational symmetry, the MICCA model is reflection symmetric. As explained in Sec. 2.3 to sat-

Algorithm 5.1: Function to obtain FEM discretization matrices featuring Bloch-periodic boundary conditions from discretization matrices with Neumann boundary conditions

function BLOCHIFY($\mathbf{L}$)
  set $\mathbf{A}_+$,$\mathbf{A}_-$, **and** $\mathbf{A}$ to $\mathbf{0} \in \mathbb{C}^{N_{\mathrm{cll}} N_{\mathrm{img}} \times N_{\mathrm{cll}} N_{\mathrm{img}}}$
  for $k \leftarrow 1, \ldots, N_{\mathrm{cll}} + N_{\mathrm{img}}$ **do**
    for $l \leftarrow 1, \ldots, N_{\mathrm{cll}} + N_{\mathrm{img}}$ **do**
      if $\phi_k \in \mathbb{F}_{\mathrm{img}}$ **and** $\phi_l \notin \mathbb{F}_{\mathrm{img}}$ **then**
        $[\mathbf{A}_+]_{k,l} \leftarrow [\mathbf{L}]_{k,l}$
      else if $\phi_k \in \mathbb{F}_{\mathrm{img}}$ **and** $\phi_l \notin \mathbb{F}_{\mathrm{img}}$ **then**
        $[\mathbf{A}_-]_{k,l} \leftarrow [\mathbf{L}]_{k,l}$
      else if $k \in \mathbb{F}_{\mathrm{img}}$ **and** $k \in \mathbb{F}_{\mathrm{img}}$ **then**
        $[\mathbf{A}]_{\mathrm{map}(k),\mathrm{map}(l)} \leftarrow [\mathbf{A}]_{\mathrm{map}(k),\mathrm{map}(l)} + [\mathbf{L}]_{k,l}$
      else
        $[\mathbf{A}]_{k,l} \leftarrow [\mathbf{A}]_{k,l} + [\mathbf{L}]_{k,l}$
      end if
    end for
  end for
  remove all rows and columns corresponding to the image boundary from $\mathbf{A}_+$,$\mathbf{A}_-$, and $\mathbf{A}$
  return $\mathbf{A}_+$,$\mathbf{A}_-$, $\mathbf{A}$
end function

isfy the matching condition and obtain a perfectly symmetric model discretization of the MICCA combustor, only half of a unit cell was discretized and by reflections and rotations a unit cell and finally the full combustor mesh was obtained.

5.6 Application to the Kronig-Penney model

In this section the Bloch-wave theory is applied to the Kronig-Penney model. Both the network and the finite element discretization of the model are considered. Section 2.2 introduced local ansatz functions $\widehat{p}_k(\varphi) = A_{2k}\cos(\omega\varphi_k) + A_{2k+1}\sin(\omega\varphi_k)$ to obtain a network discretization of the problem. Because the ansatz functions form a set of fundamental solutions they can still be used in unit cell computations. Yet, imposing the Bloch-periodicity changes the conditions found for the continuity in the pressure Eq. (2.18) and the jump in the derivative Eq. (2.20). The former yields

$$\widehat{p}_{k+1}(0) - \widehat{p}_k\left(\frac{2\pi}{K}\right) = 0 \qquad \text{| Bloch periodicity} \tag{5.41}$$

$$\Rightarrow e^{\mathrm{i}b2\pi/K}\widehat{p}_k(0) - \widehat{p}_k\left(\frac{2\pi}{K}\right) = 0 \qquad \text{|Ansatz} \tag{5.42}$$

$$\Rightarrow e^{\mathrm{i}b2\pi/K}A_{2k} - A_{2k}\cos\left(\omega\frac{2\pi}{K}\right) - A_{2k+1}\sin\left(\omega\frac{2\pi}{K}\right) = 0 \tag{5.43}$$

while for the latter

$$\frac{\mathrm{d}}{\mathrm{d}\varphi}\widehat{p}_{k+1}(0) - \frac{\mathrm{d}}{\mathrm{d}\varphi}\widehat{p}_k\left(\frac{2\pi}{K}\right) = -\mathrm{i}\omega Q_k\widehat{p}_{k+1}(0) \qquad \text{| Bloch periodicity} \tag{5.44}$$

$$\Rightarrow e^{\mathrm{i}b2\pi/K}\frac{\mathrm{d}}{\mathrm{d}\varphi}\widehat{p}_k(0) - \frac{\mathrm{d}}{\mathrm{d}\varphi}\widehat{p}_k\left(\frac{2\pi}{K}\right) = -\mathrm{i}\omega Q_k e^{\mathrm{i}b2\pi/K}\widehat{p}_k(0) \qquad \text{|Ansatz} \tag{5.45}$$

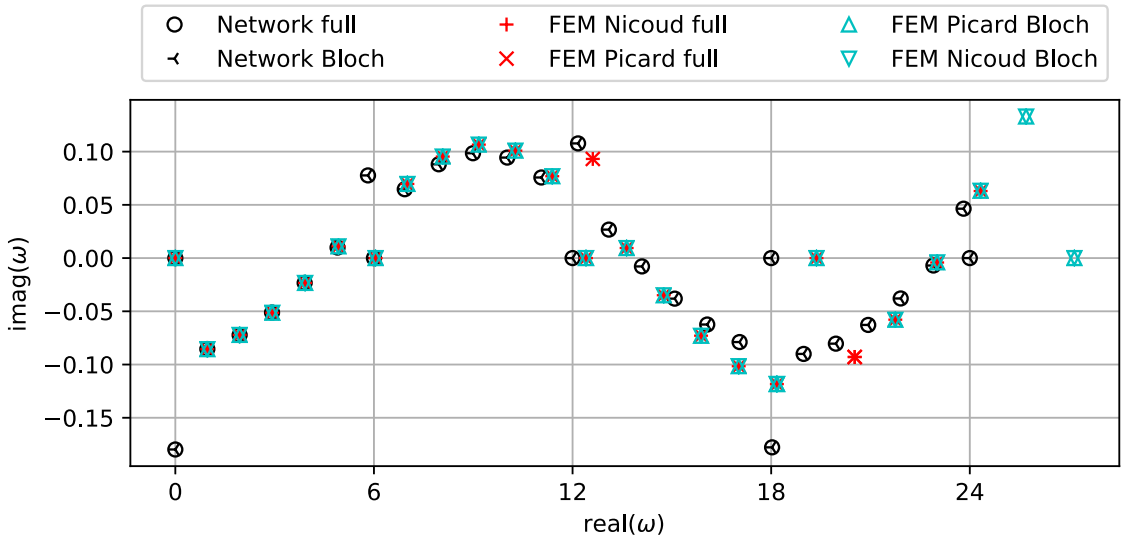

Figure 5.3: Eigenfrequencies found for the Kronig-Penney model using Bloch-wave theory. Results for both the network and the FEM discretization are shown. Also both iteration schemes are deployed. For comparison, solutions obtained from the full model are shown. They are identical to the results obtained from Bloch-wave theory.

$$\Rightarrow e^{\mathrm{i}b2\pi/K}\omega A_{2k+1} + \omega A_{2k}\sin\left(\omega\frac{2\pi}{K}\right) - \omega A_{2k+1}\cos\left(\omega\frac{2\pi}{K}\right) + \mathrm{i}\omega Q_k e^{\mathrm{i}b2\pi/K} A_{2k} = 0 \tag{5.46}$$

is found. Note that as for the network formulation there are as many continuity (Eq. (5.43)) and jump conditions (Eq. (5.46)) as there are local ansatz functions $\widehat{p}_k(\varphi)$. Nonetheless, each pair of continuity and jump condition contains the coefficients A_{2k} and A_{2k+1}, i.e., it is associated with one local ansatz function only and, hence, one unit cell. Bloch periodicity has diagonalized the block-circulant network discretization matrix with 2×2-blocks on the main diagonal satisfying:

$$\underbrace{\begin{bmatrix} e^{\mathrm{i}b2\pi/K} - \cos\left(\omega\frac{2\pi}{K}\right) & -\sin\left(\omega\frac{2\pi}{K}\right) \\ \sin\left(\omega\frac{2\pi}{K}\right) + \mathrm{i}Q_k e^{\mathrm{i}b2\pi/K} & e^{\mathrm{i}b2\pi/K} - \cos\left(\omega\frac{2\pi}{K}\right) \end{bmatrix}}_{\mathbf{L}_{\mathrm{Bloch}}(\omega;b)} \underbrace{\begin{bmatrix} A_{2k} \\ A_{2k+1} \end{bmatrix}}_{\mathbf{p}_{\tilde{b}}} = 0. \tag{5.47}$$

Without loss of generality, k can be set to 0. Solving the eigenvalue problem (5.47) yields the desired eigenfrequencies ω and coefficients for A_0 and A_1. If needed, the coefficients for the ansatz functions associated to the other unit cells can be computed by means of Bloch periodicity as

$$\begin{bmatrix} A_{2k} \\ A_{2k+1} \end{bmatrix} = e^{\mathrm{i}bk2\pi/K} \begin{bmatrix} A_0 \\ A_1 \end{bmatrix}. \tag{5.48}$$

Figure 5.3 compares the eigenfrequencies computed using a full and a unit-cell model. Results are shown for both the network and the FEM discretization of the problem. The model parameters are the same as in Sec. 4.5. While there is perfect agreement for the eigenfrequencies obtained from the unit-cell and the full computation when using the network approach, the computed spectra of the finite element model deviate in a few eigenfrequencies. This is a mesh effect. The eigenfrequencies for the fixed-point algorithms were initialized with integer values $0, 1, \ldots, 24$

Table 5.1: Passive mode frequencies of the MICCA model and active mode frequencies found from a unit-cell computation using the fixed-point iterations. The columns Nicoud and Picard state the number of iteration necessary to reach the stopping criterion tol=$0.01 \times 2\pi \mathrm{s}^{-1}$ with the Nicoud and the Picard iteration, respectively.

		passive		active	Nicoud			Picard		
mode	b	$\omega \frac{\mathrm{s}}{2\pi}$	Res	$\omega \frac{\mathrm{s}}{2\pi}$	ξ	Itr.	Res.	ξ	Itr.	Res.
#M0	0	332.0	5.21E−12	154.5+67.9i	0.75	15	138	1.00	24	3.22E−3
#M1	1	471.8	4.70E−12	511.4−79.4i	0.75	18	94.8	0.75	18	2.25E−3
#M2	2	731.4	4.74E−12	713.1−2.3i	1.00	6	24.6	1.00	6	1.39E−3

and it was assumed that the azimuthal mode order coincides with that number. Consequently, the Bloch wavenumber b was set to these initial values during the computations. However, due to the purposefully poor mesh resolution, the azimuthal mode order does not coincide with the integer closest to real(ω) at high frequencies. Nonetheless, proper initialization would show that the eigenvalues of the full model are eigenvalues of the unit-cell model and vice versa. This can be achieved with contour integration methods as will be demonstrated in Chap. 8. Note that as for the full-domain computation the fixed-point iterations converged within three iteration steps.

5.7 Application to MICCA

This section discusses the application of the Bloch-wave theory to the MICCA model. Table 5.1 lists the solutions found with the Bloch-wave approach. The eigenvalues are exactly the same as found with the full chamber computation in Sec. 4.6. However, the fixed-point iterations show a slightly different behavior. Mode #M0 does converge to $\omega = 0$ when applying Nicoud's iteration without relaxation. Therefore, the relaxation parameter was set to $\xi = 0.75$. The mode then converges after 16 iterations. For mode #M1 it takes 18 not 16 iterations to converge using either of the two methods. In all other cases, the number of iterations are identical to those of the full-annulus model. Also the computed residuals feature magnitudes comparable to those from Sec. 4.6.

The passive mode shapes are depicted in Fig. 5.4. Interestingly, the absolute value of the mode shapes look nearly identical. This is because of the Bloch-wave structure of the modes: the injectors only allow for a weak acoustic coupling between the plenum and the combustion chamber. The modes shown here are plenum dominant and the speed of sound in the plenum is constant. Therefore, the azimuthal structure of the modes in the plenum is $\widehat{p}(\varphi) = C_1 \cos(m\varphi) + C_2 \sin(m\varphi)$, where m denotes the azimuthal mode order and C_1 and C_2 are free parameters to be chosen. The modes take Bloch-wave structure if $C_2 = \mathrm{i}C_1$ then $\widehat{p}(\varphi) = C_1 \cos(m\varphi) + \mathrm{i}C_1 \sin(m\varphi) = e^{\mathrm{i}m\varphi} = \widehat{p}_{\widetilde{m}}(\varphi)$. Alternatively, choosing $C_2 = -\mathrm{i}C_1$ yields $\widehat{p}_{\widetilde{-m}}(\varphi)$. Either way, the absolute value of the mode would be constant while the phase would vary like $m\varphi$. This is exactly the structure of the modes shown in Fig. 5.4. The mode shapes belong to the same eigenspaces as those shown in Fig. 4.4 as can be concluded from the residual norm. It is just that the eigenspace for the modes #M1 and #M2 is two-dimensional due to symmetry, and, therefore, two mode shapes from these eigenspaces are not necessarily identical.

Figure 5.5 shows the mode shapes for the active case. In the active case the absolute value of the mode shapes in the plenum is still very similar. Yet, in the combustion chamber the shapes

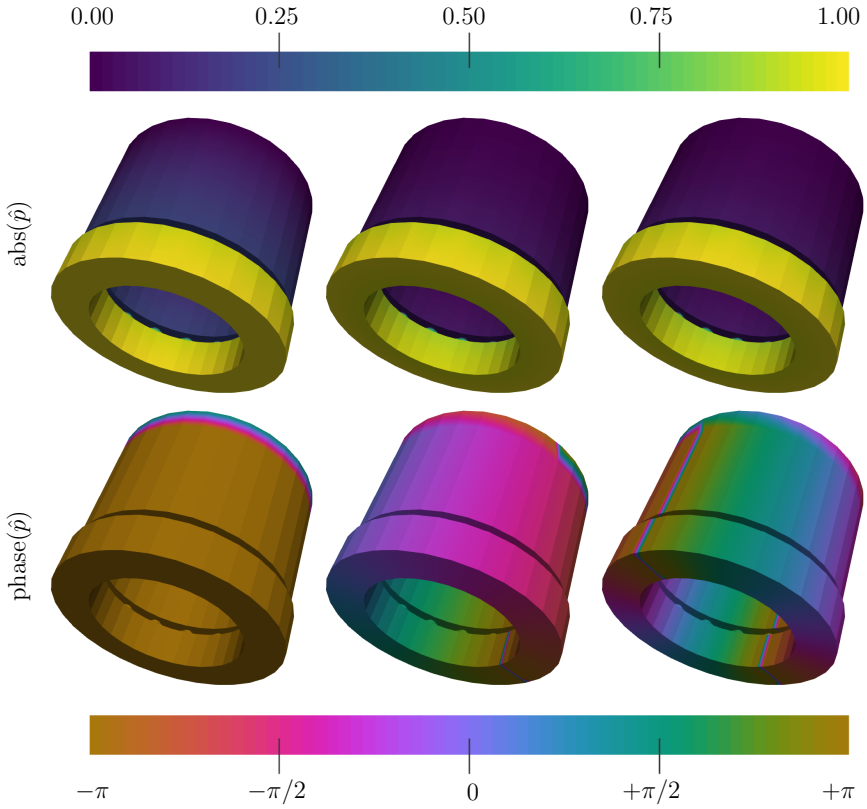

Figure 5.4: Mode shapes for the MICCA model with passive flame computed using Bloch's theorem. The figure shows from left to right the modes #M0, #M1, and #M2. The top row shows the absolute values of the modes while the phase of the mode shapes is shown in the bottom row. The similarity of the absolute value of the mode shapes is a consequence of the Bloch-wave structure. However, the mode shapes #M1 and #M2 belong to the same two-dimensional eigenspace as those shown in Fig. 4.4.

are notably different. This is due to the active flame dynamics which interacts with the pressure fluctuation amplitude in the combustion chamber.

Although the particular reason for the different convergence behavior of mode #M0 is unclear, computing the three modes with the Bloch-wave approach is faster. Figure 5.6 illustrates the reduction in matrix size obtained when utilizing Bloch-wave theory to compute thermoacoustic modes of the MICCA model. The size of the involved discretization matrices is decreased by a factor of $B^2 = 16^2 = 256$. This will yield substantial savings in the computational effort needed to obtain solutions. However, these savings do not necessarily scale with a factor of B^2. For instance, if the discretization matrices are sparse, the effort to perform a matrix vector computation involving an $N \times N$-matrix is of order $\mathcal{O}(N)$ and not $\mathcal{O}(N^2)$. The memory space required to store a matrix scales identically. For discretization methods leading to sparse matrices the performance will, therefore, increase by a factor of B and not B^2. Moreover, the performance gain might depend on other factors like the communication overhead in parallel implementations or details of the utilized hardware.

Indeed, substantially different performance increases were measured for the implementation of Nicoud's algorithm and the Picard iteration as can be seen from the results reported in Tab. 5.2.

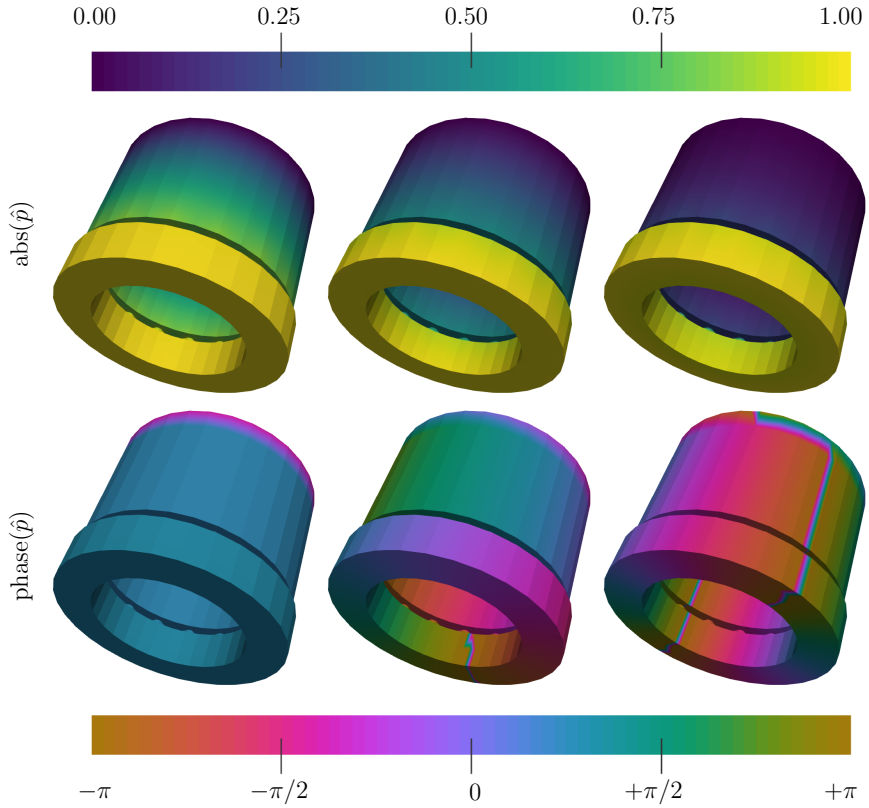

Figure 5.5: Mode shapes for the MICCA model with active flame computed using Bloch's theorem. The figure shows from left to right the modes #M0, #M1, and #M2. The top row shows the absolute values of the modes while the phase of the mode shapes is shown in the bottom row.

The larger performance gain in the case of Nicoud's algorithm is attributed to a non-sparse imple-

Table 5.2: Performance comparison

	full	Bloch	factor
Nicoud	4627.55s	10.81s	428.08
Picard	82.68s	6.43s	12.86

mentation of the reshaping steps necessary to convert a quadratic into a linear eigenvalue problem. However, these results are in line with the considerations on how the sparsity may affect the computational time. Nicoud's algorithm accelerated by a factor of about 428 which is of a comparable magnitude as $B^2 = 256$, while the fully sparse implementation of the Picard algorithm sped up by a factor of about 13 as compared to an expected acceleration of $B = 16$. Note that these results are only a rough estimate as the theory was implemented using Python. Therefore, not all components of the software are compiled. An accurate comparison would require an implementation in a fully compiled language like C or Fortran.

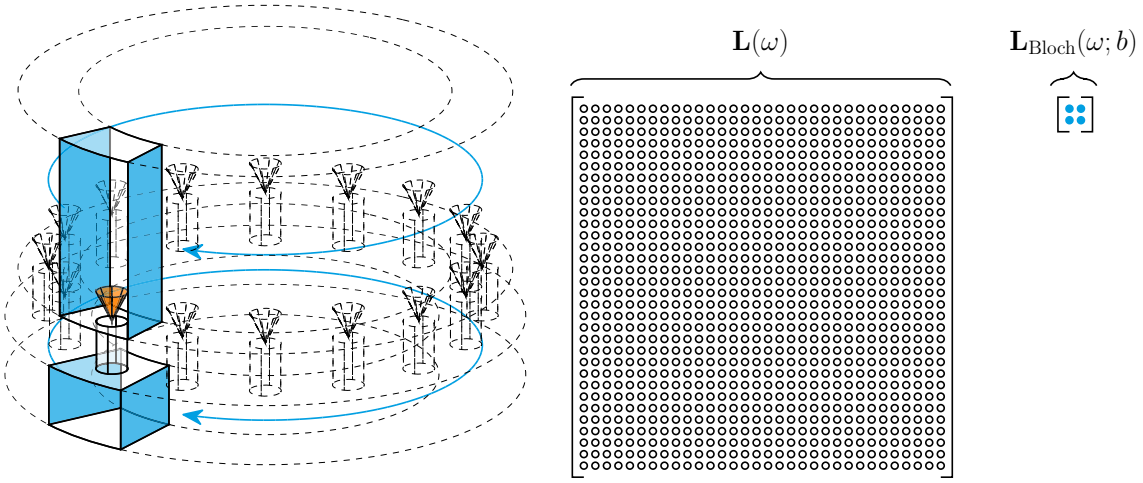

Figure 5.6: Illustration of the set-up and savings in matrix size for unit-cell computations with the MICCA model. The degree of rotational symmetry is $B = 16$. Imposing Bloch-periodic boundary conditions on the azimuthal sides (cyan) of a unit cell allows for reducing the size of the matrix by a factor of B^2 when converting the full-annulus discretization $\mathbf{L}$ to the unit-cell discretization $\mathbf{L}_{\mathrm{Bloch}}$. The specific performance gain depends on the sparsity of the discretization matrix and the implementation of the theory on a computer. In any case, however, the unit cell computation will be clearly more efficient.

5.8 Conclusions

The examples in this chapter have shown, that the unit cell computations yield the same results as full-chamber computations of Sec. 4.6. However, the computational effort to perform the calculations is substantially lower when following the unit-cell approach. Therefore, Bloch-wave theory is to be preferred over a full-annulus computation. Note that the unit cell computation also reduces the memory space required to store the computations as only the mode shape on a unit cell together with the associated Bloch wavenumber needs to be stored.

The underlying Bloch-wave theory also facilitates the explanation of symmetry-induced degeneracies. Of course, Bloch-wave theory cannot be utilized if the combustion chamber is not featuring a perfect discrete rotational symmetry. This issue may be tackled with the perturbation theory presented in the next chapter.

Chapter 6

Nonlinear eigenvalue problems II: perturbation theory

Bloch-wave theory has proven as a powerful tool to reduce the computational effort of thermoacoustic stability assessment. However, it is only applicable for configurations featuring a discrete rotational symmetry and already the slightest asymmetry impedes its application. Such asymmetries may be introduced to the combustor on purpose, e.g., acoustic dampers that are distributed along the circumference of the annulus in a non-uniform fashion [112, 113] or a circumferential variation of the fuel in order to trigger different flame dynamics in the burners and an asymmetric temperature field [114, 115]. Indeed, asymmetries are inevitable as they arise – although on a much smaller scale – from random manufacturing imprecisions.

All these examples constitute a perturbation from an ideally symmetric combustor. Hence, asymptotic perturbation theory may be considered to solve the issue. Like Bloch-wave theory the idea to use perturbation theory has been first popularized in the field of quantum mechanics to ease finding solutions to the Schrödinger equation. This was actually proposed by no other than Erwin Schrödinger himself in the third part of his seminal transactions on quantization as an eigenvalue problem [116]. He resorted to a method that has been originally utilized by Lord Rayleigh to find eigenstates of vibrating strings [9]. Thus, the theory is nowadays known as Rayleigh-Schrödinger perturbation theory. From a modern mathematical perspective, these pioneering works lacked mathematical rigor. For instance, convergence of the stipulated power series ansätze was just assumed rather than proven and – due to the nature of the considered equations – only a theory for semi-simple eigenvalues was developed. Yet, the success of the method in finding approximate solutions to otherwise unsolvable problems consolidated its popularity. Since these first applications, the theory for self-adjoint linear operator families has grown to a well established mathematical discipline. Kato's book [117] is the standard reference on the topic. A comprehensive literature review and modern introduction to the perturbation theory of non-self-adjoint boundary eigenvalue problems can be found in the book of Kirillov [118].

This chapter presents a generalized theory for non-normal and nonlinear eigenvalue problems as needed for the computation of thermoacoustic modes while following Schrödinger's work in putting a minor emphasize on the mathematical fundamentals. References to the relevant mathematical literature will be given to fill this gap.

The chapter is the result of fruitful collaborations with Jonas Moeck, Luca Magri, and Alessan-

dro Orchini. Parts of the content were previously published in [119, 120, 121].

6.1 Introduction to perturbation theory in thermoacoustic stability assessment

From an engineering perspective perturbation theory is used to predict the effect of an additional parameter ε on the eigenvalue and eigenvector. This parameter can be any relevant design variable, e.g., the mean temperature, the equivalence ratio, boundary impedances, flame transfer function properties like a characteristic time delay, or even the combustor geometry. Mathematically, the problem at hand is phrased as finding the eigenvalues and eigenfunctions of a differential operator subject to a certain set of boundary conditions

$$\mathcal{L}(\omega;\varepsilon)\,\widehat{p} := \begin{cases} \mathcal{L}_\Omega(\omega;\varepsilon)\,\widehat{p} = 0 & \text{in } \Omega(\varepsilon) \\ \mathcal{L}_{\partial\Omega}(\omega;\varepsilon)\,\widehat{p} = 0 & \text{on } \partial\Omega(\varepsilon) \end{cases} \tag{6.1}$$

while only knowing a solution to the considered eigenvalue problem for a baseline value $\varepsilon = \varepsilon_0$:

$$\mathcal{L}(\omega_0;\varepsilon_0) = 0. \tag{6.2}$$

The semicolon is used here to stress that ε enters the problem as an additional parameter and not as an eigenvalue. For thermoacoustic stability assessment the considered eigenvalue problem is the thermoacoustic Helmholtz equation (1.45). Rayleigh-Schrödinger perturbation theory tackles the issue by stipulating power series ansätze for both the eigenvalue and the eigenfunctions:

$$\omega(\varepsilon) = \sum_{n=0}^{\infty} \omega_n(\varepsilon-\varepsilon_0)^n \qquad \text{and} \qquad \widehat{p}(\varepsilon) = \sum_{n=0}^{\infty} \widehat{p}_n(\varepsilon-\varepsilon_0)^n. \tag{6.3}$$

Once the coefficients for these power series are found, the problem becomes explicit in the design parameter ε and eigenpairs for perturbations of $\Delta\varepsilon := \varepsilon - \varepsilon_0$ can be predicted. This avoids repeatedly solving the eigenvalue problem over a certain range of parameters and, thus, enables quick evaluation of the effect of the parameters. However, perturbation theory is an asymptotic method. Therefore, accurate results can only be expected as $\Delta\varepsilon \to 0$.

Perturbation theory has been first considered for thermoacoustic stability assessment by Benoit and Nicoud to approximate solutions of the thermoacoustic Helmholtz equation [122]. Magri and Juniper were the first to use the approach as a sensitivity analysis tool [41], i.e., a first order perturbation theory. In that work the approach was applied to a generic Rijke-tube model. This configuration featured simple modes. Juniper et al. then presented second-order perturbation theory, incorporation into a Helmholtz solver framework, and application to semi-simple degenerate modes in [123]. Magri et al. applied first and second-order theory to study parameter sensitivity in network models of annular combustors [124]. Silva et al. [125] and Magri et al. [126] used the approach for uncertainty quantification of thermoacoustic systems.

All these studies followed an interpolative approach, i.e., perturbation to the governing equation was scaled by introducing the perturbation parameter ε to scale a set of physical parameters simultaneously. Therefore, the baseline state $\varepsilon_0 = 0$ and the perturbed state $\varepsilon = 1$ are physically meaningful. However, intermediate values of ε do not necessarily describe a physical system. The

parameter ε served mainly as a mathematical device to facilitate sensitivity analysis.

The theory presented in this chapter considers the dependence of the eigenvalue problems on physical quantities. Hence, the dependence on the perturbation parameter is in general nonlinear. It is assumed that the operator family $\mathcal{L}(z;\varepsilon)$ depends analytically on both z and ε. In order to account for the nonlinear dependence of the operator family on ω and ε, it can, therefore, also be expanded into a power series in the vicinity of ε_0:

$$\mathcal{L}(z_0+\Delta z;\varepsilon_0+\Delta\varepsilon)=\sum_{n=0}^{\infty}(\Delta\varepsilon)^n\sum_{m=0}^{\infty}(\Delta z)^m\mathcal{L}_{m,n}. \tag{6.4}$$

Here, the operators $\mathcal{L}_{m,n}$ are defined as

$$\mathcal{L}_{m,n}:=\frac{1}{m!}\frac{1}{n!}\left.\frac{\partial^{m+n}\mathcal{L}}{\partial z^m\partial\varepsilon^n}\right|_{\substack{z=z_0\\ \varepsilon=\varepsilon_0}}, \tag{6.5}$$

i.e., the expansion (6.4) is the Taylor series of $\mathcal{L}(z;\varepsilon)$ expanded at $(z_0;\varepsilon_0)$. Substituting the power series for the eigenvalue and eigenfunction (6.3), and for the operator family (6.4) back into the considered eigenvalue problem (6.1) yields

$$\left[\sum_{n=0}^{\infty}(\Delta\varepsilon)^n\sum_{m=0}^{\infty}(\Delta\omega)^m\mathcal{L}_{m,n}\right]\left[\sum_{q=0}^{\infty}(\Delta\varepsilon)^q\widehat{p}_q\right]=0 \tag{6.6}$$

where $\Delta\omega:=\omega-\omega_0=\sum_{n=1}^{\infty}\omega_n(\Delta\varepsilon)^n$ is the correction of the eigenvalue. The multinomial theorem facilitates the following rearrangement:

$$(\Delta\omega)^m=\left(\sum_{r=1}^{N}\omega_r(\Delta\varepsilon)^r\right)^m=\sum_{|\boldsymbol{\mu}|=m}\binom{m}{\boldsymbol{\mu}}\prod_{r=1}^{N}\left[\omega_r(\Delta\varepsilon)^r\right]^{\mu_r} \tag{6.7}$$

$$=\sum_{|\boldsymbol{\mu}|=m}\binom{m}{\boldsymbol{\mu}}(\Delta\varepsilon)^{|\boldsymbol{\mu}|_1}\boldsymbol{\omega}^{\boldsymbol{\mu}}. \tag{6.8}$$

In this formula $\boldsymbol{\mu}=(\mu_1,\mu_2,\cdots,\mu_N)$ denotes a multi-index of length N, $|\boldsymbol{\mu}|=\mu_1+\mu_2+\cdots+\mu_N$ the sum of the entries of a multi-index, $\binom{m}{\boldsymbol{\mu}}=\frac{m!}{\mu_1!\mu_2!\cdots\mu_N!}$ a multinomial coefficient, and $|\boldsymbol{\mu}|_1:=1\mu_1+2\mu_2+\ldots+N\mu_N$. Moreover, the notation $\boldsymbol{\omega}^{\boldsymbol{\mu}}$ is a shorthand for the product $\prod_{n=1}^{N}\omega_n^{\mu_n}=\omega_1^{\mu_1}\omega_2^{\mu_2}\cdots\omega_N^{\mu_N}$. Thus, when collecting all powers of $\Delta\varepsilon$ into one single term and truncating the series at order N, (6.6) amounts to

$$\sum_{n=0}^{N}\sum_{m=0}^{N}\sum_{|\boldsymbol{\mu}|=m}\sum_{q=0}^{N}(\Delta\varepsilon)^{n+|\boldsymbol{\mu}|_1+q}\binom{m}{\boldsymbol{\mu}}\boldsymbol{\omega}^{\boldsymbol{\mu}}\mathcal{L}_{m,n}\widehat{p}_q+\mathcal{O}\left((\Delta\varepsilon)^{N+1}\right)=0\qquad\text{as}\quad\Delta\varepsilon\to0. \tag{6.9}$$

To sort terms by equal powers of $\Delta\varepsilon$, the substitution $k=n+|\boldsymbol{\mu}|_1+q$ is made. This allows to rephrase (6.9) as

$$\sum_{k=0}^{N}(\Delta\varepsilon)^k\sum_{m=0}^{k}\sum_{|\boldsymbol{\mu}|_1=m}\sum_{n=0}^{k-|\boldsymbol{\mu}|_1}\binom{|\boldsymbol{\mu}|}{\boldsymbol{\mu}}\boldsymbol{\omega}^{\boldsymbol{\mu}}\mathcal{L}_{m,n}\widehat{p}_{k-n-|\boldsymbol{\mu}|_1}+o\left((\Delta\varepsilon)^{N+1}\right)=0\qquad\text{as}\quad\Delta\varepsilon\to0. \tag{6.10}$$

Note that there are higher powers than $(\Delta\varepsilon)^N$ explicitly appearing in (6.9). On the contrary, such powers are not explicitly stated in (6.10). The Landau symbols $\mathcal{O}\left((\Delta\varepsilon)^{N+1}\right)$ and $o\left((\Delta\varepsilon)^{N+1}\right)$ stress

this subtle difference. Because of the linear independence of different powers of $\Delta\varepsilon$, equation (6.10) is satisfied up to order N if $\forall k \in \{0,1,2,\ldots,N\}$

$$\sum_{m=0}^{k} \sum_{|\boldsymbol{\mu}|_1=m} \sum_{n=0}^{k-|\boldsymbol{\mu}|_1} \binom{|\boldsymbol{\mu}|}{\boldsymbol{\mu}} \boldsymbol{\omega}^{\boldsymbol{\mu}} \mathcal{L}_{m,n} \widehat{p}_{k-n-|\boldsymbol{\mu}|_1} = 0 \tag{6.11}$$

holds. The equation can be rearranged to

$$\mathcal{L}_{0,0} \widehat{p}_k = -r_k - \omega_k \mathcal{L}_{1,0} \widehat{p}_0, \tag{6.12}$$

where

$$r_k = \sum_{n=1}^{k} \mathcal{L}_{0,n} \widehat{p}_{k-n} + \sum_{m=1}^{k} \sum_{\substack{|\boldsymbol{\mu}|_1=m \\ \mu \neq 1_k}} \sum_{n=0}^{k-|\boldsymbol{\mu}|_1} \binom{|\boldsymbol{\mu}|}{\mu} \boldsymbol{\omega}^{\boldsymbol{\mu}} \mathcal{L}_{m,n} \widehat{p}_{k-n-|\boldsymbol{\mu}|_1}. \tag{6.13}$$

Here, 1_k denotes a multi-index where all entries are 0, with an exception at position k where it is 1.

Equation (6.12) presents an iterative scheme to determine the corrections of the eigenvalues and eigenmodes. Assuming that the corrections to the eigenmode and eigenvalue at orders lower than k are already known, the remaining unknowns in this formula are the kth-order corrections $\widehat{p}_k$ and ω_k which themselves only occur on the left-hand and right-hand side, respectively. The equations can be solved for these unknowns using inner products with the adjoint solution of the unperturbed eigenvalue problem.

Intermezzo: pseudosolutions, adjoints, and solvability

Given the linear system of equations

$$\mathcal{L}_{0,0} x = y \tag{6.14}$$

the right-hand side can be uniquely decomposed as $y = y^{\perp} + y^{\parallel}$, where $y^{\perp} \in \text{range}(\mathcal{L}_{0,0})$ and $y^{\parallel} \notin \text{range}(\mathcal{L}_{0,0})$. The definition of the adjoint solutions allows for a simple orthogonality test in order to prove whether a vector has a component outside of the range of the operator $\mathcal{L}_{0,0}$. Applying the operator to an arbitrary vector x, it trivially follows that $\mathcal{L}_{0,0} x \in \text{range}(\mathcal{L}_{0,0})$. Now taking the inner product with an adjoint solution $\widehat{p}_0^{\dagger}$ results in

$$\left\langle \widehat{p}_0^{\dagger} \middle| \mathcal{L}_{0,0} x \right\rangle = \left\langle \mathcal{L}_{0,0}^{\dagger} \widehat{p}_0^{\dagger} \middle| x \right\rangle = \langle 0 | x \rangle = 0. \tag{6.15}$$

Hence, it can be concluded that an adjoint solution is orthogonal to the range of $\mathcal{L}_{0,0}$. This necessary condition is also sufficient for finite-dimensional operators. See, e.g., [127, Chapter 9] for details. With this solvability test it can be stated that the equation $\mathcal{L}_{0,0} x = y$ has a solution if y is orthogonal to the adjoint eigenspace. This motivates the notation $y^{\perp}$ for the part of the right-hand side being in the range of the operator [1]. If this condition does not hold true, the equation is not solvable. In this case one may define the pseudosolution x^{Ψ} as the solution of the equation which

[1] Equivalently, it can be stated $y^{\perp} \notin \text{span}(p_{0,a})^{\dagger}$ and $y^{\parallel} \in \text{span}(p_{0,a}^{\dagger})$ – a theorem known as Fredholm alternative in the literature.

is mapped to the part of y which is in the range of $\mathcal{L}_{0,0}$, i.e., the solution of

$$\mathcal{L}_{0,0} x^{\Psi} = y^{\perp}. \tag{6.16}$$

This definition of a pseudosolution is consistent with the notion of a pseudoinverse because the pseudoinverse must fulfill $x^{\Psi} = \mathcal{L}_{0,0}^{\Psi} y^{\perp}$. Hence, if equation (6.14) is solvable, multiplication of the pseudoinverse with the right-hand side y results in the correct solution. However, the effect of the pseudoinverse on vectors lying not in the range of the operator $\mathcal{L}_{0,0}$ remains undetermined. Therefore, the pseudoinverse is not uniquely defined. In the present, context it is convenient to define the pseudoinverse such that $\mathcal{L}_{0,0}^{\Psi} y^{\parallel} = 0$. With this definition of the pseudoinverse the calculation of a pseudosolution to (6.14) without the computation of the pseudoinverse is straightforward: first, remove $y^{\parallel}$ from the right-hand side by use of appropriate projections to the adjoint solutions. Then, solve the remaining system. As a result the pseudosolution with minimal standard norm is obtained.

Applying the solvability condition to compute sensitivity

Equivalently to (6.15), taking the inner product of the adjoint eigenmode $\widehat{p}_0^{\dagger}$ with the left-hand side of (6.12) yields

$$\left\langle \widehat{p}_0^{\dagger} \middle| \mathcal{L}_{0,0} \widehat{p}_k \right\rangle = \left\langle \mathcal{L}_{0,0}^{\dagger} \widehat{p}_0^{\dagger} \middle| \widehat{p}_k \right\rangle = 0. \tag{6.17}$$

Hence, the inner product with the right-hand side must also vanish and a determination formula for ω_k can be obtained from (6.12) by taking the inner product with $\widehat{p}_0^{\dagger}$:

$$\left\langle \widehat{p}_0^{\dagger} \middle| r_k \right\rangle + \omega_k \left\langle \widehat{p}_0^{\dagger} \middle| \mathcal{L}_{1,0} \widehat{p}_0 \right\rangle = 0. \tag{6.18}$$

This equation is called the kth-order *eigenvalue correction determining equation.* Once ω_k is calculated from this equation, it can be substituted back into (6.12). Then, this equation can be solved even though $\mathcal{L}_{0,0} = \mathcal{L}(\omega_0, \varepsilon_0)$ has a non-vanishing null space (the eigenspace corresponding to ω_0). This is because the kth-order eigenvalue determining equation (6.18) ensures that the right-hand side of (6.12) is orthogonal to the adjoint eigenspace of $\mathcal{L}_{0,0}(\omega_0)$ and, therefore, guarantees solvability. Consequently, Eq. (6.12) yields the kth-order eigenmode correction. It is, thus, called the kth-order *eigenmode correction determining equation.*

It can be shown by induction that $r_k = \mathcal{R}_k \widehat{p}_0$, where $\mathcal{R}_k$ is a linear mapping specific to the kth-order correction step and the given problem. Thus, starting with $k = 0$ – i.e., the known eigenvalue ω_0 and its corresponding eigenmode $\widehat{p}_0$ – the aforementioned computation scheme for the correction yields the respective corrections up to kth order when applied k times.

The mapping $\mathcal{R}_k$ cannot be calculated without the computation of all correction terms of smaller order. From an algorithmic point of view, it is not necessary to know $\mathcal{R}_k$ because the definition of r_k (Eq.(6.13)) allows for its calculation from the correction terms rather than from the unperturbed eigenvalues. For instance, the first four r_k are:

$$r_1 = \mathcal{L}_{0,1} \widehat{p}_0, \tag{6.19}$$

$$r_2 = \mathcal{L}_{0,1} \widehat{p}_1 + \mathcal{L}_{0,2} \widehat{p}_0 + \omega_1 \left(\mathcal{L}_{1,0} \widehat{p}_1 + \mathcal{L}_{1,1} \widehat{p}_0 \right) + \omega_1^2 \mathcal{L}_{2,0} \widehat{p}_0, \tag{6.20}$$

$$r_3 = \mathcal{L}_{0,1}\widehat{p}_2 + \mathcal{L}_{0,2}\widehat{p}_1 + \mathcal{L}_{0,3}\widehat{p}_0 + \omega_1\left(\mathcal{L}_{1,0}\widehat{p}_2 + \mathcal{L}_{1,1}\widehat{p}_1 + \mathcal{L}_{1,2}\widehat{p}_0\right) + \omega_2\left(\mathcal{L}_{1,0}\widehat{p}_1 + \mathcal{L}_{1,1}\widehat{p}_0\right) + \omega_1^2\left(\mathcal{L}_{2,0}\widehat{p}_1 + \mathcal{L}_{2,1}\widehat{p}_0\right) + 2\omega_1\omega_2\mathcal{L}_{2,0}\widehat{p}_0 + \omega_1^3\mathcal{L}_{3,0}\widehat{p}_0, \tag{6.21}$$

and

$$\begin{aligned} r_4 = {} & \mathcal{L}_{0,1}\widehat{p}_3 + \mathcal{L}_{0,2}\widehat{p}_2 + \mathcal{L}_{0,3}\widehat{p}_1 + \mathcal{L}_{0,4}\widehat{p}_0 + \omega_1\left(\mathcal{L}_{1,0}\widehat{p}_3 + \mathcal{L}_{1,1}\widehat{p}_2 + \mathcal{L}_{1,2}\widehat{p}_1 + \mathcal{L}_{1,3}\widehat{p}_0\right) \\ & + \omega_2\left(\mathcal{L}_{1,0}\widehat{p}_2 + \mathcal{L}_{1,1}\widehat{p}_1 + \mathcal{L}_{1,2}\widehat{p}_0\right) + \omega_3\left(\mathcal{L}_{1,0}\widehat{p}_1 + \mathcal{L}_{1,1}\widehat{p}_0\right) + \omega_1^2\left(\mathcal{L}_{2,0}\widehat{p}_2 + \mathcal{L}_{2,1}\widehat{p}_1 + \mathcal{L}_{2,2}\widehat{p}_0\right) \\ & + 2\omega_1\omega_2\left(\mathcal{L}_{2,0}\widehat{p}_1 + \mathcal{L}_{2,1}\widehat{p}_0\right) + \omega_2^2\mathcal{L}_{2,0}\widehat{p}_0 + 2\omega_1\omega_3\mathcal{L}_{2,0}\widehat{p}_0 + \omega_1^3\left(\mathcal{L}_{3,0}\widehat{p}_1 + \mathcal{L}_{3,1}\widehat{p}_0\right) + 3\omega_1^2\omega_2\mathcal{L}_{3,0}\widehat{p}_0 \\ & + \omega_1^4\mathcal{L}_{4,0}\widehat{p}_0. \end{aligned} \tag{6.22}$$

Thus, the solution scheme is truly incremental. This means that the kth-order corrections cannot be calculated without the computation of all $(k-1)$th-order corrections but are obtained in increasing order.

6.2 Normalization

The eigenmode correction of kth order is not uniquely defined through the eigenmode correction determining equation (6.12). If $\widetilde{p}_k$ is one particular solution to that equation, then adding arbitrary multiples of homogeneous solutions to it, would also yield a valid solution[2]. This homogeneous form of (6.12) is by definition identical to the the unperturbed eigenvalue problem (6.1). Therefore, the homogeneous solutions are known and can be labeled as $\widehat{p}_0$. Following this notation, in the non-degenerate case all solutions to the eigenmode correction determining equation (6.12) can be written as

$$\widehat{p}_k = \widetilde{p}_k + \gamma_k\widehat{p}_0, \tag{6.23}$$

where γ_k denotes an arbitrary constant. This free parameter is a direct consequence of the fact that multiples of eigenfunctions are still eigenfunctions. Usually, an eigenfunction is defined as a member of a vector space featuring a norm equal to 1. This normalization condition could also be used to determine the unknown parameter γ_k [71]. The normalization procedure can be incorporated in the perturbation theory before or after evaluating the power series for the eigenmode evolution. Both methods are discussed in this section.

A priori normalization

Requiring that the asymptotic series expansion (6.3) yields an eigenmode of norm 1, a condition to compute γ_k can be obtained.

Starting with the normalization conditions, yields:

$$1 \stackrel{!}{=} \left\langle \widehat{p}(\varepsilon)\middle|\widehat{p}(\varepsilon)\right\rangle = \left\langle \sum_{l=0}^{\infty}\widehat{p}_l(\Delta\varepsilon)^l \middle| \sum_{k=0}^{\infty}\widehat{p}_k(\Delta\varepsilon)^k \right\rangle \tag{6.24}$$

[2]Without loss of generality the particular solution $\widetilde{p}_k$ can be chosen to be a pseudosolution $\widehat{p}_k^{\Psi}$, compare Eq (6.16).

$$= \sum_{k=0}^{\infty} \sum_{l=0}^{\infty} (\Delta\varepsilon)^{k+l} \langle \widehat{p}_l | \widehat{p}_k \rangle \qquad \text{| sort by powers of } \Delta\varepsilon \text{ and truncate at order } N \tag{6.25}$$

$$= \underbrace{\langle \widehat{p}_0 | \widehat{p}_0 \rangle}_{=1} + \sum_{k=1}^{N} (\Delta\varepsilon)^k \sum_{l=1}^{k} \langle \widehat{p}_l | \widehat{p}_{k-l} \rangle + o\left((\Delta\varepsilon)^{N+1}\right) \qquad \text{as } \Delta\varepsilon \to 0 \tag{6.26}$$

Thus, for the normalization condition to hold $\sum_{k=1}(\Delta\varepsilon)^k \sum_{l=1}^{k} \langle \widehat{p}_l | \widehat{p}_{k-l} \rangle = 0$, must be satisfied. At each order k this yields

$$\langle \widehat{p}_k | \widehat{p}_0 \rangle + \langle \widehat{p}_0 | \widehat{p}_k \rangle = - \underbrace{\sum_{l=1}^{k-1} \langle \widehat{p}_l | \widehat{p}_{k-l} \rangle}_{:= s_k}. \tag{6.27}$$

The right-hand side term s_k only depends on correction terms $\widehat{p}_n$ of order $n < k$. Hence, the normalization procedure can also be performed in an incremental fashion. Note that $\langle a|b\rangle + \langle b|a\rangle = 2\,\mathrm{real}\,\langle a|b\rangle$. Consequently, s_k must be real and $\langle \widehat{p}_k | \widehat{p}_0 \rangle + \langle \widehat{p}_0 | \widehat{p}_k \rangle = 2\,\mathrm{real}(\langle \widehat{p}_0 | \widehat{p}_k \rangle)$. Therefore, normalization of the eigenvectors imposes the following normalization to the correction coefficients:

$$\mathrm{real}(\langle \widehat{p}_0 | \widehat{p}_k \rangle) = \frac{-s_k}{2}. \tag{6.28}$$

It is convenient to choose $\mathrm{imag}(\langle \widehat{p}(0) | \widehat{p}(\varepsilon) \rangle) = 0$ as a phase condition. Inserting the power series ansatz results in $\mathrm{imag}(\langle \widehat{p}_0 | \sum_{k=0}^{N} \widehat{p}_k \varepsilon^k \rangle) = \mathrm{imag}(\sum_{k=0}^{N} \varepsilon^k \langle \widehat{p}_0 | \widehat{p}_k \rangle) = 0$. Hence, the phase condition at each order k simply reads:

$$\mathrm{imag}(\langle \widehat{p}_0 | \widehat{p}_k \rangle) = 0. \tag{6.29}$$

Note that the phase condition is actually determining the eigenvector except for a change in sign. However, because the eigenvector trajectory should depend smoothly on the perturbation parameter, the evolution from a certain eigenvector is uniquely determined.

It is convenient to state the equations (6.28) and (6.29) as a single expression:

$$\langle \widehat{p}_0 | \widehat{p}_k \rangle = \frac{-s_k}{2}. \tag{6.30}$$

The first order normalization condition simplifies to $\langle \widehat{p}_0 | \widehat{p}_1 \rangle = 0$, which is a common choice (e.g., [127]). However, only a few authors stress the link of this choice to normalization, e.g., [71].

A posteriori normalization

Finding the coefficients γ_k such that the power series (6.3) yields a normalized mode is not necessary to compute the eigenvalue coefficients ω_n. Consequently, normalization can also be applied after computing the coefficients ω_k and $\widehat{p}_k$ and evaluating the power series. This method requires

to collect the coefficients γ_k for the already computed Nth-order power series in a single factor:

$$\widehat{p}(\varepsilon) = \widehat{p}_0 + \sum_{k=1}^{\infty} (\widetilde{p}_k + \gamma_k \widehat{p}_0)(\Delta\varepsilon)^k = \underbrace{\left(\sum_{k=1}^{N} \gamma_k (\Delta\varepsilon)^k\right)}_{:=\gamma(\varepsilon)} \widehat{p}_0 + \underbrace{\left(\widehat{p}_0 + \sum_{k=1}^{N} \widetilde{p}_k (\Delta\varepsilon)^k\right)}_{:=\widetilde{p}(\varepsilon)} + o\left((\Delta\varepsilon)^{N+1}\right) \qquad \text{as } \Delta\varepsilon \to 0. \tag{6.31}$$

Substituting the known information, i.e., computed power series for ω and $\widehat{p}$ back into the considered eigenvalue problem then yields

$$\mathcal{L}(\sum_{k=0}^{N} \omega_k (\Delta\varepsilon)^k; \varepsilon) \left(\widetilde{p}(\varepsilon) + \gamma(\varepsilon)\widehat{p}_0\right) + \mathcal{O}\left((\Delta\varepsilon)^{N+1}\right) = 0 \qquad \text{as } \Delta\varepsilon \to 0. \tag{6.32}$$

Note that while the power series are truncated at Nth order, inserting them into the eigenvalue problem might produce higher powers of $\Delta\varepsilon$. Again the change from $o\left((\Delta\varepsilon)^k\right)$ to $\mathcal{O}\left((\Delta\varepsilon)^k\right)$ stresses this aspect.

Equation (6.32) motivates choosing $\gamma(\varepsilon)$ such that the norm of $\mathcal{L}(\sum_{k=0}^{N} \omega_k (\Delta\varepsilon)^k; \varepsilon) \left(\widetilde{p}(\varepsilon) + \gamma(\varepsilon)\widehat{p}_0\right)$ is as small as possible. This expression has two independent components, the images of $\widetilde{p}(\varepsilon)$ and $\gamma(\varepsilon)\widehat{p}_0$ under the operator $\mathcal{L}(\sum_{k=0}^{N} \omega_k (\Delta\varepsilon)^k; \varepsilon)$. For the sake of brevity, the images are abbreviated as $a := \mathcal{L}(\sum_{k=0}^{N} \omega_k (\Delta\varepsilon)^k; \varepsilon)\widetilde{p}(\varepsilon)$ and $b := \mathcal{L}(\sum_{k=0}^{N} \omega_k (\Delta\varepsilon)^k; \varepsilon)\widehat{p}_0$. It is convenient to decompose the vector a into components parallel and orthogonal to b:

$$a = a_{\parallel} + a_{\perp} = \frac{\langle a|b\rangle}{\langle b|b\rangle} b + a_{\perp}. \tag{6.33}$$

With these conventions Eq. (6.32) reads:

$$\left(\frac{\langle a|b\rangle}{\langle b|b\rangle} + \gamma(\varepsilon)\right) b + a_{\perp} + \mathcal{O}\left((\Delta\varepsilon)^{N+1}\right) = 0 \qquad \text{as } \Delta\varepsilon \to 0. \tag{6.34}$$

The first term here is exactly eliminated if

$$\gamma(\varepsilon) = -\frac{\langle a|b\rangle}{\langle b|b\rangle} = \frac{\left\langle \mathcal{L}(\sum_{k=0}^{N} \omega_k (\Delta\varepsilon)^k; \varepsilon)\widetilde{p}(\varepsilon) \middle| \mathcal{L}(\sum_{k=0}^{N} \omega_k (\Delta\varepsilon)^k; \varepsilon)\widehat{p}_0 \right\rangle}{\left\langle \mathcal{L}(\sum_{k=0}^{N} \omega_k (\Delta\varepsilon)^k; \varepsilon)\widehat{p}_0 \middle| \mathcal{L}(\sum_{k=0}^{N} \omega_k (\Delta\varepsilon)^k; \varepsilon)\widehat{p}_0 \right\rangle}. \tag{6.35}$$

Thus, given the information available at order N, this is the best possible choice for γ. In comparison to the a priori approach, the a posteriori method is computationally more demanding because it is to be computed for each new instance of ε. Nonetheless, as it is not computed incrementally, it is more robust against round-off errors.

6.3 Notes on implementation

Rayleigh-Schrödinger perturbation theory has started as a pen-and-paper discipline. To date it is common to apply it using computer algebra software like Maple, Mathematica, or Maxima performing the necessary manipulations symbolically [128]. Yet, symbolic modeling is not a common practice in engineering. Implementation of the large-order perturbation theory must seamlessly integrate in software frameworks that solve the eigenvalue problems by discretization of the con-

sidered operators ($\mathcal{L}(z;\varepsilon) \mapsto \mathbf{L}(z;\varepsilon)$). This section discusses the details of such an implementation. The only aspect that will not be addressed in this section is how to efficiently obtain a highly accurate baseline solution. This is the topic of Chap. 8.

Data structuring

A considerable obstacle when implementing the theory is the accurate computation of the Taylor-series coefficients $\mathbf{L}_{m,n}$ because these require the computation of large-order partial derivatives. Although the problem has been tackled using finite differences in [129, 125], it is not an efficient means to compute large order derivatives featuring an accuracy which is commensurate with the truncation order of the stipulated power series. The issue can be resolved by implementing a flexible data structure representing the considered operator family. The data structure decomposes the operator family as

$$\mathbf{L}(z;\varepsilon) = \sum_{g=1}^{G} \mathbf{A}_g f_g(z,\varepsilon). \tag{6.36}$$

Here, the coefficient functions f_g are analytic and can be stored together with their derivatives in a library. Derivatives can then be algebraically computed:

$$\frac{\partial^{m+n}\mathbf{L}}{\partial z^m \partial \varepsilon^n} = \sum_{g=1}^{G} \mathbf{A}_g \frac{\partial^{m+n} f_g}{\partial z^m \partial \varepsilon^n}. \tag{6.37}$$

A similar data structure to represent monovariate operator families $\mathbf{L}(z)$ was suggested in [130] and is implemented in the SLEPc software library [131, 132] and a collection of nonlinear eigenvalue problems written in MATLAB [133]. Indeed, any analytic operator family $\mathbf{L}(z;\varepsilon)$ can be represented using such a data structure. For instance, if the operator family is D-dimensional, the number of coefficient functions can be set to $G = D^2$ and for each entry in $\mathbf{L}$ a function f_g is stored individually. If these functions are stored as pointers pointing into a library, the memory space needed to store the structure is comparable to storing an equally sized matrix of floating point numbers. However, the thermoacoustic Helmholtz equation naturally implies using a data structure based on the stiffness, the damping, the mass, and the flame matrix. For instance, when considering the time delay τ in the Rijke-tube model as a perturbation parameter, the structuring reads

$$\mathbf{L}(z;\tau) = \mathbf{K} + z\mathbf{C} + z^2\mathbf{M} + ne^{-\mathrm{i}z\tau}\mathbf{F} \tag{6.38}$$

and, e.g., $\mathbf{L}_{0,1}$ is exactly given as $\frac{\partial}{\partial\tau}\mathbf{L}(\omega_0;\tau_0) = -\mathrm{i}\omega_0 ne^{-\mathrm{i}\omega_0\tau}\mathbf{F}$.

Note that the data structure suggested in Eq. (6.36) has also a great potential for parallelization. The different terms are completely independent and also matrix-multiplication is embarrassingly parallelizable.

Numerical implementation of the perturbation theory

Algorithm 6.1 sketches a straightforward implementation of the outlined perturbation theory. The function SOLVE is assumed to return a pseudosolution $\boldsymbol{x}_k^{\Psi}$ to the linear system $\mathbf{L}_{0,0}\boldsymbol{x}^{\Psi} = \boldsymbol{y}^{\perp}$ as dis-

Algorithm 6.1: Brute-force implementation of the perturbation theory

function PERTURB($\mathsf{L}_{m,n}, \boldsymbol{p}_0, \boldsymbol{p}_0^\dagger, N$)

  for $k \leftarrow 1,\dots,N$ **do** ▷ loop to compute $\sum_{n=1}^{k} \mathsf{L}_{0,n}\boldsymbol{p}_{k-n}$
    $\boldsymbol{r}_k \leftarrow 0$
    for $n \leftarrow 1,\dots,k$ **do**
      $\boldsymbol{r}_k \leftarrow \boldsymbol{r}_k + \mathsf{L}_{0,n}\boldsymbol{p}_{k-n}$
    end for

    for $m \leftarrow 1,\dots,k$ **do** ▷ loops to compute $\sum_{\substack{0<|\boldsymbol{\mu}|_1\le k \\ \boldsymbol{\mu}\neq \mathbf{1}_k}}$
      for $\boldsymbol{\mu} \in \{\boldsymbol{\mu} : |\boldsymbol{\mu}|_1 = m\} \setminus \{\mathbf{1}_k\}$ **do** ▷ the ACCELASC algorithm [134] is used to find the multi-indices $\boldsymbol{\mu}$
        for $n \leftarrow 0,\dots,k-m$ **do**
          $\boldsymbol{r}_k \leftarrow \boldsymbol{r}_k + \mathsf{L}_{|\boldsymbol{\mu}|,n}\boldsymbol{p}_{k-n-m}\boldsymbol{\omega}^{\boldsymbol{\mu}}\binom{|\boldsymbol{\mu}|}{\boldsymbol{\mu}}$
        end for
      end for
    end for

    $\omega_k \leftarrow -\frac{\boldsymbol{p}_0^{\dagger\mathrm{H}}\boldsymbol{r}_k}{\boldsymbol{p}_0^{\dagger\mathrm{H}}\mathsf{L}_{1,0}\boldsymbol{p}_0}$
    $\boldsymbol{p}_k \leftarrow$ SOLVE($\mathsf{L}_{0,0}, -\boldsymbol{r}_k - \omega_k\mathsf{L}_{1,0}\boldsymbol{p}_0$) ▷ is solvable due to solvability condition
  end for

  return $\omega_1,\dots,\omega_N, \boldsymbol{p}_1,\dots,\boldsymbol{p}_N$
end function

cussed in Sec. 6.1. The algorithm uses results from number theory to generate the increasingly complex set of multi-indices $\boldsymbol{\mu}$ occurring at each incremental step of the procedure. In particular, it exploits a connection to the partition function. This connection has been discussed in [135] for perturbations of linear eigenvalue problems arising in quantum mechanics. Here, it is generalized to the case of nonlinear eigenvalue problems. The partition function part(m) is defined as the number of partitions of an integer m – i.e., the number of decompositions of m into sums of integers. Because

$$|\boldsymbol{\mu}|_1 := \sum_{k=1}^{N} \mu_k k = \sum_{k=1}^{N}\sum_{n=0}^{\mu_k} k = m, \tag{6.39}$$

the multi-index $\boldsymbol{\mu}$ can be interpreted as a representation of a partition of m. Thus, there are part(m) multi-indices $\boldsymbol{\mu}$ in the set $\{\boldsymbol{\mu}||\boldsymbol{\mu}|_1 = m\}$. These are exactly the multi-indices summed over in Eq. (6.10) and equations thereafter. Moreover, any algorithm generating a full sequence of partitions of the integer m can be used to generate a sequence of all $\boldsymbol{\mu} \in \{\boldsymbol{\mu}||\boldsymbol{\mu}|_1 = m\}$. A fast algorithm to generate partitions of a given integer is the accelerated ascending composition generation algorithm ACCELASC proposed in [134]. See Appendix B for a pseudocode of this algorithm. Interpreting the multi-indices as partitions also allows for assessing the computational effort of Alg. 6.1. The number of terms appearing in the expansion (6.10) of the eigenvalue problem into a power

series is

$$\text{number of terms} = \sum_{k=0}^{N}\sum_{m=1}^{k}\sum_{|\boldsymbol{\mu}|_1=m}\sum_{n=0}^{k-m} 1 = \sum_{k=1}^{N}\sum_{m=1}^{k} \text{part}(m)(k-m+1). \tag{6.40}$$

Because of the rapid growth of the partition function (see Fig. 6.1), the computational effort to compute the power series coefficients also rises rapidly with the perturbation order. The computationally most expensive operation in Alg. 6.1 is the matrix-vector multiplication $\mathbf{L}_{|\boldsymbol{\mu}|,n}\boldsymbol{p}_{k-n-m}$. Fortunately, the same matrices $\mathbf{L}_{|\boldsymbol{\mu}|,n}$ appear multiple times in the expansion. Factorizing them as

$$\sum_{k=0}^{N}(\Delta\varepsilon)^k \sum_{m=0}^{k}\sum_{n=0}^{k-m} \mathbf{L}_{m,n} \underbrace{\sum_{\substack{|\boldsymbol{\mu}|=m \\ |\boldsymbol{\mu}|_1\leq k}} \binom{m}{\boldsymbol{\mu}} \boldsymbol{\omega}^{\boldsymbol{\mu}} \boldsymbol{p}_{k-n-|\boldsymbol{\mu}|_1}}_{:=\boldsymbol{v}_{m,n}}, \tag{6.41}$$

would, consequently, save a lot of matrix-vector multiplications and accelerate the computations. Note that the last summation is conducted over the set of multi-indices $\boldsymbol{\mu}$ satisfying $|\boldsymbol{\mu}| = m$ and $|\boldsymbol{\mu}|_1 \leq k$. The total number of matrix-vector multiplications is now polynomial:

$$\text{number of matrix-vector multiplications} = \sum_{k=0}^{N}\sum_{m=0}^{k}\sum_{n=0}^{k-m} 1 = \frac{1}{6}N^3 + N^2 + \frac{11}{6}N + 1. \tag{6.42}$$

Of course, the number of vector-vector additions remains unchanged and is, therefore, still identical to the total number of terms. Nonetheless, vector-vector addition has lower computational costs than matrix-vector multiplications. Algorithms that factorize the matrices will, thus, be faster than those that factorize vectors.

The considerations concerning the computational effort strictly apply to operators $\mathbf{L}(z,\varepsilon)$ which are non-polynomial in z and ε. If they depend polynomially on these values, the Taylor-series coefficients $\mathbf{L}_{m,n}$ vanish if m or n are greater than the degree of the polynomials in z or ε, respectively.

Figure 6.1 shows the computational effort necessary to assemble the vectors r_k at each incremental step for nonlinear operator families and those which are linear in both z and ε. It also shows the evolution of the partition function.

Algorithm 6.2 outlines an implementation of the theory based on factorizing the coefficients $\mathbf{L}_{m,n}$ for efficiency. It also demonstrates a possible implementation of the a priori normalization. In contrast to Alg. 6.1, there is no known algorithm to efficiently generate the multi-indices in the order they are needed. However, all multi-indices can be generated using the same method as in Alg. 6.1, sorted and then stored to a library to avoid generation at run-time. Also note that the for-loops started in the lines 4 and 5 are embarrassingly parallel. Given the high number of terms appearing in the algorithm, even if factorizing $\mathbf{L}_{m,n}$, this parallelization of the algorithm is crucial for conducting large order perturbation theory.

6.4 Application to the Rijke-tube model

In this section the perturbation theory is applied to the Rijke-tube model. Perturbation expansions up to 30th order are computed and compared with exact solutions of the model equations. To

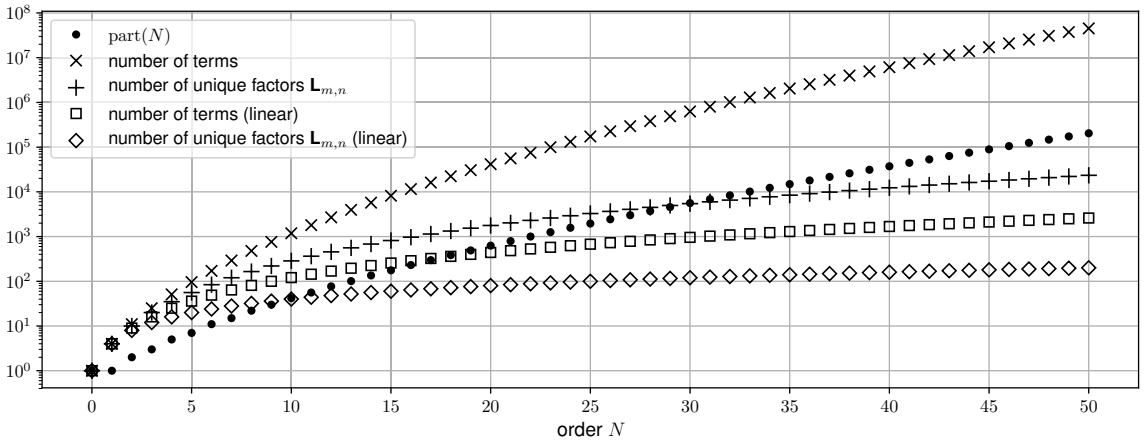

Figure 6.1: Number of terms and the number of unique factors $\mathbf{L}_{m,n}$ necessary to assemble $\boldsymbol{r}_k$ for (i) a generic dependence of $\mathbf{L}(z,\varepsilon)$ on its parameters z and ε and (ii) the special case of a linear dependence. The behavior of the partition function is shown for reference. The number of matrix-vector multiplications required by Alg. 6.1 is equivalent to the number of terms while it reduces to the number of unique factors $\mathbf{L}_{m,n}$ when using Alg. 6.2. The number of vector-vector additions required by the two algorithms is identical, and is equal to the number of terms.

solve the eigenvalue problem, a modification of the generalized Rayleigh-quotient iteration proposed in [136] is deployed as it converges much faster to machine-precise solutions than Nicoud's algorithm and the Picard iteration. The details of the algorithm will be discussed in Chap. 8. The model data is structured as

$$\mathbf{L}(z;n,\tau,c_2) = c_1^2\mathbf{K}_1 + c_2^2\mathbf{K}_2 + zc_2\mathbf{B} + z^2\mathbf{M} + n\exp(-\mathrm{i}\omega\tau)\mathbf{F} \tag{6.43}$$

to enable perturbations of the interaction index n, the time delay τ, and the hot gas speed of sound c_2. Here, $\mathbf{K}_1$ and $\mathbf{K}_2$ are special stiffness matrices assembled with unit speed of sound for the hot and cold gas domain, respectively. Similarly, $\mathbf{B}$ denotes a boundary mass matrix for the outlet assembled with unit speed of sound to enable explicit factorization of c_2. The other matrices follow the definitions of Chap. 3. c_1 denotes the cold gas temperature.

Evolution of mode #R1 when perturbing τ

The first example concerns the effect of a perturbation of the time delay τ on mode #R1. Because the perturbation theory yields truncated power series as approximations to the relation $\omega = \omega(\varepsilon)$, the range $[\varepsilon-\delta, \varepsilon+\delta]$ in which the approximation yields reliable results can be estimated from the radius of convergence δ of the power series. A simple formula to estimate the convergence radius from the coefficients of the power series is

$$\delta \approx \left| \frac{\omega_n}{\omega_{n+1}} \right|. \tag{6.44}$$

This formula is obtained as consequence of the ratio test for series convergence, see, e.g., [137, Chapter 2]. Figure 6.2 shows the estimate for the convergence radius obtained from the 30 computed power series coefficients. The estimate quickly settles to a value of $\delta \approx 1.236$. Compari-

Algorithm 6.2: Factorized implementation of the perturbation theory with a priori normalization

function PERTURB($\mathbf{L}_{m,n}, \boldsymbol{p}_0, \boldsymbol{p}_0^\dagger, N$)

  for $k \leftarrow 1,\ldots,N$ **do**
    $\boldsymbol{r}_k \leftarrow 0$
    for $m \leftarrow 0,\ldots,k$ **do** ▷ parallelizable loops
      for $n \leftarrow 0,\ldots,k-m$ **do**
        if (m,n)=(0,0) **then**
          continue ▷ the term carrying $\mathbf{L}_{0,0}$ is not part of $\boldsymbol{r}_k$
        end if
        $\boldsymbol{v} \leftarrow 0$
        for $\boldsymbol{\mu} \in \{\boldsymbol{\mu} : |\boldsymbol{\mu}| = m, |\boldsymbol{\mu}|_1 \leq k\} \setminus \{\mathbf{1}_k\}$ **do** ▷ read this set from prepared file
          $\boldsymbol{v} \leftarrow \boldsymbol{v} + \boldsymbol{p}_{k-n-|\boldsymbol{\mu}|_1} \boldsymbol{\omega}^{\boldsymbol{\mu}} \binom{m}{\boldsymbol{\mu}}$
        end for
        $\boldsymbol{r}_k \leftarrow \boldsymbol{r}_k + \mathbf{L}_{m,n}\boldsymbol{v}$
      end for
    end for

    $\omega_k \leftarrow -\frac{\boldsymbol{p}_0^{\dagger\mathrm{H}} \boldsymbol{r}_k}{\boldsymbol{p}_0^{\dagger\mathrm{H}} \mathbf{L}_{1,0} \boldsymbol{p}_0}$
    $\boldsymbol{p}_k \leftarrow$SOLVE($\mathbf{L}_{0,0}, -\boldsymbol{r}_k - \omega_k \mathbf{L}_{1,0}\boldsymbol{p}_0$) ▷ is solvable due to solvability condition

    $c_k \leftarrow 0$
    for $l \leftarrow 1,\ldots,k-1$ **do** ▷ a priori normalization
      $c_k \leftarrow c_k - \frac{1}{2}\langle \boldsymbol{p}_l | \boldsymbol{p}_{k-l} \rangle$
    end for
    $\boldsymbol{p}_k \leftarrow \boldsymbol{p}_k + c_k \boldsymbol{p}_0$
  end for

  return $[\omega_1,\ldots,\omega_N], [\boldsymbol{p}_1,\ldots,\boldsymbol{p}_N]$
end function

son of the power series expansion and the exact results is, therefore, conducted in a range $[\tau_0 + 1.05\delta, \tau_0 + 1.05\delta]$. This is a relatively large range because its span is greater than the baseline value ($2\delta > \tau_0 = 2$).

Figure 6.3 a) shows the trajectory of the exact evolution of the eigenvalue and estimates for this trajectory obtained using first, second, fifth, tenth, fifteenth, and thirtieth order perturbation theory. It can be clearly seen how increasing the perturbation order yields better estimates for values of τ within the convergence interval of the power series. However, for values outside of the convergence interval, increasing the perturbation order is not necessarily improving the approximation and may lead to even worse predictions. For instance, the tail of the fifteenth-order approximation is closer to the tail of the exact trajectory than the thirtieth-order approximation.

Figure 6.3 b) shows the normalized mode shape of mode #R1 at $\tau = 0.08057$. This value is close to the convergence limit. Nonetheless, it is inside the convergence interval. It is obvious how increasing the perturbation order improves the quality of the approximation.

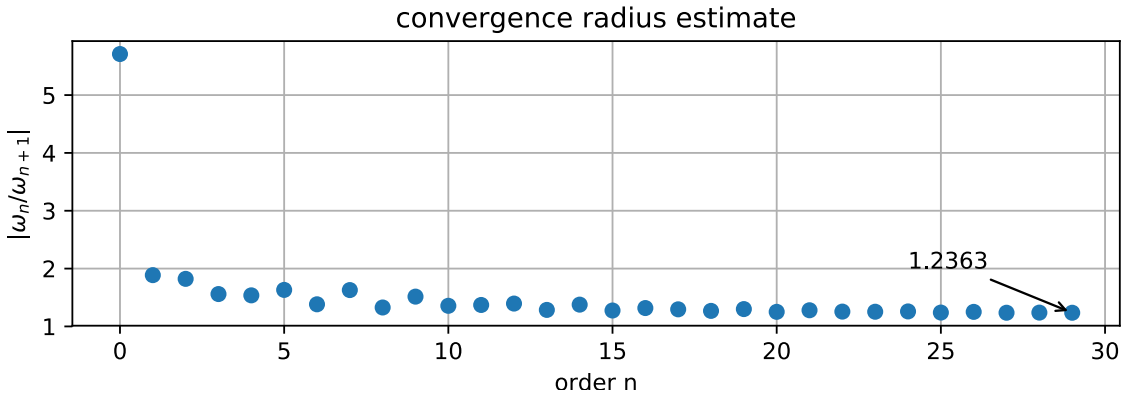

Figure 6.2: Estimate of the convergence radius of the power series modeling the evolution of mode #R1 when perturbing the time delay τ.

Figure 6.4 a) shows the evolution of the difference between the exact eigenvalue and the predictions from perturbation theory when the order is increased for various values of τ ($\circ$-markers). For comparison, the magnitude of the first truncated term $|\omega_{N+1}(\Delta\tau)^{N+1}|$ is also shown ($\times$-markers). Because the series is asymptotic, this value should dominate the truncation error close to the expansion point. As expected, the closer the value of τ is to the expansion point, the better is the approximation obtained from perturbation theory given a fixed order N. This indicates that inside the convergence interval, the rate at which the error decreases is getting faster as τ approaches $\tau_0 = 2$. That the error saturates after decreasing by about 15 orders of magnitude can be attributed to machine precision. Yet, machine precision is not an issue for the magnitude of the first truncated term using IEEE-754 numbers. Thus – although not shown here – these continue to decrease. The truncation error is also correctly estimated from the first truncated term for moderate perturbations ($\tau = 1.974$, $\tau = 1.6885$). However, the truncation error is increasingly underestimated for increasing perturbation strengths. Note how the error for $\tau = 0.07019$ reaches a minimum at an order $N \approx 15$. This value of τ is exactly the value of the lower end of the examined range of values and lies slightly beyond the convergence limit. The power series will, thus, diverge for $N \to \infty$. Hence, truncating the series at $N = 15$ yields the best possible estimate obtainable from a power series expansion. Although the error is underestimated by the first truncated term, the optimal truncation order could be obtained from it, because the sequence of the first truncated terms shows a minimum at the same position. Truncation of divergent power series in order to obtain optimal prediction is a common strategy known as super asymptotics, see, e.g., [138].

Figure 6.4 b) shows the evolution of the error for the mode shape predictions for both the a priori normalization (circles) and the a posteriori method (squares). The same values of τ as in Fig. 6.4 a) are examined. The error evolution is qualitatively identical to the evolution of the error in ω: the closer the value of τ is to the expansion point, the better is the estimate. Saturation of the error appears after it has decreased by 14 orders of magnitude due to machine precision, and the error for $\tau = 0.07019$ reaches a minimum at $N \approx 15$. Note that the a posteriori method yields slightly better results. Because the a posteriori method rests on the idea of minimizing the residual, this is not surprising. Nonetheless, the difference between the two methods is negligible and, given the lower computational costs of the a priori normalization, this strategy should be preferred.

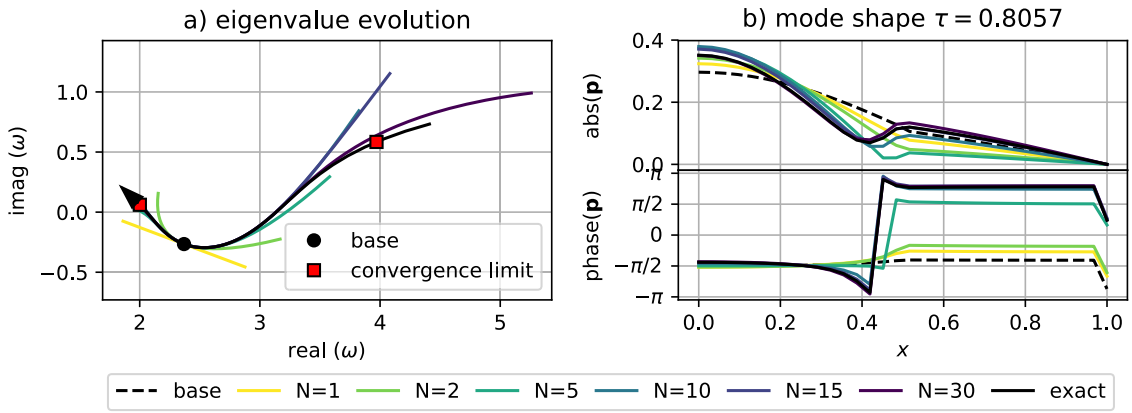

Figure 6.3: a): Eigenvalue trajectory of mode #R1 if the time delay τ is varied. The black line represents the exact solution while the colored lines show approximations obtained from perturbation theory of various orders. The arrowhead indicates the direction of increasing τ. The black dot highlights the position of the unperturbed eigenvalue. The red squares mark eigenvalues obtained at the estimated convergence limit.
b): Evolution of the normalized mode shape close to the convergence limit ($\tau = 0.8057$). The dashed black line represents unperturbed mode shape and the solid black line indicates the exact perturbed mode shape. Colored lines highlight predictions for the mode shape obtained from perturbation theory of various orders.

Evolution of mode #R1 when perturbing n

Qualitatively similar results are obtained when considering another parameter than τ. For instance, Fig. 6.5 shows the results for a perturbation of the interaction index n. The convergence radius $\delta \approx 1.4273$ is larger than the baseline value $n = 1$ and for the shown example of $n = -0.3788$ the mode shape is not much different from the baseline solution. Yet, the results are equivalent to those discussed for perturbations of the time delay τ.

Evolution of mode #R1 when perturbing c_2

Similar results are also obtained when perturbing the hot gas speed of sound as shown in Fig. 6.6. However, for this case the estimate for the convergence radius seems not to have fully converged at $N = 29$, see Fig. 6.6 a). Indeed, given the results presented in Fig. 6.6, the estimated convergence limit (red squares) appears to be slightly overestimated. Apart from these issues, the results show the same characteristics as for the other cases.

Evolution of mode #R2 when perturbing τ

Also when considering mode #R2 the perturbation results show similar behavior. This can be seen in Fig. 6.7 where the evolution of #R2 subject to perturbations of the time delay τ is studied. Again, the estimate for the convergence limit appears not to have fully converged. In order not to overestimate the convergence radius δ, the estimate obtained from $|\omega_{28}/\omega_{29}|$ instead of $|\omega_{29}/\omega_{30}|$ is marked by the red squares in Fig. 6.7 b). In contrast to the other cases, the plotted range of values is not the interval $\pm 1.05\delta$ but $\pm 1.75\delta$. Obviously, the mode shape does not depend strongly

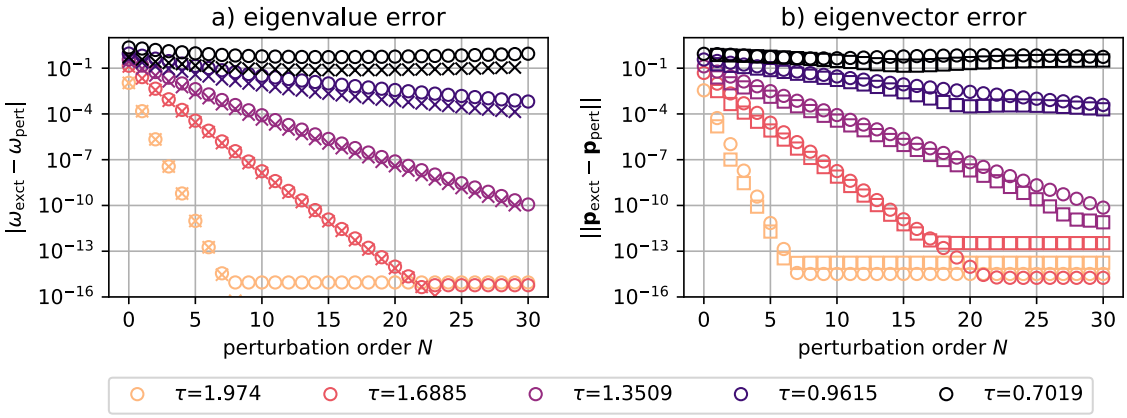

Figure 6.4: a) Evolution of the error of the eigenvalue estimate over perturbation order N when predicting the eigenvalue shift of mode #R1 due to a perturbation in τ ($\circ$-markers) and magnitude of the first truncated term $|\omega_{N+1}(\Delta\tau)^{N+1}|$ ($\times$-markers). The magnitude of the first truncated term is an estimate for the error. The saturation of the error curve at about $1E{-}15$ is due to machine precision. The magnitude of the first truncated term is not saturating and keeps falling, but this is not shown here.
b) Norm of the error of the predicted normalized mode shape using the a priori method ($\circ$-markers) and the a posteriori method ($\square$-markers). The two methods yield nearly equivalent results. Again saturation is attributed to machine precision.

on τ. As explained in Sec. 4.4, the mode is actually independent of the flame response and the variations appearing here are attributed to the discretization of the problem. Discretization effects also cause the variations in the eigenvalue for this specific case. Perturbation theory based on the discretized model will, therefore, also suffer from these limitations. Nonetheless, the error characteristics behave similar to the previous examples.

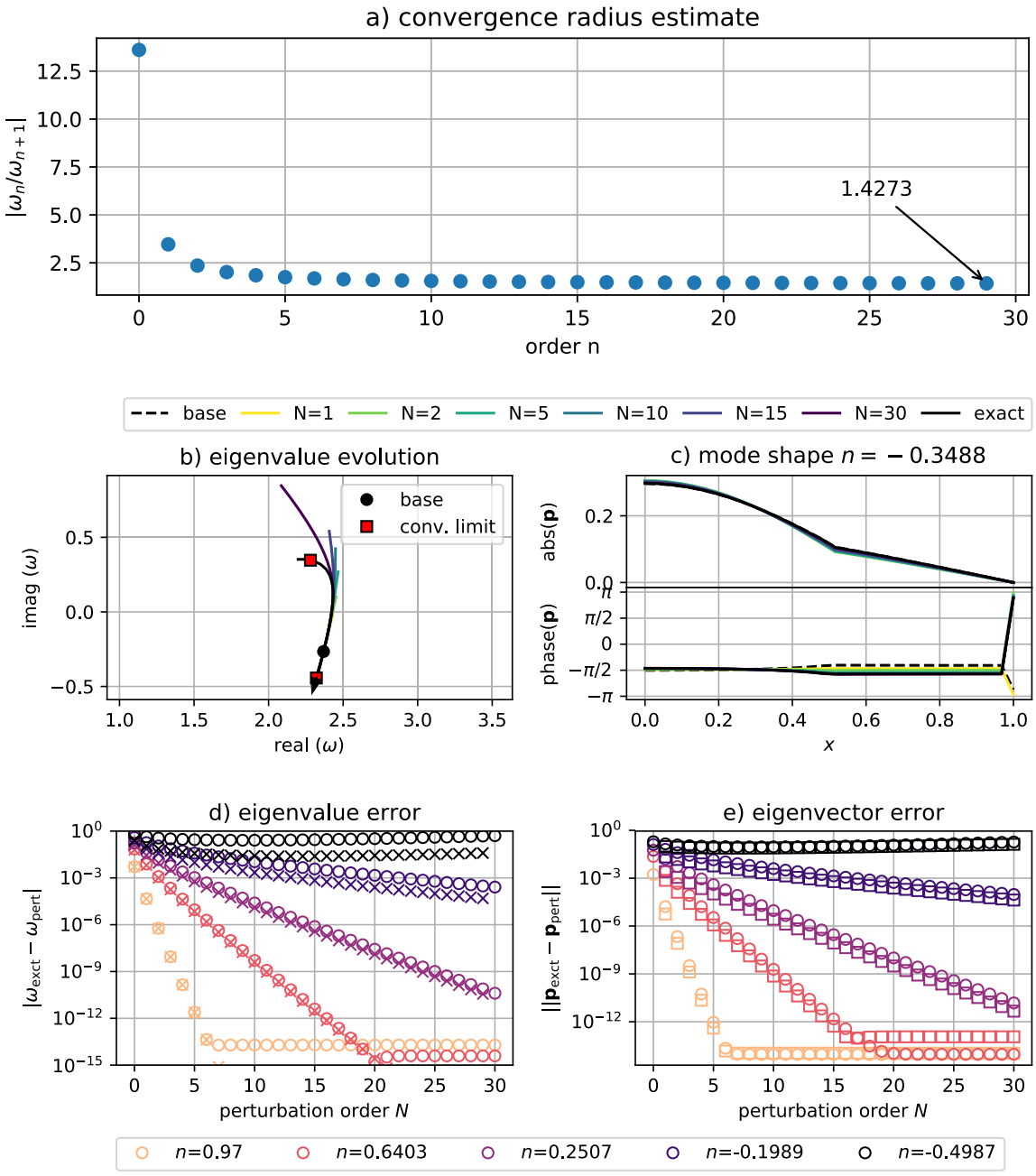

Figure 6.5: Results for mode #R1 when perturbing the interaction index n. The same quantities as in the Figs. 6.2-6.4 are shown, using the same markers. The results are qualitatively similar to those obtained from perturbations of τ.

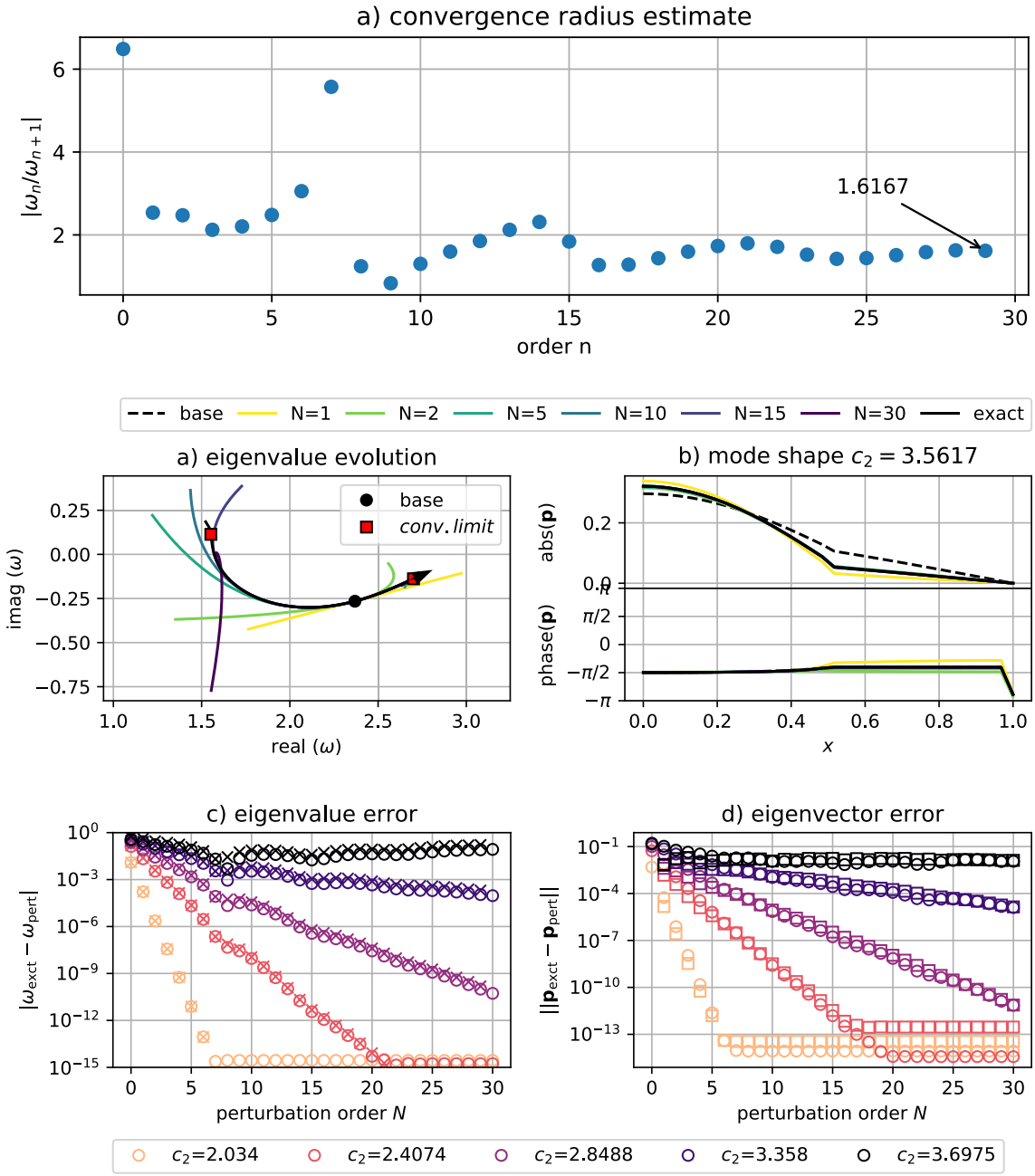

Figure 6.6: Results for mode #R1 when perturbing the speed of sound c_2 of the hot gas. The same quantities as in the Figs. 6.2-6.4 are shown, using the same markers. In contrast to the examples studied before, the estimate for the convergence limit seems not to be accurate. However, the other characteristics are similar.

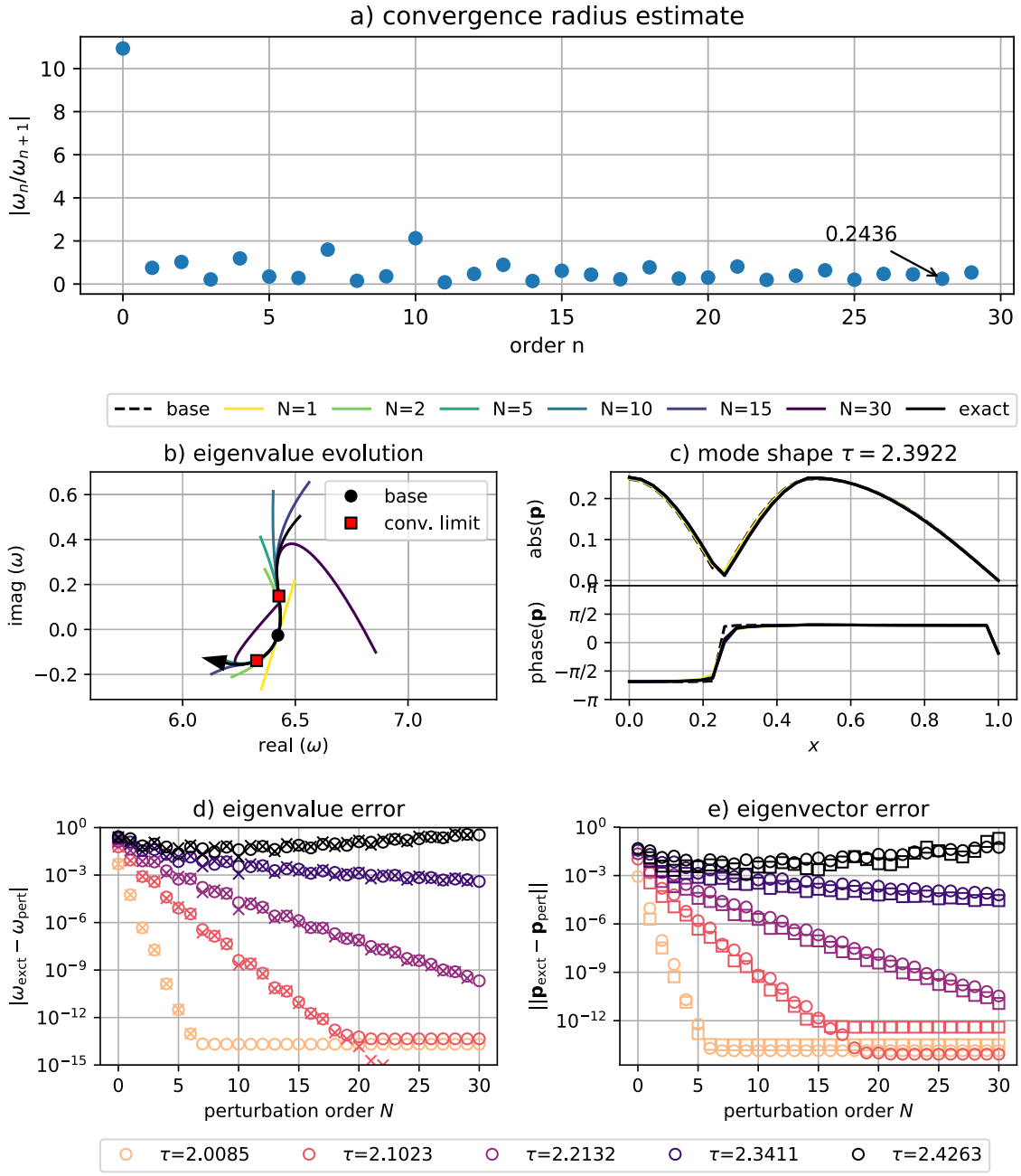

Figure 6.7: Results for mode #R2 when perturbing the time delay τ. The same quantities as in the Figs. 6.2-6.4 are shown, using the same markers.

6.5 Convergence enhancement by Padé approximation

The examples have shown that perturbation theory is capable of predicting the eigenvalue drift within the convergence interval of the power series. Yet, it takes an increasing number of terms to obtain an accurate approximation the closer the evaluation point is to the convergence limit. Moreover, for evaluation points outside the convergence limit the series diverges. An optimal truncation strategy might be considered in this case. This would, however, not yield very accurate predictions. This section shortly discusses Padé approximation to tackle both slow convergence within the convergence interval and divergence outside of it.

Theory

In general, the domains in which a series expansion $\omega(\varepsilon) = \sum_{n=0}^{N} \omega_n (\Delta\varepsilon)^n$ converges are limited by the non-removable singularities closest to the expansion points ε_0 of the series[3]. More precisely, if $\omega(\varepsilon)$ has poles or even essential singularities, the one closest to the expansion point ε_0, at $\varepsilon_{\mathrm{sng}}$ say, determines the radius of convergence to be $\delta = |\varepsilon_{\mathrm{sng}} - \varepsilon_0|$.

Singularities in $\omega(\varepsilon)$ might originate from singularities with respect to ε already present in the considered operator family $\mathcal{L}(z;\varepsilon)$. For example, consider the operator family

$$\mathcal{L}(z;\varepsilon) = \begin{bmatrix} \varepsilon - z & 0 \\ 0 & \frac{1}{\varepsilon} - z \end{bmatrix}. \tag{6.45}$$

It is diagonal and the eigenvalues can be directly obtained as $\omega = \varepsilon$ and $\omega = 1/\varepsilon$. The second one clearly has a first-order pole at $\varepsilon = 0$. The reparametrization $1/\varepsilon = \eta$ might solve the issue. It would, however, introduce a pole to the first branch with respect to the new parameter η. Nonetheless, poles which originate from the operator family are not a big issue as they are known. As in the example, reparametrization can then be utilized. For instance, the impedance can be expressed as an admittance $Y = 1/Z$ to avoid poles for sound-soft conditions. It might be also considered to shift the expansion points from the singularities in order to obtain power series approximations featuring a large radius of convergence. However, singularities in the relation $\omega = \omega(\varepsilon)$ also arise at points $\varepsilon_{\mathrm{sng}}$ where the eigenvalue ω becomes defective. As will be discussed in Chap. 10, it cannot be directly red off from the definition of the operator family $\mathcal{L}(z;\varepsilon)$ at which points this is happening.

Singularities are a feature that cannot be captured by polynomials and, thus, by truncated power series. This is because polynomials never possess singularities (they are entire functions). From this viewpoint, approaching the problem with a polynomial/power-series ansatz is an ill-conceived idea. It is natural to consider a rational-function ansatz instead, as this allows to incorporate singularities. For instance, rational polynomials are a standard method in hydrodynamic stability when approximating a global stability analysis from a sequence of local stability analyses [139, 140, 141]. Using a rational polynomial as an asymptotic expansion ansatz is known as Padé approximation and is well known to feature better approximation properties than Taylor-series expansions in domains that are relatively far from the expansion point [142, Chapter 3]. In particular, they have proven to show good approximations for values ε beyond the convergence radius of Taylor series expanded from the same point [138].

[3] Note that $\Delta\varepsilon := \varepsilon - \varepsilon_0$, which manifests in the notation $\omega = \omega(\varepsilon)$.

The Padé ansatz $[L/M]_\omega$ is defined as the ratio of polynomials of degree L and M, respectively:

$$[L/M]_\omega(\varepsilon) := \frac{\sum_{l=0}^{L} a_l(\Delta\varepsilon)^l}{1+\sum_{m=1}^{M} b_m(\Delta\varepsilon)^m}. \tag{6.46}$$

Note that the coefficient b_0 of the denominator polynomial is set to 1 in order to define a unique representation of the ansatz.

The ansatz features $L+M+1 = N+1$ unknown coefficients $a_0,\ldots,a_L$ and $b_1,\ldots,b_m$. They are determined by requiring

$$\omega(\varepsilon) = [L/M]_\omega(\varepsilon) + o\left((\Delta\varepsilon)^{N+1}\right) \text{ as } \Delta\varepsilon \to 0. \tag{6.47}$$

In particular, this means that – if it exists – the Padé approximant features the same asymptotic behavior as a Nth order power series approximation expanded at the same point as $\Delta\varepsilon \to 0$. Therefore, the N unknown coefficients of the Padé approximant can be computed from the N coefficients of the power series approximation. This allows to treat Padé approximation within the same framework as the power-series approximation presented before. Indeed, Padé ansätze are a generalization of power series ansätze as $[N/0]_\omega$ reduces to a Nth order polynomial. Only a single extra step is needed to convert the power-series coefficients to the Padé coefficients. This extra step is solving a linear system of equations obtained by equating the two ansätze and sorting for equal powers of $\Delta\varepsilon$. If the system possesses a solution, it can be found by Alg. 6.3. If the system has no solution, the Padé approximant does not exist.

Example

As an example again the effect of perturbing the time delay τ on mode #R1 is studied. Only Padé approximations of the form $[M/M]_\omega$ are considered, i.e., both the numerator and the denominator are polynomials of degree M. Such approximants are commonly referred to as diagonal Padé approximants. There has been the conjecture that diagonal Padé approximants are convergent in almost the entire complex plane if used to approximate meromorphic functions, see, e.g., [143]. Although counter examples were found at the beginning of this century (see, e.g., [144]), as a rule of thumb these approximants are believed to yield good results. Indeed, tests with non-diagonal Padé approximants yielded worse approximation compared to those shown here. Diagonal approximants are a reasonable choice because the eigenvalue trajectory $\omega_{\#R1}(\tau)$ is expected to be bounded and diagonal Padé approximants are bounded for real-valued parameters as long as their poles – i.e., the roots of the denominator – do not lie on the real axis. Note that the trajectory of an intrinsic mode is unbounded (see Chap.10) and might require a non-diagonal Padé approximant.

Figure 6.8 shows the results of the example. In Fig. 6.8 a) the exact evolution of the eigenvalue when perturbing τ is shown together with the Padé approximants $[5,5]_\omega$, $[10,10]_\omega$, and $[15,15]_\omega$. For comparison the results obtained from thirtieth-order power series approximation ($[30,0]_\omega$) is also shown. Red squares again indicate the convergence limits. Note that the shown parameter range is larger than in Fig. 6.3 a). The parameter range in Fig. 6.8 a) is $\tau \in [0.5,5]$. Because the thirtieth-order power series approximation (red) is unbounded, it significantly deviates from the correct results after passing the convergence limit. This is why only part of the trajectory is shown. However, note how the trajectory turns the direction by about 180° at the upper convergence limit. On the contrary, the Padé approximants stay relatively close to the exact trajectory. For $[10,10]_\omega$

Algorithm 6.3: Convert power series coefficients to Padé coefficients. The pseudocode is based on the solution scheme presented in [142, Chapter 3]

function PADE($\omega_0, \ldots, \omega_{L+M}, L, M$)
  $\mathbf{A} \leftarrow \mathbf{0} \in \mathbb{C}^{M \times M}$ ▷ initialize system matrix A
  for $i \leftarrow 1, \ldots, M$ **do**
    for $j \leftarrow 1, \ldots, M$ **do**
      if $L + i - j \geq 0$ **then**
        $[\mathbf{A}]_{i,j} \leftarrow \omega_{L+i-j}$
      end if
    end for
  end for
  $b_0 \leftarrow 1$ ▷ b_0 is not an unknown but needed later
  $\begin{bmatrix} b_1 \\ \vdots \\ b_M \end{bmatrix} \leftarrow \text{SOLVE}(\mathbf{A}, -\begin{bmatrix} \omega_{L+1} \\ \vdots \\ \omega_{L+M} \end{bmatrix})$ ▷ If the system is not solvable, $\omega_{[L/M]}$ does not exist.
  for $l \leftarrow 0, \ldots, L$ **do**
    $a_l \leftarrow 0$
    for $m \leftarrow 0, \ldots, l$ **do**
      if $m \leq M$ **then**
        $a_l \leftarrow a_l + \omega_{l-m} b_m$
      end if
    end for
  end for
  return $a_0, \ldots, a_L, b_1, \ldots, b_M$
end function

(orange) and $[15,15]_\omega$ (green), no differences from the exact trajectory can be seen in Fig. 6.8 a) for values $\tau > \tau_0 = 2$. This is the case even when exceeding the convergence limit of the power series expansion. However, for lower values of τ there is a clear deviation. Although obtained from twentieth-order power series approximation, $[10,10]_\omega$ yields better estimates than the thirtieth-order power-series approximation $[30,0]_\omega$. This indicates that Padé approximation improved the convergence properties.

Figure 6.8 b) further illustrates these improvements. It compares the error evolution of even-ordered power-series approximations (o-markers) with the error evolution of the corresponding diagonal Padé approximants ($\Diamond$-markers). Converting the power series into diagonal Padé approximants clearly reduces the error.

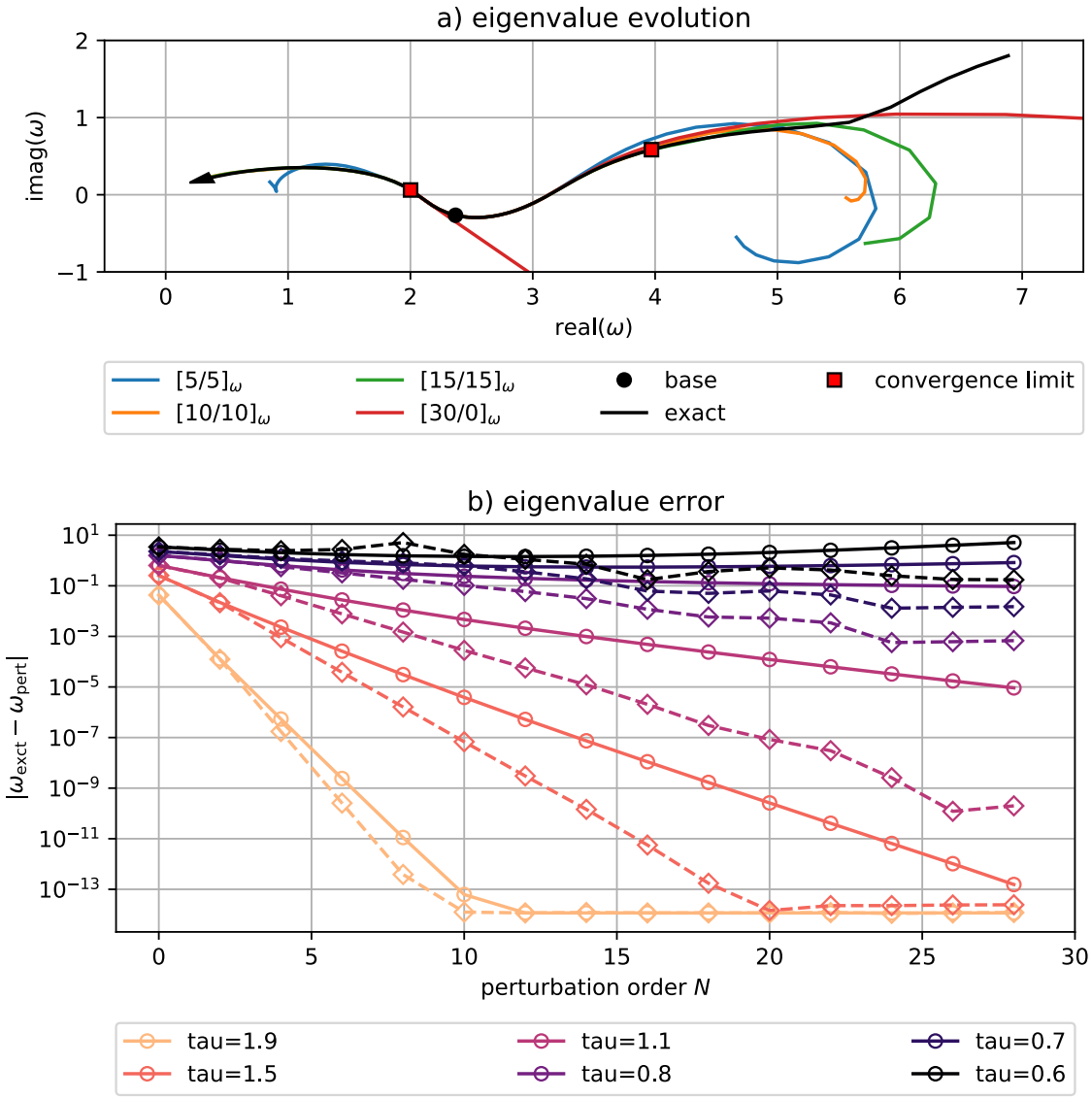

Figure 6.8: a) Exact evolution of the eigenvalue of mode #R1 and diagonal Padé approximations. For comparison the thirtieth-order power-series approximation is also shown. The diagonal Padé approximants yield better estimates than the power series approximation. This is especially true for values of τ which are outside the convergence interval of the power series.
b) Comparison of the error evolution of power series (solid lines with $\circ$-markers) and diagonal Padé approximants (dashed line with $\Diamond$ markers) of the same asymptotic order. Conversion to diagonal Padé approximants clearly improves the convergence properties.

Conclusion

Padé approximations improve the convergence of the power series at negligible extra costs. Moreover, the theory of Padé approximations and its generalizations is a rich mathematical field already utilized in other disciplines to enhance the convergence of asymptotic expansions, see, e.g., [138]. Albeit addressed only shortly here, it should, thus, be considered in more detail to improve the quality of large order perturbation theory in the future. For instance, it can be readily applied to the approximations of the mode shapes. In the remainder of this thesis more examples will demonstrate the benefits of the method.

6.6 The semi-simple degenerate case

Perturbation theory for degenerate eigenvalues is more involved. Indeed, defective eigenvalues cannot be treated with a power-series approach. This will be discussed in Chap. 10. This section focuses on the particular case of twofold degenerate semi-simple eigenvalues as they commonly arise from the symmetry of annular combustion chambers. In the considered case both the direct and the adjoint eigenspace are two-dimensional. If a perturbation of the system breaks its symmetry, the direct and the adjoint eigenspace will each unfold into two one-dimensional eigenspaces with distinct eigenvalues. These two eigensolutions will be referred to as branches 1 and 2 in the following. Of course, perturbations that retain the symmetry will not resolve the degeneracy.

If the unperturbed solution features a two-dimensional eigenspace, there are two linearly independent direct eigenfunctions $\widetilde{p}_{0,1}$ and $\widetilde{p}_{0,2}$ and two linearly independent adjoint eigenfunctions $\widetilde{p}^\dagger_{0,1}$ and $\widetilde{p}^\dagger_{0,2}$ corresponding to the same eigenvalue ω_0. Denoting them with tildes emphasizes that these basis vectors are rather arbitrary, while a possible mode unfolding would require basis vectors that span the two unfolded eigenspaces at zeroth order.

When considering the kth-order equations various scenarios are possible: an unfolding of the twofold degenerate eigenspace became apparent at a previous order or the degenerate perturbation theory has not yet predicted any unfolding. For simplicity, the discussion focuses on the special case where mode unfolding can be already seen at first order. The generalization to cases where the unfolding is revealed at higher orders or even never happens at all is straightforward. It will be shortly discussed at the end of this section.

The unfolding at first order

In order to find the correct basis vectors for the unfolding, these are expressed as linear combinations of the known but not further specified basis vectors:

$$\widehat{p}_{0,i} = z_{1,i}\,\widetilde{p}_{0,1} + z_{2,i}\,\widetilde{p}_{0,2} \tag{6.48}$$

$$\widehat{p}^\dagger_{0,i} = z^\dagger_{1,i}\,\widetilde{p}^\dagger_{0,1} + z^\dagger_{2,i}\,\widetilde{p}^\dagger_{0,2}. \tag{6.49}$$

Introducing them into the first order eigenvalue correction determining equation (6.18) and demanding solvability will then yield a linear 2×2 eigenvalue problem that not only determines the eigenvalue corrections ω_1 but also the correct bases. This section discusses the derivation of this auxiliary eigenvalue problem.

Introducing the linear combinations into (6.18) yields

$$\left\langle z_{2,i}^{\dagger}\widetilde{p}_{0,1}^{\dagger}+z_{2,i}^{\dagger}\widetilde{p}_{0,2}\middle|\mathcal{L}_{0,1}\left(z_{1,i}\widetilde{p}_{0,1}+z_{2,i}\widetilde{p}_{0,2}\right)\right\rangle+\omega_1\left\langle z_{2,i}^{\dagger}\widetilde{p}_{0,1}^{\dagger}+z_{2}^{\dagger}\widetilde{p}_{0,2}\middle|\mathcal{L}_{1,0}\left(z_{1,i}\widetilde{p}_{0,1}+z_{2,i}\widetilde{p}_{0,2}\right)\right\rangle=0 \tag{6.50}$$

$$\underbrace{\begin{bmatrix}\overline{z_{1,i}^{\dagger}} & \overline{z_{2,i}^{\dagger}}\end{bmatrix}}_{:=z_i^{\dagger}}\left(\underbrace{\begin{bmatrix}\langle\widetilde{p}_{0,1}|\mathcal{L}_{0,1}\widetilde{p}_{0,1}\rangle & \langle\widetilde{p}_{0,1}|\mathcal{L}_{0,1}\widetilde{p}_{0,2}\rangle\\ \langle\widetilde{p}_{0,2}|\mathcal{L}_{0,1}\widetilde{p}_{0,1}\rangle & \langle\widetilde{p}_{0,2}|\mathcal{L}_{0,1}\widetilde{p}_{0,2}\rangle\end{bmatrix}}_{:=\mathbf{X}}+\omega_1\underbrace{\begin{bmatrix}\langle\widetilde{p}_{0,1}|\mathcal{L}_{1,0}\widetilde{p}_{0,1}\rangle & \langle\widetilde{p}_{0,1}|\mathcal{L}_{1,0}\widetilde{p}_{0,2}\rangle\\ \langle\widetilde{p}_{0,2}|\mathcal{L}_{1,0}\widetilde{p}_{0,1}\rangle & \langle\widetilde{p}_{0,2}|\mathcal{L}_{1,0}\widetilde{p}_{0,2}\rangle\end{bmatrix}}_{:=\mathbf{Y}}\right)\underbrace{\begin{bmatrix}z_{1,i}\\ z_{2,i}\end{bmatrix}}_{z_i}=\mathbf{0}. \tag{6.51}$$

Due to the biorthonormality relation Eq. (4.12), the direct and adjoint eigenvectors can be chosen such that $\mathbf{Y}$ amounts to $\mathbf{I}$. The above equation then reduces to the following linear eigenvalue problem:

$$\mathbf{X}z+\omega_1 z_i=\mathbf{0}\qquad\text{and}\qquad\mathbf{X}^{\mathrm{H}}z^{\dagger}+\overline{\omega_1}z_i^{\dagger}=\mathbf{0}. \tag{6.52}$$

This auxiliary 2×2 eigenvalue problem determines the mode unfolding. Here, it is assumed that splitting is revealed at first order. By assumption, there will be, thus, two distinct eigentriplets $\omega_{1,1}, z_1, z_1^{\dagger}$ and $\omega_{1,2}, z_2, z_2^{\dagger}$ solving the auxiliary eigenvalue problem (6.52). Note that $\omega_{1,1}$ and $\omega_{1,2}$ denote the two eigenvalues of $\mathbf{X}$. The zeroth order approximation to the unfolded direct eigenspaces will be $\widehat{p}_{0,1}=z_{1,1}\widetilde{p}_{0,1}+z_{2,1}\widetilde{p}_{0,2}$ and $\widehat{p}_{0,2}=z_{1,2}\widetilde{p}_{0,2}+z_{2,2}\widetilde{p}_{0,2}$. Equivalently, the unfolding of the adjoint eigenspace is given at zeroth order as $\widehat{p}_{0,1}^{\dagger}=z_{1,1}^{\dagger}\widetilde{p}_{0,1}^{\dagger}+z_{2,1}^{\dagger}\widetilde{p}_{0,2}^{\dagger}$ and $\widehat{p}_{0,2}^{\dagger}=z_{1,2}\widetilde{p}_{0,2}^{\dagger}+z_{2,2}^{\dagger}\widetilde{p}_{0,2}^{\dagger}$. The new bases $\widehat{p}_{0,1}, \widehat{p}_{0,2}$ and $\widehat{p}_{0,1}^{\dagger}, \widehat{p}_{0,2}^{\dagger}$ will remain biorthonormalized with respect to $\mathcal{L}_{1,0}$ if the coefficient vectors are biorthonormalized, i.e., $z_j^{\dagger\mathrm{H}}z_i=\delta_{i,j}$. This is because then

$$\begin{aligned}\left\langle\widehat{p}_{0,j}^{\dagger}\middle|\mathcal{L}_{1,0}\widehat{p}_{0,i}\right\rangle&=\left\langle z_{1,j}^{\dagger}\widetilde{p}_{0,1}^{\dagger}+z_{2,j}^{\dagger}\widetilde{p}_{0,2}^{\dagger}\middle|\mathcal{L}_{1,0}\left(z_{1,i}\widetilde{p}_{0,i}+z_{2,i}\widetilde{p}_{0,2}\right)\right\rangle &(6.53)\\ &=\overline{z_{1,j}^{\dagger}}\underbrace{\left\langle\widetilde{p}_{0,1}^{\dagger}\middle|\mathcal{L}_{1,0}\widetilde{p}_{0,1}\right\rangle}_{=1}z_{1,i}+\overline{z_{1,j}^{\dagger}}\underbrace{\left\langle\widetilde{p}_{0,1}^{\dagger}\middle|\mathcal{L}_{1,0}\widetilde{p}_{0,2}\right\rangle}_{=0}z_{2,i}\\ &\quad+\overline{z_{2,j}^{\dagger}}\underbrace{\left\langle\widetilde{p}_{0,2}^{\dagger}\middle|\mathcal{L}_{1,0}\widetilde{p}_{0,1}\right\rangle}_{=0}z_{1,i}+\overline{z_{2,j}^{\dagger}}\underbrace{\left\langle\widetilde{p}_{0,2}^{\dagger}\middle|\mathcal{L}_{1,0}\widetilde{p}_{0,2}\right\rangle}_{=1}z_{2,i} &(6.54)\\ &=\overline{z_{1,j}^{\dagger}}z_{1,i}+\overline{z_{2,j}^{\dagger}}z_{2,i}=z_j^{\dagger\mathrm{H}}z_i=\delta_{i,j} &(6.55)\end{aligned}$$

holds.

The computed linear combinations together with the corresponding eigenvalue corrections yield a solvable right-hand side when reintroduced into the eigenvector correction determining equation (6.12):

$$\mathcal{L}_{0,0}\widetilde{p}_{1,i}=-\mathcal{L}_{0,1}\widehat{p}_{0,i}-\omega_{1,i}\mathcal{L}_{1,0}\widehat{p}_{0,i}. \tag{6.56}$$

This equation is solvable because the auxiliary eigenvalue problem guarantees that the right-hand side is orthogonal to the two-dimensional adjoint eigenspace for both branches $i=1$ and $i=2$. Again a tilde indicates ambiguity. This time, the computed eigenvector corrections $\widetilde{p}_{1,i}$ are not

unique. This is because by definition $\widehat{p}_{0,1}$ and $\widehat{p}_{0,2}$ span the kernel of $\mathcal{L}_{0,0}$. Hence, if $\widetilde{p}_{1,i}$ is a solution to (6.56), so is $\widehat{p}_{1,i} = \widetilde{p}_{1,i} + \gamma_{1,i,1}\widehat{p}_{0,1} + \gamma_{1,i,2}\widehat{p}_{0,2}\ \forall \gamma_{1,i,j} \in \mathbb{C}$. In the case of simple eigenvalues, this ambiguity was tackled by normalization. However, in the twofold degenerate, semi-simple case, there are two not one free constants to be determined. In addition to a normalization condition, a second condition is required to fully determine $\widehat{p}_{1,i}$. This second condition is the solvability of the second-order equation. In contrast to the normalization condition, it is absolutely necessary to account for this equation.

The unfolded equations

At second order the equation reads:

$$\mathcal{L}_{0,0}\widehat{p}_{2,i} = -\left[\mathcal{L}_{0,1}\widehat{p}_{1,i} + \mathcal{L}_{0,2}\widehat{p}_{0,i} + \omega_{1,i}\mathcal{L}_{1,0}\widehat{p}_{1,i} + \omega_{1,i}\mathcal{L}_{1,1}\widehat{p}_{0,i} + \omega_{1,i}^2\mathcal{L}_{2,0}\widehat{p}_{0,i}\right] - \omega_{2,i}\mathcal{L}_{1,0}\widehat{p}_{0,i} \tag{6.57}$$

which can be rearranged to

$$\begin{aligned}\mathcal{L}_{0,0}\widehat{p}_{2,i} = &-\underbrace{\left[\mathcal{L}_{0,1}\widetilde{p}_{1,i} + \mathcal{L}_{0,2}\widehat{p}_{0,i} + \omega_{1,i}\mathcal{L}_{1,0}\widetilde{p}_{1,i} + \omega_{1,i}\mathcal{L}_{1,1}\widehat{p}_{0,i} + \omega_{1,i}^2\mathcal{L}_{2,0}\widehat{p}_{0,i}\right]}_{:=\widetilde{r}_{2,i}} - \omega_{2,i}\mathcal{L}_{1,0}\widehat{p}_{0,i} \\ &- \left[\mathcal{L}_{0,1} + \omega_{1,i}\mathcal{L}_{1,0}\right]\left[\gamma_{1,i,1}\widehat{p}_{0,1} + \gamma_{1,i,2}\widehat{p}_{0,2}\right].\end{aligned} \tag{6.58}$$

Note that $\widetilde{r}_{2,i}$ is formed from $\widehat{p}_{0,i}$ and $\widetilde{p}_{0,i}$ analogously to r_2 in the simple case (see Eq. (6.13)). Solvability is given if the inner product of the right-hand side with $\widehat{p}_{0,j}^{\dagger}$ vanishes simultaneously for $j = 1$ and $j = 2$:

$$\begin{aligned}0 = &\left\langle \widehat{p}_{0,j}^{\dagger}\middle|\widetilde{r}_{2,i}\right\rangle + \omega_{2,i}\left\langle \widehat{p}_{0,j}^{\dagger}\middle|\mathcal{L}_{1,0}\widehat{p}_{0,i}\right\rangle + \gamma_{i,1}\left\langle \widehat{p}_{0,j}^{\dagger}\middle|\mathcal{L}_{0,1}\widehat{p}_{0,1}\right\rangle + \gamma_{1,i,1}\omega_{1,i}\left\langle \widehat{p}_{0,j}^{\dagger}\middle|\mathcal{L}_{1,0}\widehat{p}_{0,1}\right\rangle \\ &+ \gamma_{i,2}\left\langle \widehat{p}_{0,j}^{\dagger}\middle|\mathcal{L}_{0,1}\widehat{p}_{0,2}\right\rangle + \gamma_{1,i,2}\omega_{1,i}\left\langle \widehat{p}_{0,j}^{\dagger}\middle|\mathcal{L}_{1,0}\widehat{p}_{0,2}\right\rangle.\end{aligned} \tag{6.59}$$

Because of the biorthonormalization $\left\langle \widehat{p}_{0,j}^{\dagger}\middle|\mathcal{L}_{1,0}\widehat{p}_{0,i}\right\rangle = \delta_{i,j}$. Moreover, $\widehat{p}_{0,i}$ and $\widehat{p}_{0,j}^{\dagger}$ are the specialized basis vectors that diagonalize the auxiliary eigenvalue problem (6.52). Hence, $\left\langle \widehat{p}_{0,j}^{\dagger}\middle|\mathcal{L}_{0,1}\widehat{p}_{0,i}\right\rangle = -\omega_{1,i}\delta_{i,j}$. Without loss of generality, it can be assumed that $i = 1$. Setting j to 2 then reduces (6.59) to

$$0 = \left\langle \widehat{p}_{0,2}^{\dagger}\middle|\widetilde{r}_{2,1}\right\rangle - \gamma_{1,1,2}\omega_{1,2} + \gamma_{1,1,2}\omega_{1,1}. \tag{6.60}$$

Provided that the first order equation has been solved already, there is no unknown except for $\gamma_{1,1,2}$ in (6.60). Solving for the unknown coefficient yields

$$\gamma_{1,1,2} = \frac{\left\langle \widehat{p}_{0,j}^{\dagger}\middle|\widetilde{r}_{2,i}\right\rangle}{\omega_{1,2} - \omega_{1,1}}. \tag{6.61}$$

Note that this is a cross-branch relation because the first-order eigenvalue sensitivity $\omega_{1,2}$ from branch 2 is needed to determine the coefficient $\gamma_{1,1,2}$ from branch 1.

On the other hand, setting $i = 1$ and $j = 1$ results in

$$0 = \left\langle \widehat{p}_{0,1}^{\dagger} \middle| \widetilde{r}_{2,1} \right\rangle + \omega_{2,1} \underbrace{-\gamma_{1,1,1}\omega_{1,1} + \gamma_{1,1,1}\omega_{1,1}}_{=0}. \tag{6.62}$$

It allows for computing the second-order eigenvalue sensitivity for branch 1:

$$\omega_{2,1} = -\left\langle \widehat{p}_{0,1}^{\dagger} \middle| \widetilde{r}_{2,1} \right\rangle. \tag{6.63}$$

No condition for $\gamma_{1,1,1}$ has been obtained. However, the normalization strategies discussed in Sec. 6.2 can be used to determine it. Equivalent results are obtained for branch 2. Moreover, the scheme repeats at each order $k > 1$. This is because the eigenvector determining equation at kth order can be written as

$$\mathcal{L}_{0,0}\widehat{p}_{k,i} = -\widetilde{r}_{k,i} - \omega_k \mathcal{L}_{1,0}\widehat{p}_{0,i} - \left[\mathcal{L}_{0,1} + \omega_{1,i}\mathcal{L}_{1,0}\right]\left[\gamma_{k-1,i,1}\widehat{p}_{0,1} + \gamma_{k-1,i,2}\widehat{p}_{0,2}\right]. \tag{6.64}$$

This result can be readily obtained from the definition of r_k in Eq. (6.13).

For $i \neq j$ a cross-branch relation determines the content of $\widehat{p}_{0,j}$ in $\widehat{p}_{k-1,i}$

$$\gamma_{k-1,i,j} = \frac{\left\langle \widehat{p}_{0,j}^{\dagger} \middle| \widetilde{r}_{k,i} \right\rangle}{\omega_{1,j} - \omega_{1,i}}, \tag{6.65}$$

while the remaining solvability condition determines the kth-order eigenvalue sensitivity

$$\omega_{k,i} = -\left\langle \widehat{p}_{0,i}^{\dagger} \middle| \widetilde{r}_{k,i} \right\rangle. \tag{6.66}$$

Pseudocode for a degenerate algorithm

Algorithm 6.4 sketches an implementation of a twofold degenerate algorithm assuming first-order splits. The algorithm assumes that the computed but not specialized bases $\widetilde{\boldsymbol{p}}_{0,1}$, $\widetilde{\boldsymbol{p}}_{0,2}$ and $\widetilde{\boldsymbol{p}}_{0,1}^{\dagger}$, $\widetilde{\boldsymbol{p}}_{0,2}^{\dagger}$ are already biorthonormalized. While the correct determination of $\widehat{p}_{k,i}$ requires the computation of $\gamma_{k,i,j}$, $\gamma_{k,i,j}$ is obtained at order $k+1$. Therefore, the algorithm returns eigenvalue sensitivities $\omega_{k,i}$ up to order N but the mode shape sensitivities only up to order $N-1$.

Splittings at orders $s \neq 1$

The theory can be generalized to cases where the split is not revealed at first order. In these cases auxiliary eigenvalue problems will arise at higher orders until their solutions yield two distinct eigenvalues and splitting is, thus, detected. The procedure is then almost identical to that presented for a first-order split. The main difference will be that the contribution from the adjoint eigenfunction $\widehat{p}_{0,j}^{\dagger}$ from the cross branch j to the eigenvector sensitivity $\widehat{p}_{k,i}$ of the branch i will be determined at much higher orders. More precisely, if s is the order at which the splitting was revealed, then the cross coefficients are determined by

$$\gamma_{k-s,i,j} = \frac{\left\langle \widehat{p}_{0,j}^{\dagger} \middle| \widetilde{r}_{k,i} \right\rangle}{\omega_{s,j} - \omega_{s,i}}. \tag{6.67}$$

Algorithm 6.4: Twofold degenerate perturbation theory assuming a first order-split. The algorithm also assumes that direct and adjoint eigenvectors are already biorthogonalized, i.e., $\boldsymbol{p}_{0,j}^\dagger \mathsf{L}_{1,0} \boldsymbol{p}_{0,i} = \delta_{i,j}$.

function PERTURB2($\mathsf{L}_{m,n}, \boldsymbol{p}_{0,1}, \boldsymbol{p}_{0,2}, \boldsymbol{p}_{0,1}^\dagger, \boldsymbol{p}_{0,2}^\dagger, N$)
  $\mathbf{X} \leftarrow -\begin{bmatrix} \left\langle \boldsymbol{p}_{0,1}^\dagger \middle| \mathsf{L}_{0,1} \boldsymbol{p}_{0,1} \right\rangle & \left\langle \boldsymbol{p}_{0,1}^\dagger \middle| \mathsf{L}_{0,1} \boldsymbol{p}_{0,2} \right\rangle \\ \left\langle \boldsymbol{p}_{0,2}^\dagger \middle| \mathsf{L}_{0,1} \boldsymbol{p}_{0,1} \right\rangle & \left\langle \boldsymbol{p}_{0,2}^\dagger \middle| \mathsf{L}_{0,1} \boldsymbol{p}_{0,2} \right\rangle \end{bmatrix}$
  $\boldsymbol{\Omega}, \mathbf{Z}, \mathbf{Z}^\dagger \leftarrow \mathrm{EIG}(\mathbf{X})$
  biorthonormalize coefficients $z_{i,j}$ such that $\mathbf{Z}^{\dagger \mathrm{H}} \mathbf{Z} = \mathbf{I}$
  $\begin{bmatrix} \boldsymbol{p}_{0,1} & \boldsymbol{p}_{0,2} \end{bmatrix} \leftarrow \begin{bmatrix} \boldsymbol{p}_{0,1} & \boldsymbol{p}_{0,2} \end{bmatrix} \mathbf{Z}$
  $\begin{bmatrix} \boldsymbol{p}_{0,1}^\dagger & \boldsymbol{p}_{0,2}^\dagger \end{bmatrix} \leftarrow \begin{bmatrix} \boldsymbol{p}_{0,1}^\dagger & \boldsymbol{p}_{0,2}^\dagger \end{bmatrix} \mathbf{Z}^\dagger$
  $\omega_{1,1} \leftarrow [\boldsymbol{\Omega}]_{1,1}$
  $\omega_{1,2} \leftarrow [\boldsymbol{\Omega}]_{2,2}$
  for $i \leftarrow 1,2$ **do**
    $\boldsymbol{p}_{1,i} \leftarrow \mathrm{SOLVE}(\mathsf{L}_{0,0}, -\mathsf{L}_{0,1} \boldsymbol{p}_{0,i} - \omega_{1,i} \mathsf{L}_{1,0} \boldsymbol{p}_{0,i})$
  end for
  for $k \leftarrow 2, \ldots, N$ **do**
    for $i \leftarrow 1,2$ **do**
      $j \leftarrow 2$ **if** $i = 1$ **else** $j \leftarrow 1$
      assemble $\boldsymbol{r}_{k,i}$ ▷ see Alg. 6.2 for how to do it
      $\gamma_{k-1,i,j} \leftarrow \left\langle \boldsymbol{p}_{0,j} \middle| \boldsymbol{r}_{k,i} \right\rangle / (\omega_{1,j} - \omega_{1,i})$
      $\boldsymbol{p}_{k-1,i} \leftarrow \boldsymbol{p}_{k-1,i} + \gamma_{k-1,i,j} \boldsymbol{p}_{0,j}$
      $\boldsymbol{r}_{k,i} \leftarrow \boldsymbol{r}_{k,i} + \gamma_{k-1,i,j} \left(\mathsf{L}_{0,1} + \omega_{1,i} \mathsf{L}_{1,0} \right) \boldsymbol{p}_{0,j}$
      $\omega_{k,i} \leftarrow -\left\langle \boldsymbol{p}_{0,i}^\dagger \middle| \boldsymbol{r}_{k,i} \right\rangle$
      $\boldsymbol{p}_{k,i} \leftarrow \mathrm{SOLVE}(\mathsf{L}_{0,0}, -\boldsymbol{r}_{k,i} - \omega_{k,i} \mathsf{L}_{1,0} \boldsymbol{p}_{0,i})$
    end for
  end for
  return $\omega_{1,1}, \ldots, \omega_{N,1}, \omega_{1,2}, \ldots, \omega_{N,2}, \boldsymbol{p}_{0,1}, \ldots, \boldsymbol{p}_{N-1,1}, \boldsymbol{p}_{0,2}, \ldots, \boldsymbol{p}_{N-1,2}$
end function

For the special case of non-degeneracy-breaking perturbations, only the first-order auxiliary eigenvalue problem needs to be solved. The two basis vectors $\widehat{p}_{0,i}$ and $\widehat{p}_{0,j}^\dagger$ will diagonalize the auxiliary eigenvalue problems at each order. Thus, after solving the first-order auxiliary eigenvalue problem the branches can be treated as if there would be simple. For instance, if the considered system features a reflection symmetry and a discrete rotational symmetry, the unperturbed basis vectors could be chosen to be Bloch waves with Bloch wavenumbers of opposite sign (Eq. (5.33)). If the perturbation does not break the symmetries, then these vectors are also the basis vectors that diagonalize the auxiliary eigenvalue problem (6.52). This is because by assumption all Taylor coefficients $\mathcal{L}_{m,n}$ of the operator family $\mathcal{L}(z;\varepsilon)$ will feature the same symmetry properties as the unperturbed problem (otherwise the perturbation would be symmetry breaking). Because applying a discrete rotation operator to a Bloch wave will result in a Bloch wave of the same Bloch wavenumber (Eq. (5.22)) and Bloch waves of independent Bloch wavenumbers are pairwise or-

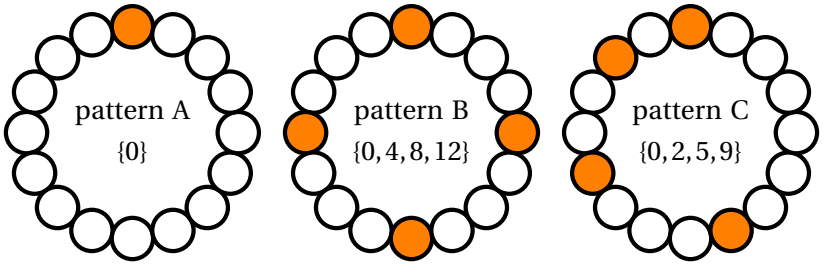

Figure 6.9: Considered perturbation patterns

thogonal (Eq. (5.30)),

$$\mathbf{X} = \begin{bmatrix} \left\langle \widehat{p}^{\dagger}_{0,\tilde{b}} \middle| \mathbf{L}_{0,1} \widehat{p}_{0,\tilde{b}} \right\rangle & \left\langle \widehat{p}^{\dagger}_{0,\tilde{b}} \middle| \mathbf{L}_{0,1} \widehat{p}_{0,\widetilde{-b}} \right\rangle \\ \left\langle \widehat{p}^{\dagger}_{0,\widetilde{-b}} \middle| \mathbf{L}_{0,1} \widehat{p}_{0,\tilde{b}} \right\rangle & \left\langle \widehat{p}^{\dagger}_{0,\widetilde{-b}} \middle| \mathbf{L}_{0,1} \widehat{p}_{0,\widetilde{-b}} \right\rangle \end{bmatrix} \tag{6.68}$$

will be diagonal. Forming $\widetilde{r}_{k,\tilde{b}}$ at higher orders for the two (Bloch-wave) branches will then result in Bloch waves of the same Bloch wavenumber. Due to orthogonality of the Bloch waves, the cross-branch relation will satisfy

$$\gamma_{k-1,\tilde{b},\widetilde{-b}} = \frac{\left\langle \widehat{p}^{\dagger}_{0,\widetilde{-b}} \middle| \widetilde{r}_{k,\tilde{b}} \right\rangle}{\omega_{1,\widetilde{-b}} - \omega_{1,\tilde{b}}} = 0, \tag{6.69}$$

although, $\omega_{1,\widetilde{-b}} - \omega_{1,\tilde{b}} = 0$. Thus, there will not be any cross-branch influence after the degenerate space has been decomposed into Bloch waves. This viewpoint could also be proven by considering the two surrogate systems $\mathcal{L}_{\mathrm{Bloch}}(z;\varepsilon,b)$ and $\mathcal{L}_{\mathrm{Bloch}}(z;\varepsilon,-b)$ because they feature independent simple eigenvalue trajectories that evolve identically.

6.7 Symmetry breaking in the MICCA combustor

A main motivation for the introduction of perturbation theory in this work was to utilize the benefits of the Bloch-wave theory discussed in Chap. 5 even if the system is slightly asymmetric. This section studies perturbations of the MICCA model which may break its discrete rotational symmetry. The section, therefore, demonstrates how to combine Bloch-wave and perturbation theory.

Symmetry breaking in annular combustors has been investigated recently in various experimental and theoretical studies, see, e.g., [145, 114, 146, 147]. The perturbation theory presented in this section will prove as a powerful tool to extend the understanding of symmetry breaking in such combustors.

An increase of the gains of a subset of the 16 flame transfer functions is considered as a perturbation. Three different patterns are studied. They are illustrated in Fig. 6.9. Pattern A affects the gain of one flame transfer function only. It will, thus, break the discrete rotational symmetry B of the system, i.e., B reduces to $B = 1$. Pattern B identically modifies the flame transfer functions of four burners which are equidistantly distributed along the circumference. This pattern will, therefore, reduce the degree of discrete rotational symmetry from $B = 16$ to $B = 4$. Pattern C also modifies four flame transfer functions; however, not only the discrete rotational symmetry of the system will be completely lost ($B = 1$) but there also will not be any reflection symmetry.

To implement the perturbation, a factor ε is multiplied to each of the affected flame transfer functions:

$$\mathbf{L}(z;\varepsilon) = \mathbf{K} + z\mathbf{B} + z^2\mathbf{M} + \sum_{i \notin \text{pattern}} \text{FTF}(z)\mathbf{F}_i + \varepsilon \sum_{i \in \text{pattern}} \text{FTF}(z)\mathbf{F}_i. \tag{6.70}$$

Here $\mathbf{F}_i$ denotes the discretization matrix from the flame response of the 16 burners $i = 0,\dots,15$. Setting $\varepsilon_0 = 1$ is equivalent to the unperturbed MICCA model and varying ε will then simultaneously modify the flame transfer functions of the considered burners.

Figure 6.10 shows the exact evolution of the two eigenvalue branches together with results obtained from power series truncated at first, second, fifth, and tenth order when applying the three patterns to the the modes #M0, #M1, and #M2. Mode #M0 is not degenerate. Hence, there is only one eigenvalue branch. Non-degenerate perturbation theory is used to approximate its evolution. The characteristics are the same as those found for the Rijke-tube model in Sec. 6.4: for all three patterns the plots indicate the convergence limit at $\varepsilon \approx 1$. Up to this value the truncated power series yield better results, the higher the truncation order is. For higher values of ε the power series significantly diverge from the exact trajectory of the eigenvalue. Note that the inclination of the trajectories at $\varepsilon = \varepsilon_0$ is identical for all three considered patterns. This is not a coincidence, as will be proven at the end of this section. However, the patterns B and C have nearly identical effects on the eigenvalue of mode #M0. The reason for this is unclear but seems to be a peculiarity of this specific configuration.

Mode #M1 is a first order azimuthal mode and, thus, twofold degenerate. The semi-simple degenerate perturbation theory is correctly predicting the quality of a possible mode unfolding: application of pattern A to #M1 results in two independent branches. One is deviating the farther from the baseline eigenvalue, the stronger the perturbation is. The other branch is constant and remains at the baseline eigenvalue independently of variations of ε. The latter branch arises because a nodal line of the velocity fluctuation – the derivative of the mode shape – is aligning with the perturbed burner. Hence, the flame transfer function is not excited and this flame is not contributing to the mode. For symmetry reasons the remaining branch must feature a nodal line which is aligned with the burner. The derivative of the mode shape will, therefore, be extremal and an effect of the burner on the eigenfrequency will result. When applying pattern B to mode #M1 the degree of discrete rotational symmetry is reduced to $B = 4$. A first order azimuthal mode, consequently, remains degenerate. This is because the azimuthal mode order m satisfies $(2m) \bmod B = 2 \bmod 4 = 2 \neq 0$ (see the comments on Bloch waves and azimuthal mode orders in Sec. 5.1 and Eq. (5.34)). Pattern C completely breaks the symmetries of the system and it is impossible for the nodal line to align with all four perturbed burners simultaneously. Thus, the mode unfolds into two branches that evolve independently as ε is varied. As for #M0, the inclination of the trajectories at $\varepsilon = \varepsilon_0$ is independent of the applied patterns. Note that the convergence limits of the two branches are different.

Equivalently to mode #M1, pattern A triggers mode #M2 to split into a varying and a constant branch. Again the reason is that a nodal line aligns with the single perturbed burner. However, #M2 is a second-order azimuthal mode and, therefore, features two nodal lines that are mutually perpendicular. Thus, when pattern B is applied, the two nodal lines can align with all four perturbed burners. As a consequence, one branch will remain constant again while the other will be affected by the perturbation. This loss of degeneracy is due to the reduction of the degree of discrete rotational symmetry ($(2m) \bmod B = 4 \bmod 4 = 0$). Pattern C does not allow the nodal lines

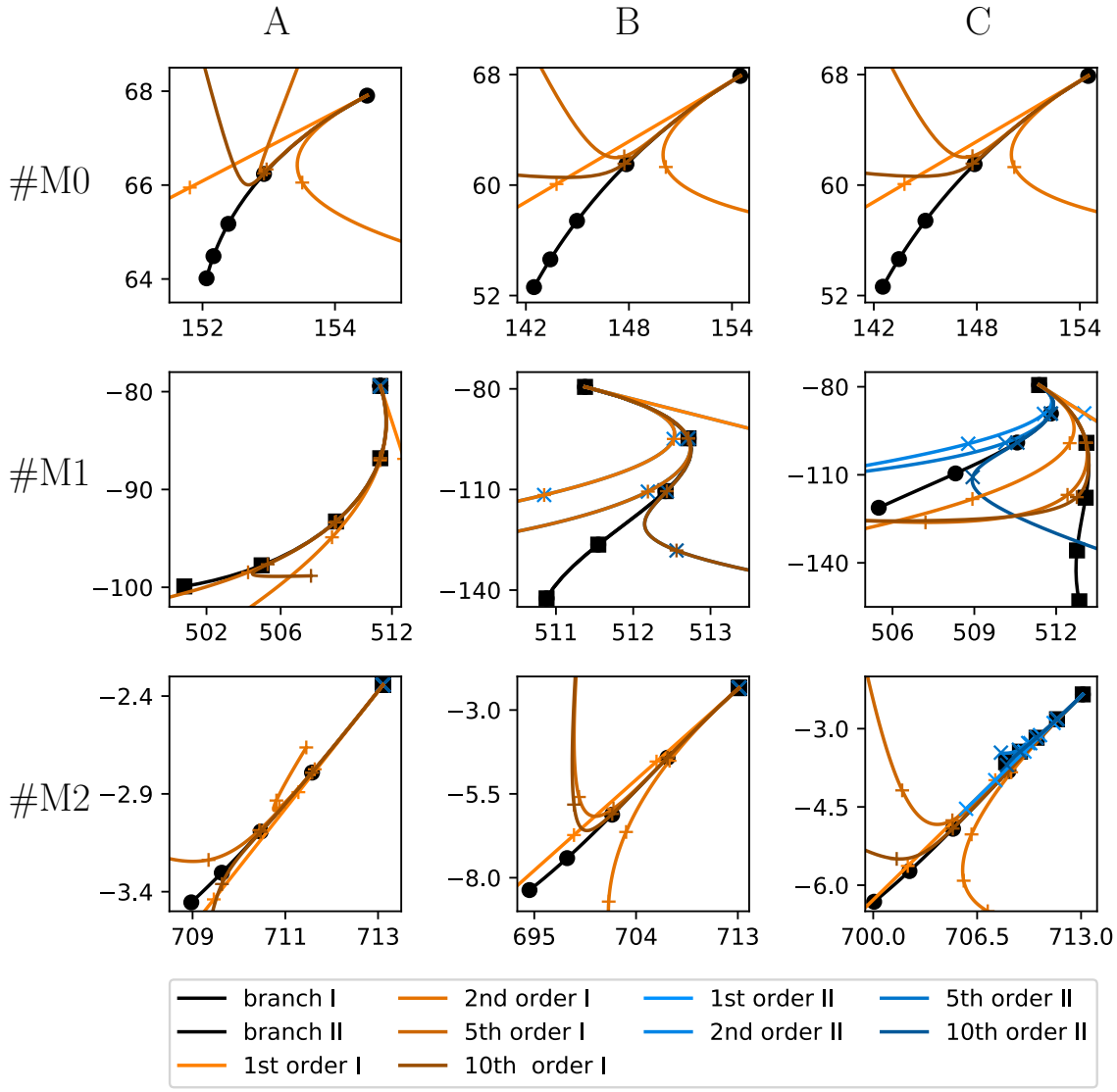

Figure 6.10: Exact and approximated eigenvalue trajectories of the modes #M0, #M1, and #M2 when applying the patterns A, B, and C. The modes #M1 and #M2 are semi-simple degenerate and, thus, feature two branches. The x-axes and y-axes denote the real and the imaginary part of $\omega/2\pi$, respectively. The exact evolution is highlighted by black lines with ●-markers (branch I) and ■-markers (branch II). The approximations are indicated by orange lines with +-markers (branch I) and blue lines with ×-markers (branch II) of different shading. The markers denote values ε of 1, 2, 3, 4, and 5. No + and × markers are plotted for $\varepsilon = \varepsilon_0 = 1$. Degenerate perturbation theory correctly predicts a possible mode unfolding. Up to a case-dependent limit value the results from perturbation theory agree the better with the exact trajectory the higher the perturbation order is. Note that the inclination of the first order prediction is independent of the perturbation patterns.

to align with all burners simultaneously. Note that exactly as with the modes #M0 and #M1, the inclinations of the trajectories at $\varepsilon = \varepsilon_0$ do not depend on the applied patterns.

Padé approximants

Because the power series coefficients $\omega_{k,1}$ and $\omega_{k,2}$ of the two branches are independent, obtaining Padé approximants from them is not different from the simple case. Indeed, using the tenth-order coefficient to compute diagonal Padé approximants yields significantly better results. They are shown in Fig. 6.11. For all tested cases the approximants agree well with the exact evolution of the complex eigenfrequency. Considering that the gain of the perturbed burners is increased up to a factor of 5, the results definitely satisfy the requirements encountered in practical applications. From an academic perspective it remains an interesting question up to which limit accurate results might be obtained from Padé approximation. This is, however, beyond the scope of the thesis.

The inclination rule

For all considered cases the inclination of the trajectories at $\varepsilon = \varepsilon_0$ is only dependent on the mode but not the chosen perturbation pattern. The reason for this is the high symmetry of the combustor. The discrete rotational symmetry and the reflection symmetry allow to span the direct and the adjoint unperturbed degenerate eigenspace by two Bloch wavenumbers of opposite sign. In general, the entries of the auxiliary eigenvalue problem (6.52) are given by

$$\left\langle \widehat{p}^{\dagger}_{0,\widetilde{\beta}} \middle| \sum_{l\in\text{pat.}} \underbrace{\text{FTF}(z)\mathcal{F}_l}_{\mathcal{Q}_l} \widehat{p}_{0,\widetilde{b}} \right\rangle = \sum_{l\in\text{pat.}} \left\langle \widehat{p}^{\dagger}_{0,\widetilde{\beta}} \middle| \mathcal{Q}_l \widehat{p}_{0,\widetilde{b}} \right\rangle = \sum_{l\in\text{pat.}} \left\langle \widehat{p}^{\dagger}_{0,\widetilde{\beta}} \exp(\mathrm{i}\beta\Delta\varphi l) \middle| \mathcal{Q}_0 \widehat{p}_{0,\widetilde{b}} \exp(\mathrm{i}b\Delta\varphi l) \right\rangle \tag{6.71}$$

$$= \left\langle \widehat{p}^{\dagger}_{0,\widetilde{\beta}} \middle| \mathcal{Q}_0 \widehat{p}_{0,\widetilde{b}} \right\rangle \sum_{l\in\text{pat.}} \exp(\mathrm{i}[b-\beta]\Delta\varphi l). \tag{6.72}$$

These equations utilize Bloch periodicity and the fact that the perturbed burners are manipulated in the same manner. There is only one branch in case of a simple eigenvalue and, hence, $b = \beta$. This implies

$$\left\langle \widehat{p}^{\dagger}_{0,\widetilde{\beta}} \middle| \mathcal{Q}_0 \widehat{p}_{0,\widetilde{b}} \right\rangle \sum_{l\in\text{pat.}} \exp(\mathrm{i}[b-\beta]\Delta\varphi l) = \left\langle \widehat{p}^{\dagger}_{0,\widetilde{\beta}} \middle| \mathcal{Q}_0 \widehat{p}_{0,\widetilde{b}} \right\rangle \sum_{l\in\text{pat.}} 1. \tag{6.73}$$

The first order sensitivity will, thus, feature the phase angle of $\left\langle \widehat{p}^{\dagger}_{0,\widetilde{\beta}} \middle| \mathcal{Q}_0 \widehat{p}_{0,\widetilde{b}} \right\rangle$ independently of the applied perturbation pattern. It is the phase angle of the first-order sensitivity that determines the inclination of the eigenvalue trajectory at $\varepsilon = \varepsilon_0$. Consequently, the inclination is independent of the applied pattern. In the semi-simple degenerate case the auxiliary matrix $\mathbf{X}$ becomes

$$\mathbf{X} = \begin{bmatrix} \left\langle \widehat{p}^{\dagger}_{0,\widetilde{b}} \middle| \mathcal{L}_{0,1} \widehat{p}_{0,\widetilde{b}} \right\rangle & \left\langle \widehat{p}^{\dagger}_{0,\widetilde{b}} \middle| \mathcal{L}_{0,1} \widehat{p}_{0,\widetilde{-b}} \right\rangle \\ \left\langle \widehat{p}^{\dagger}_{0,\widetilde{-b}} \middle| \mathcal{L}_{0,1} \widehat{p}_{0,\widetilde{b}} \right\rangle & \left\langle \widehat{p}^{\dagger}_{0,\widetilde{-b}} \middle| \mathcal{L}_{0,1} \widehat{p}_{0,\widetilde{-b}} \right\rangle \end{bmatrix}$$

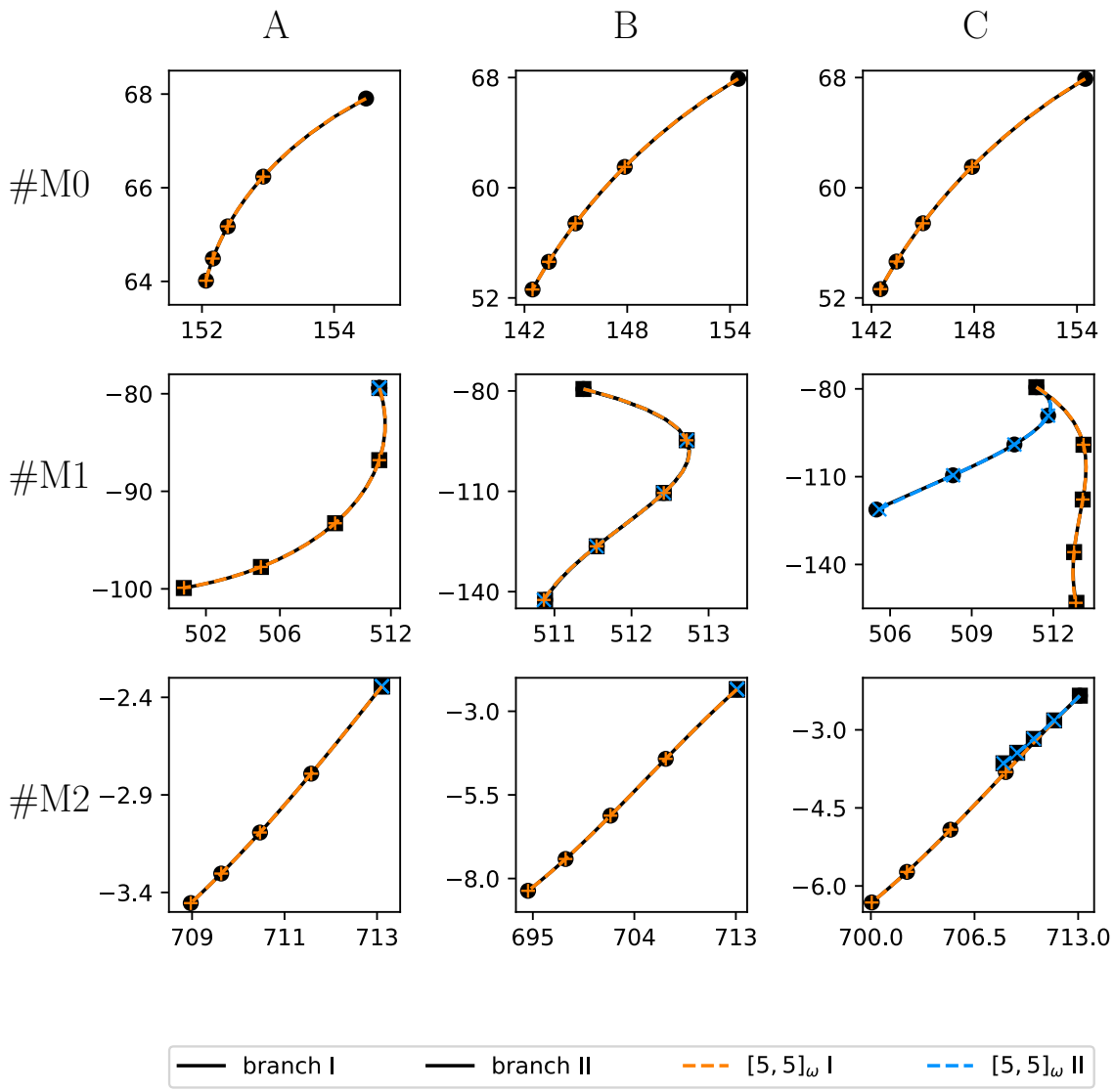

Figure 6.11: The symmetry breaking study of the MICCA model using Padé approximation. The axes, markers, and colors correspond to those in Fig. 6.10. The Padé approach clearly satisfies the requirements of a fast practical design tool.

$$= \left\langle \widehat{p}^{\dagger}_{0,\widetilde{\beta}} \middle| \mathcal{Q}_0 \widehat{p}_{0,\widetilde{b}} \right\rangle \underbrace{\sum_{l \in \text{pat.}} \begin{bmatrix} 1 & \exp(-\mathrm{i}2b\Delta\varphi l) \\ \exp(\mathrm{i}2b\Delta\varphi l) & 1 \end{bmatrix}}_{:=\Xi}. \tag{6.74}$$

Ξ is a Hermitian matrix. Its eigenvalues are, thus, real. They feature equal phases modulo a phase shift of π due to possibly different signs of the eigenvalues. $\mathbf{X}$ is a multiple of Ξ by the factor of $\left\langle \widehat{p}^{\dagger}_{0,\widetilde{b}} \middle| \mathcal{Q}_0 \widehat{p}_{0,\widetilde{b}} \right\rangle$. For this reason, the eigenvalues of $\mathbf{X}$ also share the phase of $\left\langle \widehat{p}^{\dagger}_{0,\widetilde{b}} \middle| \mathcal{Q}_0 \widehat{p}_{0,\widetilde{b}} \right\rangle$. Analogous to the simple case, this phase is independent of the applied perturbation pattern and determines the inclination of the eigenvalue trajectories at $\varepsilon = \varepsilon_0$. This concludes the proof that the inclination is only dependent on the mode but not the deployed pattern. The Bloch wavenumber can be chosen to the azimuthal mode order of the considered mode. Hence, $\sum_{n \in \text{per.}} \exp(\mathrm{i}2bn\frac{2\pi}{N})$ is the second coefficient of the Fourier transform of the burner arrangement pattern. Thus, the above first-order splitting theory has analogies with the so called C_{2n}-criterion presented in [114].

The inclination rule can be specialized to design a perturbation such that the two unfolding eigenvalues will evolve in opposite directions. This is the case when not only the gains of some burners are increased but also the gains of the other burners are decreased such that on average there is no change in the gain of all burners. The problem then reads

$$\mathcal{L}(z,\varepsilon) = \mathcal{W}(z) + \varepsilon \sum_{l \in \text{pat.}} \mathcal{Q}_l + \left(\frac{B + N_{\text{pert.}}}{B} - \varepsilon \frac{N_{\text{pert.}}}{B} \right) \sum_{l \notin \text{pat.}} \mathcal{Q}_l. \tag{6.75}$$

Where $\mathcal{W}$ is the part of L unaffected by the perturbation – i.e., the wave operator – N_{pert} is the number of burners in the set pert. and B the degree of rotational symmetry. The auxiliary matrix then amounts to

$$\mathbf{X} = \left\langle \widehat{p}^{\dagger}_{0,\widetilde{\beta}} \middle| \mathcal{Q}_0 \widehat{p}_{0,\widetilde{b}} \right\rangle \underbrace{\begin{bmatrix} 0 & 1 \\ 1 & 0 \end{bmatrix}}_{\Xi}. \tag{6.76}$$

The eigenvalues of Ξ are 1 and -1. First order sensitivity analysis will, therefore, predict a split of a twofold semi-simple degenerate eigenvalue in opposite directions in the complex plane. This means that such a perturbation would not further stabilize a combustor because if the imaginary part of one branch decreases, the imaginary part of the other part increases by the same amount. This complements the findings of [148]. This study considered a combustor with two types of flames but constant global power. It was shown that, in a weakly coupled, linear limit, when considering arbitrary patterns to arrange the two flame types, the most stable configuration is the one that consists of a single type of flames. Figure 6.12 shows the eigenvalue trajectories if perturbation pattern C is applied but the gain of the 12 originally unchanged burners is decreased such that the average gain of all burners remains constant. Indeed, the first order sensitivity predicts a split of the eigenvalue in opposite directions. However, for very large perturbations $\varepsilon = 5$ both branches feature imaginary parts which are less than the imaginary part of the unperturbed eigenvalue. This cannot be predicted by a first order theory. As compared to the previous cases also the tenth-order diagonal Padé approximants do not accurately predict the exact trajectories. This is because the considered perturbation is stronger as it also decreases the gain of some burners to keep the average gain constant. Higher order Padé approximants may yield better results but this is beyond the scope of the thesis and left for future work.

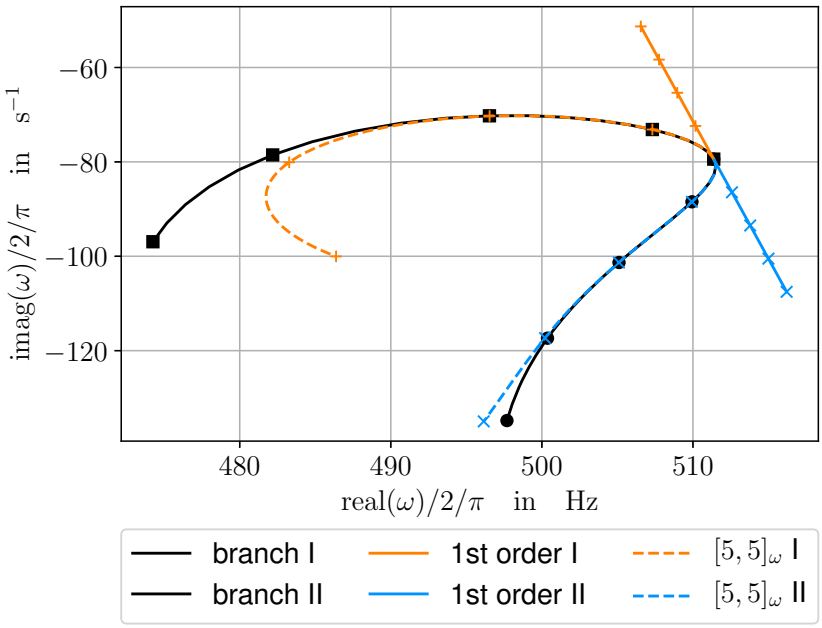

Figure 6.12: Eigenvalue trajectories of mode #M1 when pattern C is applied but the gain of the remaining burners is decreased such that on average there is no change in the gain of all burners. As predicted the eigenvalues split at first order in opposite directions but with equal strength. For small perturbations it is, thus, impossible to stabilize a combustor by such a perturbation. This generalizes the statement given in [148]. However, for strong perturbations the eigenvalue drifts do not adhere to this linear rule. Indeed, for the shown test case at $\varepsilon = 5$, the imaginary part of both trajectories is less than the imaginary part of the unperturbed eigenvalue. This behavior can be captured by high-order perturbation theory. In contrast to the cases studied before, the tenth-order Padé approximant is not fully capturing the exact trajectory. This can be attributed to the stronger perturbation as now all burners are perturbed. Surely, larger order would improve the approximant. However, this is not relevant for practical purposes.

6.8 Conclusions

Adjoint-based perturbation theory to approximate the solutions of the thermoacoustic eigenvalue problem has been presented. It was discussed how to implement the theory into a modern numerical framework. As exemplified with the Rijke-tube model, the theory can be used to study perturbations of arbitrary modeling paramaters. If singularities in the dependence of the eigenfrequency on these parameters limit the convergence of the power series, Padé approximations may serve as a remedy.

The perturbation theory also accurately predicts the evolution of eigenvalues that split due to a loss of symmetry. This was demonstrated for the MICCA model. When combined with a Bloch-wave approach to compute solutions for the symmetric baseline configuration, the theory constitutes a powerful tool for efficient computation of thermoacoustic modes in annular combustors. Combination with Bloch-wave theory also allows to establish fundamental insight in how eigenvalues split in the course of symmetry loss. For instance, the presented inclination rule clarifies, how the spatial pattern of a perturbation affects the combustor stability at first order.

Although the discussion covered both simple and semi-simple eigenvalues, the theory is not suited for expansions starting from defective eigenvalues. This aspect will be further discussed in Chap. 10. Nevertheless, there is a multitude of applications for perturbation theory. These will be discussed in the next chapters.

Chapter 7

Computation of limit cycles in annular combustors

The previous chapters focused on solving the thermoacoustic Helmholtz equation. This equation comprises only linear operators and the eigenvalue problem arising from it is linear with respect to the mode shape, i.e., the complex pressure fluctuation amplitude. While such linear models estimate the frequency of the mode to an adequate degree [37], they cannot model any nonlinear saturation effects. This issue is addressed by flame describing functions. In comparison to flame transfer functions, flame describing functions also account for the amplitude of the mode when modeling the flame response [37, 38]:

$$\frac{\widehat{q}}{\widehat{q}_0} = \mathrm{FDF}(\omega, a)\frac{\widehat{u}_{\mathrm{ref}}}{u_0}. \tag{7.1}$$

The ratio $a := \frac{u'_{\mathrm{ref}}}{u_0}$ is called the amplitude level. Because $u'_{\mathrm{ref}} \propto \nabla\widehat{p}\big|_{\mathrm{ref}} \cdot \vec{n}_{\mathrm{ref}}$, the eigenvalue problem at hand will then also be nonlinear with respect to the eigenvector. This will be denoted as:

$$\mathcal{N}(\omega, \widehat{p}) = 0. \tag{7.2}$$

This chapter discusses how to efficiently solve the eigenvalue problem (7.2) using both Bloch-wave and perturbation theory. The content has been partly published in [149].

7.1 Introduction to the computations of limit-cycle amplitudes

In the case of a single burner, the eigenvalue problem (7.2) is "almost" linear in $\widehat{p}$. This is because for a given amplitude level the flame describing functions reduce to flame transfer functions. Therefore, a thermoacoustic Helmholtz equation

$$\mathcal{L}(\omega, a)\widehat{p} = 0 \tag{7.3}$$

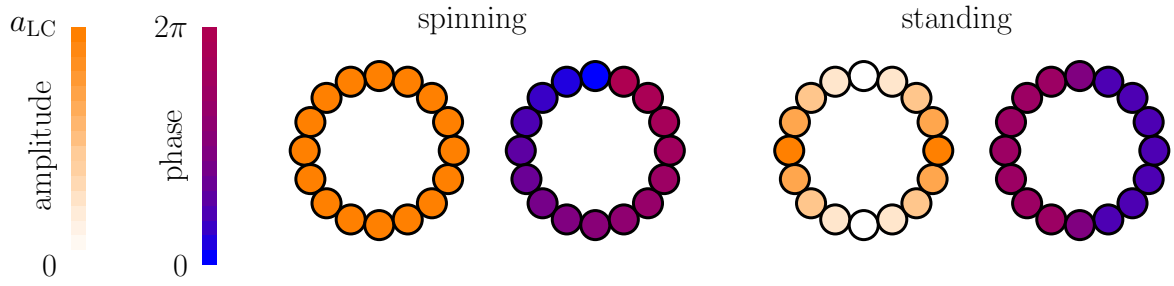

Figure 7.1: Illustration of amplitude and phase of spinning and standing modes. While spinning modes feature an equal amplitude and a different phase in the various unit cells, the amplitudes in the unit cells of standing modes vary and are perfectly in phase or antiphase to each other. The examples shown here are first order azimuthal modes.

can be solved where the amplitude level enters the problem as a single parameter. Subsequent normalization of $\hat{p}$ such that

$$\frac{u_{\mathrm{ref}}}{u_0} = \left| \frac{\mathrm{i}\,\nabla \hat{p}|_{\vec{x}_{\mathrm{ref}}} \cdot \vec{n}_{\mathrm{ref}}}{u_0 \rho_0 \omega} \right| = a \tag{7.4}$$

then yields a solution to Eq. (7.2). If an amplitude level a_{LC} is found such that the growth rate of the corresponding mode equals the dissipative losses α of the system, i.e.,

$$-\,\mathrm{imag}(\omega(a_{\mathrm{LC}})) = \alpha, \tag{7.5}$$

then the limit-cycle amplitude is determined. This approach has been successfully deployed for network models [150] and Helmholtz solvers [49] to compute limit cycles in axial burners. Recently, Laera et al. generalized this idea to compute limit-cycle amplitudes in annular combustors [62]. In annular combustors two types of limit cycles are distinguished: spinning and standing modes. They are illustrated in Fig. 7.1.

Spinning modes feature equal amplitudes in each unit cell. However, along the circumference their phase increases from 0 to a multiple of 2π. Because the amplitude level at each burner is identical, parametrization of the problem using a single amplitude level is possible. The problem can be approached as in the single-burner case. Standing modes are more involved. All unit cells either have the same phase as the reference cell or differ from this phase by π. Moreover, the amplitude is varying along the circumference. In order to find a limit cycle, multiple amplitude level parameters for the various burners must, thus, be considered simultaneously.

The choice of the dissipation rate α depends on the deployed model. If a detailed model is used that accounts for all dissipative losses, e.g., those at the boundaries or due to viscous losses inside the considered domain, α is 0. On the other hand, if these effects are not fully captured by the model, α must be adapted accordingly. In any case, an explicit relation $\omega = \omega(a)$ is needed to determine the limit-cycle amplitude. In the aforementioned studies this relation has been obtained by repeatedly solving Eq. (7.3) for various amplitude levels a. The numerical costs for this approach are high. It is natural to consider perturbation theory as a means to accelerate the computation by obtaining an explicit relation for $\omega = \omega(a)$. Additionally, for spinning-mode limit cycles in annular combustors, Bloch-wave theory can ease the computations. Both will be discussed

in the next section. The computation of standing-mode limit cycles remains special. This is because of the different amplitude levels at the various burners, the discrete rotational symmetry will be broken. Moreover, a multi-parameter perturbation theory would be needed to account for the amplitude levels of the individual burners. Remarks at the end of the chapter will further discuss these aspects.

Note that a limit cycle satisfying the condition (7.5) does not necessarily manifest itself in reality. This is because, the limit cycle might be unstable, i.e., small perturbations of this system might cause saturation at a different state. However, given a system that features a discrete rotational symmetry, spinning-mode limit cycles are always stable if they exist, as was recently proven by Ghirado et al. [151].

7.2 Efficient computation of spinning-mode limit cycles

This section considers spinning-mode limit cycles. Such cycles feature a discrete rotational symmetry and are, therefore, amenable to a Bloch-wave approach. The unit-cell surrogate systems are essentially single burner systems. For this reason, the perturbation theory that will be used to compute limit cycles of these systems also applies to axial burners featuring only a single flame. Given an analytic flame describing function FDF(ω, a), a procedure to compute the limit-cycle amplitude is straightforward:

1. Simplify the eigenvalue problem by means of Bloch's theorem.
2. Solve it for some starting amplitude level a_0 to obtain the unperturbed solution ω_0 and $\widehat{p}_0$.
3. Compute the coefficients of the perturbation series $\omega = \sum_{n=0}^{N} \omega_n (\Delta a)^n$.
4. Approximate the amplitude level, $a_{\mathrm{LC}} \approx a_0 + \mathrm{Re}(\Delta a_{\mathrm{LC}})$ of the limit cycle by finding the solution with the smallest real part of $\mathrm{Im}\left(\sum_{n=0}^{N} \omega_n (\Delta a)^n\right) = \alpha$.
5. If desired, approximate the limit-cycle eigenfrequency by $\omega_{\mathrm{LC}} \approx \sum_{n=0}^{N} \omega_n (\Delta a_{\mathrm{LC}})^n$.
6. Solve the eigenvalue problem for the new amplitude level a_{LC}. If the growth rate is not vanishing, repeat steps 2–5.

These steps will be referred to as the *direct method*, because they assume the explicit availability of an analytic function FDF(ω, a). The first step accelerates the computations by Bloch-wave theory. Note that in a symmetric combustor, only degenerate modes can feature spinning limit cycles, because, by reflection, a clockwise spinning mode can be converted into a counter-clockwise spinning one (see Sec. 5.4). The Bloch waves which describe the corresponding degenerate eigenspace are such clockwise and counter-clockwise spinning modes. This is because they are Bloch waves of opposite Bloch wavenumbers $\widehat{p}_{\tilde{b}}$ and $\widehat{p}_{\widetilde{-b}}$ (see Eq. (5.33)) and are due to the Bloch-periodicity (Eq. (5.4)) extending from the unit cell with increasing and decreasing phase, respectively. To avoid repeatedly solving the eigenvalue problem (7.3), a polynomial approximation for $\omega = \omega(a)$ is computed in step 3. While increasing the order of the polynomial might improve its accuracy, the number of solutions of the limit-cycle condition considered in step 4 corresponds to this order. All found solutions are candidates for a limit-cycle amplitude. Because the amplitude level is a real number, it is natural to choose the solution closest to the real axis. On the other hand, there is the

risk that solutions do not lie inside the convergence radius of the power series expansion. Thus, a solution that is close to the expansion point a_0 is preferable. Also, to get a consistent estimate, the update Δa should be small. Because a change in the amplitude level is a small perturbation for physical reasons, it can be expected that there exists one solution satisfying all these requirements (smallest imaginary part, within the convergence radius, smallest real part). The method explicitly uses the smallest real part to aid convergence[1] in case it needs to be iterated (step 6). If needed, the limit-cycle frequency can be computed in the optional step 5.

Flame describing functions are typically obtained from experimental data. Conversion of this data into a representation that is parametrized by ω and a and analytic in both of these parameters could be a complicated task (see Sec. 3.5). As an alternative, the flame response itself can be considered as the perturbation parameter ε. This can be phrased as follows

$$\mathcal{L}(\omega; a) = \mathcal{W}(\omega) + \underbrace{\mathrm{FDF}(\omega, a)}_{=\varepsilon}. \tag{7.6}$$

Perturbation theory is then used to relate the eigenfrequency to the flame response $\omega = \omega(\varepsilon)$, find the flame response which satisfies the limit-cycle condition (7.5), and then compute a limit-cycle amplitude that corresponds to this flame response. An alternative procedure to compute the limit-cycle amplitudes, therefore, is:

1. Simplify the eigenvalue problem by means of Bloch's theorem.
2. Solve it for some starting amplitude level a_0 to obtain the unperturbed solution ω_0 and $\widehat{p}_0$.
3. Compute the coefficients of the perturbation series $\omega = \sum_{n=0}^{N} \omega_n (\Delta\varepsilon)^n$.
4. Approximate the flame response $\varepsilon_{\mathrm{LC}} \approx \varepsilon_0 + \Delta\varepsilon_{\mathrm{LC}}$ of the limit cycle by solving $\mathrm{Im}\left(\sum_{n=0}^{N} \omega_n (\Delta\varepsilon)^n\right) = \alpha$ under the restriction that the corresponding amplitude level is a real parameter.
5. Approximate the limit-cycle eigenfrequency by $\omega_{\mathrm{LC}} \approx \sum_{n=0}^{N} \omega_n (\Delta\varepsilon_{\mathrm{LC}})^n$.
6. Approximate the limit-cycle amplitude by solving $\varepsilon_{\mathrm{LC}} = \mathrm{FDF}(\omega_{\mathrm{LC}}, a_{\mathrm{LC}})$.
7. Solve the eigenvalue problem for the new amplitude level a_{LC}. If the growth rate does not vanish, repeat steps 2–6.

Because the amplitude level only implicitly occurs in these steps, this procedure is referred to as the *indirect method*. It is largely identical to the direct method. The key difference is the implicit usage of the amplitude level. Provided it exists, the restriction of finding a real-valued limit cycle is necessary to find a unique solution in step 4. Even if a limit-cycle amplitude for which the eigenvalue problem (7.3) features a solution exists, the equation in step 4 might not be solvable. This is due to the truncation error of the truncated power series expansion. Solving the equations in step 4 of the direct method and step 4 in the indirect method should, therefore, be conducted with a least squares solver.

Also note that both methods might benefit from a Padé approach. This is not only for convergence reasons but for the reduction of possible solutions to the limit-cycle condition. A Padé approximant will have no more solutions then the order of the numerator polynomial.

[1] This regards convergence of the iteration, not the power series expansion.

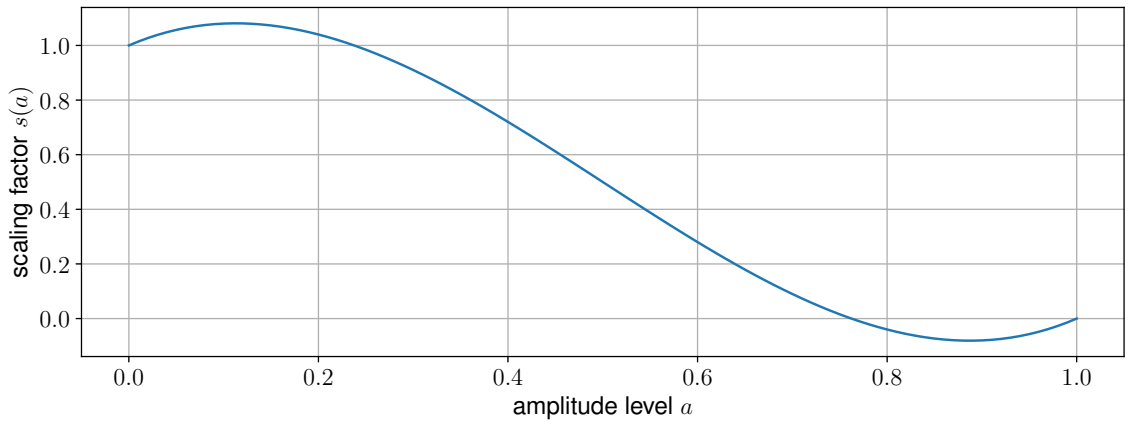

Figure 7.2: Scaling function $s(a)$ to model amplitude-level dependence of a FDF $s(a) = 1 + 1.5a - 7.5a^2 + 5a^3$.

7.3 Application to MICCA

This section applies the two methods to the MICCA model. To create an analytic flame describing function, the FTF is multiplied by a scaling function $s(a)$. This scaling function is given by the cubic polynomial $s(a) = 1+1.5a-7.5a^2+5a^3$. It is shown in Fig. 7.2. The complete flame describing function reads

$$\mathrm{FDF}(\omega, a) = \mathrm{FTF}(\omega)s(a). \tag{7.7}$$

Note that $\mathrm{FDF}(\omega, a) \to \mathrm{FTF}(\omega)$ as $a \to 0$ because $s(0) = 1$. This is consistent with the idea that flame transfer functions are valid for small amplitude levels. Because the describing function is separable in ω and a, it inherits analyticity from the two constituting functions FTF and s. More realistic flame describing functions might be generated from experiments (e.g., [62]) or numerical simulations (e.g., [152]). However, this is beyond the scope of the thesis.

The chosen flame describing function has the advantage that the constraint of having real-valued amplitude levels a in step 4 of the indirect method reduces to:

$$\mathrm{imag}(s) = \mathrm{imag}\left(\frac{\varepsilon_0 + \Delta\varepsilon_{\mathrm{LC}}}{\mathrm{FTF}(\sum_{m=1}^{N} \omega_m (\delta\varepsilon_{\mathrm{LC}})^m)}\right) = 0. \tag{7.8}$$

The discussion focuses on mode #M1. Figure 7.3 shows the eigenfrequency ω as a function of the amplitude level a for this test case using the direct and the indirect method. As a baseline solution, the eigenmode obtained for $a_0 = 0.5$ is considered. In addition to twentieth-order power-series approximation, results based on diagonal Padé approximants of the same order are also shown. In comparison to the truncated power series, the Padé approximant yields a better estimate of the exact frequency and growth rate over a wider range of amplitude levels. However, considering the range of encountered growth rates, both approximations yield good predictions of the amplitude level closest to a_0 that corresponds to a growth rate in this range. For the indirect method, both Taylor and Padé approximations perform equally well on this task. In any case, the results indicate that both the direct and the indirect method do not need to be iterated to obtain a

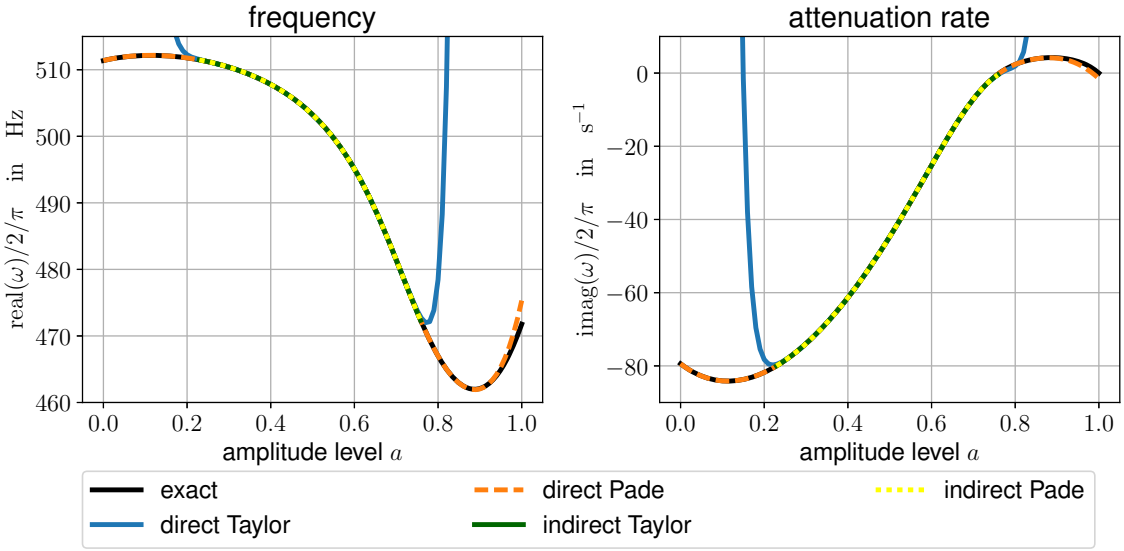

Figure 7.3: Exact (black solid) dependence of frequency and growth rate of mode #M1 on the amplitude level compared to approximations expanded at $a_0 = 0.5$ using the two methods with perturbation theory of twentieth order. For the direct method, conversion of the truncated power series to diagonal Padé approximants (orange dashed) yields an approximation quality that is satisfying over the considered range of amplitude levels ($a \in [0,1]$). On the contrary, the original power series approximation (cyan solid) yields reasonable results only in an interval ranging from about $a = 0.2$ to $a = 0.8$, indicating that the convergence radius of the power series is $\delta \approx 0.3$. Note, however, that it covers nearly the entire range of encountered growth rates which is roughly $[-80\mathrm{s}^{-1}, 0\mathrm{s}^{-1}]$. Applying the indirect method for assumed losses in this range, the corresponding amplitudes and oscillation frequencies are correctly computed using both truncated Taylor series (green solid) and diagonal Padé approximants (yellow dashed). For the current test case, an iteration of either of the methods is not necessary to compute the amplitude level of a limit cycle with reasonable accuracy, i.e., it can be obtained by solving only one eigenvalue problem.

reasonable prediction of a limit-cycle amplitude. Of course, iteration might be necessary for other configurations.

7.4 Conclusions

Computation of spinning-mode limit cycles in annular combustors can be significantly accelerated by means of perturbation and Bloch-wave theory. This is possible because the amplitude level at the various burners is identical and, thus, the problem can be solved by studying a single perturbation parameter a. The presented approach, therefore, also applies to single-burner configurations. The key savings are achieved because the number of repeated solutions to the nonlinear eigenvalue problem can be reduced. Because standing modes feature various independent amplitude levels, both perturbation theory and unit-cell computations as discussed in this part are not possible for the standing-mode case. A possible remedy is a multi-parameter perturbation theory. Together with other aspects of perturbation theory, this will be discussed in the next part.

Part III

More Applications of Perturbation Theory

Chapter 8

Nonlinear eigenvalue problems III: solution algorithms

The perturbation theory presented in Part II requires a highly accurate baseline solution. Although, fixed-point iterations like Nicoud's method and the Picard iteration are able to compute solutions of arbitrary accuracy, their convergence rate is slow. Thus, using them to find solutions for the thermoacoustic Helmholtz equation at machine precision might outweigh possible computational savings of a subsequently deployed perturbation method. Moreover, there is no guarantee that these methods find all eigenvalues inside a specified subdomain of the complex plane. Indeed, for the Rijke-tube example some modes could not be found by these methods. This chapter discusses how to use perturbation theory for both assessment and improvement of the convergence properties of the fixed-point methods. This is possible because perturbation theory allows for the computation of high-order derivatives of an eigenvalue ω with respect to some parameter ε: the perturbation theory stipulated the power-series ansatz $\omega(\varepsilon) = \sum_{n=0}^{N} \omega_n (\varepsilon - \varepsilon_0)^n$. Taking the derivatives at ε_0 yields

$$\frac{\partial^n}{\partial \varepsilon^n} \omega(\varepsilon_0) = n! \omega_n \tag{8.1}$$

which is only a variant of Taylor's theorem. Perturbation theory, therefore, provides gradient information. Because of the generality of perturbation theory, gradients can be computed for eigenvalue problems that do not model a physical phenomenon. In particular, this applies to the eigenvalue problems that need to be solved at each iteration step of Nicoud's fixed-point method and the Picard iteration. The computed derivatives can then be used to study the convergence properties of the methods by means of Banach's fixed point theorem. This will be the topic of the first sections in this chapter. The computed derivatives are then also used to perform generalizations of Newton's method – so-called Householder methods – which are known to feature very fast convergence rates. Finally, a combination of these methods with the contour-integration-based solution algorithm presented in [130] is discussed that efficiently finds all eigenvalues of the thermoacoustic Helmholtz equation inside of a predefined region in the complex plane.

8.1 Convergence of Nicoud's iteration and its variant

As with all fixed-point iterations, the convergence of Nicoud's fixed-point iteration can be analyzed in virtue of Banach's fixed-point theorem. Nicoud et al. discussed this idea when presenting the method for the first time [30]. However, Banach's theorem requires the derivative of the fixed point mapping $f(\omega)$. A quantity that was not explicitly computed in [30]. For this reason, the convergence properties of the method were not further discussed in that publication. This section fills this gap by showing how to compute the derivatives using perturbation theory.

Banach's fixed-point theorem

A fixed-point ω of f is an attracting point if the absolute value of the first derivative of f at ω is less than 1

$$|f'(\omega)| < 1, \tag{8.2}$$

because then there is a neighborhood around the fixed-point where the absolute value of the derivative is also less than 1 and hence the mapping f is a contraction in the vicinity of ω. In virtue of Banach's fixed-point theorem, the fixed-point can be found if the initial guess is sufficiently close to the fixed-point. After solving for the adjoint solutions, perturbation theory offers a formula for the calculation of the derivative of f.

Nicoud's iteration

The fixed-point mapping underlying Nicoud's iteration is implicitly defined by the eigenvalue problem (4.15). To compute the derivative of f, also the adjoint eigenvalue problem needs to be considered:

$$\mathsf{L}^{\dagger}_{\mathrm{Nic}}(f;\omega)\tilde{\boldsymbol{p}}^{\dagger} = \left(\begin{bmatrix} \mathbf{0} & \mathsf{K}^{\mathrm{H}} + \mathsf{Q}^{\mathrm{H}}(\omega) \\ -\mathbf{I} & \mathsf{C}^{\mathrm{H}} \end{bmatrix} + \overline{f} \begin{bmatrix} \mathbf{I} & \mathbf{0} \\ \mathbf{0} & \mathsf{M}^{\mathrm{H}} \end{bmatrix} \right) \begin{bmatrix} \tilde{\boldsymbol{p}}^{\dagger}_{\mathrm{I}} \\ \tilde{\boldsymbol{p}}^{\dagger}_{\mathrm{II}} \end{bmatrix} = \mathbf{0}. \tag{8.3}$$

The second line of this matrix-equation system is $\tilde{\boldsymbol{p}}^{\dagger}_{\mathrm{I}} = \left(\mathsf{C}^{\mathrm{H}} + \overline{\omega}\mathsf{M}^{\mathrm{H}}\right)\tilde{\boldsymbol{p}}^{\dagger}_{\mathrm{II}}$. Multiplying this equation by $\overline{\omega}$ and substituting it into the first line then yields $\mathsf{L}^{\dagger}(\omega)\tilde{\boldsymbol{p}}^{\dagger}_{\mathrm{II}} = 0$. Hence, the adjoint eigenvectors of the two problems are related by

$$\tilde{\boldsymbol{p}}^{\dagger} = \begin{bmatrix} \left(\mathsf{C}^{\mathrm{H}} + \overline{\omega}\mathsf{M}^{\mathrm{H}}\right)\boldsymbol{p}^{\dagger} \\ \boldsymbol{p}^{\dagger} \end{bmatrix}. \tag{8.4}$$

Now, using perturbation theory yields the derivative of f:

$$f' = \frac{\mathrm{d}f}{\mathrm{d}\omega} = \frac{\left\langle \tilde{\boldsymbol{p}}^{\dagger} \middle| \partial_{\omega}\mathsf{L}_{\mathrm{Nic}}\tilde{\boldsymbol{p}} \right\rangle}{\left\langle \tilde{\boldsymbol{p}}^{\dagger} \middle| \partial_{f}\mathsf{L}_{\mathrm{Nic}}\tilde{\boldsymbol{p}} \right\rangle}. \tag{8.5}$$

Here, the numerator is

$$\left\langle \tilde{\boldsymbol{p}}^{\dagger} \middle| \partial_{\omega}\mathsf{L}_{\mathrm{Nic}}\tilde{\boldsymbol{p}} \right\rangle = \left\langle \tilde{\boldsymbol{p}}^{\dagger} \middle| \mathsf{X}'(\omega)\tilde{\boldsymbol{p}} \right\rangle = \begin{bmatrix} \boldsymbol{p}^{\dagger\mathrm{H}}(\mathsf{C} + \omega\mathsf{M}) & \boldsymbol{p}^{\dagger\mathrm{H}} \end{bmatrix} \begin{bmatrix} \mathbf{0} & \mathbf{0} \\ \mathsf{Q}'(\omega) & \mathbf{0} \end{bmatrix} \begin{bmatrix} \boldsymbol{p} \\ \omega\boldsymbol{p} \end{bmatrix} = \boldsymbol{p}^{\dagger\mathrm{H}}\mathsf{Q}'(\omega)\boldsymbol{p} \tag{8.6}$$

and the denominator can be computed as

$$\left\langle \tilde{\boldsymbol{p}}^{\dagger} \middle| \partial_f \mathbf{L}_{\mathrm{Nic}} \tilde{\boldsymbol{p}} \right\rangle = \left\langle \tilde{\boldsymbol{p}}^{\dagger} \middle| \mathbf{Y} \tilde{\boldsymbol{p}} \right\rangle = \begin{bmatrix} \boldsymbol{p}^{\dagger \mathrm{H}} (\mathbf{C} + \omega \mathbf{M}) & \boldsymbol{p}^{\dagger \mathrm{H}} \end{bmatrix} \begin{bmatrix} \mathbf{I} & \mathbf{0} \\ \mathbf{0} & \mathbf{M} \end{bmatrix} \begin{bmatrix} \boldsymbol{p} \\ \omega \boldsymbol{p} \end{bmatrix} = \boldsymbol{p}^{\dagger \mathrm{H}} (\mathbf{C} + 2\omega \mathbf{M}) \, \boldsymbol{p}. \tag{8.7}$$

This finally yields

$$f'(\omega) = \frac{\boldsymbol{p}^{\dagger \mathrm{H}} \mathbf{Q}'(\omega) \boldsymbol{p}}{\boldsymbol{p}^{\dagger \mathrm{H}} (\mathbf{C} + 2\omega \mathbf{M}) \, \boldsymbol{p}}. \tag{8.8}$$

Note that this formula computes the exact derivative of f at ω and not an approximation. It is the key for the utilization of Banach's fixed-point theorem.

The Picard iteration

The fixed-point map of the Picard iteration is defined by

$$\mathbf{L}_{\mathrm{Pic}}(f;\omega)\boldsymbol{p} = \left(\mathbf{K} + \omega \mathbf{C} + \mathbf{Q}(\omega) + f^2 \mathbf{M}\right) \boldsymbol{p}. \tag{8.9}$$

The derivative of the fixed-point mapping, thus, is

$$f'(\omega) = \frac{\boldsymbol{p}^{\dagger \mathrm{H}} (\mathbf{Q}'(\omega) + \mathbf{C}) \boldsymbol{p}}{\boldsymbol{p}^{\dagger \mathrm{H}} 2\omega \mathbf{M} \boldsymbol{p}}. \tag{8.10}$$

The formulae (8.8) and (8.10) assess the convergence properties of a fixed-point of the respective fixed-point mappings. While these fixed-points are solutions to the discretized thermoacoustic Helmholtz equation (3.41), they are not necessarily attracting (see the examples below). Note that for FEM discretizations of models featuring only sound-soft and sound-hard boundary conditions, Nicoud's algorithm and the Picard iteration feature identical derivatives $f'(\omega)$. This is because Eq. (8.8) and Eq. (8.10) only differ in the influence of the damping matrix $\mathbf{C}$. Sound-hard boundary conditions naturally arise from the finite element discretization and, therefore, do not contribute to this matrix. On the other hand, sound-soft boundary conditions will result in some entries in $\mathbf{C}$. However, the corresponding entries in the solution vector $\mathbf{p}$ will be zero. Also note that evaluating the formulae with the discretization matrices arising from the unit-cell computation will yield identical results, because all unit cells contribute identically to the two inner products in these equations. Their ratio is, therefore, the same if evaluated on one unit cell only.

Convergence rates

The computed derivatives also clarify the convergence rate of the methods. A sequence generated in the vicinity of some fixed-point $\omega = f(\omega)$ is said to feature a rate of convergence m if there is a bound $G > 0$ such that for two consecutive iterates $\omega^{\{n\}}$ and $\omega^{\{n+1\}}$

$$|\omega^{\{n+1\}} - \omega| \leq G |\omega^{\{n\}} - \omega|^m \tag{8.11}$$

holds. It can be shown that the rate of convergence m at which an iteration sequence approaches a fixed-point ω is identical to the smallest positive integer m satisfying $\frac{\partial^m}{\partial z^m} f(z = \omega) \neq 0$, [73, Chap-

ter 7]. Without relaxation it is unlikely that the first derivative of the fixed-point mappings of Nicoud's method and the Picard iteration will vanish, see Sec. 4.3. Indeed, there is no guarantee that $|f'(\omega)| < 1$ and the methods converge at all. However, if they converge it can be assumed that they converge at a linear convergence rate.

8.2 An adjoint-based variant of Newton's method

Newton's method is known to be superior to simple fixed-point iteration. It always converges if initialized sufficiently close to a solution and does so at a quadratic convergence rate. The next section discusses a Newton-type iteration for the solution of nonlinear eigenvalue problems. This technique has been successfully applied to solve nonlinear eigenvalue problems. It could be applied to the characteristic equation of the nonlinear eigenvalue problem for systems arising from thermoacoustic network models (as in [48, 124]) or can be applied to the vectorial equation directly. See, for instance, the reviews [87, 86] or the thesis [153]. Yet, there is another way to utilize Newton's method which, except for a note in [86], seems not to be discussed in the recent literature.

When choosing an appropriate matrix $\mathbf{Y}$, the nonlinear eigenvalue problem itself can be considered to be a linear eigenvalue problem in some auxiliary eigenvalue λ:

$$\mathbf{L}(\omega)\boldsymbol{p} = \lambda \mathbf{Y}\boldsymbol{p}. \tag{8.12}$$

From this point of view, the eigenfrequency ω is merely a parameter to a classic eigenvalue problem with eigenvalue λ and eigenvector $\boldsymbol{p}$. If the parameter ω is chosen such that one eigenvalue λ vanishes, ω and the corresponding vector $\boldsymbol{p}$ solve the nonlinear eigenvalue problem $\mathbf{L}(\omega)\boldsymbol{p} = \mathbf{0}$. It is, therefore, natural to seek the roots of the implicitly given relation

$$\lambda = \lambda(\omega). \tag{8.13}$$

Perturbation theory enables the utilization of Newton's method to solve this problem by providing the derivative:

$$\lambda'(\omega^{\{n\}}) = -\frac{\boldsymbol{p}^{\dagger\mathrm{H}}\mathbf{L}(\omega^{\{n\}})\boldsymbol{p}}{\boldsymbol{p}^{\dagger\mathrm{H}}\mathbf{Y}\boldsymbol{p}}. \tag{8.14}$$

This approach has been first derived by Lancaster for eigenvalue problems that are polynomial in ω and is known as the *generalized Rayleigh quotient iteration* [136]. In this first work $\mathbf{Y}$ was set to $\mathbf{L}'(\omega^{\{n\}})$. If the derivatives of the implicit relation (8.13) are not known, instead of Newton's method a secant method may be utilized based on the difference $\lambda^{\{k\}} - \lambda^{\{k-1\}}$ in two consecutive iterations. For instance, such a secant method has been used in [154] with $\mathbf{Y} = \mathbf{I}$ to solve eigenvalue problems arising in electrodynamics.

The derivative of the thermoacoustic Helmholtz equation $\mathbf{L}'$ is in general not positive-definite. Therefore, it is not a suitable choice for $\mathbf{Y}$, because the large sparse eigenvalue problem is to be solved with an implicitly restarted Arnoldi algorithm. $\mathbf{Y} = \mathbf{I}$ would be appropriate. However, a more natural choice is to set $\mathbf{Y}$ to the mass matrix $\mathbf{M}$. Because then the inner product used to spur Arnoldi's algorithm is a discretization of the continuous inner product used to per-

Algorithm 8.1: Newton iteration for solving the nonlinear eigenvalue problem

function ITERATE($\omega^{\{1\}}, \boldsymbol{p}^{\{1\}}, \boldsymbol{p}^{\dagger\{1\}}, \mathbf{L}, \mathrm{tol}_\omega, \mathrm{maxiter}$)
  $\omega^{\{0\}} \leftarrow \infty$
  $n \leftarrow 1$
  while $|\omega^{\{n\}} - \omega^{\{n-1\}}| > \mathrm{tol}_\omega$ **and** $n <$ maxiter **do**
    $\lambda^{\{n\}}, \boldsymbol{p}^{\{n+1\}} \leftarrow \mathrm{EIGS}(\mathbf{L}(\omega^{\{n\}}), \mathbf{M}, 0, \boldsymbol{p}^{\{n\}})$
    $\overline{\lambda^{\{n\}}}, \boldsymbol{p}^{\dagger\{n+1\}} \leftarrow \mathrm{EIGS}(\mathbf{L}^{\mathrm{H}}(\omega^{\{n\}}), \mathbf{M}, 0, \boldsymbol{p}^{\dagger\{n\}})$
    $\lambda'^{\{n\}} \leftarrow -\frac{\boldsymbol{p}^{\dagger\{n+1\}\mathrm{H}} \mathbf{L}'(\omega^{\{n\}}) \boldsymbol{p}^{\{n+1\}}}{\boldsymbol{p}^{\dagger\{n+1\}\mathrm{H}} \mathbf{M} \boldsymbol{p}^{\{n+1\}}}$
    $\omega^{\{n+1\}} \leftarrow \omega^{\{n\}} - \frac{\lambda^{\{n\}}}{\lambda'^{\{n\}}}$
    $n \leftarrow n+1$
  end while
  $\lambda^{\{n\}} \leftarrow \mathrm{EIGS}(\mathbf{L}(\omega^{\{n\}}), \mathbf{M}, 0, \boldsymbol{p}^{\{n\}})$ ▷ This line basically computes the residual for possible later use
  return $\omega^{\{n\}}, \boldsymbol{p}^{\{n\}}, \boldsymbol{p}^{\dagger\{n\}}, \lambda^{\{n\}}, n$
end function

form the FEM discretization. Often this product has a physical meaning. Note that although not further considered in this thesis, setting $\mathbf{Y}$ as a Cholesky factor of the mass matrix (i.e., $\mathbf{M} = \mathbf{Y}\mathbf{Y}^{\mathrm{H}}$) might also be an interesting choice. A Cholesky factor $\mathbf{Y}$ is not positive-definite but easily invertible and, therefore, also suited for quick ARPACK computations. Moreover, given an approximate eigenpair $\omega^{\{n\}}, \boldsymbol{p}^{\{n\}}$, where $\|p^{\{n\}}\|_{\mathbf{M}} = 1$, the standard norm of the corresponding residual vector $r^{\{n\}} := \mathbf{L}(\omega^{\{n\}})\boldsymbol{p}^{\{n\}}$ is determined by $\|r^{\{n\}}\|_2^2 = \boldsymbol{r}^{\{n\}\mathrm{H}}\boldsymbol{r}^{\{n\}} = \overline{\lambda^{\{n\}}}\boldsymbol{p}^{\{n\}\mathrm{H}}\mathbf{Y}^{\mathrm{H}}\mathbf{Y}\boldsymbol{p}^{\{n\}}\lambda^{\{n\}} = |\lambda^{\{n\}}|^2\boldsymbol{p}^{\{n\}}\mathbf{M}\boldsymbol{p}^{\{n\}} = |\lambda^{\{n\}}|^2$.

An implementation of the complete algorithm, is outlined in Alg. 8.1. The algorithm requires the solution of both the direct and the adjoint problem. This might be problematic when used in software frameworks which are designed to perform only left-multiplication of the considered operators. Such *matrix-free* approaches provide only functions returning the product $\mathbf{A}\boldsymbol{v}$ for a given vector $\boldsymbol{v}$, instead of storing the matrix $\mathbf{A}$ explicitly. Arnoldi's algorithm is an example of an eigenvalue procedure using only this type of operation and, for instance, CERFACS' Helmholtz solver AVSP is implemented in a matrix-free fashion [91]. However, when solving for the adjoint eigenvectors as required in the Newton method presented above, right-multiplication of the matrices is needed. More precisely, products $\mathbf{A}^{\mathrm{H}}\boldsymbol{v}$ are to be computed. Hence, the Newton method cannot be implemented in such codes without further considerations. One possibility would be to simply provide a function performing the adjoint operation. However, as such a function would be implemented from the continuous adjoint equation[1], it would not be consistent to the discrete adjoint utilized in the algorithm. The Python code written for this thesis explicitly stores the matrices. The Newton method can, therefore, be readily implemented. As discussed in Chap. 3, the discretization method utilized is Bubnov-Galerkin FEM and, therefore, continuous and discrete adjoint approaches are identical, nevertheless.

[1] See [72] for the use of adjoints in AVSP.

Householder's methods

Newton's method for root finding can be generalized to higher orders by considering derivatives of orders higher than 1. The generalization to second order was given by Halley [155] and is, therefore, known as Halley's method[2]:

$$\omega^{\{n+1\}} = \omega^{\{n\}} - \frac{2\lambda(\omega^{\{n\}})\lambda'(\omega^{\{n\}})}{2\left(\lambda'(\omega^{\{n\}})\right)^2 - \lambda(\omega^{\{n\}})\lambda''(\omega^{\{n\}})}. \tag{8.15}$$

This method features a convergence rate of 3.

Newton's and Halley's methods are just the first two members of a complete generalization scheme presented by Householder [158]

$$\omega^{\{n+1\}} = \omega^{\{n\}} + m\frac{(1/\lambda)^{[m-1]}(\omega^{\{n\}})}{(1/\lambda)^{[m]}(\omega^{\{n\}})}. \tag{8.16}$$

Considering simple roots, the mth order scheme generally possesses a convergence rate of $m+1$. Yet, these methods are not practically applied because the increase in function evaluations per iteration outweighs the improved convergence rate when the order is increased. A limitation not valid for the present application. Because for a simple eigenvalue adjoint-perturbation theory basically requires one scalar product, a few matrix-vector products, and the solution of one linear system per derivative order, the computationally most costly operation in one iteration is the solution of the linear eigenvalue problem.

In addition to Newton's method, the computation of higher order derivatives is required. Algorithm 8.2 outlines a possible implementation of a Householder iteration based solver. The function HOUSE computes the Householder update to $\omega^{\{n\}}$ from $\lambda^{\{n\}}$ and its derivatives according to (8.16).

Degeneracy

Special care needs to be taken if the eigenvalue to be found is a multiple root of the characteristic function of $\mathbf{L}$ (i.e., the eigenvalue is degenerate). Two cases are to be distinguished. In the case of defective eigenvalues, the scheme presented here is inappropriate because defective eigenvalues are not analytic in their parameters. However, they can only appear as isolated points in the parametrized spectrum of $\mathbf{L}$ [117] and are, thus, not considered generic. For degenerate semi-simple eigenvalues, perturbation theory is still capable of computing the necessary derivatives [159]. This type of degeneracy might occasionally occur with respect to λ as a so-called accidental degeneracy. The degenerate perturbation theory outlined in Sec. 6.6 can be used to appropriately extend the theory for this case. However, like defective degeneracies, accidental semi-simple degeneracies are not considered generic. On the other hand, if the degeneracy is symmetry-induced, the eigenvalue λ will be degenerate at each iteration step. It will, thus, be a multiple-root of the implicit relation (8.13) throughout the entire iteration procedure. To retain the high convergence rate of Householder's methods, the scheme must be applied to the ath root of λ, assuming that a

[2] Fun fact: Halley's method is credited for being the most frequently rediscovered iterative method in mathematics [156]. The frequent rediscovery of iteration methods for solving nonlinear equations is even the topic of a 10-pages paper [157].

Algorithm 8.2: Iteration for solving the nonlinear eigenvalue problem based on Householder methods

function ITERATE($\omega^{\{1\}}, \mathbf{L}, \boldsymbol{p}^{\{1\}}, \boldsymbol{p}^{\dagger\{1\}}, \mathrm{tol}_\omega, \mathrm{maxiter}, \mathrm{order}$)
  $\omega_0 \leftarrow \infty$
  $n \leftarrow 1$
  while $|\omega^{\{n\}} - \omega^{\{n-1\}}| > \mathrm{tol}_\omega$ **and** $n < \mathrm{maxiter}$ **do**
    $\lambda^{\{n\}}, \boldsymbol{p}^{\{n+1\}} \leftarrow \mathrm{EIGS}(\mathbf{L}(\omega^{\{n\}}), \mathbf{M}, 0, \boldsymbol{p}^{\{n\}})$
    $\overline{\lambda^{\{n\}}}, \boldsymbol{p}^{\dagger\{n+1\}} \leftarrow \mathrm{EIGS}(\mathbf{L}^{\mathrm{H}}(\omega^{\{n\}}), \mathbf{M}, 0, \boldsymbol{p}^{\dagger\{n\}})$
    $\lambda^{\{n\}}_{\mathrm{derivs}} \leftarrow \mathrm{PERTURB}(\mathbf{L}(\omega^{\{n\}}) - \lambda^{\{n\}}\mathbf{M}, \boldsymbol{p}^{\{n+1\}}, \boldsymbol{p}^{\dagger\{n+1\}}, \mathrm{order})$ ▷ see Alg. 6.2 for PERTURB()
    $\omega^{\{n+1\}} \leftarrow \omega^{\{n\}} + \mathrm{HOUSE}(\lambda^{\{n\}}_{\mathrm{derivs}}, \mathrm{order})$
    $n \leftarrow n+1$
  end while
  $\lambda^{\{n\}} \leftarrow \mathrm{EIG}(\mathbf{L}(\omega^{\{n\}}), \mathbf{M}, 0, \boldsymbol{p}^{\{n\}})$ ▷ This line basically computes the residual for possible later use
  return $\omega^{\{n\}}, \boldsymbol{p}^{\{n\}}, \boldsymbol{p}^{\dagger\{n\}}, \lambda^{\{n\}}, n$
end function

is the algebraic multiplicity of the eigenvalue:

$$\omega^{\{n+1\}} = \omega^{\{n\}} + m\frac{\left(1/\lambda^{\frac{1}{a}}\right)^{[m-1]}(\omega^{\{n\}})}{\left(1/\lambda^{\frac{1}{a}}\right)^{[m]}(\omega^{\{n\}})}\,. \tag{8.17}$$

The necessary outer derivatives used in (8.17) read up to fifth order:

$$\frac{\mathrm{d}}{\mathrm{d}\omega}\lambda(\omega)^{-a} = -a\lambda\omega^{-a-1}\lambda'(\omega) \tag{8.18}$$

$$\frac{\mathrm{d}^2}{\mathrm{d}\omega^2}\lambda(\omega)^{-a} = a\lambda(\omega)^{-a-2}\left((a+1)\lambda'(\omega)^2 - \lambda(\omega)\lambda''(\omega)\right) \tag{8.19}$$

$$\frac{\mathrm{d}^3}{\mathrm{d}\omega^3}\lambda(\omega)^{-a} = -a\lambda(\omega)^{-a-3}\left((a^2+3a+2)\lambda'(\omega)^3 - 3(a+1)\lambda(\omega)\lambda'(\omega)\lambda''(\omega) + \lambda(\omega)^2\lambda^{[3]}(\omega)\right) \tag{8.20}$$

$$\begin{aligned}\frac{\mathrm{d}^4}{\mathrm{d}\omega^4}\lambda(\omega)^{-a} = a\lambda(\omega)^{-a-4}\big(&-6(a^2+3a+2)\lambda(\omega)\lambda'(\omega)^2\lambda''(\omega) + (a^3+6a^2+11a+6)\lambda'(\omega)^4 \\ &+\lambda(\omega)^2(3(a+1)\lambda''(\omega)^2 - \lambda(\omega)\lambda^{[4]}(\omega)) + 4(a+1)\lambda(\omega)^2\lambda^{[3]}(\omega)\lambda'(\omega)\big)\end{aligned} \tag{8.21}$$

$$\begin{aligned}\frac{\mathrm{d}^5}{\mathrm{d}\omega^5}\lambda(\omega)^{-a} = -a\lambda(\omega)^{-a-5}\big(&(a+1)(a+2)(a+3)(a+4)\lambda'(\omega)^5 + 10(a+1)(a+2)\lambda(\omega)^2\lambda^{[3]}(\omega)\lambda'(\omega)^2 \\ &-10(a+1)(a+2)(a+3)\lambda(\omega)\lambda'(\omega)^3\lambda''(\omega) + \lambda(\omega)^3(\lambda(\omega)\lambda^{[5]}(\omega) \\ &-10(a+1)\lambda^{[3]}(\omega)\lambda''(\omega)) + 5(a+1)\lambda(\omega)^2\lambda'(\omega)(3(a+2)\lambda''(\omega)^2 - \lambda(\omega)\lambda^{[4]}(\omega))\big).\end{aligned} \tag{8.22}$$

Of course, this approach requires the multiplicity of an eigenvalue to be known in advance. If carefully designed, this information can be retrieved from an estimator of the initial guess. As will be discussed in Sec. 8.4, Beyn's contour-integration-based method can be used as such an estimator. However, in annular combustion chambers the degeneracy is typically of order two and can be explained from the discrete rotational symmetry and an additional symmetry of the system, see Sec. 5.4. These degeneracies might, therefore, be removed from the problems by Bloch-wave theory, as the surrogate $\mathcal{L}_{\mathrm{Bloch}}(\omega; b)$ systems will usually not be degenerate.

8.3 Further remarks on iterative solvers

This section shortly addresses aspects of the presented iterative solvers which are of minor importance for the goals of the thesis. However, they might help to improve the algorithms in the future.

Threading and multiple eigenvalues

Each of the proposed fixed-point iterations solves a linear eigenvalue problem $\mathbf{L}_{\text{fix}}(f;\omega^{\{n\}})\boldsymbol{p} = 0$ or $\mathbf{L}_{\text{fix}}(\lambda;\omega^{\{n\}})\boldsymbol{p} = 0$ at each iteration step. However, using fixed-point iterations as a means to find eigenvalues of operator families differs from their utilization as root-finding algorithms of scalar functions in one major aspect, namely, that eig($\mathbf{L}_{\text{fix}}$) is a multi-valued function. Because only one out of the many eigenvalues of $\mathbf{L}_{\text{fix}}(z;\omega^{\{n\}})$ can be fed into the next iteration step, one eigenvalue must be chosen at each iteration[3]. The easiest choice would be to take the eigenvalue of smallest magnitude. The choice might be improved by computing one further iteration step for each of the available eigenvalues, and then proceeding with the one corresponding to the smallest change in $\omega^{\{n\}}$. Actually, all of the eigenvalues are associated with a holomorphic scalar function which if 0 yields an eigenvalue. This can be concluded from the holomorphy of the operator family and basic definitions of eigenvalues. The scalar functions are to be disentangled like various threads in a tangled web. Therefore, the problem will be referred to as *threading*. Storing the disregarded eigenvalues for later use in order to find different eigenvalues might be beneficial. Yet, this appears to be inefficient as the same thread might be found at several iteration steps. As threading is not the topic of this report, the problem should not be further discussed. For the current study only the eigenvalue with the smallest magnitude is considered. In any case if the initial guess is sufficiently close to an eigenvalue, this should be the best choice, because then by continuity the smallest eigenvalue can be related to the desired thread. This consideration just translates the problem to finding high-quality initial guesses.

Stopping criteria and residuals

All iterative algorithms for solving the nonlinear eigenvalue problem presented so far used $|\omega^{\{n\}} - \omega^{\{n-1\}}| > \text{tol}_\omega$ as a stopping criterion. This choice guarantees the eigenvalue to be of a similar accuracy as can be concluded from the convergence of these methods. If an iteration converges, the convergence rate allows the assessment of how the error $\eta^{\{n\}} := \omega^{\{n\}} - \omega$ decreases with each iterative step. The aim of each iteration is to reduce the modulus of the error $|\eta^{\{n\}}|$ as much as possible with reasonable computational effort. Given at least linear convergence, the modulus of $\omega^{\{n+1\}} - \omega^{\{n\}}$ is an estimate of the modulus of the error because:

$$|\omega^{\{n+1\}} - \omega^{\{n\}}| = |\omega^{\{n+1\}} - \omega + \omega - \omega^{\{n\}}| = |\eta^{\{n+1\}} - \eta^{\{n\}}| = |\eta^{\{n+1\}}| + \mathcal{O}(|\eta^{\{n\}}|^m). \tag{8.23}$$

Therefore, stopping a fixed-point iteration at a given tolerance tol_ω justifies the assumption that the computed $\omega^{\{n\}}$ is an approximation to a fixed-point of that iteration map with similar accuracy. Such a difference test is sufficient for simple iterations like Nicoud's algotihm and the Picard iteration, because each fixed-point of the iteration map is a solution to the eigenvalue prob-

[3] A similar problem arises in the numerical computation of pseudospectra [160].

lem. However, fixed-points of the Householder iterations are not necessarily solutions, unless $\lambda(\omega) = 0$. Thus, a positive difference test is a necessary but not sufficient criterion for finding solutions. The easiest answer to this issue is testing whether $|\lambda^{\{n\}}| \leq \mathrm{tol}_\lambda$. How to choose this tolerance relative to tol_ω is an open question. Note that $\lambda^{\{n\}}$ is a measure for the residual, because $r^{\{n\}} := \mathbf{L}(\omega^{\{n\}})\boldsymbol{p}^{\{n\}} = \lambda^{\{n\}}\boldsymbol{p}^{\{n\}}$. Thus, a test on $\lambda^{\{n\}}$ is equivalent to a residual test. [86] uses

$$\frac{\|\mathbf{L}(\omega^{\{n\}})\boldsymbol{p}^{\{n\}}\|_2}{\|\mathbf{L}(\omega^{\{n\}})\|_{\mathrm{Fro}}\|\boldsymbol{p}^{\{n\}}\|_2} < \mathrm{tol}_{\mathrm{res}} \tag{8.24}$$

as a stopping criterion based on the residual. Here, $\|\cdot\|_{\mathrm{Fro}}$ denotes the Frobenius norm. This residual test might also be used as an additional test for convergence in thermoacoustic applications. Yet, developing a residual notion based on a norm which is more physics-related would be preferable. A possible norm would be the norm induced by the mass matrix.

Note, however, that if initializing the iterations with an initial guess which is close to an eigenfrequency of the problem, the difference test $|\omega^{\{n\}} - \omega^{\{n-1\}}| > \mathrm{tol}_\omega$ will be sufficient. As with threading the problem is, thus, avoided by finding a good initial guess. How to compute such an initial guess using Beyn's integration-based algorithm will be the topic of the next section.

8.4 Getting the initial guess from Beyn's algorithm

Eigenvalue solvers based on contour integration are capable of finding all eigenvalues inside a given contour $\Gamma \subset \mathbb{C}$ (see [86] and references therein). For practical eigenvalue problems arising in gas turbine engineering, these regions are trapezoids in the complex plane. This is because as a rule of thumb, eigenvalues with imaginary parts whose modulus is not more than 15% of the real part are considered realistic and relevant. The reasonability of this rule shall not be discussed here. Note, however, that the recent discovery of intrinsic thermoacoustic modes [93] suggest a reconsideration of it.

In this thesis, Beyn's integral algorithm 1 which was presented in [130] is used as a nonlinear eigenvalue solver for finding initial guesses to iterative solvers. This is a rather arbitrary choice and other integration-based solvers like [161] or [162] might also be considered. Global integration-based solvers are not a completely new concept in thermoacoustics. Based on [163, 164, 165] an integration-based algorithm named RootLocker has been developed at CERFACS. This algorithm finds the roots of the dispersion relations of network models. See the thesis [166, Chapter 2] for details.

Beyn's integral algorithm 1

Beyn's algorithm[4] is presented in Alg. 8.3. Like all contour-based algorithms the procedure reduces the nonlinear eigenvalue problem to a linear eigenvalue problem by integration. This reduction is possible due to Keldysh's theorem, see Beyn's original publication or the review from Güttel and Tisseur [86]. The algorithm is designed to find all m eigenvalues inside the contour Γ. Of course, this number is not known in advance. Thus, the algorithm is set up for finding M eigenvalues. If $M > m$, $M - m$ singular-values in line 8.3.5 will be zero in exact arithmetics. In computer

[4] The original algorithm presented in [130] has factors $\frac{1}{2\pi\mathrm{i}}$ multiplied with the results of the integrations in the lines 8.3.3 and 8.3.4 . However, these cancel in line 8.3.7.

Algorithm 8.3: Beyn's contour-integration-based method

```
1: function BEYN(L, Γ, M, npoints, tol_σ)
2:     choose Ṽ at random from ℂ^{N×M}
3:     A_0 ← INTEGRATE(L^{-1}(z)Ṽ, Γ, npoints)
4:     A_1 ← INTEGRATE(zL^{-1}(z)Ṽ, Γ, npoints)
5:     U, Σ, V ← SVD(A_0)
6:     Check which singular values feature σ < tol_σ and remove them
7:     Ω, P ← EIG(U^H A_1 V Σ^{-1})
8:     P ← UP
9:     Check which ω lie outside of Γ and remove them
10:    return Ω, P
11: end function
```

arithmetics, these singular values will be close to zero. Beyn suggested disregarding singular values smaller than a predefined specific tolerance tol_σ, as they will merely lead to spurious modes found by the algorithm. Note that if all M singular values are greater than the tolerance, there might be more than M eigenvalues enclosed by Γ and the algorithm should be restarted with a larger M. Also note that the algorithm cannot deal with situations where there are more eigenvalues inside the contour than the matrix dimension N. In these cases, the contour must be changed to enclose a smaller region with possibly less eigenvalues, or Beyn's integral algorithm 2 is to be utilized. Because the dimension of the finite element discretization of the thermoacoustic Helmholtz equation is typically much higher than the number of eigenvalues in relevant subdomains of the complex plane, Beyn's integral algorithm 1 is well suited for such problems. Additionally, the computed eigenvalues are tested for lying truly inside the contour Γ.

The computationally most expensive steps in the algorithm are the integrations in the lines 8.3.3 and 8.3.4. A suitable quadrature rule is to be deployed here. In his original publication, Beyn discussed the application of the trapezoidal rule to circular domains. [86] emphasizes the optimal convergence properties of the trapezoidal rule for circular domains and outlines two strategies for non-circular contours: (i) a conformal mapping is used to transform an arbitrary contour to a circle – e.g., by appropriate Schwarz-Christoffel maps – and solve the problem using the trapezoidal rule or (ii) use Gauss-Legendre quadrature. Because of the broad availability of software libraries for Gauss-Legendre quadrature this approach is used in the current work. Regardless of which quadrature strategy is deployed, at each evaluation point, M linear systems have to be solved. Note that the same systems appear in both lines and, therefore, just need to be solved once. The high costs of this operation prohibit Beyn's method as a solver for large systems. However, the method is feasible for small ($N < 100$) and middle-sized ($N < 10\,000$) problems as they appear in thermoacoustic network models and discretizations of the Helmholtz equation. Therefore, using such models together with Beyn's algorithm as an estimator for initial guesses is a reasonable idea.

Beyn's algorithm as an initializer

In this thesis, Beyn's algorithm will serve as an initializer to the locally convergent Householder methods. For this reason, the algorithm is slightly simplified.

(i) Because only an estimate is to be computed, the algorithm can be applied to discretizations

from a coarser grid. The subsequent refinement of the solution is then performed on the actual grid. As the discretization matrices will be smaller, the high costs for contour integration remain manageable. Yet, the final result will be accurate. Although not necessarily needed, the coarse eigenvector found from Beyn's integration might be interpolated on the actual grid and passed to the Householder method in order to support the convergence of Krylov subspace methods.

(ii) Feeding the eigenvalues obtained from contour integration into Householder iteration can actually be seen as a plausibility test. If the eigenvalue found by the contour method is a valid approximation to an eigenvalue, iteration by a Householder method will only slightly modify the eigenvalue (i.e., the eigenvalue is refined). If, on the other hand, the Householder method converges to a solution very different from the contour-integration result, this result was likely spurious. These considerations allow the tests of the singular values in Beyn's algorithm to be avoided. Especially, finding a proper rule for choosing tol_σ is, thus, obsolete. Validity of the results is revealed after the refinement step.

(iii) Also, eigenvalues that lie outside of, but close to, the contour Γ might be considered for the refinement step. This is because after the local iteration, the eigenvalues might be inside the contour. Similar to the singular value test, instead of defining a tolerance to determine how close is sufficiently close, all eigenvalues could be taken to the refinement step and their position evaluated after the refinement. In this way, no eigenvalue is falsely excluded from the scheme.

8.5 Rijke-tube example

This section assesses and compares the presented solution algorithms using the Rijke-tube model.

Nicoud's algorithm and Picard iteration

Figure 8.1 illustrates the convergence properties of Nicoud's algorithm and the Picard iteration when setting the stopping tolerance to $\mathrm{tol}_\omega = 10^{-2}$. The complex domain $[0, 10] \times [-\mathrm{i}, \mathrm{i}]$ was rasterized using an equidistant grid of 1001×201 points. These points were fed into the algorithms as initial points for solving the FEM discretization of the Rijke-tube model. For this study, the eigenvectors for the Krylov-subspace methods were initialized as a vector made up of ones only (i.e., $\boldsymbol{p}_1 = \begin{bmatrix} 1 & 1 & 1 & 1 & \dots \end{bmatrix}^\mathrm{T}$). The color indicates (i) whether the algorithm converges if initialized from the respective position, (ii) if it converges, to which eigefrequency it will converge and (iii) how many iteration steps it took to get there with the prescribed tolerance. The large orange and blue shaded areas indicate that the two algorithms are capable of finding the eigenfrequencies (and mode shapes) of #R1 and #R2. Unsurprisingly, the fastest convergence to these solutions is obtained if the algorithms are initialized in the immediate vicinity of the respective eigenfrequencies. However, none of the iterations converged to the modes #R3 and #R4, although these lie in the sampled region of the complex plane. These results complement the findings of Sec. 4.4, where it was found that #R1 and #R2 are acoustic modes, which can be computed by initializing the algorithm with the (nearby) passive eigenfrequencies. The results presented in Fig. 8.1 suggest that there is actually no initialization point from which the algorithms would converge to the

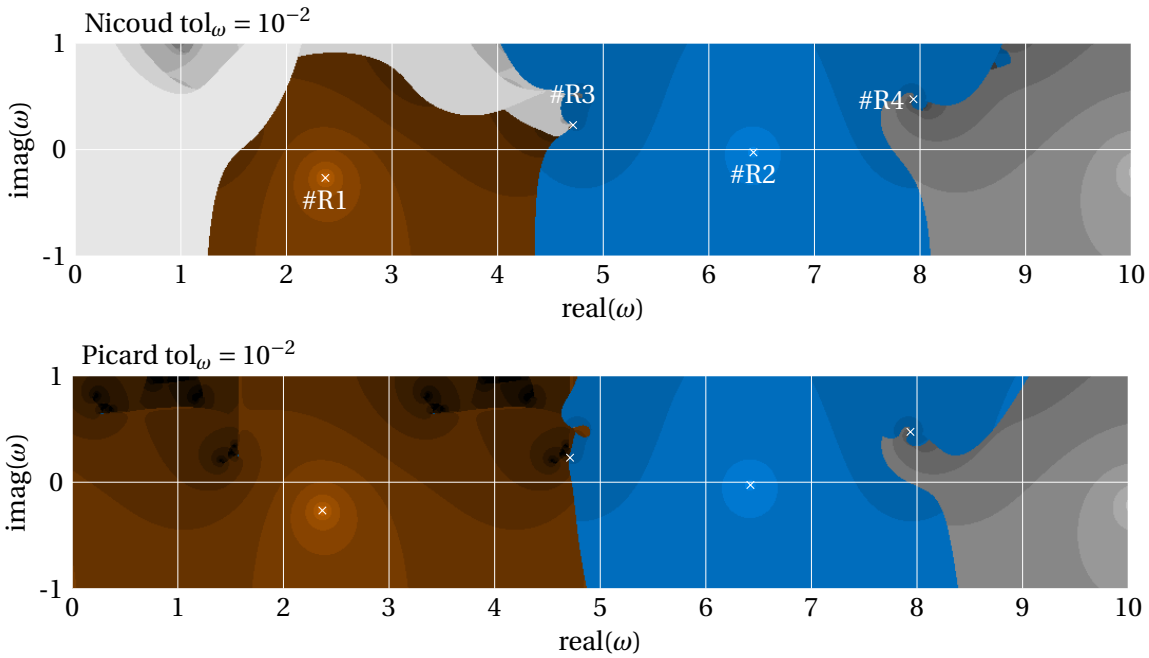

Figure 8.1: Convergence maps for 1001×201 initialization points in the complex plane. The top image shows results for Nicoud's algorithm, the bottom image is obtained from the Picard iteration. In both cases the stopping tolerance was set to $\text{tol}_\omega = 10^{-2}$. The white crosses highlight the position of the four eigenfrequencies. The color shading indicates to which solution the iteration will converge: orange – #R1, blue – #R2, gray – any mode outside of the considered domain, black – no convergence within 15 iterations. The darker the shading, the more iteration steps it takes for the solution to converge to the prescribed accuracy. Apparently, the modes #R3 and #R4 cannot be found.

modes #R3 and #R4.

While a tolerance of $\text{tol}_\omega = 10^{-2}$ is clearly sufficient to reason about the stability of the computed modes, it is far too large when using the computed solution as a baseline solution for perturbation theory. Due to their linear convergence rate, Nicoud's algorithm and the Picard iteration will take many more iterations to converge if stricter tolerances are set. This is illustrated in Fig. 8.2. It shows results obtained with a tolerance of $\text{tol}_\omega = 10^{-12}$ which is much better suited for perturbation theory. The results clearly show that it is almost impossible to find one of the four modes at the prescribed tolerance with no more than 16 iterations. Clearly, the modes #R1 and #R2 could be found when allowing for more iteration steps. This is because they were found when a lower tolerance was set. Yet, from a practical perspective, too many iterations are inconvenient.

Householder methods

Householder methods have better convergence properties than Nicoud's algorithm and the Picard iteration, as can be seen in Fig. 8.3. It shows how the same initial guesses converge when using Householder's methods up to fifth order. The tolerance for ω is still $\text{tol}_\omega = 10^{-12}$. The convergence properties have clearly improved compared to Nicoud's method. Note that for very few initial guesses (less than 100) the algorithm appeared to diverge. This can be concluded from ARPACK

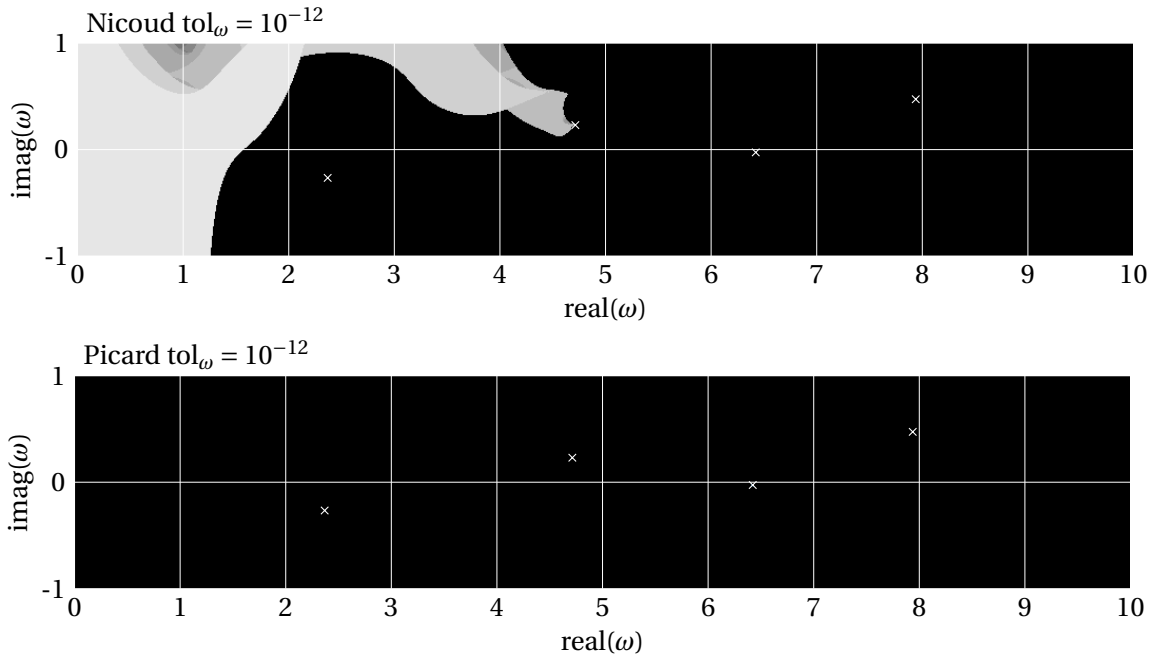

Figure 8.2: Convergence maps for Nicoud's algorithm (top) and the Picard iteration (bottom) obtained with a tolerance of tol$_\omega$ = 10^{-12}. White crosses highlight the position of the four known eigenfrequencies in the region shown. The two algorithms are not capable of finding either of the modes #R1, #R3, or #R4 within 16 iterations at this accuracy. A few samples converged to #R2 if initialized in the immediate vicinity of this eigenfrequency, however, this is not visible from the picture.

error messages indicating that `NaN` values appeared. The reason is unclear.

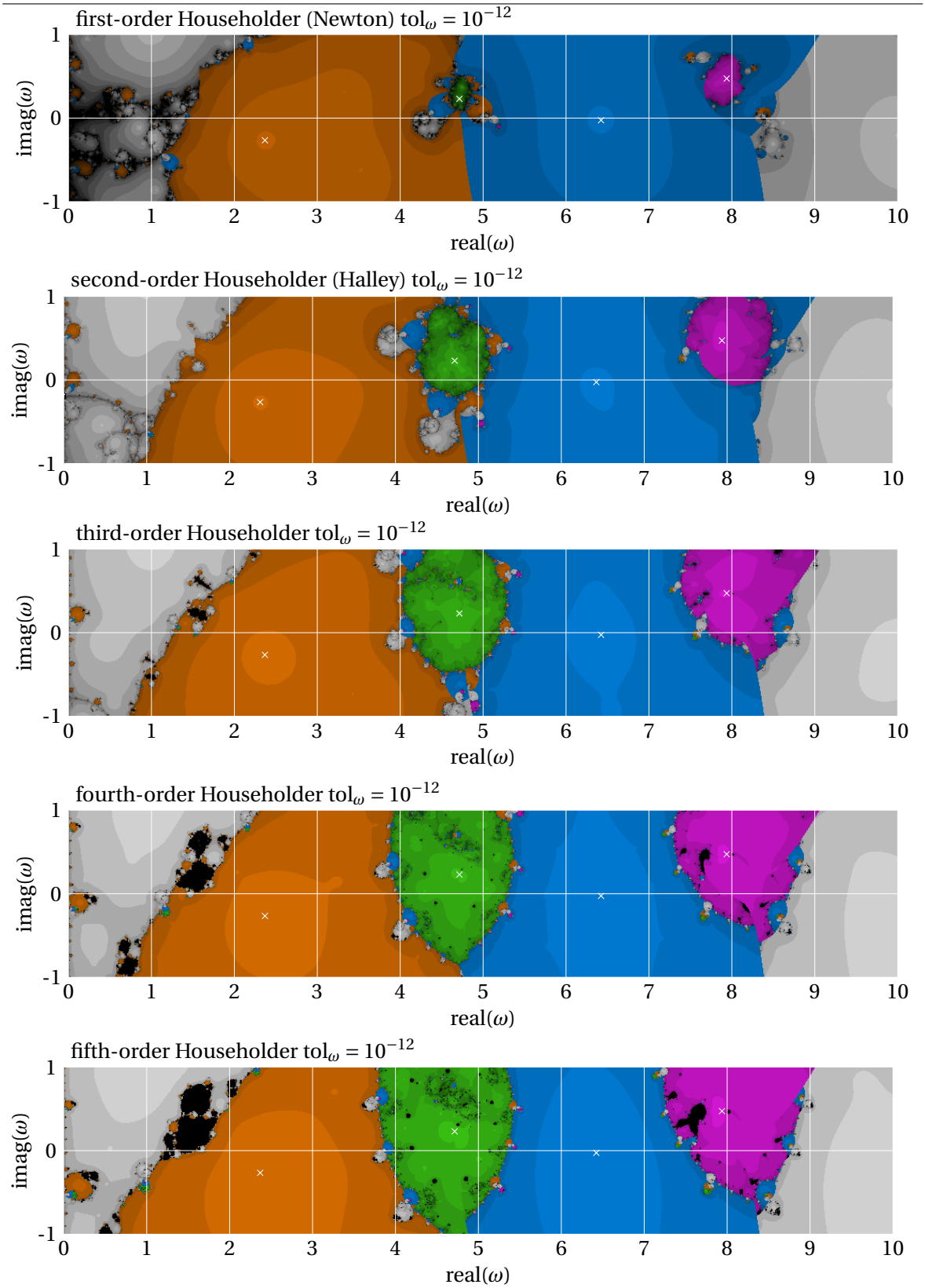

Figure 8.3: Convergence maps for Householder iterations. The color code for the modes is as follows: orange – #R1, blue – #R2, green – #R3, purple – #R4 , gray again indicates convergence to modes outside of the domain while black highlights no convergence within 16 iterations. The third-order method constitutes the best compromise between large basins of attractions and small domains of non-convergence.

It might be attributed to evaluations of the exponential in the flame transfer function at large intermediate $\omega^{\{n\}}$. However, this computational issue is rather irrelevant for the overall results. All different modes can be found and even with fewer iteration steps, as can be seen from the generally brighter images. Each mode possesses a domain of attraction in its vicinity. The convergence maps show a fractal nature at the boundary of different domains of attraction. This is a known feature of Newton maps when being applied as a root-finding method to scalar equations, e.g., [167]. However, some of the boundaries are non-fractal. This can be attributed to threading.

The basins of attraction of the modes #R3 and #R4 appear to grow when increasing the order of the method. However, the Householder methods of fourth and fifth order show significant portions of non-convergence domains. It is unclear whether this is a numerical issue or a generic feature of these methods. Yet, the example suggests that a third-order Householder scheme is a good compromise between computational effort and improved convergence properties.

Threading example

For the current example, threading seems not to be an issue. This is exemplified in Fig. 8.4. It shows the two smallest, linear eigenvalues λ of the matrix $\mathbf{A}(z) = \mathbf{L}(z) - \lambda\mathbf{M}$ for values z taken from the straight line $z(\zeta)$ between $\omega_{\#R1}$ and $\omega_{\#R2}$. The line is parameterized such that $z(0) = \omega_{\#1}$ and $z(1) = \omega_{\#2}$. For the shown example, following the slope of the smallest eigenvalue thread will apparently yield a nearby eigenvalue. Because the two threads cross at $\zeta \approx 0.65$, except for the range $\zeta \in [0.5, 0.65]$, this will be the eigenvalue with the closest distance to the evaluation point.

Initialization with Beyn's algorithm

Because of its good convergence properties, the third-order Householder method is used in conjunction with Beyn's method as a global solution algorithm. Beyn's method was set up to find all eigenvalues on the rectangular domain already examined for the convergence map. As a quadrature method, 10-point Gauss-Legendre-integration was utilized on each of the four edges of the domain. The dimension of the subspace created in Beyn's algorithm was set to $M = 16$.

Table 8.1 lists the eigenvalues found by Beyn's algorithm and the fixed-points they converged to when feeding them into the third-order Householder method, together with the number of iterations it took them to converge. Obviously, all four eigenvalues can be found with this two-step approach. Moreover, spurious modes from Beyn's algorithm are reliably eliminated after the refinement step, as they converge to solutions that are outside of the considered domain or significantly away from the initial estimate. The overall costs for this two-step procedure are moderate as no more than 10 iterations were needed to refine the solutions.

The table also lists the derivatives of the fixed-point map of Nicoud's algorithm at the solutions. Because of the set boundary conditions, this derivative is not different from the derivative of the Picard-iteration mapping. The absolute value of the derivatives of the modes #R3 and #R4 are greater than 1. This finally proves that they can neither be found with Nicoud's algorithm nor the Picard iteration if no relaxation strategy is employed. The Householder methods, however, are capable of finding these modes and when using Beyn's method as an initializer, the lack of passive modes corresponding to #R3 and #R4 (see Sec. 4.4) is also not a problem.

The Rijke-tube example clearly shows that a combination of Beyn's algorithm and a locally

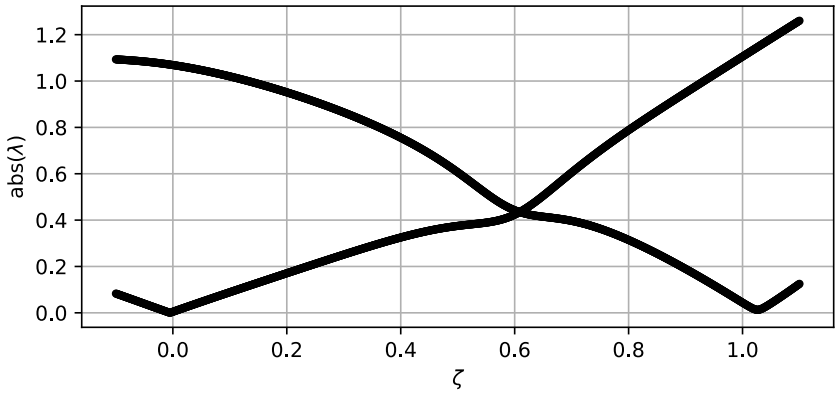

Figure 8.4: Absolute value of the two smallest eigenvalues value on the straight line between the modes #1 and #2.

convergent perturbation-based iteration algorithm is a reliable means of accurately finding all eigensolutions with eigenvalues inside a given region of the complex plane.

8.6 Application to the Kronig-Penney model

In this section, it is shortly exemplified how to handle symmetry-induced degeneracies when dealing with the Householder methods. The FEM discretization of the Kronig-Penney model that was already used in Sec 4.5 will serve as a test case. Because of its simplicity, it also allows for a brute force convergence study. First-order Householder iterations (i.e., Newton iterations) are initialized with 1201×201 points equidistantly taken from the domain $[0, 12] \times [-\mathrm{i}, +\mathrm{i}]$. The initial vector for the generation of the Krylov subspace is again a vector featuring ones only. Bloch-periodic boundary conditions resolve the symmetry-induced degeneracy. Figure 8.5 shows convergence maps for Bloch wavenumbers $b = 1$, 2, 3, and 4. Because the Kronig-Penney model is reflection-symmetric and features a degree of discrete rotational symmetry of $B = 12$, the modes corresponding to these Bloch wavenumbers are degenerate in the original system ($2b \bmod B \neq 0$). Nevertheless, they are simple eigenvalues in the surrogate systems $\mathbf{L}_{\mathrm{Bloch}}(\omega; b)$. Moreover, these systems contain only a subset of the full spectrum of $\mathbf{L}(\omega)$. Hence, already rough estimates for the eigenvalues are sufficient to find them with the Householder iteration. This can be clearly seen from the large orange and blue shaded areas in Fig. 8.5. The results show that in addition to the computational savings obtained from the reduction to a unit cell, Bloch-wave theory supports the convergence of iterative solution methods for the nonlinear eigenvalue problem: it removes symmetry-induced degeneracies and leads to large basins of attraction around the eigenvalues.

Table 8.1: Eigenvalues of the Rijke tube computed by first leveraging Beyn's algorithm and then feeding the results into a third-order Householder solver. ω_{Beyn} are the eigenvalues found from Beyn's method on the coarse grid. The column *step* lists the number of iteration steps that are necessary to converge to an accuracy of $\text{tol}_\omega = 10^{-12}$ in the Householder step. The column ω_{House3} indicates the finally computed eigenvalue. The last column reports the derivative of Nicoud's fixed-point map at that eigenvalue. Due to the boundary conditions, it is identical to the derivative of the mapping of Picard iteration. The colored rows highlight the four modes inside the contour. Note that due to the symmetry of the spectrum, the solutions 7 and 8 might also be considered as mode #R1.

#	ω_{Beyn}	steps	ω_{House3}	$\lvert f'(\omega)\rvert$
1	$10.01492 + 0.12512\text{i}$	3	$10.07616 - 0.2076\text{i}$	0.43055
2	$11.15125 + 0.57175\text{i}$	10	$11.44825 + 1.02266\text{i}$	2.06045
3→#R4	$8.09011 + 0.70095\text{i}$	4	$7.93791 + 0.47319\text{i}$	6.5542
4→#R2	$6.5507 - 0.10248\text{i}$	3	$6.42264 - 0.02614\text{i}$	0.18992
5→#R3	$4.72368 + 0.17207\text{i}$	5	$4.71422 + 0.23043\text{i}$	29.89721
6→#R1	$2.34166 - 0.26615\text{i}$	3	$2.3687 - 0.26568\text{i}$	0.52602
7	$-0.69827 - 1.72177\text{i}$	6	$-2.3687 - 0.26568\text{i}$	0.52602
8	$-1.365 + 0.15319\text{i}$	5	$-2.3687 - 0.26568\text{i}$	0.52602
9	$1.83929 + 1.68595\text{i}$	4	$0.98728 + 1.04804\text{i}$	1.5512
10	$0.99196 + 1.04255\text{i}$	3	$0.98728 + 1.04804\text{i}$	1.5512
11	$0.80395 + 1.51899\text{i}$	4	$0.98728 + 1.04804\text{i}$	1.5512
12→#R1	$2.12233 - 0.0351\text{i}$	4	$2.3687 - 0.26568\text{i}$	0.52602
13→#R1	$0.75773 - 1.54027\text{i}$	6	$2.3687 - 0.26568\text{i}$	0.52602
14	$0.47706 - 1.04179\text{i}$	7	$-0.98728 + 1.04804\text{i}$	1.5512
15	$0.06112 + 0.0693\text{i}$	6	$0.98728 + 1.04804\text{i}$	1.5512
16	$0.67451 + 0.46365\text{i}$	4	$0.98728 + 1.04804\text{i}$	1.5512

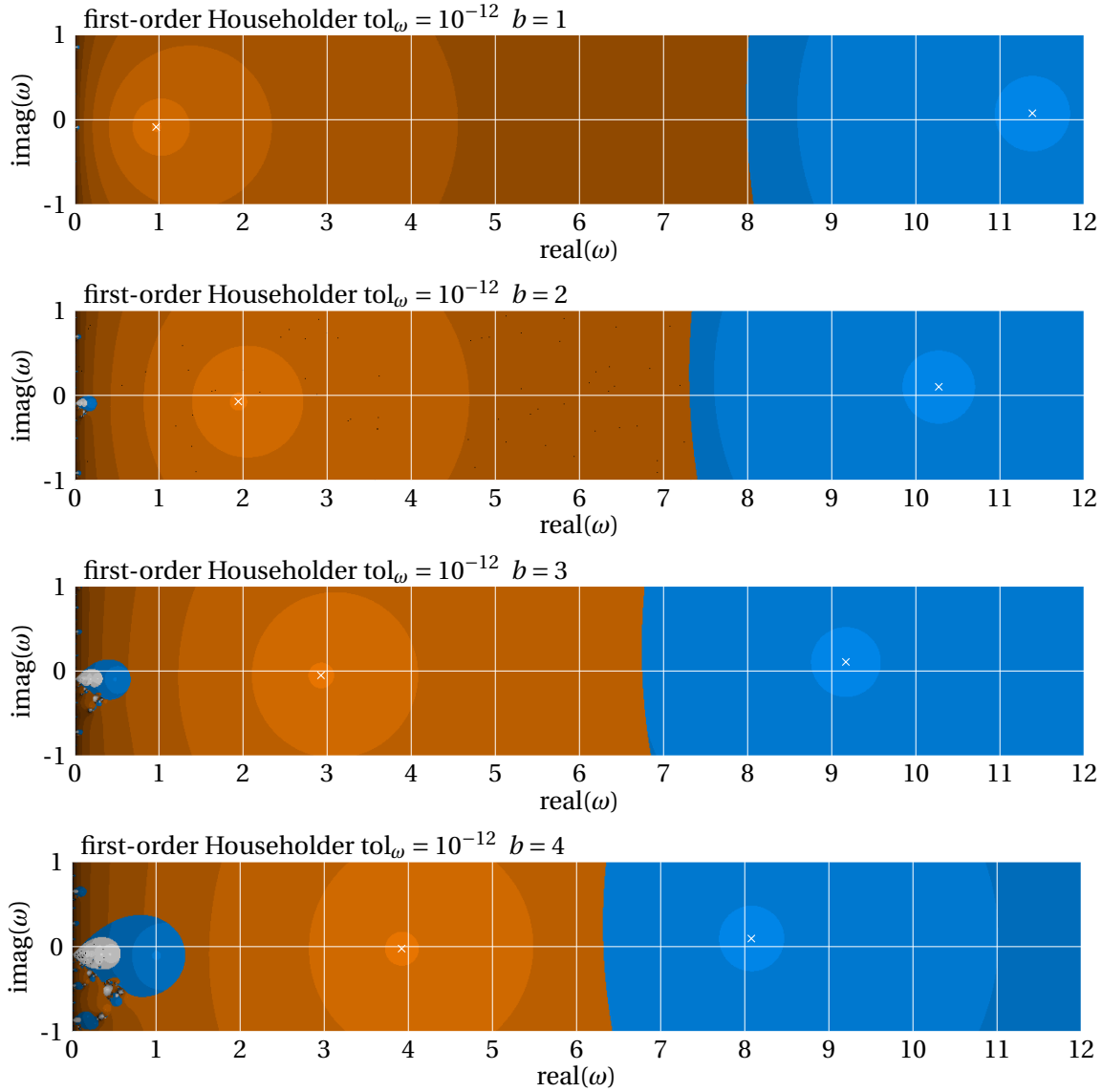

Figure 8.5: Convergence maps for first-order Householder iterations applied to the Kronig-Penney model. The shown region is resolved with 1201×201 points. The four images illustrate the convergence of the spectra of Bloch-surrogate systems corresponding to Bloch wavenumbers $b = 1$, 2, 3, and 4. For each of these systems, two eigenvalues can be found inside the examined domain. They are highlighted with white crosses. The orange and blue shadings illustrate the initial guesses that converge to these two eigenfrequencies. Gray shaded points converge to solutions outside of the shown domain. The darker the shading, the more iteration steps were needed for the solution to converge.

8.7 Application to the MICCA model

In this section, the two-step solution algorithm is applied to the model of the MICCA combustor. Because of its complexity, the brute-force analysis of the convergence properties is conducted. However, based on the previous results, Beyn's algorithm is combined with the third-order Householder method in order to find all eigenvalues inside a subdomain of the complex plane.

The same grid is used in both steps. Figure 8.6 shows the initialization points obtained from Beyn's algorithm and the eigenvalues they finally converged to. Further details are listed in Tab. 8.2. Several initialization points are already fairly close to the eigenvalues. This includes the initialization points 0.2, 1.1, and 1.2 which converge to the modes #M0, #M1, and #M2, respectively. For these modes the difference of the initial points and the converged eigenvalues is so small that it cannot be concluded from the digits given in the table. This is clearly because the same mesh is used in both steps of the solution scheme. However, the eigenvalues obtained from the first step have not reached the set accuracy as two additional iteration steps were required for convergence.

As for the Rijke-tube example, false eigenvalues obtained from Beyn's algorithm are revealed as such in the iteration step. The table also lists the derivatives of the fixed-point map of Nicoud's algorithm at the solutions. Because of the set boundary conditions, these derivatives are identical to the derivatives of the Picard iteration. Although obtained from a unit-cell solution, they are also identical to the derivatives of the full-annulus models. The absolute value of the derivative for #M1 is slightly larger than one. This explains why it was impossible to compute this mode without relaxation, regardless of using the full annulus or a unit-cell model (see Sec. 4.6 and Sec. 5.7). Note that there are more modes than implied by the number of passive solutions. This suggests that some modes are intrinsic. The relatively large derivatives of the modes found from the initialization points 2.3 and 2.5 support this hypothesis, as will be outlined in Chap. 10.

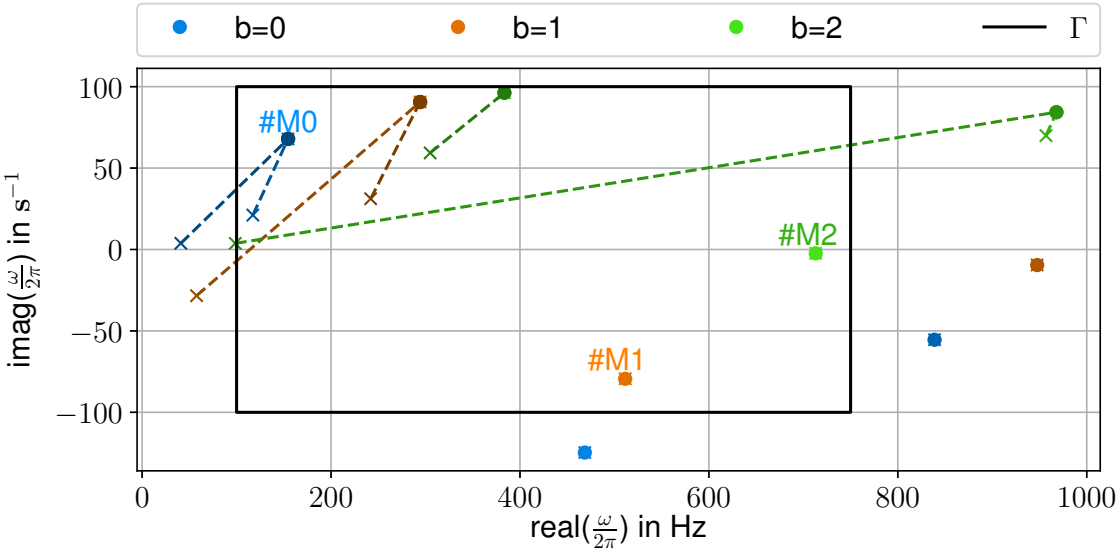

Figure 8.6: Eigenvalues of the MICCA model obtained from the two-step solution procedure. The black rectangle highlights the integration path. Each of its four edges was numerically integrated using ten point Gauss-Legendre quadrature. Crosses highlight the initializing points obtained from Beyn's algorithm. Dots indicate the finally computed eigenvalues. The dashed lines illustrate the convergence. Shades of blue, orange, and green correspond to the Bloch wavenumbers $b = 0$, 1, and 2, respectively. More details are given in Tab. 8.2.

Table 8.2: Eigenvalues of the MICCA model computed by first leveraging Beyn's algorithm and then feeding the results into a third-order Householder solver. ω_{Beyn} are the eigenvalues found from Beyn's method. The column *step* lists the number of iteration steps that are necessary to converge to an accuracy of $\text{tol}_\omega = 10^{-10}\,\text{s}^{-1}$ in the Householder step. The column ω_{House3} indicates the final computed eigenvalue. The last column reports the derivative of Nicoud's fixed-point map at that eigenvalue. Due to the boundary conditions, it is identical to the derivative of the mapping of Picard iteration.

#	ω_{Beyn}	steps	ω_{House3}	$\lvert f'(\omega)\rvert$
Bloch wavenumber $b = 0$				
0.1	468.64721 − 124.70772i	2	468.64721 − 124.70772i	2.10908
0.2→#M0	154.48403 + 67.9054i	2	154.48403 + 67.9054i	0.61227
0.3	838.90268 − 55.44074i	2	838.89931 − 55.44309i	1.00159
0.4 →#M0	117.22876 + 21.12695i	4	154.48403 + 67.9054i	0.61227
0.5→#M0	40.98417 + 3.8081i	5	154.48403 + 67.9054i	0.61227
Bloch wavenumber $b = 1$				
1.1 →#M1	511.37591 − 79.41652i	2	511.37591 − 79.41652i	1.00872
1.2	294.27721 + 90.57508i	2	294.27721 + 90.57508i	1.05457
1.3	947.44172 − 9.49448i	2	947.53909 − 9.5742i	2.35846
1.4	57.65177 − 28.37992i	5	294.27721 + 90.57508i	1.05457
1.5	241.93713 + 31.15392i	4	294.27721 + 90.57508i	1.05457
Bloch wavenumber $b = 2$				
2.1 →#M2	713.10633 − 2.34317i	2	713.10633 − 2.34317i	0.19599
2.2	383.49947 + 96.23613i	2	383.49947 + 96.23613i	10.43539
2.3	956.8928 + 69.92512i	4	967.92717 + 84.30999i	17.50286
2.4	98.57958 + 3.76724i	8	967.92717 + 84.30999i	17.50286
2.5	304.85998 + 59.32842i	5	383.49947 + 96.23613i	10.43539

8.8 Conclusions

The perturbation theory developed in Chap. 6 was used to study the convergence properties of Nicoud's algorithm and the Picard iteration. Additionally, the theory was used to improve Lancaster's generalized Rayleigh quotient iteration. The key modification is the usage of large-order perturbation theory to enable Householder iterations. This improved method can be combined with Beyn's integration-based algorithm, resulting in a solution scheme that is capable of finding all eigenvalues inside a given domain at high accuracy. Although the original incentive to design such a scheme was the need for highly accurate baseline solutions for the perturbation theory, the new solution method in and off itself is a valuable tool.

Both Beyn's algorithm and the Householder iteration impose the same regularity conditions on the nonlinear eigenvalue problem considered. Most notably, it is required that the operator family is analytic in the considered domain. These conditions are stronger than those for Nicoud's algorithm and the Picard iteration. If they are met, the new scheme is definitively to be preferred over these simple fixed-point iterations. See Sec. 3.5 on how to conceive analytic models.

Because the focus of this thesis is on perturbation methods, the discussion focused on Lancaster's algorithm which is a Newton iteration on the eigenvalue level. However, Newton iterations on the vector level might also be considered as a refinement step for solutions obtained from Beyn's algorithm. For instance, *inverse iteration* could be used. The convergence properties might then further improve because the eigenvector information obtained from Beyn's algorithm is exploited. However, this discussion is beyond the scope of this thesis.

Chapter 9

Uncertainty Quantification

Even if a perfect mathematical model would be employed for thermoacoustic stability assessment, it is impossible to manufacture a real-world equivalent which features exactly the parameters specified for the model computation. Modeling of thermoacoustic instabilities inevitably suffers from uncertainties in the parameters. This is a serious issue because stability assessment is a binary decision: a system is stable or not. Especially systems that are predicted to be *marginally* stable might become unstable if an assumed model parameter ε is slightly detuned by some amount $\Delta\varepsilon$. More precisely, while for the modeled system the growth rate $-\mathrm{imag}(\omega(\varepsilon_0))$ is predicted to be less than the assumed system damping α but close to the stability boundary, the actual system might satisfy $-\mathrm{imag}(\omega(\varepsilon_0+\Delta\varepsilon)) > \alpha$.

Uncertainty quantification addresses the question of how uncertainties in the model parameters propagate through the model and affect the predicted outcome. In the thermoacoustics community Monte-Carlo-based risk-factor analysis is a commonly employed method to quantify uncertainties (see, e.g.,[147]). It computes the probability that a system is unstable provided that the uncertainties in the model parameters are known in terms of probability density functions. The probability density functions are used to randomly generate a set of parameter samples and the model is fully evaluated for each of these samples. Finally, the share of sample points that map to unstable eigenfrequencies is considered an estimate for the probability of the system to be unstable.

A general challenge with uncertainty quantification is the sheer number of uncertain parameter combinations to be quantified. In thermoacoustics, possible uncertain parameters other than the interaction index or a time-delay are, e.g., the exact fuel composition, geometry parameters, boundary impedances. The rapid growth of potential parameter combinations with the dimension of the parameter space is commonly referred to as *curse of dimensionality*. Especially annular combustors suffer from this problem because each burner section is associated with an individual set of uncertain parameters. To reduce the computational effort, recently principal component analysis of the uncentered covariance matrix of the gradient vector has been suggested to identify the most influential directions in parameter space [168]. This so-called *active subspace* method was used by Bauerheim et al. to reduce the dimension of the considered parameter space for UQ analysis of the thermoacoustics of an annular combustor based on Monte-Carlo sampling [148]. Ndiaye et al. performed risk-factor analysis for a longitudinal single-flame combustor [169]. As uncertain parameters they considered the interaction index and time delay in a fit n–τ-model.

They showed that 4000 Monte-Carlo samples are sufficient to obtain a reasonable estimate of the statistics of the growth rate. They additionally showed that tuning first-order bi-variate models to the computed dataset allows to reduce the necessary sample size to a few tens. Regression models were also considered by Bauerheim et al. in [147] for annular combustors. The computational cost reductions achieved by the active-subspace and regression methods were complemented by Magri et al. by an adjoint-based perturbation method to quickly evaluate the thermoacoustic Helmholtz equation [126]. A similar analysis was succesfully appplied by Silva et al. to compute the risk factor of an axial laboratory-scale combustor by first and second-order perturbation methods [125].

This chapter aims at further improving the existing UQ methods by (i) suggesting a multi-parameter perturbation theory that allows to estimate the stability for all relevant parameters in an explicit expression $\omega = \omega(\varepsilon_1, \varepsilon_1, \ldots)$ and (ii) using this relation to explicitly compute the stability boundary. This will reduce risk-factor analysis to an integration in parameter space requiring one solution of the thermoacoustic Helmholtz equation only. The proposed method avoids extensive Monte-Carlo simulations or other sample-based UQ strategies.

The content of this chapter is the result of a collaboration with Luca Magri and the presented theory was previously published in [170].

9.1 Multi-parameter perturbation theory

This section presents multi-parameter perturbation theory up to second order. Like for the single-parameter case power series are stipulated to model the dependencies $\omega = \omega(\boldsymbol{\varepsilon})$ and $\widehat{p} = \widehat{p}(\boldsymbol{\varepsilon})$, where $\boldsymbol{\varepsilon} = [\varepsilon_1, \varepsilon_2, \ldots, \varepsilon_P]$ is the vector of considered parameters. Truncation at second order yields the ansätze

$$\omega(\boldsymbol{\varepsilon}_0 + \Delta\boldsymbol{\varepsilon}) = \omega_0 + \sum_{i=1}^{P} \omega_{(i)} \Delta\varepsilon_i + \sum_{i=1}^{P} \sum_{j=1}^{i} \omega_{(i,j)} \Delta\varepsilon_i \Delta\varepsilon_j \tag{9.1}$$

and

$$\widehat{p}(\boldsymbol{\varepsilon}_0 + \Delta\boldsymbol{\varepsilon}) = \widehat{p}_0 + \sum_{i=1}^{P} \widehat{p}_{(i)} \Delta\varepsilon_i + \sum_{i=1}^{P} \sum_{j=1}^{i} \widehat{p}_{(i,j)} \Delta\varepsilon_i \Delta\varepsilon_j. \tag{9.2}$$

They imply that the solution is totally differentiable with respect to the parameters. In particular, the coefficients will be related to the partial derivatives of ω and $\widehat{p}$ by:

$$\omega_{(i)} = \left.\frac{\partial\omega}{\partial\varepsilon_i}\right|_{\boldsymbol{\varepsilon}=\boldsymbol{\varepsilon}_0}, \quad \omega_{(i,j)} = \frac{1}{(1+\delta_{i,j})} \left.\frac{\partial^2\omega}{\partial\varepsilon_i\partial\varepsilon_j}\right|_{\boldsymbol{\varepsilon}=\boldsymbol{\varepsilon}_0}, \quad \widehat{p}_{(i)} = \left.\frac{\partial\widehat{p}}{\partial\varepsilon_i}\right|_{\boldsymbol{\varepsilon}=\boldsymbol{\varepsilon}_0} \tag{9.3}$$

and

$$\widehat{p}_{(i,j)} = \frac{1}{(1+\delta_{i,j})} \left.\frac{\partial^2\widehat{p}}{\partial\varepsilon_i\partial\varepsilon_j}\right|_{\boldsymbol{\varepsilon}=\boldsymbol{\varepsilon}_0}. \tag{9.4}$$

Total differentiability with respect to multiple parameters cannot be assumed for degenerate eigenvalues. This is because of the possible splitting of the degenerate eigenvalue into separate eigen-

values. An example for semi-simple points of a linear eigenvalue problem can be found in [117, p.116]. In general, defective points are not amenable to power-series expansion even in the single-parameter case, see, e.g., [171] for a theory on linear eigenvalue problems. Note that although these references apply to linear eigenvalue problems, they also rule out cases of nonlinear eigenvalue problems because they locally behave like linear eigenvalue problems. Also note that this explains the observation of Bauerheim et al. that polynomial models do not fully capture the stability behavior of a degenerate mode [147]. However, simple eigenvalues admit a multi-parameter expansion into power series [117].

The expansions (9.1) and (9.2) reduce to single-parameter expansions in ε_i if the change $\Delta\varepsilon_j = 0$ for all $j \neq i$. The coefficients $\omega_{(i)}$, $\omega_{(i,i)}$, $\widehat{p}_{(i)}$, and $\widehat{p}_{(i,i)}$ can, therefore, be computed by means of the single-parameter perturbation theory. Only the mixed-term coefficients $\omega_{(i,j)}$ and $\widehat{p}_{(i,j)}$ require an extension of the theory. The reasoning is equivalent to the single-parameter case. The considered operator family is to be expanded into power series. For the second-order multi-parameter series this is:

$$\mathcal{L}(z,\boldsymbol{\varepsilon}) \approx \mathcal{L}_{0,0} + \sum_{i=1}^{P} \left(\mathcal{L}_{0,(i)} + \mathcal{L}_{1,(i)}\Delta z\right)\Delta\varepsilon_i + \sum_{i=1}^{P}\sum_{j=1}^{i} \mathcal{L}_{0,(i,j)}\Delta\varepsilon_i\Delta\varepsilon_j + \mathcal{L}_{1,0}\Delta z + \mathcal{L}_{2,0}(\Delta z)^2. \tag{9.5}$$

By assumption $\mathcal{L}$ is analytic in all its parameters so the coefficients can be found by partial differentiation at $z = z_0$ and $\boldsymbol{\varepsilon} = \boldsymbol{\varepsilon}_0$. They read:

$$\begin{aligned}
&\mathcal{L}_{0,0} = \mathcal{L}|_{\substack{z=z_0\\ \boldsymbol{\varepsilon}=\boldsymbol{\varepsilon}_0}}, \quad \mathcal{L}_{0,(i)} = \frac{\partial}{\partial\varepsilon_i}\mathcal{L}\bigg|_{\substack{z=z_0\\ \boldsymbol{\varepsilon}=\boldsymbol{\varepsilon}_0}}, \quad \mathcal{L}_{0,(i,j)} = \frac{1}{1+\delta_{i,j}}\frac{\partial^2}{\partial\varepsilon_i\partial\varepsilon_j}\mathcal{L}\bigg|_{\substack{z=z_0\\ \boldsymbol{\varepsilon}=\boldsymbol{\varepsilon}_0}},\\
&\mathcal{L}_{1,0} = \frac{\partial}{\partial z}\mathcal{L}\bigg|_{\substack{z=z_0\\ \boldsymbol{\varepsilon}=\boldsymbol{\varepsilon}_0}}, \quad \mathcal{L}_{1,(i)} = \frac{\partial^2}{\partial z\partial\varepsilon_i}\mathcal{L}\bigg|_{\substack{z=z_0\\ \boldsymbol{\varepsilon}=\boldsymbol{\varepsilon}_0}}, \quad \text{and} \quad \mathcal{L}_{2,0} = \frac{1}{2}\frac{\partial^2}{\partial z^2}\mathcal{L}\bigg|_{\substack{z=z_0\\ \boldsymbol{\varepsilon}=\boldsymbol{\varepsilon}_0}}.
\end{aligned} \tag{9.6}$$

The equations determining the coefficients in the ansätze (9.1) and (9.2) are obtained by plugging these ansätze into the eigenvalue problem (6.1) and expanding the operator $\mathcal{L}$ according to Eq. (9.6). Sorting for equal powers of $\Delta\boldsymbol{\varepsilon}$ then yield the desired equations. For the quadratic mixed term $\Delta\varepsilon_i\Delta\varepsilon_j$ it reads:

$$\mathcal{L}_{0,0}\widehat{p}_{(i,j)} = -r_{(i,j)} - \omega_{(i,j)}\mathcal{L}_{1,0}\widehat{p}_0 \tag{9.7}$$

where

$$\begin{aligned}
r_{(i,j)} =& \mathcal{L}_{0,(i)}\widehat{p}_{(j)} + \mathcal{L}_{0,(j)}\widehat{p}_{(i)} + \mathcal{L}_{0,(i,j)}\widehat{p}_0 + \mathcal{L}_{1,0}\left(\omega_{(i)}\widehat{p}_{(j)} + \omega_{(j)}\widehat{p}_{(i)}\right)\\
&+ \mathcal{L}_{1,(i)}\omega_{(j)}\widehat{p}_0 + \mathcal{L}_{1,(j)}\omega_{(i)}\widehat{p}_0 + 2\mathcal{L}_{2,0}\omega_{(i)}\omega_{(j)}\widehat{p}_0.
\end{aligned} \tag{9.8}$$

Except for the coefficients $\omega_{(i,j)}$ and $\widehat{p}_{(i,j)}$, all variables in equation (9.7) are known. The structure of the equation is completely analogous to Eq. (6.12). A solution can, therefore, be found by (i) taking the inner product of the right-hand side with the adjoint solution of the unperturbed problem, (ii) tuning $\omega_{(i,j)}$ such that this inner product vanishes and, thus, solvability is achieved, and (iii) finally solving the above equation for $\widehat{p}_{(i,j)}$ (compare Sec. 6.1).

Although, this section only derived the theory up to second order, generalization to arbitrary orders is straightforward. See Sec. A.2 in the appendix for notes on how to derive the formulae.

9.2 Risk-factor analysis

The risk factor RF is defined as the probability of a mode to be unstable given a specific system with known uncertainties in its parameters. This UQ approach is called a "forward problem" as it studies the propagation of the input parameters to the output quantity. The notion is opposed to "backward problem", which aims at quantifying the uncertainties in the parameters from known fluctuations in the output of the system [172].

Risk-factor evaluation based on statistics of the growth rate

Previous studies [148, 169, 125, 126, 147] computed the risk factor from a probability density function $\mathrm{PDF}_\sigma(\sigma)$ for the growth rate $\sigma := -\mathrm{imag}(\omega)$

$$\mathrm{RF} := \int_0^\infty \mathrm{PDF}_\sigma(\sigma)\,\mathrm{d}\sigma, \tag{9.9}$$

i.e., it is computed as the probability that the growth rate of the mode is positive. Unfortunately, the probability density function PDF_σ is not explicitly known.

The dependence of the growth rate σ on the system parameters $\boldsymbol{\varepsilon}$ is only implicitly known from the model equations. Computing PDF_σ from a known $\mathrm{PDF}_{\boldsymbol{\varepsilon}}$ is, therefore, difficult. It is this difficulty that previous thermoacoustic studies tackled by generating an estimate of PDF_σ by Monte-Carlo sampling. A set of N_{MC} random sample points is generated from the known parameter-statistics and the system is repeatedly solved for each sample point. The results allow to derive statistics on the occurrence of specific growth rates. In particular, an estimate for the risk factor is obtained from the share of sample points that map to positive growth rates. However, given an explicit model $\omega = \omega(\boldsymbol{\varepsilon})$, direct propagation of the parameters to the output variable is possible. This allows to compute the risk factor in parameter space without computing statistics of the growth rate in an intermediate step.

Risk-factor evaluation in parameter space

The probability density function of the growth rate depends on the probability of the parameters $\boldsymbol{\varepsilon}$ to take a certain value. Thus, the risk factor can equivalently be formulated from the statistics of the complex frequency ω or the considered parameters $\boldsymbol{\varepsilon}$:

$$\mathrm{RF} = \int_{E_{\mathrm{unst.}}} \mathrm{PDF}_{\boldsymbol{\varepsilon}}(\boldsymbol{\varepsilon})\,\mathrm{d}\boldsymbol{\varepsilon}. \tag{9.10}$$

Here, $E_{\mathrm{unst.}}$ denotes the set of parameters for which the eigenfrequency of interest is unstable:

$$E_{\mathrm{unst.}} := \left\{\boldsymbol{\varepsilon} \in \mathbb{R}^P \,|\, -\mathrm{imag}(\omega(\boldsymbol{\varepsilon})) = \sigma > \alpha\right\}. \tag{9.11}$$

Given an explicit relation $\omega = \omega(\boldsymbol{\varepsilon})$ the parameter set $E_{\mathrm{unst.}}$ is well defined. As it is assumed that the statistics of the parameters $\boldsymbol{\varepsilon}$ and, in particular, $\mathrm{PDF}_{\boldsymbol{\varepsilon}}(\varepsilon)$ are explicitly known, Eq. (9.10) reduces the risk-factor evaluation to an integration in parameter space. Risk-factor analysis can, therefore, be performed in two steps:

1. Calculation of the stability margin, i.e., the parameters for which $-\mathrm{imag}(\omega(\boldsymbol{\varepsilon})) = \alpha$ in order

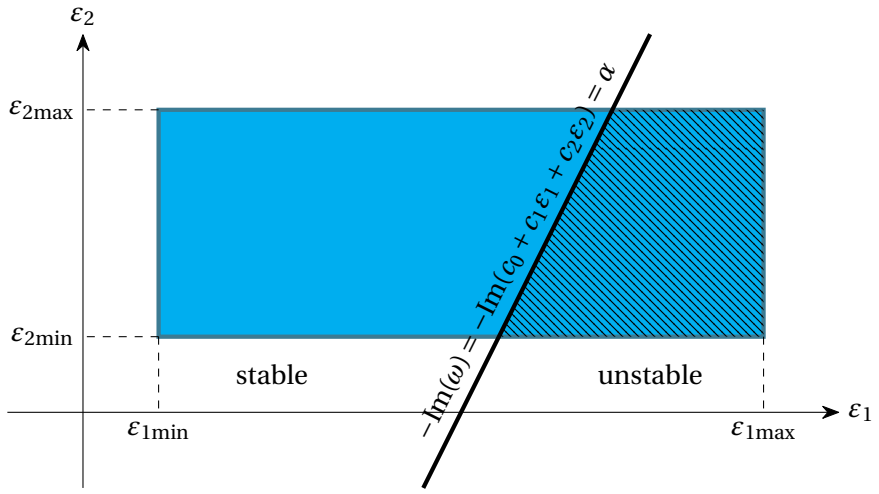

Figure 9.1: Illustration of risk-factor evaluation in parameter space. A linear eigenfrequency model approximates the dependence of the eigenvalue on two parameters ε_1 and ε_2. A uniform parameter distribution is assumed for both parameters. Thus, the parameters may take values within the blue shaded area with same probability. The stability boundary is well defined from the linear model. It divides this area into two parts. The part lying in the unstable region is highlighted by the hatching. Its size relative to the total parameter set (blue) is a measure for the risk factor.

to define $E_{\text{unst.}}$.

2. Algebraic integration of $\mathrm{PDF}_{\boldsymbol{\varepsilon}}(\varepsilon)$ over $E_{\text{unst.}}$ in order to compute the risk factor.

Taking a two-parameter model with uniformly distributed parameters as an example, the probability density function reads:

$$\mathrm{PDF}_{\boldsymbol{\varepsilon}}(\varepsilon_1,\varepsilon_2) = \begin{cases} \frac{1}{(\varepsilon_{1\max}-\varepsilon_{1\min})(\varepsilon_{2\max}-\varepsilon_{2\min})} & \text{if } \boldsymbol{\varepsilon} \in [\varepsilon_{1\min},\varepsilon_{1\max}] \times [\varepsilon_{2\min},\varepsilon_{2\max}] \\ 0 & \text{else} \end{cases} \tag{9.12}$$

Assuming a linear parameter model

$$\omega(\varepsilon_1,\varepsilon_2) = c_0 + c_1\varepsilon_1 + c_2\varepsilon_2 \tag{9.13}$$

the stability boundary is a straight line. How it intersects the set of considered parameters will determine the risk factor. For this two-dimensional example the risk factor will be the ratio of the share of the unstable set of parameters to the total set of parameters, because each parameter point is uniformly weighted. Figure 9.1 schematically illustrates the example.

In this work the model will be conceived by perturbation theory. Note that *polynomial chaos expansion* might also be considered as a technique to generate such a model. See, e.g., [173] for an applications of such a method in computational fluid mechanics. Following the traditional classification of UQ methods, the method proposed in this work is characterized as intrusive, as the perturbation theory requires the implementation of a special data structure for the discretized operator family $\mathbf{L}(z;\boldsymbol{\varepsilon})$ (see Sec. 6.3).

Table 9.1: Risk factor of #R1 computed with various methods. The RF was computed using 4225 uniform sample points, as many MC sample points, as well as first and second-order multi-parameter perturbation theory. All methods were tested with the FEM and the network discretization of the Rijke-tube model.

	uniform	MC	1st ord.	2nd ord.
FEM	0.7299	0.7309	0.7646	0.7319
network	0.6698	0.6755	0.6964	0.6753

9.3 Application to the Rijke-tube model

This section exemplifies the theory by considering #R1 of the Rijke-tube model. Both the network and the FEM discretization of the model are studied. The interaction index n and time delay τ are considered as uncertain parameters. The respective probability density functions are assumed to be uniform and centered around the baseline values $n_0 = 1$ and $\tau_0 = 2$. The maximum deviation from these mean values is $\pm 10\%$. In virtue of the principle of maximum entropy, uniform distributions are the least biased PDF for the input parameters taking into account that no further assumption is made for the input parameters [174]. For a short discussion of this principle with regard to UQ in thermoacoustics see also the remarks in [125]. Note, however, that any other PDF can also be used with the methods exemplified here. For the current test case it is assumed that the system damping is $\alpha = 0.25$. This renders mode #R1 marginally unstable. Four methods are tested and compared:

(i) uniform sampling of the considered parameter set using a grid of $65^2 = 4225$ equidistant sample points,

(ii) MC sampling with the same number of points,

(iii) leveraging first order multi-parameter perturbation theory, and

(iv) second-order multi-parameter perturbation theory.

All methods are applied to both the FEM and the network discretization of the Rijke-tube model. Table 9.1 compares results from these four approaches. The tests show similar characteristics for the FEM and the network discretization: uniform sampling, the MC approach, and the second-order perturbation method yield similar results. In comparison to these three methods, the linear perturbation method yields slightly deviating results. Nonetheless, the risk-factors estimates differ for the two discretization methods. This can be attributed to the discretization error. As explained in Sec. 4.4, the FEM model is not as accurate as the network discretization. Uncertainty quantification inherits the biases of the model it is based on. Although the problem can be fixed for the current example by increasing the resolution of the FEM mesh, modeling and discretization errors are, in general, to be considered when interpreting computed risk factors. With respect to the deployed numerical models, however, risk factors are computed correctly.

Figure 9.2 further illustrates how the considered parameters $n, \tau \in [0.9, 1.1] \times [1.8, 2.2]$ are mapped into the complex plane. The graphics explicitly depict 17 out of 65 parameter levels for both the interaction index and the time delay and their images in the complex plane. The data for these levels is a subset of the 4225 equidistantly distributed sample points. The figure also shows

the stability boundary computed by (i) a line-search algorithm, (ii) linear, and (iii) the quadratic multi-parameter adjoint-based perturbation method. The line-search algorithm exploits the entire data obtained from the 4225 equidistantly distributed sample points. Provided it exists, for each of the 65 explored levels of n a pair of directly neighbored data points is identified which is mapped to different sides of the stability boundary. The position of the stability boundary between these two points is then obtained by linearly interpolating their growth rate and solving the interpolant for $\sigma(\tau) = \alpha$. Because of the high density of the sample points, the line-search result can be considered as exact. The stability boundary is slightly curved. This explains why the second-order perturbation theory gives a better estimate than the linear theory.

Figure 9.3 shows results obtained from MC sampling. The same set of 4225 random MC sample points drawn from a uniform PDF is used for both discretization types of the model. As for the grid sampling the MC strategy allows for a reasonable prediction of the stability boundary and, hence, the risk factor. The convergence of both sampling strategies is illustrated in Fig. 9.4. Additionally, the risk-factor estimates obtained from perturbation theory are also shown. For the example discussed here, about 1000 sample points are necessary to reach the accuracy of the second-order perturbation result. This underlines the savings in the computational costs that are enabled by perturbation theory.

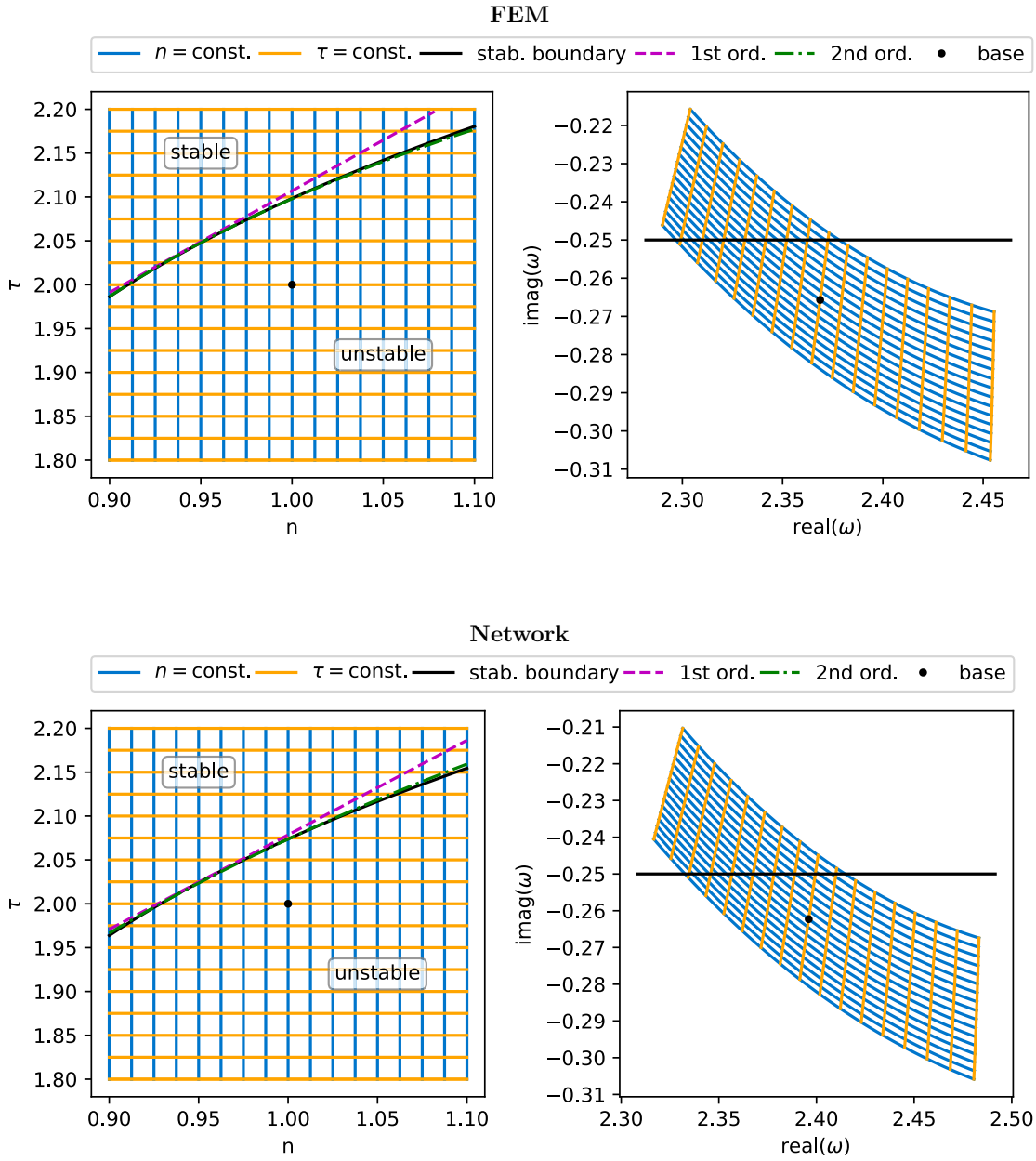

Figure 9.2: Illustration of the mapping of the parameters to complex eigenfrequencies using a uniform grid of sample points. 17 levels are shown for both parameters n and τ. The computation of the stability boundary (solid black) from a line-search algorithm is based on 65 levels for both parameters. Both the FEM and the network discretization show the same characteristics. Already, linear multi-parameter perturbation theory results in a fair estimate (dashed purple) of the stability boundary. However, because the stability boundary is slightly curved the second-order theory gives a much better estimate (dashed green).

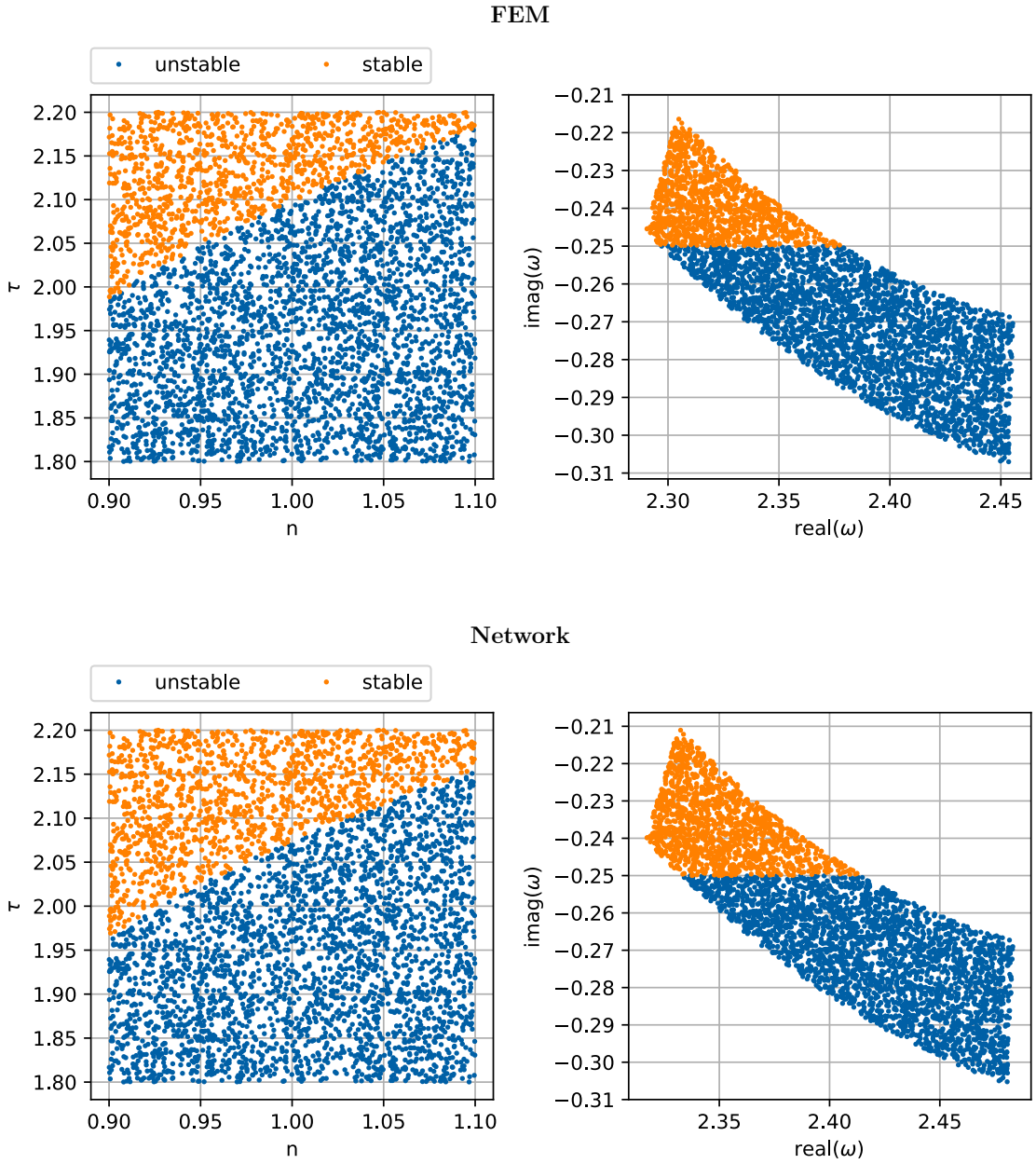

Figure 9.3: Results of the Monte Carlo study. The same set of 4225 randomly generated points is used to study both the FEM and the network discretization of the model. These sample points were drawn from a uniform probability density function. The color of the dots indicates whether the sample points are mapped to stable (orange) or unstable (blue) solutions. Extensive MC sampling results in a good estimate for the portion of the considered parameter set that results in unstable solutions, i.e., the risk factor. However, this approach is rather slow. See Fig. 9.4 for information on the convergence.

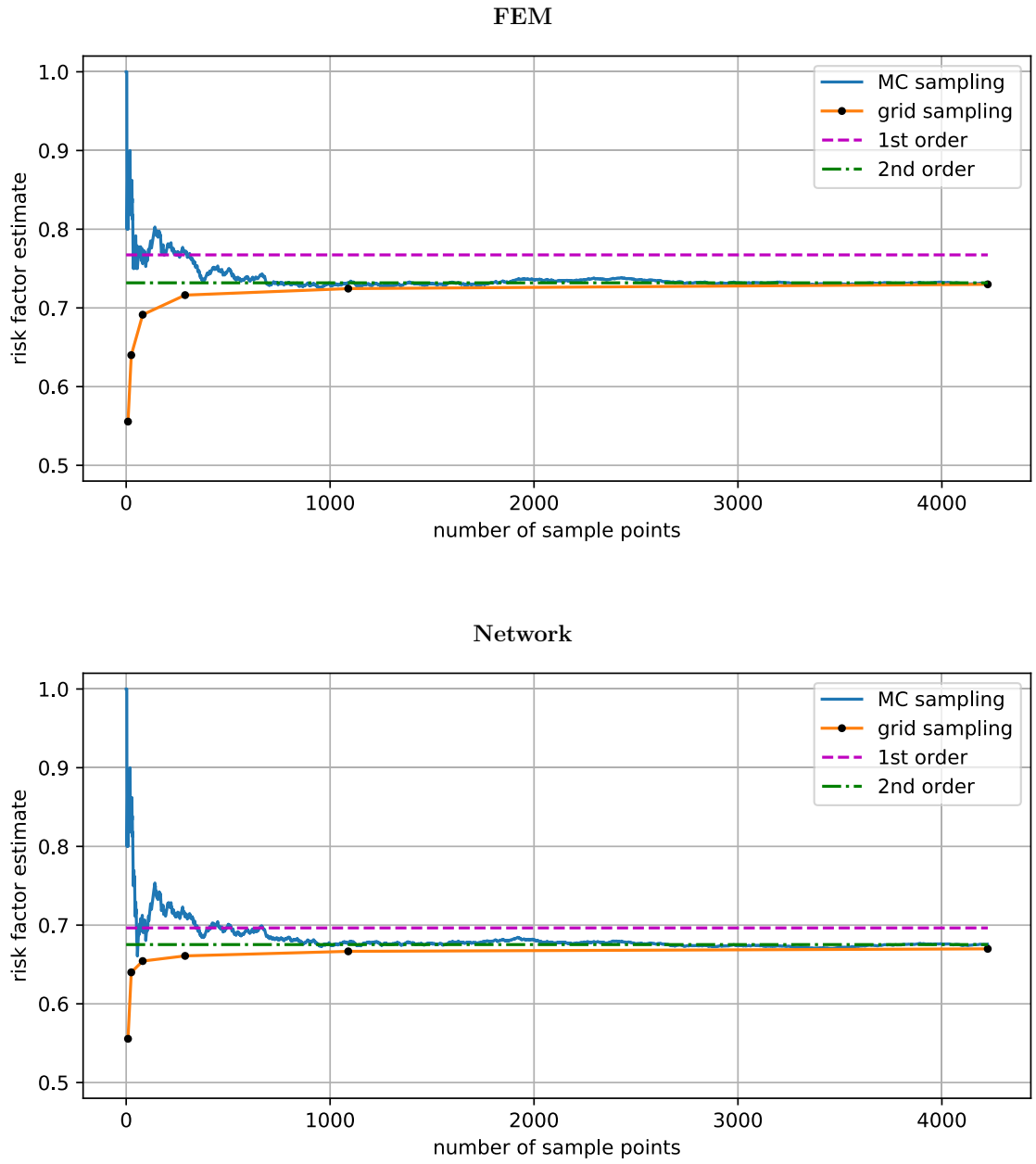

Figure 9.4: Convergence of the sampling methods. The uniform sampling was only peformed for sampling grids featuring 2^2,4^2, 9^2, 17^2, 33^2, and 65^2 sample points (black dots). The estimates obtained from linear and quadratic perturbation theory are depicted for comparison. They require only a single solution of thermoacoustic Helmholtz equation. The estimate obtained from quadratic perturbation theory is accurate as results obtained from a few thousand samples.

9.4 Conclusions

In previous works, the risk factor was computed via computationally expensive sampling techniques. Multi-parameter perturbation theory allows for estimating the risk factor based on a single solution of the nonlinear eigenvalue problem. Second-order approximations to the stability boundary showed very good agreement with exact results. A third-order theory might result in even better estimates. If the domain of convergence of the power series is small, a few more baseline solutions distributed along the stability boundary might be needed to approximate it. Such an algorithm would also start with a single baseline solution and then successively reevaluate the eigenvalue problem at parameter points for which the truncation error of the already obtained asymptotic expansions becomes unacceptably large. This truncation error would be estimated from perturbation theory of the next order (compare Sec. 6.4). However, for the current test case, the estimate obtained from the second-order theory and a single baseline solution appears to be reasonable. In view of these rather small perturbations, a second-order theory may also be sufficient in practical applications. In many cases, the new method is to be preferred over the traditional sampling-based techniques. A notable exception are operating conditions close to an *exceptional point* as will be explained in the next chapter. A further challenge are degenerate eigenvalues which cannot be expanded into multi-variate power series. Future work should investigate how to expand these into asymptotic series.

Part IV

Exceptional Points

Chapter 10

Nonlinear eigenvalue problems IV: exceptional points

It is well known that spectra of annular combustion chambers feature degenerate eigenvalues. However, the thermoacoustic literature mainly focuses on semi-simple eigenvalues (see Part II of this thesis and references therein). This chapter shows that even the spectra of a simple thermoacoustic system like the Rijke tube, parameter combinations exist for which the eigenvalue is defective. Following a classification introduced by Kato [117], these points are called *exceptional points*.

The chapter is a first step towards a better understanding of exceptional points in thermoacoustic spectra. The implications of EPs on eigenvalue sensitivity are discussed. In particular, this includes a deep connection to the convergence radii of the power series obtained from perturbation theory. Furthermore, it is shown how to compute parameter combinations to yield exceptional points. The theory is exemplified on the basis of the Rijke-tube model.

The presented theory is the result of intense discussions with Luca Magri, Camilo Silva, Philip Buschmann, Alessandro Orchini and Jonas Moeck. Parts of the theory were previously published in [175].

10.1 Introduction

Beginning with problems from non-Hermitian quantum mechanics more and more physical phenomena in various fields have been found that are associated with exceptional points. This includes mechanics, electromagnetism, laser physics and many more, see [176] for a collection of topics involving EPs. In particular, there are acoustic phenomena that are governed by exceptional points (see, e.g., [177, 178]).

This raises the question whether exceptional points also play a role in the spectra of thermoacoustic operator families. Ignoring symmetry effects, it is, indeed, more likely for non-normal operators to encounter defective eigenvalues than semi-simple degenerate ones because less parameters are needed to find an exceptional point [179]. However, until recently, the thermoacoustic literature did not focus on aspects of defective eigenvalues. Consequently, the exceptional points were neither named as such nor explicitly considered to explain the dependence of thermoacous-

tic spectra on their parameters. It was tacitly assumed that defective eigenvalues cannot be found in the spectra of thermoacoustic systems. Yet, not identified as such, they can be found in recent work related to thermoacoustics. Sogaro et al. discuss an interaction of acoustic and intrinsic modes using a network discretization of a Rijke tube. They report high sensitivities with respect to the flame position and the reflection coefficients at the inlet and outlet of the tube [180]. Similar results were found by Silva et al. when studying the sensitivity with respect to the time-delay and the interaction index [181]. Note that high eigenvalue sensitivities are typically encountered in the vicinity of exceptional points. Indeed, the eigenvalue sensitivity at an exceptional point is infinite. Juniper and Sujith already related the high eigenvalue sensitivity in discretizations of a Rijke tube to eigenvalue multiplicities larger than one [182] – i.e., degenerate eigenvalues. The discussion, however, did not focus on the distinction of defective and semi-simple degenerate eigenvalues.

The next section outlines why the eigenvalue sensitivity in the vicinity of exceptional points is high. The high eigenvalue sensitivity will be used as key criterion to compute the parameter combinations that lead to exceptional points in thermoacoustic spectra.

10.2 Eigenvalue sensitivity at exceptional points

The perturbation methods introduced in Chap. 6 express the dependence of the eigenvalue ω on some parameter in terms of power-series expansions. These power-series expansions, only exist if the relation $\omega = \omega(\varepsilon)$ is analytic, i.e., is infinitely often differentiable with respect to the parameter. In particular, this implies a finite sensitivity with respect to the model parameter, viz:

$$\left|\frac{\partial\omega}{\partial\varepsilon}\right| < \infty. \tag{10.1}$$

A major result from the algebra of linear eigenvalue problems is that, if the corresponding eigenvalue is semi-simple (i.e., algebraic and geometric multiplicity coincide), the parameter sensitivity is finite [117, Theorem II-2.3]. Because the operator families discussed in this thesis can be linearized with respect to both the eigenvalue and the parameter

$$\mathbf{L}(z_0 + \Delta z; \varepsilon_0 + \Delta\varepsilon) \approx \mathbf{L}_{0,0} + \Delta z\mathbf{L}_{1,0} + \Delta\varepsilon\mathbf{L}_{0,1} \tag{10.2}$$

the sensitivity of semi-simple eigenvalues must also be finite.

If the eigenvalue is defective, however, the sensitivity might be infinite. Thus, an exceptional point cannot be approximated in terms of power-series expansions. Instead, Puiseux series have to be used [117, 179, 183]. These are series expansions in fractional powers of $\Delta\varepsilon$. This chapter considers defective eigenvalues with algebraic multiplicity 2 and geometric multiplicity 1. In this case the asymptotic expansion of the eigenvalue drift reads:

$$\omega = \omega_0 + \omega_1(\Delta\varepsilon)^{\frac{1}{2}} + o(\Delta\varepsilon) \quad \text{as} \quad \Delta\varepsilon \to 0. \tag{10.3}$$

Except for the special case $\omega_1 = 0$ the sensitivity will, thus, be infinite.

10.3 Computation of exceptional points from the dispersion relation

Mathematically, it is well known that non-Hermitian complex-valued operator families can be tuned by two real parameters to feature exceptional points, see, e.g., [179] and references therein. Because exceptional points are the root cause for the infinitely large parameter sensitivity, the sensitivity can be employed to identify exceptional points.

Assume the thermoacoustic system depends on two real modeling parameters ε_1 and ε_2. Then, the thermoacoustic eigenvalue problem in finite-dimensional form reads

$$\mathbf{L}(\omega;\varepsilon_1,\varepsilon_2)\boldsymbol{p} = 0\,. \tag{10.4}$$

By taking the determinant of $\mathbf{L}$, a dispersion relation can be obtained, the roots of which define solutions of the eigenvalue problem:

$$\det(\mathbf{L}(\omega;\varepsilon_1,\varepsilon_2)) =: D(\omega;\varepsilon_1,\varepsilon_2) = 0\,. \tag{10.5}$$

In order for the eigenvalue to feature an algebraic multiplicity greater than one, at least the first derivative of the dispersion relation with respect to ω must also vanish

$$\frac{\partial D}{\partial \omega}(\omega;\varepsilon_1,\varepsilon_2) = 0\,. \tag{10.6}$$

Finding a solution $(\omega,\varepsilon_1,\varepsilon_2)$ to the equations (10.5) and (10.6) will, hence, yield a degenerate eigenvalue. This eigenvalue will be defective if the sensitivity of ω with respect to ε_1 is infinitely large. The derivative of ω with respect to ε_1 can be computed in virtue of the implicit function theorem from the dispersion relation:

$$\frac{\partial \omega}{\partial \varepsilon_1} = -\frac{\partial D}{\partial \varepsilon_1} \Big/ \frac{\partial D}{\partial \omega}. \tag{10.7}$$

Because of the degeneracy condition (10.6), the denominator in the above equation vanishes. Consequently, the eigenvalue sensitivity will be indeed infinite as long as $\frac{\partial D}{\partial \varepsilon_1} \neq 0$. If the eigenvalue is semi-simple, then $\frac{\partial D}{\partial \varepsilon_1} \neq 0$ because these eigenvalues feature a finite sensitivity. However, if the degeneracy is not induced by a special symmetry, this is a non-generic case. This is the main reason why in absence of symmetry it is more likely to encounter defective than semi-simple degenerate eigenvalues.

10.4 Application to the network discretization of the Rijke-tube model

This section exemplifies the theory with the network model of the Rijke tube. The interaction index n and the time delay τ are considered as the two parameters of interest. All other parameters are fixed to the same values as in the previous chapters ($c_1 = 1$, $c_2 = 2$, $L = 1$, $x_{\mathrm{ref}} = x_{\mathrm{flm}} = 1/2$, $Z_{\mathrm{in}} = \infty$ and $Z_{\mathrm{out}} = 0$). In this case the dispersion relation reduces to:

$$D(\omega;n,\tau) = \left(1 + n\exp(-\mathrm{i}\omega\tau)\right)\sin\left(\frac{\omega}{2}\right)\sin\left(\frac{\omega}{4}\right) + 2\cos\left(\frac{\omega}{2}\right)\cos\left(\frac{\omega}{4}\right) \tag{10.8}$$

which can be easily differentiated with respect to ω

$$\frac{\partial}{\partial\omega}D(\omega;n,\tau) = -\mathrm{i}n\tau\exp(-\mathrm{i}\omega\tau)\sin\left(\frac{\omega}{2}\right)\sin\left(\frac{\omega}{4}\right)+\frac{1}{2}(1+n\exp(-\mathrm{i}\omega\tau))\cos\left(\frac{\omega}{2}\right)\sin\left(\frac{\omega}{4}\right) + \frac{1}{4}(1+n\exp(-\mathrm{i}\omega\tau))\sin\left(\frac{\omega}{2}\right)\cos\left(\frac{\omega}{4}\right)-\sin\left(\frac{\omega}{2}\right)\cos\left(\frac{\omega}{4}\right)-\frac{1}{2}\cos\left(\frac{\omega}{2}\right)\sin\left(\frac{\omega}{4}\right). \quad (10.9)$$

Solving the equations (10.8) and (10.9) numerically using SciPy's FSOLVE command allows to find several exceptional points. Table 10.1 lists the eigenvalue of the passive mode #R1 ($n = 0$) together with exceptional points found in its vicinity.

Table 10.1: Eigenvalue of the passive mode #R1 (highlighted in black) and some nearby exceptional points. The parameters n and τ are given to ten decimal places. With this precision, two eigenvalues are found to be identical to 6 decimal places.

#	n	τ	real(ω)	imag(ω)
#R1	0	-	2.461918	0
1.a	0.7181285732	0.8523499542	2.846933	0.812364
1.b	0.2323023022	3.2641053136	2.513530	0.290073
1.c	−0.3600234302	2.0270435614	2.578045	0.437400
1.d	0.1335954015	5.7851804857	2.479662	0.169601
1.e	0.0715946446	10.8696641251	2.467093	0.091488
1.f	−0.0810286207	−9.5966148444	2.468534	−0.103464

The list is not meant to be exhaustive in any regard, nor are the listed exceptional points chosen by any systematic rule. However, it exemplifies that various exceptional points can be found. Note that the exceptional point 1.f is unphysical as it features a negative delay time. This is not surprising as the exceptional points were merely defined as an algebraic feature rather than a physically motivated aspect. However, taking for instance the exceptional point 1.a from Tab. 10.1 the role of exceptional points for the interaction of acoustic and intrinsic modes can be exemplified. This is the topic of the next section.

Interaction of intrinsic and acoustic modes at an exceptional point

In line with the findings of [180] and [181], at an exceptional point, an acoustic and an intrinsic mode interact. This section studies the phenomenon in the vicinity of the exceptional point 1.a. Because two eigenmodes are involved in the process, Beyn's algorithm is used to compute all eigenvalues that occur in a circular domain around the eigenfrequency corresponding to the exceptional point. This allows to track the trajectories of the eigenfrequencies when varying the system parameters. The circle has a radius of $R = 1.25$, and 16 equidistantly distributed points were used for trapezoidal quadrature.

Figure 10.1 a) shows the interaction of an acoustic and an intrinsic mode at the considered exceptional point, when fixing the time delay to the exceptional value and increasing the interaction index n from 0. Two eigenfrequency trajectories are found to coalesce at the exceptional point. One originates from the real axis and can, therefore, be classified as acoustic eigenfrequency. The other one features an increasingly high imaginary part, the lower the interaction index is. Indeed, for $n = 0$ its imaginary part would be infinite, i.e., the mode does not exist in the absence of a

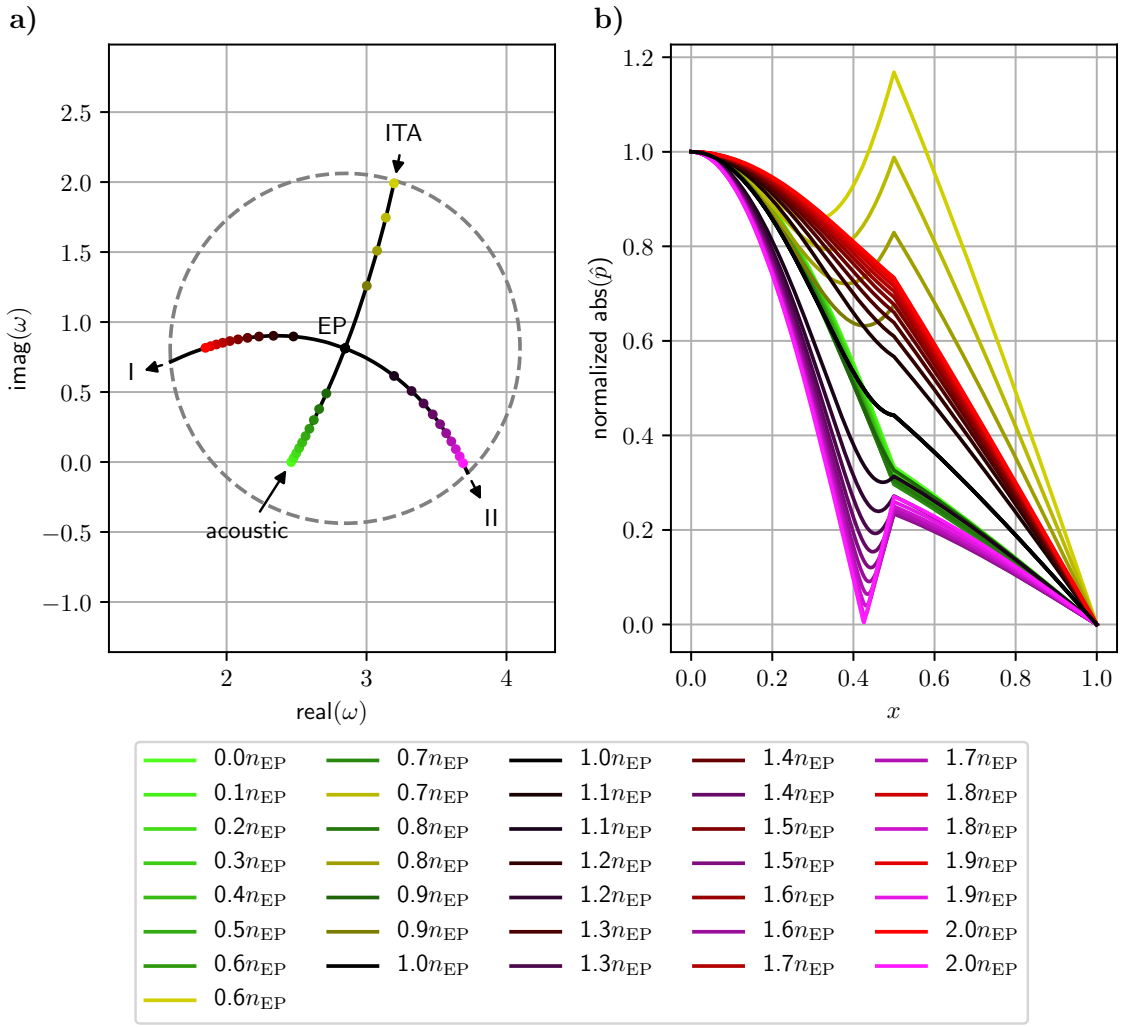

Figure 10.1: Interaction of acoustic and intrinsic modes at the exceptional point 1.a.
a) Eigenvalue trajectories in the complex plane when setting $\tau = \tau_{\mathrm{EP}}$ and varying n. The dashed circle illustrates the contour Γ utilized for the solution of the eigenvalue problem with Beyn's method. As the interaction index n is increased from 0, an acoustic and an intrinsic eigenvalue trajectory coalesce, merge at $n = n_{\mathrm{EP}}$, and finally depart in opposite directions.
b) Mode shapes for various values of n corresponding to the eigenvalues marked by dots of the same color in the left subfigure. As the eigenvalues coalesce, also the mode shapes become identical at $n = n_{\mathrm{EP}}$ (black line).

flame. It is, thus, an intrinsic thermoacoustic mode. At $n = n_{\mathrm{EP}}$ the two trajectories merge. A further increase of the interaction index causes the trajectories to depart in opposite directions along lines that are orthogonal to the previous paths. Note that while the trajectories can be uniquely associated to either the acoustic or the intrinsic mode for values of $n < n_{\mathrm{EP}}$, this is not possible for larger values of n. The trajectories for $n > n_{\mathrm{EP}}$ will, therefore, be referred to as branch I and II in the following. That the branches I and II are orthogonal to the acoustic and the thermoacoustic branch is a generic feature of an exceptional point with algebraic multiplicity 2 and real parameters. This is because due to Eq. (10.3) the eigenvalue drift is proportional to $(\varepsilon - \varepsilon_{EP})^{\frac{1}{2}}$, which in turn is proportional to $\pm$i if $\varepsilon < \varepsilon_0$ and ± 1 if $\varepsilon > \varepsilon_0$. Thus, there is a 90° degree phase shift in the eigenvalue drift. Note that this kink in the trajectories is a graphical manifestation of the infinite parameter sensitivity, as the trajectories would be smooth lines for finite sensitivities.

Figure 10.1 b) depicts the modes shapes corresponding to the trajectories shown in Fig. 10.1 a). As the interaction index is increased, the mode shapes corresponding to the acoustic (green) and the intrinsic (yellow) branch become increasingly similar. At the exceptional point ($n = n_{\mathrm{EP}}$, black) there is only one distinct mode shape, because the corresponding eigenvalue is defective. Further increasing the interaction index yields distinct mode shapes associated to branch I (red) and II (purple) that increasingly deviate from each other. Note how the mode shape corresponding to the exceptional point appears to be rather isolated in the center of the figure. While the shown mode shapes correspond to 20 equidistantly distributed samples of n, the largest change in the mode shapes is found for interaction indices n close to n_{EP}. This indicates that the mode-shape sensitivity is also high around the exceptional point. Indeed the mode shape is also to be expanded in a Puiseux series [179]. Similarly, a large spread of the illustrated eigenvalues can be seen around the EP in Fig. 10.1 a).

Both figures show that in the vicinity of the exceptional point the eigenvalue sensitivity is high. Indeed, the high parameter sensitivity observed in previous work can be explained with the presence of an exceptional point. This is further illustrated in Fig. 10.2. It shows the dependence of the eigenvalue on the parameters n and τ in the vicinity of the exceptional point.

When varying n (Fig. 10.2 a)), the eigenvalue trajectories originating from the acoustic mode cannot penetrate the exceptional branches. Therefore, even if initially stabilized by an increase of n, increasing n will finally destabilize the associated eigenmodes. Similarly, intrinsic trajectories also cannot penetrate the exceptional branches. Four trajectories highlight slightly mistuned exceptional branches where $\tau = \tau_{\mathrm{EP}} \pm 0.003\tau_{\mathrm{AC}}$. These trajectories follow paths close to the exceptional ones. Yet, they do not cross each other. Like two ships approaching each other very closely, the two trajectories eventually veer, avoiding their paths to cross. This behavior of eigenfrequency trajectories is known as *avoided crossings* in quantum mechanics (e.g., [179]) and *mode veering* in structural mechanics (e.g., [184]) and generally appears if the chosen parameters are close to a degenerate point. This scenario is more relevant, because it is much less likely to encounter an exceptional point in a thermoacoustic model than being just close to it. Note that the only trajectory crossing the exceptional branches is not associated to the two eigenmodes interacting at the exceptional point.

When varying τ at the exceptional point, the topology of the trajectories changes (Fig. 10.2). Parametrization in terms of the time delay does not allow for a classification of the branches in terms of acoustic and intrinsic modes. However, the EP induces the same characteristics: two trajectories coalesce, and split again and the sensitivity around the exceptional point is high (note

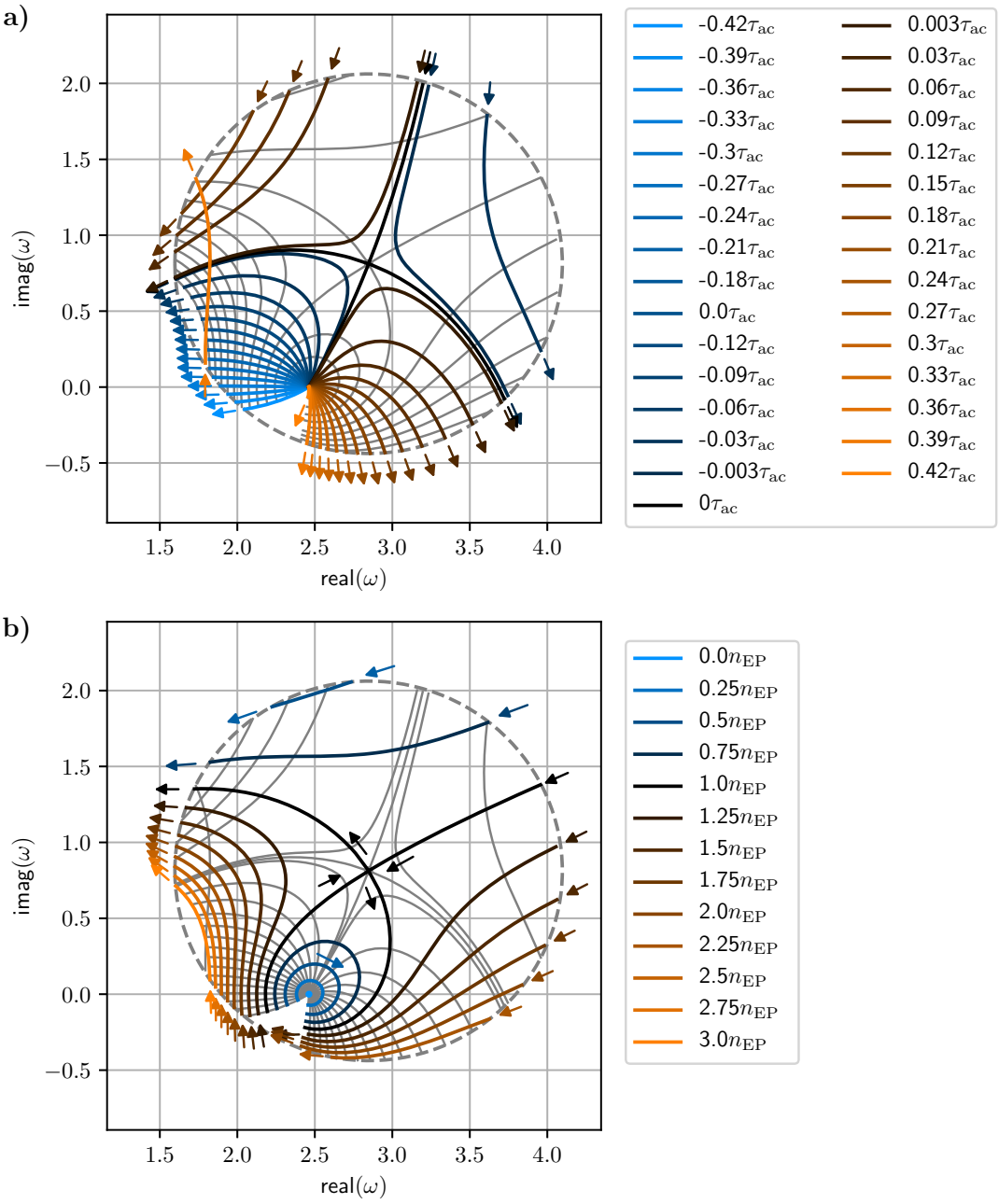

Figure 10.2: Eigenvalue dependence on n and τ in the vicinity of an exceptional point.
a) Trajectories parametrized in n for various levels of τ. The arrows indicate the direction of increasing values of n. Thin gray lines highlight constant values of n. The values in the labels indicate the deviation from τ_{EP}. Note that $\tau_{\mathrm{ac}} = \frac{2\pi}{\omega_{\#R1}}$.
b) Trajectories parametrized in τ for various levels of n. The arrows indicate the direction of increasing values of τ. Thin gray lines highlight constant values of τ.

the spread between the lines close to the exceptional value).

Because the trajectories cannot cross the exceptional branches, for $n < n_{\mathrm{EP}}$ some trajectories are trapped and appear to circle around the passive eigenfrequency. Please note, however, that trajectories parametrized in τ cannot be periodic. As can be concluded from the following rationale.

Trivially, if all model parameters stay the same, the same eigenvalues are found. In the current case, the flame response f is only a function of complex frequency, interaction index, and time delay $f = f(-\omega, n, \tau) = n\exp(-\mathrm{i}\omega\tau)$. In order to find the same eigenfrequency ω with different values of τ and n, the following equation must, therefore, hold:

$$n\exp(-\mathrm{i}\omega\tau) = n'\exp(-\mathrm{i}\omega\tau'). \tag{10.10}$$

Division by $n'\exp(-\mathrm{i}\omega\tau)$ yields

$$\frac{n}{n'} = \exp(-\mathrm{i}\omega\underbrace{(\tau'-\tau)}_{:=\Delta\tau}) = \exp(\omega_{\mathrm{I}}\Delta\tau)\left[\cos(\omega_{\mathrm{R}}\Delta\tau) - \mathrm{i}\sin(\omega_{\mathrm{R}}\Delta\tau)\right] \tag{10.11}$$

where ω_{R} and ω_{I} denote the real and imaginary part of ω, respectively. Because n and n' are real parameters the shift in the delay time $\Delta\tau$ must be such that $\sin(\omega_{\mathrm{R}}\Delta\tau) = 0$. Hence, $\omega_{\mathrm{R}}\Delta\tau$ is a multiple of π. This in turn implies that $\cos(\omega_{\mathrm{R}}\Delta\tau) = (-1)^k$ where k is some integer. Finally, by substitution of $\Delta\tau_k = \frac{k\pi}{\omega_{\mathrm{R}}}$ into Eq. (10.11), a corresponding factor for n can be found:

$$\frac{n}{n'_k} = (-1)^k \exp\left(k\pi\frac{\omega_{\mathrm{I}}}{\omega_{\mathrm{R}}}\right). \tag{10.12}$$

Thus, there are changes to τ which permit to find the same eigenfrequency again. However, this is only possible if the interaction index is adjusted accordingly. Only solutions with purely real eigenfrequencies do not require any adjustment of the interaction index. However, the assumption that trajectories of the eigenfrequency in the complex plane when parameterized by τ are, at least for small interaction indices, periodic loops around the passive eigenfrequencies is wrong. This is because such a loop by definition contains almost exclusively eigenfrequencies with non-vanishing imaginary parts. And the above rationale shows that one such eigenfrequency cannot be recovered by changing τ without appropriately changing n, too. A complete discussion of the true topology of such trajectories is beyond the scope of this thesis. The key point here is that the exceptional point determines whether the trajectories circle around the passive eigenfrequency or not. Bauerheim et al. report similar trajectories for an annular combustor when varying the time delay [147, Fig. 8]. Depending on whether the interaction index is less or greater than a certain threshold, the trajectories encircle one or two eigenmodes. Apparently, this *weak* or *strong coupling* of eigenmodes is also governed by an exceptional point. However, it concerns the interaction of two acoustic modes.

Because the determinant of large matrices cannot be reliably calculated, the proposed approach is only suited for low-dimensional discretizations such as network models. The next section discusses a the connection between exceptional points and perturbation theory and presents a method for the computation of exceptional points that is not based on determinants.

10.5 Implications for perturbation theory

From a mathematical viewpoint, the choice of taking the interaction index n and the time delay τ as the two model parameters to obtain an exceptional point is rather arbitrary. Another choice of parameters for finding an exceptional point would be the real and the imaginary part of the interaction index n. Although unphysical, this choice has a deep connection to perturbation theory, as it finally explains the limited convergence radii of single-parameter perturbation theory.

Because exceptional points feature an infinite parameter sensitivity, expansion into power series is not possible at these points. Moreover, these points are singularities of the relation $\omega = \omega(\varepsilon)$, and, hence, limit the convergence radii of power-series expansions of this relation. This is because the convergence radius is precisely the distance from the expansion point ε_0 to the nearest singularity in the complex parameter plane. The exceptional points discussed in this section are complex-valued instances of usually real-valued parameters defining the thermoacoustic model. Their relevance arises from the constraints they impose on power-series expansions of the eigenfrequency as they are utilized in adjoint perturbation theory.

In the simplest case the dependence of the eigenvalue on some parameter close to a singularity is

$$\omega(\varepsilon) \sim (\varepsilon - \varepsilon_{\mathrm{sng}})^k \tag{10.13}$$

where $k \notin \mathbb{N}$. Because of (10.3) for the singularities discussed in this section, the exponent will be $k = \frac{1}{2}$. The position $\varepsilon_{\mathrm{sng}}$ and the exponent k of a singularity can be estimated from the coefficients ω_j of a power series that is expanded in the vicinity of the singularity, using the relations

$$\varepsilon_{\mathrm{sng}} = \varepsilon_0 + \frac{\omega_j \omega_{j-1}}{(j+1)\omega_{j+1}\omega_{j-1} - j\omega_j^2} \tag{10.14}$$

$$k = \frac{(j^2-1)\omega_{j+1}\omega_{j-1} - (j\omega_j)^2}{(j+1)\omega_{j+1}\omega_{j-1} - j\omega_j^2}. \tag{10.15}$$

The estimates should become increasingly accurate as $j \to \infty$. Also moving the expansion point of the power series closer to the singularity improves the accuracy of the estimates. See [128, chapter 6] and references therein for further details on this method.

Because high-order power series coefficients can be computed using the perturbation theory presented in Chap. 6, it allows to find exceptional points without computations of determinants. To achieve this, high-order power series coefficients are computed for some value of ε and the position of the singularity is estimated from Eq. (10.14). A power-series expansion at the estimated position is then computed in order to obtain an even better estimate. Repetition of these steps should converge to the position of the singularity. Table 10.2 lists the estimates obtained from three iterations of this procedure applied to the FEM discretization of the network model.

The interaction index n was considered as complex parameter and the series coefficients ω_{13}, ω_{14}, and ω_{15} were used to compute the estimates. Two cases are reported. The first computes the singularity that limits the convergence of the power series of mode #R1. For the second case the time delay is set from $\tau = 2$ to $\tau = 0.8523$ for comparison with the exceptional point 1.a that was discussed in detail in the previous section. Both cases converge within the three steps. The exponents converged to $k = 0.5$, indicating that the computed singularity is indeed a defective

Table 10.2: Estimates for singularities in the relation $\omega = \omega(n)$ obtained from 15th-order perturbation theory.

#	real(n)	imag(n)	real(ω_{sng})	imag(ω_{sng})	real(k)	imag(k)
			$\tau = 2$			
init	1	0	2.368703	−0.265683		
1	−0.362744	0.058128	2.467858	0.445948	0.361423	−0.020634
2	−0.356843	0.058614	2.547452	0.439656	0.501201	0.000420
3	−0.356843	0.058614	2.548034	0.439676	0.500000	0.000000
			$\tau = 0.8523$			
init	1	0	2.128628	0.828271		
1	0.7073003	−0.044042	2.798139	0.801249	0.499277	0.047050
2	0.7068817	−0.044386	2.833042	0.800846	0.500035	0.000056
3	0.7068817	−0.044386	2.833042	0.863643	0.500000	0.000000

eigenvalue with multiplicity 2. Moreover, solving the system with Beyn's algorithm yields indeed two eigenvalues that are identical to 6 decimal places and feature identical mode shapes. The mode shapes are shown in Fig. 10.3.

Note that for the second case, the eigenfrequency at the singularity agrees well with the eigenfrequency obtained from evaluations of the dispersion relation of the network model. Because the method uses the real and the imaginary part of the interaction index as the two parameters to find the singularity, the converged value of n is complex and, hence, different from the parameter reported in Tab. 10.1.

10.6 Conclusions

Exceptional points in thermoacoustic spectra were discussed. They are characterized by a high-parameter sensitivity and explain aspects of the interaction of intrinsic and acoustic modes as recently reported in the literature. Although not found for the presented examples, they may also govern other types of mode interactions.

Two methods were presented to compute parameter combinations that yield exceptional points. While the first is based on evaluations of the dispersion relation and its derivative, the second exploits the fact that exceptional points are singularities that limit the convergence of power-series expansions. The second method does not require evaluations of the determinant and is, therefore, better suited for three-dimensional Helmholtz solvers and other high-dimensional methods. However, the exceptional points found with this method are complex valued and, thus, not directly linked to physically realizable quantities. Future work should investigate how to improve this method. Quantum mechanics may again give inspiration on how to achieve this, see [185] and references therein.

The high sensitivity of exceptional points may also give rise to practical applications such as efficient control schemes for the mitigation of thermoacoustic instabilities that utilize only small changes in the design variables. Conversely, exceptional points might be a particular challenge because due to the high sensitivity small uncertainties might be strongly amplified. A deeper understanding of the role of exceptional points should, thus, be the aim of future research.

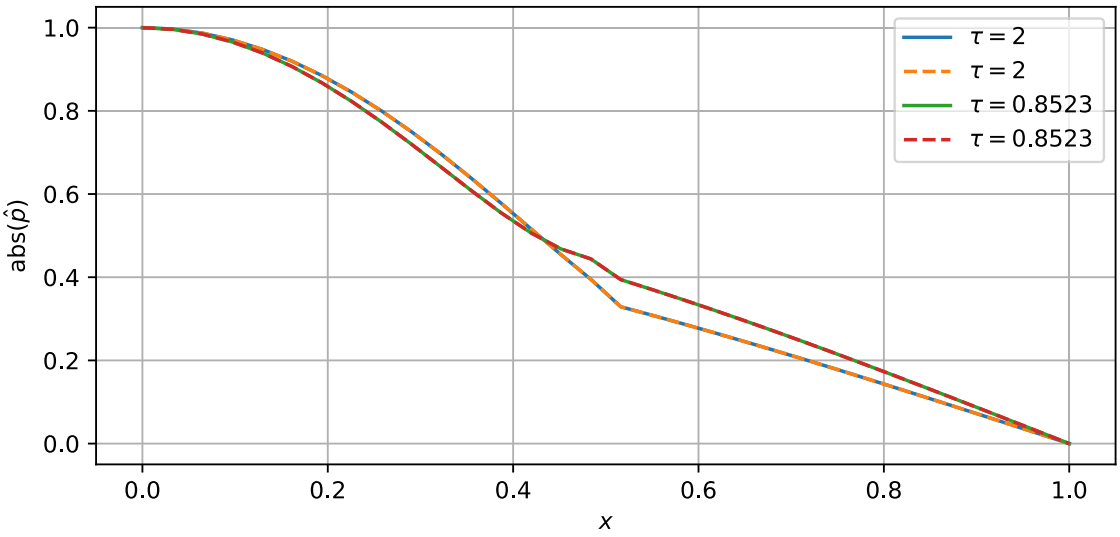

Figure 10.3: Mode shapes obtained for the two test cases. For each test case the two mode shapes are identical. The singularities computed from the perturbation coefficients, therefore, correspond to defective eigenvalues with multiplicity two.

Conclusions and Outlook

One approach for the assessment of thermoacoustic instabilities is linear stability analysis. Regardless whether the discretization approach is based on wave-based network models or Helmholtz solvers, linear stability analysis results in a nonlinear eigenvalue problem. This thesis discussed several approaches to ease the solution of this problem.

Part I introduced the fundamental mathematical concepts, models, and algorithms that are considered in the thesis. The thermoacoustic Helmholtz equation was derived. The discussion of the derivation of the adjoint Helmholtz equation and a Bubnov-Galerkin finite element discretization outlined the kinship of these topics. In particular, it was emphasized that the classic distinction between continuous and discrete adjoint approaches is not necessary when using this FEM method. It is, thus, well suited for the study of adjoint-based algorithms. However, as discussed in [71], perturbations of the domain shape would require to take high-order derivatives at the perturbed boundaries. The presented finite element method would be inappropriate for this task and spectral method as presented in [186] might be considered. Future work should address this question. The current standard fixed-point methods for the solution of the thermoacoustic eigenvalue problem were also discussed in Part I. Moreover, various example cases for comparison with the other methods in this thesis were presented.

Part II exploited the discrete rotational symmetry of annular combustion chambers by Bloch-wave theory. For practical combustors this theory may lead to an acceleration of the computation time by a factor of 400. Moreover, the findings were also useful for the discussion of theoretical questions such as the occurrence of degenerate eigenvalues. The theory might be further improved by explicitly incorporating reflection symmetries. If the considered combustor model features both discrete rotational and reflection symmetry, reduction of the computational domain to an irreducible unit cell would then be possible. This would reduce the computational domain size by an additional factor of two. Such a theory is already established in other fields to ease the modeling of wave propagation in highly symmetric periodic structures, see [67] and references therein.

Perturbation theory was proposed to complement the Bloch-wave theory when the discrete rotational symmetry is broken. Therefore, existing adjoint-based perturbation methods were extended to arbitrary order. As exemplified with the model of the MICCA combustor, when studying symmetry breaking, the baseline solution for the perturbation methods can still be obtained efficiently from Bloch-wave theory and asymmetries are accounted for using the improved perturbation methods. Perturbation theory was also applied to compute spinning-mode limit cycles in annular combustors. Computation of standing-mode limit cycles, however, is not possible with the discussed schemes. Because standing-mode limit cycles feature different amplitude levels at the individual flames, this would require a multi-parameter theory that can handle a mode un-

folding due to a loss of symmetry. As the presented perturbation theory is largely independent of the particular application to thermoacoustic stability analysis, other fields may also benefit from this theory. For instance, second-order perturbation theory is already used for stability analysis of fluid flows [187] and generalization to arbitrary order may further improve the analysis.

However, there are other applications for the perturbation methods than combining them with Bloch-wave theory. Part III discussed how to use perturbation theory to study and improve iterative solution algorithms for nonlinear eigenvalue problems. When compared to the standard fixed-point iteration used in the field, the improved methods converge much faster to machine-precise solutions. Combination with integration-based eigenvalue solvers allowed to efficiently compute all eigenvalues inside of a predefined region of the complex plane. In particular, this enables the computation of intrinsic thermoacoustic modes, because no initial guesses such as the passive flame eigenvalues are needed. In view of the abundance of solution algorithms [87, 86] for nonlinear eigenvalue problems, extensive comparison of the discussed methods with other solution methods described in the literature should be done in the future.

Utilization of the perturbation theory for risk-factor analysis was also discussed in Part III. A second-order multi-parameter theory was introduced for that purpose. Because the theory yields an explicit expression for the dependence of the eigenfrequency on the model parameters, an approximation to the stability boundary can be computed from a single solution of the thermoacoustic Helmholtz equation. This expression can then be used to calculate the risk factor by algebraic integration in parameter space. Similar to the case of standing-mode limit cycles, the theory cannot be applied to degenerate eigenvalues. Future work should address this question.

Also note that because perturbation theory provides gradient information, future work should also focus on its utilization as an optimization tool.

The last part discussed exceptional points. It was shown that these points play a role in the interaction of intrinsic and acoustic modes. The high sensitivity poses a particular challenge for the perturbation theory presented in this thesis. Future work should investigate methods for asymptotic series expansions at these points. The high sensitivity of exceptional points is also relevant for the control of thermoacoustic instabilities. This regards both the opportunity to achieve large damping effects by well calculated design changes as well as the challenge to design robust design schemes that can cope with the high sensitivity of the parameters.

Appendix

Appendix A

Inductive proofs for large order perturbation theory

In the thesis the equations for the large-order perturbation theory were derived by explicitly sorting for equal powers of the perturbation parameter. However, they can also be derived by induction.

Some notes on power series

Given a power series expansion of a function

$$f(z) = \sum_{n=0}^{\infty} a_n (z - z_0)^n , \tag{A.1}$$

the coefficients a_n depend on the expansion point z_0, i.e., $a_n = a_n(z_0)$. This can be used to relate a_n to a_{n+1}, by taking the partial derivative of Eq. (A.1) with respect to z_0:

$$0 = \sum_{n=0}^{\infty} \frac{\partial a_n}{\partial z_0} (z - z_0)^n - n a_n (z - z_0)^{n-1} \tag{A.2}$$

$$\Leftrightarrow \sum_{n=0}^{\infty} n a_n (z - z_0)^{n-1} = \sum_{n=0}^{\infty} \frac{\partial a_n}{\partial z_0} (z - z_0)^n \tag{A.3}$$

$$0 + \sum_{n=1}^{\infty} n a_n (z - z_0)^{n-1} = \sum_{n=0}^{\infty} \frac{\partial a_n}{\partial z_0} (z - z_0)^n \tag{A.4}$$

$$\sum_{n=0}^{\infty} (n+1) a_{n+1} (z - z_0)^n = \sum_{n=0}^{\infty} \frac{\partial a_n}{\partial z_0} (z - z_0)^n . \tag{A.5}$$

Comparing the coefficients of the left and right-hand side then yields:

$$(n+1) a_{n+1} = \frac{\partial a_n}{\partial z_0} \Leftrightarrow a_{n+1} = \frac{1}{n+1} \frac{\partial a_n}{\partial z_0} . \tag{A.6}$$

Note that the above relation is nothing else than a recursive definition of Taylor coefficients. It can be used to find the perturbation formulae by induction.

For convenience the following notation is introduced:

$$|\boldsymbol{\alpha}\boldsymbol{\beta}| = \sum_{i=1}^{\infty} \alpha_i \beta_i \tag{A.7}$$

$$\mathbb{M}_{\leq k} = \left\{ \boldsymbol{\mu} \in N_0^{\infty} \middle| |\boldsymbol{\mu}|_1 \leq k \right\} \tag{A.8}$$

$$\mathbb{M}_{=k} = \left\{ \boldsymbol{\mu} \in N_0^{\infty} \middle| |\boldsymbol{\mu}|_1 = k \right\}. \tag{A.9}$$

With these definitions it can be directly concluded that $\mathbb{M}_{\leq k} \cap \mathbb{M}_{\leq k+1} = \mathbb{M}_{=k+1}$. Interestingly, $\mathbb{M}_{=k+1}$ can be constructed from $\mathbb{M}_{=k}$ by

$$\mathbb{M}_{=k+1} = \{(k+1)1_k\} \cup \left\{ \boldsymbol{\mu} - 1_g + 1_{g+1} \middle| \mu \in \mathbb{M}_{=k}, \mu_g \neq 0 \right\}. \tag{A.10}$$

A.1 An inductive proof for the coefficient determining equation

This section uses a proof by induction to show that Eq. (6.11), which in the current notation reads

$$\sum_{m=0}^{k} \sum_{\boldsymbol{\mu} \in \mathbb{M}_{\leq k}} \sum_{n=0}^{k-|\boldsymbol{\mu}|_1} \binom{|\boldsymbol{\mu}|}{\boldsymbol{\mu}} \boldsymbol{\omega}^{\boldsymbol{\mu}} \mathcal{L}_{|\boldsymbol{\mu}|,n} \widehat{p}_{k-n-|\boldsymbol{\mu}|_1} = 0, \tag{A.11}$$

is the valid equation to determine the coefficients for the perturbation series at any order k.

Base case

The base case is trivial as for $k = 0$

$$\mathcal{L}_{0,0} \widehat{p}_0 = 0 \tag{A.12}$$

which is the unperturbed eigenvalue problem evaluated at ε_0.

Inductive step

The inductive step is more complicated. It requires to take the derivative of (A.11) with respect to ε_0 according to (A.6) this will spawn a lot of new terms including the correction coefficients of order $k+1$. Rearranging the terms will then yield (A.11) for order $k+1$.

Due to the product rule, taking the derivative of $\boldsymbol{\omega}^{\boldsymbol{\mu}} \mathcal{L}_{m,n} \widehat{p}_{k-n-|\boldsymbol{\mu}|_1}$ comes down to the three derivatives:

$$\partial_{\varepsilon_0} \widehat{p}_{k-n-|\boldsymbol{\mu}|_1} = (k - n - |\boldsymbol{\mu}|_1 + 1) \widehat{p}_{k-n-|\boldsymbol{\mu}|_1+1}, \tag{A.13}$$

$$\partial_{\varepsilon_0} \mathcal{L}_{m,n} = \omega_1 \mathcal{L}_{m+1,n}(m+1) + \mathcal{L}_{m,n+1}(n+1), \tag{A.14}$$

and

$$\partial_{\varepsilon_0} \boldsymbol{\omega}^{\boldsymbol{\mu}} = \partial_{\varepsilon_0} \prod_{g=1}^{k} \omega_g^{\boldsymbol{\mu}_g} = \sum_{g=1}^{k} \boldsymbol{\mu}_g \omega_g^{\boldsymbol{\mu}_g - 1} \omega_{g+1} (g+1) \prod_{\substack{l=1 \\ l \neq g}}^{k} \omega_l^{\boldsymbol{\mu}_l} = \sum_{g=1}^{k} (g+1) \boldsymbol{\mu}_g \boldsymbol{\omega}^{\boldsymbol{\mu} - 1_g + 1_{g+1}}. \tag{A.15}$$

Note that $\mathcal{L}_{m,n}$ was defined as $\frac{\partial^{m+n}}{\partial\omega^m\partial\varepsilon^n}\mathcal{L}(\omega(\varepsilon),\varepsilon)\Big|_{\varepsilon=\varepsilon_0}$, thus, one factor ω_1 is obtained from the chain rule, when taking the derivative:

$$\partial_{\varepsilon_0}\sum_{\boldsymbol{\mu}\in\mathbb{M}_{\leq k}}\sum_{n=0}^{k-|\boldsymbol{\mu}|_1}\binom{|\boldsymbol{\mu}|}{\boldsymbol{\mu}}\boldsymbol{\omega}^{\boldsymbol{\mu}}\mathcal{L}_{|\boldsymbol{\mu}|,n}\widehat{p}_{k-n-|\boldsymbol{\mu}|_1}=\partial_{\varepsilon_0}0=0 \tag{A.16}$$

$$=\sum_{\boldsymbol{\mu}\in\mathbb{M}_{\leq k}}\sum_{n=0}^{k-|\boldsymbol{\mu}|_1}\binom{|\boldsymbol{\mu}|}{\boldsymbol{\mu}}\partial_{\varepsilon_0}\boldsymbol{\omega}^{\boldsymbol{\mu}}\mathcal{L}_{|\boldsymbol{\mu}|,n}\widehat{p}_{k-n-|\boldsymbol{\mu}|_1} \tag{A.17}$$

$$=\underbrace{\sum_{\boldsymbol{\mu}\in\mathbb{M}_{\leq k}}\sum_{n=0}^{k-|\boldsymbol{\mu}|_1}\binom{|\boldsymbol{\mu}|}{\boldsymbol{\mu}}\boldsymbol{\omega}^{\boldsymbol{\mu}}\mathcal{L}_{|\boldsymbol{\mu}|,n}\widehat{p}_{k-n-|\boldsymbol{\mu}|_1+1}(k-n-|\boldsymbol{\mu}|_1+1)}_{\text{term I}} \tag{A.18}$$

$$+\underbrace{\sum_{\boldsymbol{\mu}\in\mathbb{M}_{\leq k}}\sum_{n=0}^{k-|\boldsymbol{\mu}|_1}\binom{|\boldsymbol{\mu}|}{\boldsymbol{\mu}}\left[\boldsymbol{\omega}^{\boldsymbol{\mu}+1_1}\mathcal{L}_{|\boldsymbol{\mu}|+1,n}(|\boldsymbol{\mu}|+1)+\boldsymbol{\omega}^{\boldsymbol{\mu}}\mathcal{L}_{|\boldsymbol{\mu}|,n+1}(n+1)\right]\widehat{p}_{k-n-|\boldsymbol{\mu}|_1}}_{\text{term II}}$$

$$+\underbrace{\sum_{\boldsymbol{\mu}\in\mathbb{M}_{\leq k}}\sum_{n=0}^{k-|\boldsymbol{\mu}|_1}\binom{|\boldsymbol{\mu}|}{\boldsymbol{\mu}}\sum_{g=1}^{k}\boldsymbol{\omega}^{\boldsymbol{\mu}-1_g+1_{g+1}}\mathcal{L}_{|\boldsymbol{\mu}|,n}\widehat{p}_{k-n-|\boldsymbol{\mu}|_1}(g+1)\boldsymbol{\mu}_g}_{\text{term III}}.$$

The terms I, II, and III arose from the product rule utilized for the differentiation of $\boldsymbol{\omega}^{\boldsymbol{\mu}}\mathcal{L}_{|\boldsymbol{\mu}|,n}\widehat{p}_{k-n-|\boldsymbol{\mu}|_1}$:

$$\text{term II}=\underbrace{\sum_{\boldsymbol{\mu}\in\mathbb{M}_{\leq k}}\sum_{n=0}^{k-|\boldsymbol{\mu}|_1}\binom{|\boldsymbol{\mu}|}{\boldsymbol{\mu}}\boldsymbol{\omega}^{\boldsymbol{\mu}+1_1}\mathcal{L}_{|\boldsymbol{\mu}|+1,n}\widehat{p}_{k-n-|\boldsymbol{\mu}|_1}(|\boldsymbol{\mu}|+1)}_{\text{term IIa}} \tag{A.19}$$

$$+\sum_{\boldsymbol{\mu}\in\mathbb{M}_{\leq k}}\sum_{n=0}^{k-|\boldsymbol{\mu}|_1}\binom{|\boldsymbol{\mu}|}{\boldsymbol{\mu}}\boldsymbol{\omega}^{\boldsymbol{\mu}}\mathcal{L}_{|\boldsymbol{\mu}|,n+1}\widehat{p}_{k-n-|\boldsymbol{\mu}|_1}(n+1)$$

$$=\text{term IIa}+\sum_{\boldsymbol{\mu}\in\mathbb{M}_{\leq k}}\sum_{n=1}^{k-|\boldsymbol{\mu}|_1+1}\binom{|\boldsymbol{\mu}|}{\boldsymbol{\mu}}\boldsymbol{\omega}^{\boldsymbol{\mu}}\mathcal{L}_{|\boldsymbol{\mu}|,n}\widehat{p}_{k-(n-1)-|\boldsymbol{\mu}|_1}n \tag{A.20}$$

$$=\text{term IIa}+\sum_{\boldsymbol{\mu}\in\mathbb{M}_{\leq k}}\left(0+\left[\sum_{n=1}^{k-|\boldsymbol{\mu}|_1}\binom{|\boldsymbol{\mu}|}{\boldsymbol{\mu}}\boldsymbol{\omega}^{\boldsymbol{\mu}}\mathcal{L}_{|\boldsymbol{\mu}|,n}\widehat{p}_{k-(n-1)-|\boldsymbol{\mu}|_1}n\right]+\binom{|\boldsymbol{\mu}|}{\boldsymbol{\mu}}\boldsymbol{\omega}^{\boldsymbol{\mu}}\mathcal{L}_{|\boldsymbol{\mu}|,n}\widehat{p}_0(k-|\boldsymbol{\mu}|_1+1)\right) \tag{A.21}$$

$$=\text{term IIa}+\underbrace{\sum_{\boldsymbol{\mu}\in\mathbb{M}_{\leq k}}\sum_{n=0}^{k-|\boldsymbol{\mu}|_1}\binom{|\boldsymbol{\mu}|}{\boldsymbol{\mu}}\boldsymbol{\omega}^{\boldsymbol{\mu}}\mathcal{L}_{|\boldsymbol{\mu}|,n}\widehat{p}_{k-n-|\boldsymbol{\mu}|_1+1}n}_{\text{term IIb}} \tag{A.22}$$

$$+\sum_{\boldsymbol{\mu}\in\mathbb{M}_{\leq k}}\sum_{n=k-|\boldsymbol{\mu}|_1+1}^{k-|\boldsymbol{\mu}|_1+1}\binom{|\boldsymbol{\mu}|}{\boldsymbol{\mu}}\boldsymbol{\omega}^{\boldsymbol{\mu}}\mathcal{L}_{|\boldsymbol{\mu}|,k-n-|\boldsymbol{\mu}|_1+1}\widehat{p}_0(k-|\boldsymbol{\mu}|_1+1)$$

$$=\text{term IIa}+\text{term IIb}+\underbrace{\sum_{\boldsymbol{\mu}\in\mathbb{M}_{\leq k}}\sum_{n=k-|\boldsymbol{\mu}|_1+1}^{k-|\boldsymbol{\mu}|_1+1}\binom{|\boldsymbol{\mu}|}{\boldsymbol{\mu}}\boldsymbol{\omega}^{\boldsymbol{\mu}}\mathcal{L}_{|\boldsymbol{\mu}|,k-n-|\boldsymbol{\mu}|_1+1}\widehat{p}_0(k+1)}_{\text{term IIc}} \tag{A.23}$$

$$\underbrace{-\sum_{\boldsymbol{\mu}\in\mathbb{M}_{\leq k}}\binom{|\boldsymbol{\mu}|}{\boldsymbol{\mu}}\boldsymbol{\omega}^{\boldsymbol{\mu}}\mathcal{L}_{|\boldsymbol{\mu}|,k-|\boldsymbol{\mu}|_1+1}\widehat{p}_0|\boldsymbol{\mu}|_1}_{\text{term IId}}$$

Adding $0 = 1_1 - 1_1$ to the multi-index μ allows for the following algebraic manipulations:

$$\boldsymbol{\mu} = \boldsymbol{\mu} + 1_1 - 1_1, \tag{A.24}$$

$$|\boldsymbol{\mu}| = |\boldsymbol{\mu} + 1_1 - 1_1| = |\boldsymbol{\mu} + 1_1| - |1_1| = |\boldsymbol{\mu} + 1_1| - 1, \tag{A.25}$$

$$|\boldsymbol{\mu}|_1 = |\boldsymbol{\mu} + 1_1 - 1_1|_1 = |\boldsymbol{\mu} + 1_1|_1 - |1_1|_1 = |\boldsymbol{\mu} + 1_1|_1 - 1, \tag{A.26}$$

and

$$\binom{|\boldsymbol{\mu}|}{\boldsymbol{\mu}}(|\boldsymbol{\mu}|+1) = \binom{|\boldsymbol{\mu}+1_1|-1}{\boldsymbol{\mu}}(|\boldsymbol{\mu}+1_1|) = \binom{|\boldsymbol{\mu}+1_1|}{\boldsymbol{\mu}} = \binom{|\boldsymbol{\mu}+1_1|}{\boldsymbol{\mu}+1_1}(\boldsymbol{\mu}_1+1). \tag{A.27}$$

Using these relations, term IIa can be further recast:

$$\text{term IIa} = \sum_{\boldsymbol{\mu}\in\mathbb{M}_{\leq k}}\sum_{n=0}^{k-|\boldsymbol{\mu}+1_1|_1+1}\binom{|\boldsymbol{\mu}+1_1|}{\boldsymbol{\mu}+1_1}\boldsymbol{\omega}^{\boldsymbol{\mu}+1_1}\mathcal{L}_{|\boldsymbol{\mu}+1_1|,n}\widehat{p}_{k-n-|\boldsymbol{\mu}+1_1|_1+1}(\boldsymbol{\mu}_1+1). \tag{A.28}$$

By substituting $\boldsymbol{\mu} + 1_1 = \boldsymbol{\alpha}$ this gives:

$$\text{term IIa} = \sum_{\boldsymbol{\alpha}\in\mathbb{M}_{\leq k}+1_1}\sum_{n=0}^{k-|\boldsymbol{\alpha}|_1+1}\binom{|\boldsymbol{\alpha}|}{\boldsymbol{\alpha}}\boldsymbol{\omega}^{\boldsymbol{\alpha}}\mathcal{L}_{|\boldsymbol{\alpha}|,n}\widehat{p}_{k-n-|\boldsymbol{\alpha}|_1+1}\boldsymbol{\alpha}_1. \tag{A.29}$$

Here, $\mathbb{M}_{\leq k}+1_1$ denotes the set of all multi-indices which can be constructed by taking all elements of $\mathbb{M}_{\leq k}$ and increasing their first value by 1. For all multi-indices $\boldsymbol{\mu}\in\mathbb{M}_{\leq k}$ which satisfy $|\boldsymbol{\mu}|_1 < k$ the corresponding $\boldsymbol{\alpha} = \boldsymbol{\mu} + 1_1$ satisfies $|\boldsymbol{\alpha}|_1 = |\boldsymbol{\mu}+1_1|_1 = |\boldsymbol{\mu}|_1 + 1 < k+1 \leq k$. Hence, the corresponding $\boldsymbol{\alpha}$ is still in $\mathbb{M}_{\leq k}$. The only multi-indices for which this condition is not satisfied, are $\boldsymbol{\mu}\in\mathbb{M}_{=k}$. Note that by definition for each $\boldsymbol{\alpha}\in\mathbb{M}_{\leq k}$ where $\boldsymbol{\alpha}_1 \neq 0$ a preimage $\boldsymbol{\mu}$ can be found that $\boldsymbol{\mu} + 1_1 = \boldsymbol{\alpha}$. The $\mathbb{M}_{\leq k} + 1_1$ set can, therefore, be decomposed as follows:

$$\mathbb{M}_{\leq k} + 1_1 = \{\boldsymbol{\alpha}\in\mathbb{M}_{=k+1}|\boldsymbol{\alpha}_1 \neq 0\} \cup \{\boldsymbol{\alpha}\in\mathbb{M}_{\leq k}|\alpha_1 \neq 0\}. \tag{A.30}$$

Hence,

$$\text{term IIa} = \sum_{\{\boldsymbol{\alpha}\in\mathbb{M}_{=k+1}|\boldsymbol{\alpha}_1\neq 0\}}\sum_{n=0}^{k-|\boldsymbol{\alpha}|_1+1}\binom{|\boldsymbol{\alpha}|}{\boldsymbol{\alpha}}\boldsymbol{\omega}^{\boldsymbol{\alpha}}\mathcal{L}_{|\boldsymbol{\alpha}|,n}\widehat{p}_{k-n-|\boldsymbol{\alpha}|_1+1}\boldsymbol{\alpha}_1 \tag{A.31}$$

$$+ \sum_{\{\boldsymbol{\alpha}\in\mathbb{M}_{\leq k}|\boldsymbol{\alpha}_1\neq 0\}}\sum_{n=0}^{k-|\boldsymbol{\alpha}|_1+1}\binom{|\boldsymbol{\alpha}|}{\boldsymbol{\alpha}}\boldsymbol{\omega}^{\boldsymbol{\alpha}}\mathcal{L}_{|\boldsymbol{\alpha}|,n}\widehat{p}_{k-n-|\boldsymbol{\alpha}|_1+1}\boldsymbol{\alpha}_1. \tag{A.32}$$

Both terms do not account for multi-indices with vanishing first entry. Taking these into account would, however, make no difference. This is because each addend carries a coefficient $\boldsymbol{\alpha}_1$. Hence,

accounting for multi-indices with $\boldsymbol{\alpha}_1 = 0$ would add 0 to the sums. Thus, it can be stated that

$$\text{term IIa} = \underbrace{\sum_{\boldsymbol{\alpha}\in\mathbb{M}_{=k}} \sum_{n=0}^{k-|\boldsymbol{\alpha}|_1+1} \binom{|\boldsymbol{\alpha}|}{\boldsymbol{\alpha}} \boldsymbol{\omega}^{\boldsymbol{\alpha}} \mathcal{L}_{|\boldsymbol{\alpha}|,n} \widehat{p}_{k-n-|\boldsymbol{\alpha}|_1+1} \boldsymbol{\alpha}_1}_{\text{term IIa1}} \tag{A.33}$$

$$+ \sum_{\boldsymbol{\alpha}\in\mathbb{M}_{\leq k}} \sum_{n=0}^{k-|\boldsymbol{\alpha}|_1+1} \binom{|\boldsymbol{\alpha}|}{\boldsymbol{\alpha}} \boldsymbol{\omega}^{\boldsymbol{\alpha}} \mathcal{L}_{|\boldsymbol{\alpha}|,n} \widehat{p}_{k-n-|\boldsymbol{\alpha}|_1+1} \boldsymbol{\alpha}_1$$

$$= \text{term IIa1} + \underbrace{\sum_{\boldsymbol{\alpha}\in\mathbb{M}_{\leq k}} \sum_{n=0}^{k-|\boldsymbol{\alpha}|_1} \binom{|\boldsymbol{\alpha}|}{\boldsymbol{\alpha}} \boldsymbol{\omega}^{\boldsymbol{\alpha}} \mathcal{L}_{|\boldsymbol{\alpha}|,n} \widehat{p}_{k-n-|\boldsymbol{\alpha}|_1+1} \boldsymbol{\alpha}_1}_{\text{term IIa2}} \tag{A.34}$$

$$+ \underbrace{\sum_{\boldsymbol{\alpha}\in\mathbb{M}_{\leq k}} \sum_{n=k-|\boldsymbol{\alpha}|_1+1}^{k-|\boldsymbol{\alpha}|_1+1} \binom{|\boldsymbol{\alpha}|}{\boldsymbol{\alpha}} \boldsymbol{\omega}^{\boldsymbol{\alpha}} \mathcal{L}_{|\boldsymbol{\alpha}|,n} \widehat{p}_0 \boldsymbol{\alpha}_1}_{\text{term IIa3}}. \tag{A.35}$$

Each summand in term III carries a coefficient $\boldsymbol{\mu}_g$. Thus, the summation can be restricted to those multi-indices $\boldsymbol{\mu}$ which satisfy $\boldsymbol{\mu}_g \neq 0$:

$$\text{term III} = \sum_{g=1}^{k} \sum_{\substack{\boldsymbol{\mu}\in\mathbb{M}_{\leq k} \\ \boldsymbol{\mu}_g\neq 0}} \sum_{n=0}^{k-|\boldsymbol{\mu}|_1} \binom{|\boldsymbol{\mu}|}{\boldsymbol{\mu}} \boldsymbol{\omega}^{\boldsymbol{\mu}-1_g+1_{g+1}} \mathcal{L}_{|\boldsymbol{\mu}|,n} \widehat{p}_{k-n-|\boldsymbol{\mu}|_1} (g+1) \boldsymbol{\mu}_g. \tag{A.36}$$

With this restriction the following rearrangement is possible:

$$\binom{|\boldsymbol{\mu}|}{\boldsymbol{\mu}} \boldsymbol{\mu}_g = \binom{|\boldsymbol{\mu}|}{\boldsymbol{\mu}-1_g+1_{g+1}} \frac{\boldsymbol{\mu}_{g+1}+1}{\boldsymbol{\mu}_g} \boldsymbol{\mu}_g = \binom{|\boldsymbol{\mu}|}{\boldsymbol{\mu}-1_g+1_{g+1}} (\boldsymbol{\mu}_{g+1}+1). \tag{A.37}$$

Note that a division by zero is not possible because of the restriction $\boldsymbol{\mu}_g \neq 0$. With this consideration

$$\text{term III} = \sum_{g=1}^{k} \sum_{\substack{\boldsymbol{\mu}\in\mathbb{M}_{\leq k} \\ \boldsymbol{\mu}_g\neq 0}} \sum_{n=0}^{k-|\boldsymbol{\mu}|_1} \binom{|\boldsymbol{\mu}|}{\boldsymbol{\mu}-1_g+1_{g+1}} \boldsymbol{\omega}^{\boldsymbol{\mu}-1_g+1_{g+1}} \mathcal{L}_{|\boldsymbol{\mu}|,n} \widehat{p}_{k-n-|\boldsymbol{\mu}|_1} (g+1)(\boldsymbol{\mu}_{g+1}+1) \tag{A.38}$$

is obtained. Taking into account that $|\boldsymbol{\mu}| = |\boldsymbol{\mu}-1_g+1_{g+1}|$ and $|\boldsymbol{\mu}|_1 = |\boldsymbol{\mu}-1_g+1_{g+1}|_1 - 1$, term III can be further manipulated:

$$\text{term III} = \sum_{g=1}^{k} \sum_{\substack{\boldsymbol{\mu}\in\mathbb{M}_{\leq k} \\ \boldsymbol{\mu}_g\neq 0}} \sum_{n=0}^{k-|\boldsymbol{\mu}-1_g+1_{g+1}|_1+1} \binom{|\boldsymbol{\mu}-1_g+1_{g+1}|}{\boldsymbol{\mu}-1_g+1_{g+1}} \times$$

$$\boldsymbol{\omega}^{\boldsymbol{\mu}-1_g+1_{g+1}} \mathcal{L}_{|\boldsymbol{\mu}-1_g+1_{g+1}|,n} \widehat{p}_{k-n-|\boldsymbol{\mu}-1_g+1_{g+1}|_1+1} (g+1)(\boldsymbol{\mu}_{g+1}+1) \tag{A.39}$$

$$= \sum_{g=1}^{k} \sum_{\substack{\boldsymbol{\beta}\in\mathbb{M}_{\leq k+1} \\ \boldsymbol{\beta}_{g+1}\neq 0}} \sum_{n=0}^{k-|\boldsymbol{\beta}|_1+1} \binom{|\boldsymbol{\beta}|}{\boldsymbol{\beta}} \boldsymbol{\omega}^{\boldsymbol{\beta}} \mathcal{L}_{|\boldsymbol{\beta}|,n} \widehat{p}_{k-n-|\boldsymbol{\beta}|_1+1} (g+1) \boldsymbol{\beta}_{g+1}. \tag{A.40}$$

Here, the substitution $\boldsymbol{\beta} = \boldsymbol{\mu} - 1_g + 1_{g+1}$ has been made to obtain the last result. Note that the set

$\{\boldsymbol{\mu} \in \mathbb{M}_{\leq k} | \boldsymbol{\mu}_g \neq 0\}$ is mapped to $\{\boldsymbol{\beta} \in \mathbb{M}_{\leq k+1} | \boldsymbol{\beta}_{g+1} \neq 0\}$ by this operation. Now, shifting the index g by 1 yields:

$$\text{term III} = \sum_{g=2}^{k+1} \sum_{\substack{\boldsymbol{\beta} \in \mathbb{M}_{\leq k+1} \\ \boldsymbol{\beta}_g \neq 0}} \sum_{n=0}^{k-|\boldsymbol{\beta}|_1+1} \binom{|\boldsymbol{\beta}|}{\boldsymbol{\beta}} \boldsymbol{\omega}^{\boldsymbol{\beta}} \mathcal{L}_{|\boldsymbol{\beta}|,n} \widehat{p}_{k-n-|\boldsymbol{\beta}|_1+1} g \boldsymbol{\beta}_g. \tag{A.41}$$

Again each summand in term III carries a coefficient $\boldsymbol{\beta}_g$, so including multi-indices with $\boldsymbol{\beta}_g = 0$ will not make any difference. Hence, term III can be recast as

$$\begin{aligned}
\text{term III} &= \sum_{g=2}^{k} \sum_{\boldsymbol{\beta} \in \mathbb{M}_{\leq k+1}} \sum_{n=0}^{k-|\boldsymbol{\beta}|_1+1} \binom{|\boldsymbol{\beta}|}{\boldsymbol{\beta}} \boldsymbol{\omega}^{\boldsymbol{\beta}} \mathcal{L}_{|\boldsymbol{\beta}|,n} \widehat{p}_{k-n-|\boldsymbol{\beta}|_1+1} g \boldsymbol{\beta}_g && \text{(A.42)} \\
&= \sum_{g=2}^{k} \sum_{\boldsymbol{\beta} \in \mathbb{M}_{\leq k}} \sum_{n=0}^{k-|\boldsymbol{\beta}|_1+1} \binom{|\boldsymbol{\beta}|}{\boldsymbol{\beta}} \boldsymbol{\omega}^{\boldsymbol{\beta}} \mathcal{L}_{|\boldsymbol{\beta}|,n} \widehat{p}_{k-n-|\boldsymbol{\beta}|_1+1} g \boldsymbol{\beta}_g && \text{(A.43)} \\
&\quad + \underbrace{\sum_{g=2}^{k} \sum_{\boldsymbol{\beta} \in \mathbb{M}_{=k+1}} \sum_{n=0}^{k-|\boldsymbol{\beta}|_1+1} \binom{|\boldsymbol{\beta}|}{\boldsymbol{\beta}} \boldsymbol{\omega}^{\boldsymbol{\beta}} \mathcal{L}_{|\boldsymbol{\beta}|,n} \widehat{p}_{k-n-|\boldsymbol{\beta}|_1+1} g \boldsymbol{\beta}_g}_{\text{term IIIa}} \\
&= \text{term IIIa} + \underbrace{\sum_{g=2}^{k} \sum_{\boldsymbol{\beta} \in \mathbb{M}_{\leq k}} \sum_{n=0}^{k-|\boldsymbol{\beta}|_1} \binom{|\boldsymbol{\beta}|}{\boldsymbol{\beta}} \boldsymbol{\omega}^{\boldsymbol{\beta}} \mathcal{L}_{|\boldsymbol{\beta}|,n} \widehat{p}_{k-n-|\boldsymbol{\beta}|_1+1} g \boldsymbol{\beta}_g}_{\text{term IIIb}} && \text{(A.44)} \\
&\quad + \underbrace{\sum_{g=2}^{k} \sum_{\boldsymbol{\beta} \in \mathbb{M}_{\leq k}} \sum_{n=k-|\boldsymbol{\mu}|_1+1}^{k-|\boldsymbol{\mu}|_1+1} \binom{|\boldsymbol{\beta}|}{\boldsymbol{\beta}} \boldsymbol{\omega}^{\boldsymbol{\beta}} \mathcal{L}_{|\boldsymbol{\beta}|,n} \widehat{p}_0 g \boldsymbol{\beta}_g}_{\text{term IIIc}}. && \text{(A.45)}
\end{aligned}$$

Now adding the various terms will complete the proof. Starting with term IIa2 and term IIIa2 we get:

$$\text{term IIa2} + \text{term IIIb} = \sum_{g=1}^{k} \sum_{\boldsymbol{\mu} \in \mathbb{M}_{\leq k}} \sum_{n=0}^{k-|\boldsymbol{\mu}|_1} \binom{|\boldsymbol{\mu}|}{\boldsymbol{\mu}} \boldsymbol{\omega}^{\boldsymbol{\mu}} \mathcal{L}_{|\boldsymbol{\mu}|,n} \widehat{p}_0 g \boldsymbol{\mu}_g = \sum_{\boldsymbol{\mu} \in \mathbb{M}_{\leq k}} \sum_{n=0}^{k-|\boldsymbol{\mu}|_1} \binom{|\boldsymbol{\mu}|}{\boldsymbol{\mu}} \boldsymbol{\omega}^{\boldsymbol{\mu}} \mathcal{L}_{|\boldsymbol{\mu}|,n} \widehat{p}_0 |\boldsymbol{\mu}|_1 \tag{A.46}$$

$$= \text{term IV}. \tag{A.47}$$

To obtain this result the multi-indices $\boldsymbol{\alpha}$ and $\boldsymbol{\beta}$ must be renamed to $\boldsymbol{\mu}$ and term IIa2 must be multiplied with $g = 1$. Equivalently for the sum of term IIa3 and term IIIc :

$$\begin{aligned}
\text{term IIa3} + \text{term IIIc} &= \sum_{g=1}^{k} \sum_{\boldsymbol{\mu} \in \mathbb{M}_{\leq k}} \sum_{n=k-|\boldsymbol{\mu}|_1+1}^{k-|\boldsymbol{\mu}|_1+1} \binom{|\boldsymbol{\mu}|}{\boldsymbol{\mu}} \boldsymbol{\omega}^{\boldsymbol{\mu}} \mathcal{L}_{|\boldsymbol{\mu}|,n} \widehat{p}_0 g \boldsymbol{\mu}_g && \text{(A.48)} \\
&= \sum_{\boldsymbol{\mu} \in \mathbb{M}_{\leq k}} \sum_{n=k-|\boldsymbol{\mu}|_1+1}^{k-|\boldsymbol{\mu}|_1+1} \binom{|\boldsymbol{\mu}|}{\boldsymbol{\mu}} \boldsymbol{\omega}^{\boldsymbol{\mu}} \mathcal{L}_{|\boldsymbol{\mu}|,n} \widehat{p}_0 |\boldsymbol{\mu}|_1 && \text{(A.49)} \\
&= \sum_{\boldsymbol{\mu} \in \mathbb{M}_{\leq k}} \binom{|\boldsymbol{\mu}|}{\boldsymbol{\mu}} \boldsymbol{\omega}^{\boldsymbol{\mu}} \mathcal{L}_{|\boldsymbol{\mu}|,k-|\boldsymbol{\mu}|_1+1} \widehat{p}_0 |\boldsymbol{\mu}|_1 = \text{term V}. && \text{(A.50)}
\end{aligned}$$

Term V cancels together with term IId.

Adding term I and term IV gives:

$$\text{term I} + \text{term IV} = \sum_{\boldsymbol{\mu}\in\mathbb{M}_{\leq k}} \sum_{n=0}^{k-|\boldsymbol{\mu}|_1} \binom{|\boldsymbol{\mu}|}{\boldsymbol{\mu}} \boldsymbol{\omega}^{\boldsymbol{\mu}} \mathcal{L}_{|\boldsymbol{\mu}|,n} \widehat{p}_0(k-n+1) := \text{term VI}. \tag{A.51}$$

Including also term IIb yields:

$$\text{term VI} + \text{term IIb} = \sum_{\boldsymbol{\mu}\in\mathbb{M}_{\leq k}} \sum_{n=0}^{k-|\boldsymbol{\mu}|_1} \binom{|\boldsymbol{\mu}|}{\boldsymbol{\mu}} \boldsymbol{\omega}^{\boldsymbol{\mu}} \mathcal{L}_{|\boldsymbol{\mu}|,n} \widehat{p}_0(k+1) := \text{term VII}. \tag{A.52}$$

With term IIc this expression amounts to:

$$\text{term VII} + \text{term IIc} = \sum_{\boldsymbol{\mu}\in\mathbb{M}_{\leq k}} \sum_{n=0}^{k-|\boldsymbol{\mu}|_1} \binom{|\boldsymbol{\mu}|+1}{\boldsymbol{\mu}} \boldsymbol{\omega}^{\boldsymbol{\mu}} \mathcal{L}_{|\boldsymbol{\mu}|,n} \widehat{p}_0(k+1) := \text{term VIII}. \tag{A.53}$$

Summing up term IIa1 and IIIa gives:

$$\begin{aligned}
\text{term IIa1} + \text{IIIa} &= \sum_{g=1}^{k} \sum_{\boldsymbol{\mu}\in\mathbb{M}_{=k+1}} \sum_{n=0}^{k-|\boldsymbol{\mu}|_1+1} \binom{|\boldsymbol{\mu}|}{\boldsymbol{\mu}} \boldsymbol{\omega}^{\boldsymbol{\mu}} \mathcal{L}_{|\boldsymbol{\mu}|,n} \widehat{p}_{k-n-|\boldsymbol{\mu}|_1+1} g\boldsymbol{\mu}_g && \text{(A.54)}\\
&= \sum_{\boldsymbol{\mu}\in\mathbb{M}_{=k+1}} \sum_{n=0}^{k-|\boldsymbol{\mu}|_1+1} \binom{|\boldsymbol{\mu}|}{\boldsymbol{\mu}} \boldsymbol{\omega}^{\boldsymbol{\mu}} \mathcal{L}_{|\boldsymbol{\mu}|,n} \widehat{p}_{k-n-|\boldsymbol{\mu}|_1+1} |\boldsymbol{\mu}|_1 && \text{(A.55)}\\
&= \sum_{\boldsymbol{\mu}\in\mathbb{M}_{=k+1}} \sum_{n=0}^{k-|\boldsymbol{\mu}|_1+1} \binom{|\boldsymbol{\mu}|}{\boldsymbol{\mu}} \boldsymbol{\omega}^{\boldsymbol{\mu}} \mathcal{L}_{|\boldsymbol{\mu}|,n} \widehat{p}_{k-n-|\boldsymbol{\mu}|_1+1}(k+1) := \text{term IX}. && \text{(A.56)}
\end{aligned}$$

Note that here only multi-indices $\boldsymbol{\mu}$ from $\mathbb{M}_{=k+1}$ are considered, so by definition $|\boldsymbol{\mu}|_1 = k+1$. Adding term VII to term IX finally yields:

$$\text{term VIII} + \text{term IX} = \sum_{\boldsymbol{\mu}\in\mathbb{M}_{\leq k+1}} \sum_{n=0}^{k-|\boldsymbol{\mu}|_1+1} \binom{|\boldsymbol{\mu}|}{\boldsymbol{\mu}} \boldsymbol{\omega}^{\boldsymbol{\mu}} \mathcal{L}_{|\boldsymbol{\mu}|,n} \widehat{p}_{k-n-|\boldsymbol{\mu}|_1+1}(k+1). \tag{A.57}$$

Thus, we have

$$\sum_{\boldsymbol{\mu}\in\mathbb{M}_{\leq k+1}} \sum_{n=0}^{k-|\boldsymbol{\mu}|_1+1} \binom{|\boldsymbol{\mu}|}{\boldsymbol{\mu}} \boldsymbol{\omega}^{\boldsymbol{\mu}} \mathcal{L}_{|\boldsymbol{\mu}|,n} \widehat{p}_{k-n-|\boldsymbol{\mu}|_1+1}(k+1) = 0. \tag{A.58}$$

Division by $(k+1)$ completes the proof. Figure A.1 graphically summarizes the steps of the prove.

Note that equation (A.58) is not surprising. From the previous section it was already known by combinatorial arguments that the eigenvalue problem can be expanded as

$$\mathcal{N}(\omega, \varepsilon, \widehat{p}) := \sum_{k=0}^{\infty} \mathcal{N}_k (\varepsilon - \varepsilon_0)^k \tag{A.59}$$

where $\mathcal{N}_k = \sum_{\boldsymbol{\mu}\in\mathbb{M}_{\leq k}} \sum_{n=0}^{k-|\boldsymbol{\mu}|_1} \binom{|\boldsymbol{\mu}|}{\boldsymbol{\mu}} \boldsymbol{\omega}^{\boldsymbol{\mu}} \mathcal{L}_{|\boldsymbol{\mu}|,n} \widehat{p}_{k-n-|\boldsymbol{\mu}|_1}$. Therefore, taking the derivative of $\mathcal{N}_k$ with respect to ε_0 yields $\mathcal{N}_k(k+1)$, which directly corresponds to (A.58). The proof by induction presented in this chapter is insofar special as it is not leveraging any combinatorial arguments at all. It estab-

lishes the fact that the coefficients $\mathscr{N}_k$ are correct by showing that $\mathscr{N}_0 = 0$ equals the unperturbed problem and proving that $\partial_{\varepsilon_0}\mathscr{N}_k = \mathscr{N}_{k+1}(k+1)$, which implies that these are the coefficients generating the power series expansion of the problem.

A.2 Multivariate perturbation theory

Differentiation can also be used to derive multi-parameter perturbation theory at arbitrary order. Using multi-index notation, the multivariate power series ansätze read:

$$\omega = \sum_{|\boldsymbol{\mu}|>0} \omega_{\boldsymbol{\mu}} \boldsymbol{\varepsilon}^{\boldsymbol{\mu}} \tag{A.60}$$

$$\widehat{p} = \sum_{|\boldsymbol{\mu}|>0} \widehat{p}_{\boldsymbol{\mu}} \boldsymbol{\varepsilon}^{\boldsymbol{\mu}}. \tag{A.61}$$

Here $\boldsymbol{\varepsilon}$ denotes the vector of design parameters under consideration. Plugging these ansätze into the eigenvalue problem and collecting like powers of $\boldsymbol{\varepsilon}$, again yields an incremental scheme for the computation of the coefficients (compare Sec. 9.1). Like the single-parameter case, the collection of like powers can be eased by utilizing the relation of the coefficients in a power-series through differentiation. For a multivariate power series we have:

$$f(\boldsymbol{z}) = \sum_{|\boldsymbol{\mu}|>0} a_{\boldsymbol{\mu}} (\boldsymbol{z} - \boldsymbol{z}_0)^{\boldsymbol{\mu}} \qquad |\partial_{\mathbf{1}_k} \tag{A.62}$$

$$0 = \partial_{\mathbf{1}_k} \sum_{|\boldsymbol{\mu}|>0} a_{\boldsymbol{\mu}} (\boldsymbol{z} - \boldsymbol{z}_0)^{\boldsymbol{\mu}} \tag{A.63}$$

$$0 = \sum_{|\boldsymbol{\mu}|>0} \partial_{\mathbf{1}_k} a_{\boldsymbol{\mu}} (\boldsymbol{z} - \boldsymbol{z}_0)^{\boldsymbol{\mu}} - a_{\boldsymbol{\mu}} (\boldsymbol{z} - \boldsymbol{z}_0)^{\boldsymbol{\mu}-\mathbf{1}_k} \boldsymbol{\mu}_k \tag{A.64}$$

$$\sum_{|\boldsymbol{\mu}|>0 \cap \boldsymbol{\mu}_k=0} a_{\boldsymbol{\mu}} (\boldsymbol{z} - \boldsymbol{z}_0)^{\boldsymbol{\mu}-\mathbf{1}_k} \boldsymbol{\mu}_k = \sum_{|\boldsymbol{\mu}|>0} \partial_{\mathbf{1}_k} a_{\boldsymbol{\mu}} (\boldsymbol{z} - \boldsymbol{z}_0)^{\boldsymbol{\mu}} \qquad |\text{shift multiindex on left side} \tag{A.65}$$

$$\sum_{|\boldsymbol{\mu}|>0} a_{\boldsymbol{\mu}+\mathbf{1}_k} (\boldsymbol{z} - \boldsymbol{z}_0)^{\boldsymbol{\mu}} (\boldsymbol{\mu}_k + 1) = \sum_{|\boldsymbol{\mu}|>0} \partial_{\mathbf{1}_k} a_{\boldsymbol{\mu}} (\boldsymbol{z} - \boldsymbol{z}_0)^{\boldsymbol{\mu}} \tag{A.66}$$

$$\Rightarrow (\boldsymbol{\mu}_k + 1) a_{\boldsymbol{\mu}+\mathbf{1}_k} = \partial_{\mathbf{1}_k} a_{\boldsymbol{\mu}}. \tag{A.67}$$

Thus, the coefficients can be incrementally computed by taking partial derivatives. Doing so, will generate a sequence of equations which again can be solved by incorporating the adjoint solution and the solvability condition.

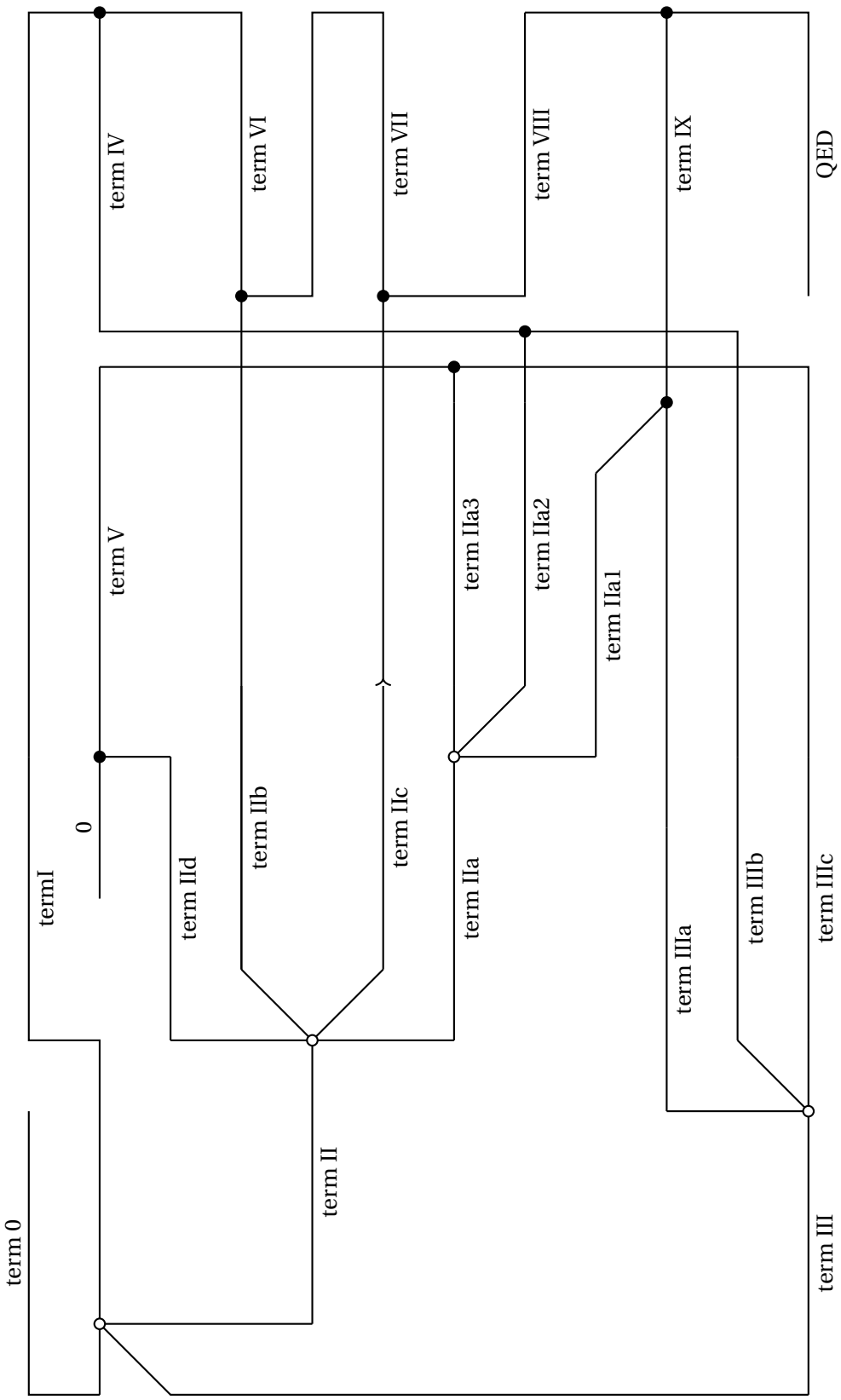

Figure A.1: Rearrangement used for the induction step of the large order perturbation theory. At open dots a term splits into multiple new terms while at filled dots terms are merged.

Appendix B

Kelleher's algorithm

All partitions of a positive integer n need to be known in order to implement the perturbation theory. Kelleher's accelerated ascending composition generation algorithm may be used for this task [134]. The algorithm is given in Alg. B.1. Please note the semantics of the **visit** keyword. At these steps a partition $a_1 \dots a_m$ is returned and the program flow is stopped until the next partition is requested. Then, the algorithm proceeds from the stopped program state. The function terminates if all partitions are found. See [188] and references therein for other fast algorithms for the computation of partitions.

Algorithm B.1: Kelleher's ACCELASC algorithm for fast computations of partitions of n

```
1:  function ACCELASC(n)
2:      k ← 2
3:      a_1 ← 0
4:      y ← n − 1
5:      while k ≠ 1 do
6:          k ← k − 1
7:          x ← a_k + 1
8:          while 2x ≤ y do
9:              a_k ← x
10:             y ← y − x
11:             k ← k + 1
12:         end while
13:         l ← k + 1
14:         while x ≤ y do
15:             a_k ← x
16:             a_l ← y
17:             visit a_1 ... a_l
18:             x ← x + 1
19:             y ← y + 1
20:         end while
21:         y ← y + x − 1
22:         a_k ← y + 1
23:         visit a_1 ... a_k
24:     end while
25: end function
```

Appendix C

Application of the perturbation theory to the Orr-Sommerfeld equation

This appendix briefly illustrates the generality of the presented perturbation theory by applying it to the Orr-Sommerfeld equation. The example was developed in close cooparation with Alessandro Orchini and Jonas Moeck.

The Orr-Sommerfeld equation describes the modal stability of parallel flows. It is non-dimensional and reads

$$\left[\left(\frac{\mathrm{d}^2}{\mathrm{d}y^2}-\lambda^2\right)^2-\mathrm{iRe}\left((\lambda U-\omega)\left(\frac{\mathrm{d}^2}{\mathrm{d}y^2}-\lambda^2\right)-\lambda U''\right)\right]v=0. \tag{C.1}$$

Here, y denotes the coordinate for the axis perpendicular to the mean flow, v the amplitude of the velocity fluctuation in that directions, U the mean flow velocity, λ the wavenumber, ω an oscillation frequency, and Re the Reynolds number. As boundary conditions, no-slip conditions are prescribed

$$v(\pm 1)=v'(\pm 1)=0. \tag{C.2}$$

Extensive discussion of the problem can be found in the literature, see, e.g., [189, 190] and references therein.

The Chebyshev collocation method that is used in [133] to discretize the problem is also applied here. This yields the finite dimensional eigenvalue problem

$$\mathbf{L}(\lambda,\mathrm{Re})=\lambda^4\mathbf{I}+\mathrm{i}\lambda^3\mathrm{Re}\mathbf{U}-2\lambda^2\mathbf{D}_2-\mathrm{i}\lambda^2\omega\mathrm{Re}\mathbf{I}-\mathrm{i}\lambda\mathrm{Re}\left(\mathbf{U}\mathbf{D}_2+2\mathbf{I}\right)+\mathrm{i}\omega\mathrm{Re}\mathbf{D}_2+\mathbf{D}_4, \tag{C.3}$$

where $\mathbf{D}_2$ and $\mathbf{D}_4$ are discretization matrices for the second and fourth-order derivative operators and the matrix $\mathbf{U}$ results from the discretization of the mean flow field. The wavenumber λ will be considered as an eigenvalue and the Reynolds number as a perturbation parameter. As in [133] the baseline values are set to $\omega_0=0.26943$ and $\mathrm{Re}_0=5772$ and a parabolic mean flow profile $U=1-y^2$ is assumed. This yields an eigenvalue $\lambda_0=1.02056+9.7\times10^{-7}\mathrm{i}$.

Perturbation theory up to fiftieth order is used to approximate solutions of the problem. The results are shown in Fig. C.1. The results show the same mathematical characteristics as the exam-

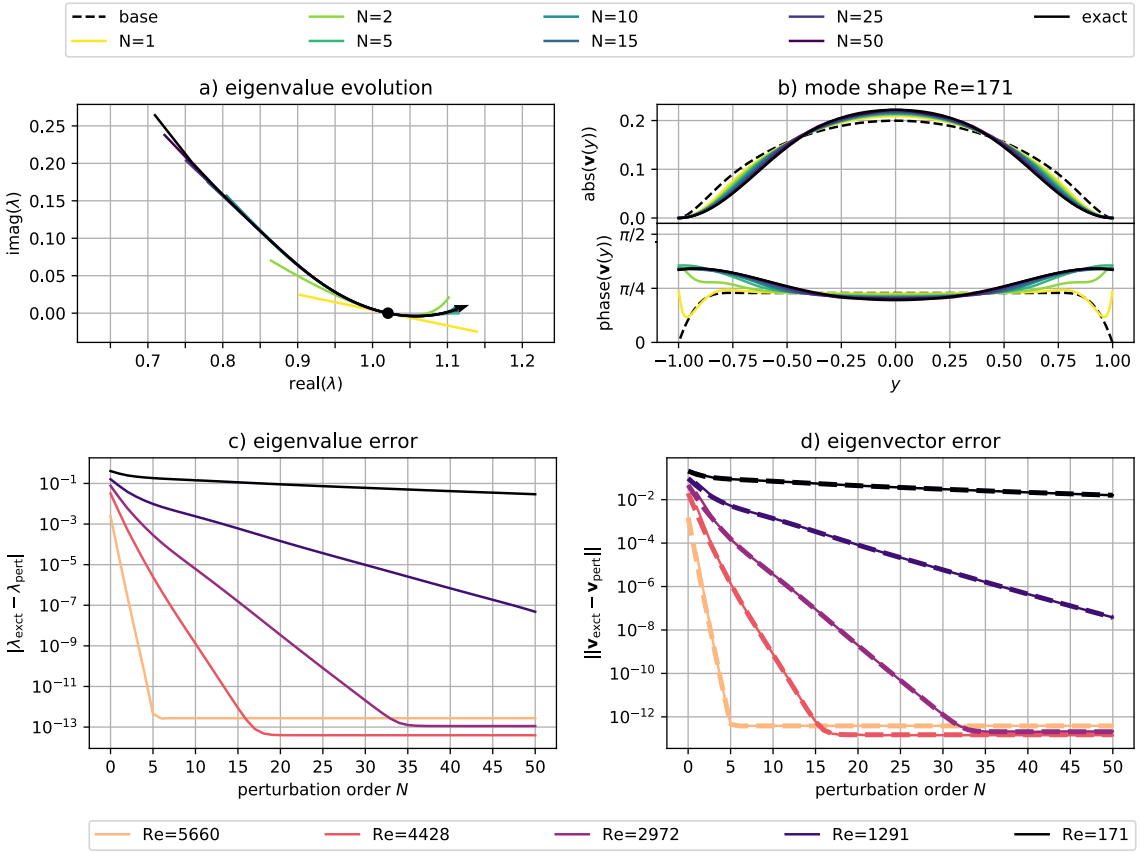

Figure C.1: Comparison of perturbation approximations to exact solutions of the Orr-Sommerfeld equation. a) Eigenvalue trajectory for variations of the Reynolds number in the range Re = 5772 ± 5601. The arrowhead indicates the direction of increasing Re. The baseline eigenvalue is highlighted by the black dot. b) Absolute value and phase of the mode shape for Re = 171. The colored lines indicate the approximations obtained from various perturbation orders. The exact and the unperturbed mode shape are illustrated by black solid and black dashed lines, respectively. c) Error between exact and estimated eigenvalue for various perturbation orders and Reynolds numbers. d) Error in the eigenvector estimate. Results from the a priori normalization are indicated with thick dashed lines, while solid lines correspond to the a posteriori method. Obviously, the two methods yield nearly identical results for this example.

ples considered in Chap. 6, i.e., a finite radius of convergence, a better approximation quality with an increasing perturbation order for values within the convergence radius etc. This underlines the universality of the theory.

Bibliography

[1] European Environment Agency. European emission inventory report 1990-2016 under the UNECE convention on long-range transboundary air pollution (LRTAP). Technical report, Publications Office of the European Union, 2018.

[2] W. Krebs, P. Flohr, B. Prade, and S. Hoffmann. Thermoacoustic stability chart for high-intensity gas turbine combustion systems. *Combust. Sci. Technol.*, 174(7):99–128, 2002.

[3] T. C. Lieuwen and V. Yang, editors. *Combustion Instabilities in Gas Turbine Engines*, volume 210 of *Progress in Astronautics and Aeronautics*. AIAA, Inc., 2005.

[4] S. Ducruix, T. Schuller, D. Durox, and S. Candel. Combustion dynamics and instabilities: Elementary coupling and driving mechanisms. *J. Propul. Power*, 19(5):722–734, 2003.

[5] B. Higgins. On the sound produced by a current of hydrogen gas passing through a tube. *A Journal of Natural Philosophy, Chemistry and the Arts*, 1:129–131, 1802.

[6] J. LeConte. On the influence of musical sounds on the flame of a jet of coal-gas. *Phil. Mag.*, 15:235–239, 1858.

[7] P. L. Rijke. Notiz über eine neue Art, die in einer an beiden Enden offenen Röhre enthaltene Luft in Schwingungen zu versetzen. *Ann. Phys.*, 183(6):339–343, 1859.

[8] J. O'Connor, V. Acharya, and T. Lieuwen. Transverse combustion instabilities: Acoustic, fluid mechanic, and flame processes. *Prog. Energy Combust. Sci.*, 49:1 – 39, 2015.

[9] Lord Rayleigh. *The Theory of Sound*. Dover Publications, 1945.

[10] F. E. C. Culick. Combustion instabilities in liquid-fueled propulsion systems - an overview. *NATO advisory group for aerospace research & development*, 1988.

[11] F. E. C. Culick. Unsteady motions in combustion chambers for propulsion systems. *The Research and Technology Organisation of NATO*, 2006.

[12] T. Lieuwen. Modeling premixed combustion–acoustic wave interactions: A review. *J. Propul. Power*, 19(5):765–781, 2003.

[13] T. J. Poinsot, A. C. Trouve, D. P. Veynante, S. M. Candel, and E. J. Esposito. Vortex-driven acoustically coupled combustion instabilities. *J. Fluid Mech.*, 177:265–292, 1987.

[14] C. S. Goh and A. S. Morgans. The influence of entropy waves on the thermoacoustic stability of a model combustor. *Combust. Sci. Technol.*, 185(2):249–268, 2013.

[15] F. Creta and M. Matalon. Strain rate effects on the nonlinear development of hydrodynamically unstable flames. *Proc. Combust. Inst.*, 33(1):1087 – 1094, 2011.

[16] B.-T. Chu. On the energy transfer to small disturbances in fluid flow (part I). *Acta Mech.*, 1(3):215–234, 1965.

[17] T. Poinsot. Simulation methodologies and open questions for acoustic combustion instability studies. *Annual Research Briefs*, Center for Turbulence Research, Standford University, 2013. pp. 179–188.

[18] K. S. Kedia, C. Safta, J. Ray, H. N. Najm, and A F. Ghoniem. A second-order coupled immersed boundary-SAMR construction for chemically reacting flow over a heat-conducting cartesian grid-conforming solid. *J. Comput. Phys.*, 272:408 – 428, 2014.

[19] D. Mejia, M. Miguel-Brebion, A. Ghani, T. Kaiser, F. Duchaine, L. Selle, and T. Poinsot. Influence of flame-holder temperature on the acoustic flame transfer functions of a laminar flame. *Combust. Flame*, 188:5 – 12, 2018.

[20] T. Poinsot and D. Veynante. *Theoretical and Numerical Combustion*. R. T. Edwards, 2nd edition, 2005.

[21] I. Hernández, G. Staffelbach, T. Poinsot, J. C. R. Casadoc, and J. B. W. Kok. LES and acoustic analysis of thermo-acoustic instabilities in a partially premixed model combustor. *C. R. Mécanique*, 341:121–130, 2013.

[22] S. Jaensch, M. Merk, T. Emmert, and W. Polifke. Identification of flame transfer functions in the presence of intrinsic thermoacoustic feedback and noise. *Combust. Theor. Model.*, 22(3):613–634, 2018.

[23] G. Staffelbach, L. Y. M. Gicquel, and T. Poinsot. Large eddy simulation of self-excited azimuthal modes in annular combustors. *Proc. Combust. Inst.*, 32(2):2909–2916, 2009.

[24] P. Wolf, R. Balakrishnan, G. Staffelbach, L. Y. M. Gicquel, and T. Poinsot. Using LES to study reacting flows and instabilities in annular combustion chambers. *Flow Turbul. Combust.*, 88:191–206, 2012.

[25] S. Evesque and W. Polifke. Low-order acoustic modelling for annular combustors: Validation and inclusion of modal coupling. *ASME Paper GT2002-30064*, 2002.

[26] B. Schuermans, V. Bellucci, and C. O. Paschereit. Thermoacoustic modeling and control of multi burner combustion systems. *ASME Paper GT2003-38688*, 2003.

[27] T. Sattelmayer and W. Polifke. Assessment of methods for the computation of the linear stability of combustors. *Combust. Sci. Technol.*, 175:453–476, 2003.

[28] L. Crocco and S-I. Cheng. *Theory of combustion instability in liquid propellant rocket motors*. AGARDograph No. 8. Butterworths Scientific Publications, 1956.

[29] C. O. Paschereit, B. Schuermans, W. Polifke, and O. Mattson. Measurement of transfer matrices and source terms of premixed flames. *J. Eng. Gas Turbines Power*, 124:239–247, 2002.

[30] F. Nicoud, L. Benoit, C. Sensiau, and T. Poinsot. Acoustic modes in combustors with complex impedances and multidimensional active flames. *AIAA Journal*, 45(2):426–441, 2007.

[31] E. Motheau, L. Selle, and F. Nicoud. Accounting for convective effects in zero-Mach-number thermoacoustic models. *J. Sound Vib.*, 333:246–262, 2014.

[32] F. Ni, M. Miguel-Brebion, F. Nicoud, and T. Poinsot. Accounting for acoustic damping in a Helmholtz solver. *AIAA Journal*, 55(4):1205–1220, 2017.

[33] K. Wieczorek and F. Nicoud. Prediction of thermoacoustic instabilities: Numerical study of Mach number effects. *16th AIAA/CEAS Aeroacoustics Conference, AIAA 2010-3927*, 2010.

[34] J. Gikadi. *Prediction of Acoustic Modes in Combustors using Linearized Navier-Stokes Equations in Frequency Space*. PhD thesis, Technische Universität München, 2014.

[35] M. Schulze, T. Hummel, N. Klarmann, F. Berger, B. Schuermans, and T. Sattelmayer. Linearized Euler equations for the prediction of linear high-frequency stability in gas turbine combustors. *J. Eng. Gas Turbines Power*, 139:031510/1–10, 2016.

[36] A. Albayrak and W. Polifke. An analytical model based on the G-equation for the response of technically premixed flames to perturbations of equivalence ratio. *Int. J. Spray Combust.*, 10(2):103–110, 2018.

[37] A. P. Dowling. Nonlinear self-excited oscillations of a ducted flame. *J. Fluid Mech.*, 346:271–290, 1997.

[38] N. Noiray, D. Durox, T. Schuller, and S. Candel. A unified framework for nonlinear combustion instability analysis based on the flame describing function. *J. Fluid Mech.*, 615:139–167, 2008.

[39] D. J. Griffiths. *Introduction to Quantum Mechanics*. Prentice Hall, 1995.

[40] P. Luchini and A. Bottaro. Adjoint equations in stability analysis. *Annu. Rev. Fluid. Mech.*, 46:493–517, 2014.

[41] L. Magri and M. P. Juniper. Sensitivity analysis of a time-delayed thermo-acoustic system via an adjoint-based approach. *J. Fluid Mech.*, 719:183–202, 2013.

[42] S.W. Rienstra and A. Hirschberg. An introduction to acoustics. *https://www.win.tue.nl/ sjoerdr/papers/boek.pdf*, 08 2018.

[43] F. A. Williams. *Combustion Theory*. Combustion Science and Engineering Series. The Benjamin/Cummings Publishing Company, Inc, 2nd edition, 1985.

[44] S. W. Rienstra. Impedance models in time domain including the extended Helmholtz resonator model. *AIAA Paper 2006-2686*, 2006.

[45] M. A. Heckl. Non-linear acoustic effects in the Rijke tube. *Acustica*, 72:63–71, 09 1990.

[46] K.I. Matveev and F.E.C. Culick. A study of the transition to instability in a Rijke tube with axial temperature gradient. *J. Sound Vib.*, 264(3):689–706, 2003.

[47] O. Bölke, D. A. Lacoste, and J. P. Moeck. Low-frequency sound generation by modulated repetitively pulsed nanosecond plasma discharges. *J. Phys. D*, 51(30):305203, 2018.

[48] A. P. Dowling. The calculation of thermoacoustic oscillations. *J. Sound Vib.*, 180(4):557–581, 1995.

[49] C. F. Silva, F. Nicoud, T. Schuller, D. Durox, and S. Candel. Combining a Helmholtz solver with the flame describing function to assess combustion instability in a premixed swirled combustor. *Combust. Flame*, 160(9):1743–1754, 2013.

[50] J. G. Aguilar, L. Magri, and M. P. Juniper. Adjoint-based sensitivity analysis of low-order thermoacoustic networks using a wave-based approach. *J. Comput. Phys.*, 341:163 – 181, 2017.

[51] R. L. Raun, M.W. Beckstead, J. C. Finlinson, and K. P. Brooks. A review of Rijke tubes, Rijke burners and related devices. *Prog. Energy Combust. Sci.*, 19(4):313–364, 1993.

[52] K. R. McManus, T. Poinsot, and S. M. Candel. A review of active control of combustion instabilities. *Prog. Energy Combust. Sci.*, 19(1):1 – 29, 1993.

[53] A. P. Dowling and S. R. Stow. Acoustic analysis of gas turbine combustors. *J. Propul. Power*, 19(5):751–764, 2003.

[54] R. D. Kronig and W.G. Penney. Quantum mechanics of electrons in crystal lattices. *Proc. R. Soc. Lond.*, 130:499–513, 1931.

[55] J. P. Moeck. *Analysis, Modeling, and Control of Thermoacoustic Instabilities*. PhD thesis, Technische Universität Berlin, 2010.

[56] R. M. Gray. Toeplitz and circulant matrices: A review. *Found. Trends Commun. Inf. Theory*, 2:155–239, 2006.

[57] J.-F. Bourgouin, D. Durox, J. P. Moeck, T. Schuller, and S. Candel. Self-sustained instabilities in an annular combustor coupled by azimuthal and longitudinal acoustic modes. *ASME Paper GT2013-95010*, 2013.

[58] J.-F. Bourgouin, D. Durox, T. Schuller, J. Beaunier, and S. Candel. Ignition dynamics of an annular combustor equipped with multiple swirling injectors. *Combust. Flame*, 160(8):1398 – 1413, 2013.

[59] J.-F. Bourgouin, D. Durox, J.P. Moeck, T. Schuller, and S. Candel. Characterization and modeling of a spinning thermoacoustic instability in an annular combustor equipped with multiple matrix injectors. *J. Eng. Gas Turbines Power*, 137:021503/1–11, 2014.

[60] J.-F. Bourgouin, D. Durox, J.P. Moeck, T. Schuller, and S. Candel. A new pattern of instability observed in an annular combustor: the slanted mode. *Proc. Combust. Inst.*, 35:3237–3244, 2015.

[61] D. Laera, K. Prieur, D. Durox, T. Schuller, S. M. Camporeale, and S. Candel. Impact of heat release distribution on the spinning modes of an annular combustor with multiple matrix burners. *ASME Paper GT2016-56309*, 2016.

[62] D. Laera, T. Schuller, K. Prieur, D. Durox, S. M. Camporeale, and S. Candel. Flame describing function analysis of spinning and standing modes in an annular combustor and comparison with experiments. *Combust. Flame*, 184:136 – 152, 2017.

[63] D. Laera, D. Yang, J. Li, and A. S. Morgans. A novel acoustic network model to study the influence of mean flow and axial temperature distribution on spinning limit cycles in annular combustors. *AIAA 2017-3191*, 2017.

[64] D. Yang and A. S. Morgans. Low-order network modeling for annular combustors exhibiting longitudinal and circumferential modes. *ASME Paper GT2018-76506*, 2018.

[65] A. Orchini, G. A. Mensah, and J. P. Moeck. Effects of nonlinear modal interactios on the thermoacoustic stability of annular combustors. *J. Eng. Gas Turbines Power*, 141(2):021002/1–10, 2018.

[66] M. L. Brillouin. Les électrons libres dans le métaux et le role des réflexions de Bragg. *J. Phys. Radium*, 1(11):377–400, 1930.

[67] M. I. Hussein. Reduced Bloch mode expansion for periodic media band structure calculations. *Proc. Royal Soc. A*, 465(2109):2825–2848, 2009.

[68] M. B. Giles and N. A. Pierce. An introduction to the adjoint approach to design. *Flow Turbul. and Combust.*, 65(3):393–415, Dec 2000.

[69] J. Donea and A. Huerta. *Finite Element Methods for Flow Problems*. Wiley, 2003.

[70] M. Hayashi, M. Ceze, and E. Volpe. Characteristics-based boundary conditions for the Euler adjoint problem. *Int. J. Numer. Methods Fluids*, 71(10):1297–1321, 2012.

[71] R. G. Parker and C. D. Jr. Mote. Exact boundary condition perturbation solutions in eigenvalue problems. *J. Appl. Mech.*, 63:128–135, 1996.

[72] A. Ndiaye. *Quantification des incertitudes pour la prédiction des instabilités thermoacoustiques dans les chambres de combustion*. PhD thesis, Université de Montpellier, 2017.

[73] G. Bärwolff. *Numerik für Ingenieure, Physiker und Informatiker*. Elsevier, 2007.

[74] A. Logg. *Automated Solution of Differential Equations by the Finite Element Method (Lecture Notes in Computational Science and Engineering)*. Springer, 2013.

[75] D. Braess. *Finite Elemente: Theorie, schnelle Löser und Anwendungen in der Elastizitätstheorie*. Springer-Verlag, 5 edition, 2013.

[76] S. M. Camporeale, B. Fortunato, and G. Campa. A finite element method for three-dimensional analysis of thermo-acoustic combustion instability. *J. Eng. Gas Turbine Power*, 133:015506/1–13, 2011.

[77] P. Wolf, G. Staffelbach, L. Y.M. Gicquel, J.-D. Müller, and T. Poinsot. Acoustic and large eddy simulation studies of azimuthal modes in annular combustion chambers. *Combust. Flame*, 159(11):3398 – 3413, 2012.

[78] G. Campa and S. M. Camporeale. Prediction of the thermoacoustic combustion instabilities in practical annular combustors. *J. Eng. Gas Turbine Power*, 136(9):091504/1–10, 2014.

[79] C. Sensiau. *Simulations numériques des instabilités thermoacoustiques dans les chambres de combustion annulaires*. PhD thesis, Université Montpellier II, 2008.

[80] M. Schmid, R. S. Blumenthal, M. Schulze, W. Polifke, and Sattelmayer T. Quantitative stability analysis using real-valued frequency response data. *J. Eng. Gas Turbines Power*, 135(12):121601/1–8, 2013.

[81] P. Subramanian, R. S. Blumenthal, W. Polifke, and R.I. Sujith. Distributed time lag response functions for the modelling of combustion dynamics. *Combust. Theor. Model.*, 19(2):223–237, 2015.

[82] L. Demanet and A. Townsend. Stable extrapolation of analytic functions. *Found. Comput. Math.*, pages 1–35, 2018.

[83] B. Gustavsen and A. Semlyen. Rational approximation of frequency domain responses by vector fitting. *IEEE Trans. Power Del.*, 14(3):1052–1061, 1999.

[84] B. Gustavsen. Improving the pole relocating properties of vector fitting. *IEEE Trans. Power Del.*, 21(3):1587–1592, 2006.

[85] J. López-Gómez and C. Mora-Corral. *Alegbraic Multiplicity of Eigenvalues of Linear Operators*. Operator Theory: Advances and Applications. Birkhäuser, 1 edition, 2007.

[86] S. Güttel and F. Tisseur. The nonlinear eigenvalue problem. *Acta Numer.*, 26:1–94, May 2017.

[87] V. Mehrmann and H. Voss. Nonlinear eigenvalue problems: a challenge for modern eigenvalue methods. *GAMM-Mitteilungen*, 27(2):121–152, 2004.

[88] W. E. Arnoldi. The principle of minimized iterations in the solution of the matrix eigenvalue problem. *Quart. Appl. Math.*, 9:17–29, 1951.

[89] R. Lehoucq, D. Sorensen, and C. Yang. *ARPACK Users' Guide*. Society for Industrial and Applied Mathematics, 1998.

[90] C. Sensiau, F. Nicoud, and T. Poinsot. A tool to study azimuthal standing and spinning modes in annular combustors. *Int. J. Aeroacoust.*, 8, 01 2009.

[91] C. Sensiau, F. Nicoud, M. van Gijzen, and J. W. van Leeuwen. A comparison of solvers for quadratic eigenvalue problems from combustion. *Int. J. Numer. Methods Fluids*, 56(8):1481–1487, 2008.

[92] P. Salas. *Aspects numériques et physiques des instabilités thermoacoustiques dans les chambres de combustion annulaires*. PhD thesis, Université Bordeaux I, 2013.

[93] T. Emmert, S. Bomberg, and W. Polifke. Intrinsic thermoacoustic instability of premixed flames. *Combust. Flame*, 162(1):75 – 85, 2015.

[94] F. Ni. *Accounting for complex flow-acoustic interactions in a 3D thermo-acoustic Helmholtz solver*. PhD thesis, Institut National Polytechnique de Toulouse, Université de Toulouse, April 2017.

[95] F. Bloch. Über die Quantenmechanik der Elektronen in Kristallgittern. *Z. Phys*, 52:555–560, 1929.

[96] C. Elachi. Waves in active and passive periodic structures: A review. *Proc. IEEE*, 64(12):1666–1698, 1976.

[97] S. D. M. Adams, R. V. Craster, and S. Guenneau. Bloch waves in periodic multi-layered acoustic waveguides. *Proc. Royal Soc. A*, 464:2669–2692, 2008.

[98] K. Manktelow, R. K. Narisetti, M. J. Leamy, and M. Ruzzene. Finite-element based perturbation analysis of wave propagation in nonlinear periodic structures. *Mech. Syst. Signal Process*, 39:32–46, 2012.

[99] F. Casadei and K. Bertoldi. Wave propagation in beams with periodic arrays of airfoil-shaped resonating units. *J. Sound Vib.*, 333(24):6532–6547, 2014.

[100] A. Khelif and A. Adibi, editors. *Phononic Crystals*. Springer-Verlag GmbH, 1. edition, 2015.

[101] G. Walz, W. Krebs, S. Hoffmann, and H. Judith. Detailed analysis of the acoustic mode shapes of an annular combustion chamber. *J. Eng. Gas Turbines Power*, 124:3–9, 2002.

[102] J. R. Dawson and N. A. Worth. Flame dynamics and unsteady heat release rate of self-excited azimuthal modes in an annular combustor. *Combust. Flame*, 161:2565–2578, 2014.

[103] G. A. Mensah and J. P. Moeck. Efficient computation of thermoacoustic modes in annular combustion chambers based on Bloch-wave theory. *ASME Paper GT2015-43476*, 2015.

[104] G. A. Mensah, G. Campa, and J. P. Moeck. Efficient computation of thermoacoustic modes in industrial annular combustion chambers based on Bloch-wave theory. *J. Eng. Gas Turbine Power*, 138(8):081502/1–7, 2016.

[105] J. I. Erdos and E. Alzner. Computation of unsteady transonic flows through rotating and stationary cascades I - method of analysis. techreport NASA Conractor Report 2900, NASA, 1977.

[106] G. Mouret, N. Gourdain, and L. Castillon. Adaptation of phase-lagged boundary conditions to large eddy simulation in turbomachinery configurations. *J. Turbomach.*, 138(4), 2015.

[107] L. E. Ballentine. *Quantum Mechanics: A Modern Development*. WORLD SCIENTIFIC PUB CO INC, 1998.

[108] C. M. Bender. Introduction to PT-symmetric quantum theory. *Contemp. Phys.*, 46(4):277–292, 2005.

[109] N. Sukumar and J. E. Pask. Classical and enriched finite element formulations for Bloch-periodic boundary conditions. *Int. J. Numer. Methh. Eng.*, 77(8):1121–1138, 2009.

[110] G. J. Tee. Eigenvectors of block circulant and alternating circulant matrices. *New Zealand J. Math.*, 36:195–211, 2007.

[111] P. J. Schmid, M. F. de Pando, and N. Peake. Stability analysis for n-periodic arrays of fluid systems. *Phys. Rev. Fluids*, 2:113902, Nov 2017.

[112] J. Lepers, W. Krebs, B. Prade, P. Flohr, G. Pollarolo, and A. Ferrante. Investigation of thermoacoustic stability limits of an annular gas turbine combustor test-rig with and without Helmholtz resonators. ASME paper GT2005-68246, 2005.

[113] S. R. Stow and A. P. Dowling. Modelling of circumferential modal coupling due to Helmholtz resonators. ASME paper GT2003-38168, 2003.

[114] N. Noiray, M. Bothien, and B. Schuermans. Investigation of azimuthal staging concepts in annular gas turbines. *Combust. Theor. Model.*, 15(5):585–606, 2011.

[115] M. Bothien, N. Noiray, and B. Schuermans. Analysis of azimuthal thermo-acoustic modes in annular gas turbine combustion chambers. *J. Eng. Gas Turbine Power*, 137:061505/1–8, 2015.

[116] E. Schrödinger. Quantisierung als Eigenwertproblem – dritte Mitteilung. *Ann. Phys.*, 80(13):437–490, 1926.

[117] T. Kato. *Perturbation Theory for Linear Operators*, volume 132 of *Grundlehren der mathematischen Wissenchaften*. Springer-Verlag, 1980.

[118] O. N. Kirillov. *Nonconservative Stability Problems of Modern Physics*, volume 14 of *De Gruyter Studies in Mathematical Physics*. de Gruyter, 1 edition, 2013.

[119] G. A. Mensah and J. P. Moeck. Assessment of thermoacoustic instabilities based on high-order adjoint perturbation theory. *Thermoacoustic Instabilities in Gas Turbines and Rocket Engines Paper GTRE-032*, 2016.

[120] G. A. Mensah and J. P. Moeck. Acoustic damper placement and tuning for annular combustors: An adjoint-based optimization study. *J. Eng. Gas Turbine Power*, 139(6):061501/1– 9, 2017.

[121] G. A. Mensah, L. Magri, A. Orchini, and J. P. Moeck. Effects of asymmetry on thermoacoustic modes in annular combustors: a higher-order perturbation study. *J. Eng. Gas Turbines Power*, 141(4):041030/1–8, 2018.

[122] L. Benoit and F. Nicoud. Numerical assessment of thermo-acoustic instabilities in gas turbines. *Int. J. Numer. Methods Fluids*, 2005.

[123] M. Juniper, L. Magri, M. Bauerheim, and F. Nicoud. Sensitivity analysis of thermo-acoustic eigenproblems with adjoint methods. *Stanford CTR Proceedings of the Summer Program 2014*, pages 189–198, 2014.

[124] L. Magri, M. Bauerheim, and M. P. Juniper. Stability analysis of thermo-acoustic nonlinear eigenproblems in annular combustors. Part I. sensitivity. *J. Comput. Phys.*, 2016.

[125] C. F. Silva, L. Magri, T. Runte, and W. Polifke. Uncertainty quantification of growth rates of thermoacoustic instability by an adjoint Helmholtz solver. *J. Eng. Gas Turbines Power*, 139:011901/1–11, 2016.

[126] L. Magri, M. Bauerheim, F. Nicoud, and M. P. Juniper. Stability analysis of thermo-acoustic nonlinear eigenproblems in annular combustors. Part II. uncertainty quantification. *J. Comput. Phys.*, 325:411–421, 2016.

[127] P. D. Miller. *Applied Asymptotic Analysis*, volume 75 of *Graduate Studies in Mathematics*. American Mathematical Society, Providence, RI, 2006.

[128] F. M. Fernández. *Introduction to Perturbation Theory in Quantum Mechanics*. CRC Press, 1 edition, 2000.

[129] L. Magri. *Adjoint methods in thermo-acoustic and combustion instability*. PhD thesis, Department of Engineering, University of Cambridge, November 2015.

[130] W.-J. Beyn. An integral method for solving nonlinear eigenvalue problems. *Linear Algebra Its Appl.*, (436):3839–3863, 2012.

[131] V. Hernandez, J. E. Roman, and V. Vidal. SLEPc: A scalable and flexible toolkit for the solution of eigenvalue problems. *ACM Trans. Math. Softw.*, 31(3):351–362, 2005.

[132] J. E. Roman, C. Campos, E. Romero, and A. Tomas. SLEPc users manual. Technical Report DSIC-II/24/02 - Revision 3.9, D. Sistemes Informàtics i Computació, Universitat Politècnica de València, 2018.

[133] T. Betcke, N. J. Higham, V. Mehrmann, C. Schröder, and F. Tisseur. NLEVP: A collection of nonlinear eigenvalue problems. *ACM Trans. Math. Softw.*, 39(2):7:1–28, February 2013.

[134] J. Kelleher. *Encoding Partitions As Ascending Compositions*. PhD thesis, Department of Computer Science University College Cork, December 2005.

[135] L. Bracci and L. E. Picasso. A simple iterative method to write the terms of any order of perturbation theory in quantum mechanics. *Eur. Phys. J.*, 127(10):119/1–5, 2012.

[136] P. Lancaster. A generalised Rayleigh quotient iteration for lambda-matrices. *Arch. Rational Mech. Anal.*, 8:309–322, 1961.

[137] S. D. Fisher. *Complex Variables: Second Edition*. DOVER PUBN INC, 2. edition, 1999.

[138] J. P. Boyd. The devil's invention: Asymptotic, superasymptotic and hyperasymptotic series. *Acta Appl. Math.*, 56:1–98, 1999.

[139] A. J. Cooper and D. G. Crighton. Global modes and superdirective acoustic radiation in low-speed axissymmetric jets. *Eur. J. Mech. B/Fluids*, 19:559–574, 2000.

[140] F. Giannetti and P. Luchini. Structural sensitivity of the first isntability of the cylinder wake. *J. Fluid Mech.*, 581:167–197, 2007.

[141] M. P. Juniper and B. Pier. The structural senitivity of open shear flows calculated with a local stability analysis. *Eur. J. Mech. B/Fluids*, 49:426–437, 2015.

[142] W. Paulsen. *Asymptotic Analysis and Perturbation Theory*. Chapman and Hall/CRC, 2014.

[143] H. Stahl. The convergence of diagonal Padé approximants and the Padé conjecture. *J. Comput. Appl. Math.*, 86(1):287 – 296, 1997. Dedicated to William B. Gragg on the ocassion of his 60th Birthday.

[144] G. A. Baker. Counter-examples to the Baker–Gammel–Wills conjecture and patchwork convergence. *J. Comput. Appl. Math.*, 179(1):1 – 14, 2005. Proceedings of the Conference on Orthogonal Functions and Related Topics, Held in Honor of Olav Njåstad.

[145] J. P. Moeck, M. Paul, and C. O. Paschereit. Thermoacoustic instabilities in an annular Rijke tube. ASME paper GT2010-23577, 2010.

[146] J.-F. Parmentier, P. Salas, P. Wolf, G.l Staffelbach, F. Nicoud, and T. Poinsot. A simple analytical model to study and control azimuthal instabilities in annular combustion chambers. *Combust. Flame*, 159(7):2374–2387, 2012.

[147] M. Bauerheim, F. Nicoud, and T. Poinsot. Progress in analytical methods to predict and control azimuthal combustion instability modes in annular chambers. *Phys. Fluids*, 28:021303/1–27, 2016.

[148] M. Bauerheim, A. Ndiaye, P. Constantine, G. Iaccarino, S. Moreau, and F. Nicoud. Uncertainty quantification of thermo-acoustic instabilities in annular combustors. *Stanford CTR Proceedings of the Summer Program 2014*, 2014.

[149] G. A. Mensah and J. P. Moeck. Limit cycles of spinning thermoacoustic modes in annular combustors: A Bloch-wave and adjoint-perturbation approach. *ASME Paper GT2017-64817*, 2017.

[150] F. Boudy, D. Durox, T. Schuller, G. Jomaas, and S. Candel. Describing function analysis of limit cycles in a multiple flame combustor. *J. Eng. Gas Turbine Power*, 133(6):061502/1–8, 2011.

[151] G. Ghirardo, M. P. Juniper, and J. P. Moeck. Weakly nonlinear analysis of thermoacoustic instabilities in annular combustors. *J. Fluid Mech.*, 805:52–87, 2016.

[152] A. Orchini. *Modelling and analysis of nonlinear thermoacoustic systems using frequency and time domain methods*. PhD thesis, Department of Engineering, University if Cambridge, 2016.

[153] C. Effenberger. *Robust solution methods for nonlinear eigenvalue problems*. PhD thesis, École Polytechnique Fédérale de Lausanne, 2013.

[154] B. T. Bandlow. *Zur Berechnung elektromagnetischer Eigenwertprobleme in der numerischen Simulation von Nanostrukturen mit periodischen und transparenten Randbedingungen*. PhD thesis, Universität Paderborn, 2011.

[155] E. Halley. Methodus nova accurata et facilis inveniendi radices aequationum quarumcumque generaliter, sine praevia reductione. *Philosophical Transactions*, 18:136–148, 1694.

[156] J. F. Traub. *Iterative Methods for the Solution of Equations*. Prentice-Hall, Englewood Cliffs, 1964.

[157] M. Petković and D. Herceg. On rediscovered iteration methods for solving equations. *J. Comput. Appl. Math.*, 107(2):275 – 284, 1999.

[158] A. S. Householder. *The numerical treatment of a single nonlinear equation*. McGraw-Hill, New York, 1970.

[159] P. Lancaster, A. S. Markus, and F. Zhou. Perturbation theory for analytic matrix functions: The semisimple case. *SIAM J. Matrix Anal. Appl.*, 25(3):606–626, 2003.

[160] L. N. Trefethen and M. Embree. *Spectra and Pseudospectra: The Behavior of Nonnormal Matrices and Operators*. Princeton University Press, 2005.

[161] J. Asakura, T. Sakurai, H. Tadano, T. Ikegami, and K. Kimura. A numerical method for nonlinear eigenvalue problems using contour integrals. *JSIAM Letters*, 1:52–55, 2009.

[162] B. Gavin, A. Miedlar, and E. Polizzi. FEAST eigensolver for nonlinear eigenvalue problems. *J. Comput. Sci.*, 27:107–117, 2018.

[163] L. M. Delvest and J. N. Lyness. A numerical method for locating the zeros of an analytic function. *Math. Comput.*, 21:543–560, 1967.

[164] M. Dellnitz, O. Schütze, and Q. Zheng. Locating all the zeros of an analytic function in one complex variable. *J. Comput. Appl. Math.*, 138:325–333, 2002.

[165] T. Johnson and W. Tucker. Enclosing all zeros of an analytic function–a rigorous approach. *J. Comput. Appl. Math.*, 228, 2009.

[166] M. Brebion. *Joint numerical and experimental Study of Thermo-Acoustic Instabilities*. PhD thesis, Institut National Polytechnique de Toulouse, Université de Toulouse, 2017.

[167] R. L. Devaney, B. Branner, L. Keen, A. Douady, P. Blanchard, J. H. Hubbard, and D. Schleicher. *Complex Dynamical Systems: The Mathematics Behind the Mandelbrot and Julia Sets*. American Mathematical Society, 1994.

[168] P. G. Constantine, E. Dow, and Q. Wang. Active subspace methods in theory and practice: Applications to kriging surfaces. *SIAM J. Sci. Comput.*, 36(4):A1500–A1524, 2014.

[169] A. Ndiaye, M. Bauerheim, S. Moreau, and F. Nicoud. Uncertainty quantification of thermoacoustic instabilities in a swirled stabilized combustor. *ASME Paper GT2015-44133*, 2015.

[170] G. A. Mensah, L. Magri, and J. P. Moeck. Methods for the calculation of thermoacoustic stability boundaries and Monte Carlo-free uncertainty quantification. *J. Eng. Gas Turbines Power*, 140(6):061501, 2018.

[171] A. P. Seyranian. Sensitivity analysis of multiple eigenvalues. *Mech. Struct. Mach.*, 21(2):261–284, 1993.

[172] T. Chantrasmi and G. Iaccarino. Forward and backward uncertainty propagation for discontinous system response using the Padé-Legendre method. *Int. J. Uncertain. Quan.*, 2(2):125–143, 2012.

[173] D. Xiu and G. E. Karniadakis. Modeling uncertainty in flow simulations via generalized polynomial chaos. *J. Comput. Phys.*, 187(1):137–167, 2003.

[174] E. T. Jaynes. Information theory and statistical mechanics. *Phys. Rev.*, 106:620–630, May 1957.

[175] G. A. Mensah, L. Magri, C. F. Silva, P. E. Buschmann, and J. P. Moeck. Exceptional points in the thermoacoustic spectrum. *J. Sound Vib.*, 433:124 – 128, 2018.

[176] W. D. Heiss. The physics of exceptional points. *J. Phys. A*, 45(44):444016, 2012.

[177] K. Ding, G. Ma, M. Xiao, Z. Q. Zhang, and C.T. Chan. Emergence, coalescence, and topological properties of multiple exceptional points and their experimental realization. *Phys. Rev. X*, 6:021007/1–13, 2016.

[178] V. Achilleos, G. Teocharis, O. Richoux, and V. Pagneux. Non-Hermitian acoustic metamaterials: Role of exceptional points in sound absorption. *Physical Review B*, 95:144303, 2017.

[179] A. P. Seyranian, O. N. Kirillov, and A. A. Mailybaev. Coupling of eigenvalues of complex matrices at diabolic and exceptional points. *J. Phys. A: Math. Gen.*, 38:1723–1740, 2005.

[180] F. Sogaro, P. Schmid, and A. S. Morgans. Sensitivity analysis of thermoacoustic instabilities. In *24th International Congress on Sound and Vibration*, 2017.

[181] C. F. Silva, K. J. Yong, and L. Magri. Thermoacoustic modes of quasi-1D combustors in the region of marginal stability. *ASME Paper GT2018-76921*, pages 1–12, 2018.

[182] M. P. Juniper and R. I. Sujith. Sensitivity and nonlinearity of thermoacoustic oscillations. *Annu. Rev. of Fluid Mech.*, 50(1):661–689, 2018.

[183] O. N. Kirillov. Eigenvalue bifurcation in multiparameter families of non-self-adjoint operator matrices. *Z. Angew. Math. Phys.*, 61:221–234, 2010.

[184] M. Sari, M. Shaat, and A. Abdelkefi. Frequency and mode veering phenomena of axially functionally graded non-uniform beams with nonlocal residuals. *Compos. Struct.*, 163(Supplement C):280 – 292, 2017.

[185] R. Lefebvre and N. Moiseyev. Localization of exceptional points with Padé approximants. *J. Phys. B*, 43(9):095401, 2010.

[186] L. N. Trefethen. *Spectral Methods in MATLAB (Software, Environments, Tools)*. SIAM: Society for Industrial and Applied Mathematics, 2001.

[187] O. Tammisola, F. Giannetti, V. Citro, and M. P. Juniper. Second-order perturbation of global modes and implications for spanwise wavy actuation. *J. Fluid Mech.*, 755:314–335, 2014.

[188] M. Merca. Fast algorithm for generating ascending compositions. *J. Math. Model. Algor.*, 11(1):89–104, 2012.

[189] P. J. Schmid and D. S. Henningson. *Stability and Transition in Shear Flows*. Springer, 2000.

[190] F. Tisseur and N. J. Higham. Structured pseudospectra for polynomial eigenvalue problems, with applications. *SIAM J. Matrix Anal. Appl.*, 23(1):187–208, 2001.